SYNTHESIS, STRUCTURAL AND MAGNETIC CHARACTERIZATION OF SPINEL NANOPARTICLE FERRITES WITH APPLICATIONS FOR ELECTROCHEMICAL SENSORS

by

Nadir S.E. Osman

BSc (Hons), MSc (Sudan University of Science and Technology)

Submitted in fulfilment of the academic
requirements for the degree of
Doctor of Philosophy in Physics
School of Chemistry and Physics
University of KwaZulu-Natal
Durban
South Africa

December 2015

Abstract

This thesis deals mainly with the structural and magnetic properties of Co-based nanoferrite samples that were simultaneously and symmetrically substituted by Mg, Sr, Mn and Ba cations. These samples were synthesized by glycol-thermal method from high purity metal chlorides as starting materials. The synthesized compounds included the series of $Mg_xSr_xMn_xCo_{1-3x}Fe_2O_4$ (x = 0, 0.1, 0.2, 0.3 and 1/3), $Ba_{0.5}Co_{0.5}Fe_2O_4$, $Sr_{1/3}Mn_{1/3}Co_{1/3}Fe_2O_4$ and $Ba_{1/3}Mn_{1/3}Co_{1/3}Fe_2O_4$ nanoferrites. The spinel phases were confirmed by X-ray diffraction (XRD). The sample morphologies were studied by high resolution transmission electron microscopy (HRTEM) and high resolution scanning electron microscopy (HRSEM). The synthesized samples show well-defined lattice fringes in HRTEM images indicative of the crystalline structure. The synthesized nanoparticles were obtained in the range of particles sizes from 7 to 9 nm. We have found a strong correlation between density and molecular weight of the synthesized $Mg_xSr_xMn_xCo_{1-3x}Fe_2O_4$ (x = 0, 0.1, 0.2, 0.3 and 1/3) compounds.

The magnetic properties were studied by using ^{57}Fe Mössbauer spectroscopy and magnetization measurements. The results reveal distortions in the hysteresis loops at low temperature which we associate with spin freezing effects. We also find good correlation between saturation magnetization and particle sizes. The temperature dependences of the saturation magnetization and coercive field show interesting trends. The magnetization data can be fitted by the modified Bloch's law and the coercive fields by Kneller's law at low temperature below the blocking temperature. The temperature dependent of coercivity follows T^{α} law with $\alpha \simeq 0.77$. However, the temperature dependence of the coercive field for $Ba_{0.5}Co_{0.5}Fe_2O_4$ follows Kneller's law with $\alpha = 1$. With increasing values of x, significant correlation between coercive field and the blocking temperatures have been observed. We also report coercive field enhancements at low temperature for the samples with x = 0, 0.1 and 0.2. The $Ba_{1/3}Mn_{1/3}Co_{1/3}Fe_2O_4$ sample shows increased magnetization from 66.5±0.3 emu/g at 300 K to 84.4±0.5 emu/g at 4 K. The Brunauer-Emmet-Teller (BET) surface area measurements and Barrett-Joyner-Halenda (BJH) measurements of $Ba_{0.5}Co_{0.5}Fe_2O_4$, $Sr_{1/3}Mn_{1/3}Co_{1/3}Fe_2O_4$ and $Ba_{1/3}Mn_{1/3}Co_{1/3}Fe_2O_4$ nanoparticle sam-

ples reveal the materials can be classified as mesoporous.

We have also studied electrochemical activities of some of the synthesized samples which show promise in the fabrication of sensors. $Ba_{0.5}Co_{0.5}Fe_2O_4$ and $Ba_{1/3}Mn_{1/3}Co_{1/3}Fe_2O_4$ nanoparticles show excellent electrochemical activity toward potassium ferricyanide $K_3[Fe(CN)_6]$. Modified electrodes by the nanoparticles in cyclic voltammetry (CV) have been used to determine trace amounts of ciprofloxacin (CFX) and didanosine (DDI) drugs. Two additional samples namely $Ti_{0.5}Ni_{0.5}Fe_2O_4$ nanoparticles and NiO-ZrO_2 nanocomposite produced by high energy ball milling were used to produce modified electrodes for CV. The $Ti_{0.5}Ni_{0.5}Fe_2O_4$ sample is interesting because single phase forms after about 1.5 hours of milling times and further milling seems to easily destroy the spinel phase. The NiO-ZrO_2 nano-composite was used for sensitive and selective determination of efavirenz, an Anti-HIV Drug. The critical parameter for electrochemical sensors based on CV appears to be significant increases in the surface area associated with the nanoparticles used to modify the glassy carbon electrode.

Preface

The research contained in this thesis was completed by the candidate while based in the Discipline of Physics, School of Chemistry and Physics, College of Agriculture, Engineering and Science, University of KwaZulu-Natal, Westville campus, South Africa from January 2013 to December 2015, under the supervision of Dr. Thomas Moyo. The contents of this work have not been submitted in any form to another university. Where use has been made of the work of others it is duly acknowledged in the text.

College of Agriculture, Engineering and Science

Declaration 1 - Plagiarism

Nadir S.E. Osman declares that

1. The research reported in this dissertation, except where otherwise indicated, is my original research.

2. This dissertation has not been submitted for any degree or examination at any university.

3. This dissertation does not contain other person's data, pictures, graphs or other information, unless specifically acknowledged as being sourced from other persons.

4. This dissertation does not contain other persons writings, unless specifically acknowledged as being sourced from other researchers. When other written sources have been quoted, then:

5. Their words have been re-written but general information attributed to them has been referenced.

6. Where their exact words have been used, their writing has been placed in italics and inside quotation, and referenced.

7. This dissertation does not contain text, graphics or tables copied and pasted from internet, unless specifically acknowledged, and the source being detailed in the dissertation and in the reference sections.

Conference contributions

1. The 20^{th} International Conference of magnetism (ICM 2015), Barcelona, Spain, 05-10 July, 2015.

2. The 60th Annual Conference of South African Institute of Physics (SAIP 2015), Port Elizabeth, South Africa, 29 June to 03 July, 2015.

3. The 59th Annual Conference of South African Institute of Physics (SAIP 2014), Johannesburg, South Africa, 07-11 July, 2014.

4. The 58^{th} Annual Conference of South African Institute of Physics (SAIP 2013), University of Zululand, South Africa, 08-12 July, 2013.

Signed: ..... Date: 11/12/2015

Name: Nadir S.E. Osman

Declaration 2

Publications

1. Simultaneous substitution of Ba, Mn and Co into Fe_3O_4 spinel structure: magnetic and electrochemical sensing properties of the synthesized nanoparticles, **Nadir S.E. Osman**, Neeta Thapliyal, Thomas Moyo and Rajshekhar Karpoormath. Oral presentation at 60th Annual Conference of South African Institute of Physics (SAIP 2015) (Submitted).

2. Influence of annealing process on the structure and magnetic behavior of $Ba_{0.5}Co_{0.5}Fe_2O_4$ nanoparticles, **Nadir S.E. Osman** and Thomas Moyo. Physics Procedia **75** (2015) 1133-1141.

3. Temperature dependence of coercivity and magnetization of $Sr_{1/3}Mn_{1/3}Co_{1/3}Fe_2O_4$ ferrite nanoparticles, **Nadir S.E. Osman** and Thomas Moyo. Journal of Superconductivity and Novel Magnetism **29** (2016) 361-366.

4. Investigation of magnetic and electrochemical sensing properties of novel $Ba_{1/3}Mn_{1/3}Co_{1/3}Fe_2O_4$ nanoparticles, **Nadir S.E. Osman**, Neeta Thapliyal, Thomas Moyo and Rajshekhar Karpoormath. New Journal of Chemistry **39** (2015) 9596-9604.

5. NiO-ZrO_2 Nanocomposite Modified Electrode for the Sensitive and Selective Determination of Efavirenz, an Anti-HIV Drug, Neeta Thapliyal, **Nadir S.E. Osman**, Harun Patel, Rajshekhar Karpoormath, Thomas Moyo and Rajkumar Patel. Royal Chemistry Society Advance **5** (2015) 40057-40064.

6. Structural and magnetic properties of $CoFe_2O_4$ nanoferrite simultaneously and symmetrically substituted by Mg, Sr and Mn, **Nadir S.E. Osman** and Thomas Moyo. Journal of Material Chemistry and Physics. **164** (2015) 138-144.

7. Synthesis and Characterization of $Ba_{0.5}Co_{0.5}Fe_2O_4$ Nanoparticle Ferrites: Application as Electrochemical Sensor for Ciprofloxacin, **Nadir S.E. Osman**,

Neeta Thapliyal, Wesam S. Alwan, Rajshekhar Karpoormath, Thomas Moyo. Journal of Material Science: Material in Electron. **24** (2015)1-9.

8. Magnetism variations and susceptibility hysteresis at the metal-insulator phase transition temperature of VO_2 in a composite film containing vanadium and tungsten oxides, Amos A. Akande, Koena E. Rammutla, Thomas Moyo, **Nadir S.E. Osman**, Steven S. Nkosi, Charl J. Jafta, Bonex W. Mwakikunga, Journal of Magnetism and Magnetic Material. **375** (2015) 1-9.

9. Structural and magnetic properties of $Sr_{0.5}Co_{0.5}Fe_2O_4$ nanoferrite, Hafiz M.I. Abdallah, Thomas Moyo, Itegbeyogene P. Ezekiel, **Nadir S.E. Osman**, Journal of Magnetism and Magnetic Material. **365** (2014) 83-87.

10. Structural and Magnetic Properties of $Mg_xSr_xMn_xCo_{1-3x}Fe_2O_4$ Nanoparticle ferrites, **Nadir S.E. Osman**, Thomas Moyo, Hafiz M. I Abdallah. in Proceedings of SAIP2013: the 58th Annual Conference of the South African Institute of Physics, edited by Roelf Botha and Thulani Jili (2014), pp. 128-133. ISBN: 978-0-620-62819-8. Available online at: http://events.saip.org.za/internalPage.py?pageId=13&confId=32.

Signed: ..... Date: 11/12/2015

Name: Nadir S.E. Osman

Dedication

To my mother Ehlam S.D. Neewbold who has done every thing possible to raise me up. I appreciate every moment that she shaded tears when I was in trouble, every moment that she laughed when I was just smiling and every moment that she prayed for me in private asking God to help me.
Thank you so much Mom.

Acknowledgements

My deepest gratitude goes to my supervisor Dr. Thomas Moyo who spared no effort to guide me throughout the research period. I am also grateful to Dr. Neeta Thapliyal for the help in doing the electrochemical measurements and Dr. Rajshekhar Karpoormath for the opportunity to perform the electrochemical measurements in his laboratory in the Department of Pharmaceutical Chemistry, Westville Campus, University of KwaZulu-Natal. I would like to thank the School of Chemistry and Physics, Westville Campus for providing all the possible help for me. I am also grateful to the Sudan University of Science and Technology (SUST) for the study leave. My thanks are extended to the National Research Foundation (NRF) of South Africa for the equipment grants for magnetization measurements in the Condensed Matter Physics Laboratory at Westville Campus. My special thanks are due to the members of the Electron Microscope Unit, Westville Campus, for the HRTEM and HRSEM measurements and to all group members of the Condensed Matter Physics laboratory at Westville Campus namely Dr J.Z. Msomi, Dr. H.M.I. Abdallah, I. Ezekiel, W. Dlamini, K. Mbela, N. Ngema and B. Ndlovu. Thank you for providing me with a happy working environment. Many thanks are also due to M.D. Farahani for helping with the digestion and sample preparation process for ICP measurements and T.N. Nzundu for the LaTex user guide.

My friends Faisal S.H. Ahmed, Gamal E. Mohamed, Ahmed T.A. Mohamed, Almontaser L.A.M. Bouray, Mohamed O. Awad, A. Hamid, M. Fadlalla, W. Alwan and Sidieg A. Zien were a constant source of support and encouragement for me. Finally, I am truly indebted to members of my family namely my dearest parents Ehlam S.D. Neewbold and Shams E. Osman, my lovely sisters Nisreen S.E. Osman and Nahid S.E. Osman, my strongest supporters (my brothers) Nezar S.E. Osman and Ayman S.E. Osman and my aunt Amani S.D Neewbold for always wishing me success in every venture. God bless you all.

Contents

List of Figures

List of Tables

Chapter 1

General overview of spinel ferrites

1.1 Ferrites

A ferrite is a ceramic mixed oxide of iron with other metals [1]. The term "ferrite" is derived from the latin equivalent "ferrum" which refers to iron [2, 3]. There are three different types of ferrites namely spinel, garnet and magnetoplumbite [4, 5, 6]. Spinel ferrites with the general formula $A\mathrm{Fe_2O_4}$ (where A is one or more of divalent elements such as Co, Mg, Zn, Mn, Ni, Sr or Ba) are considered to be important materials for applications purposes due to their interesting properties [7, 8, 9, 10]. Some of these properties include large surface to volume ratio [11], high values of electrical resistivity, high saturation magnetization, high permeability, low eddy current and dielectric losses [12], high specific heat capacity and large expansion coefficient [13]. The properties of spinel ferrites depend critically on the chemical composition, cation distribution and methods of preparation [14]. Many scientists and engineers have been attracted to the study of these types of magnetic materials because of the wide range of possible applications [15, 16] such as in sensors [17], catalysis [18], magnetocaloric refrigeration [19], microwave protection, information storage systems and biomedical (drug delivery and cancer treatment) [20], high frequency noise filters, transformer cores in power supplies, magnets for loudspeakers and motors [6, 21].

1.2 Spinel structure

The spinel structure has the space group of $F\tilde{d}3m$ [22]. Its chemical formula is of the form AB_2O_4, where A and B are metallic elements at tetrahedral and octahedral sites. The mineral $MgAl_2O_4$ which crystallizes in a cubic structure was the first spinel compound discovered by Bragg and Nishikawa [23]. The unit cell of a cubic spinel consists of eight sub-cubes called octants. When the metal ion is surrounded by four oxygen atoms, the site is referred to as a tetrahedral (A) site. In the octahedral (B) site the metal ion is surrounded by six oxygen atoms. There are sixty four tetrahedral sites which can be occupied by divalent elements and thirty two octahedral sites which can be occupied by trivalent elements [24]. In spinel ferrites, the trivalent ferric ions can also be replaced partially by tetravalent elements such as Ti or Ge. In this case, the valency of the ferric ion can be lowered by one [23]. Figure 1.1 shows the unit cell of a spinel structure [25] .

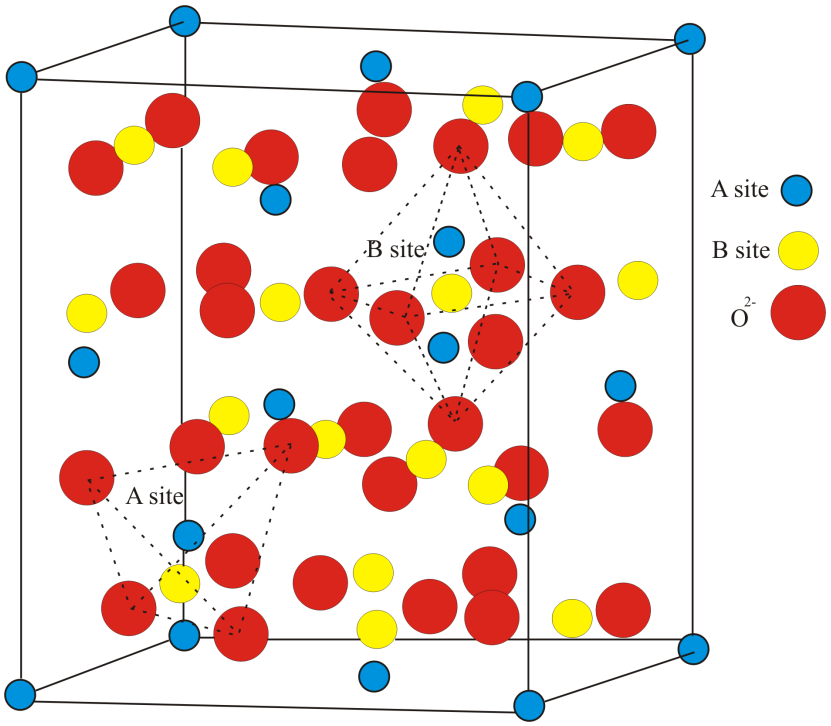

Figure 1.1: Spinel unit cell crystal structure.

The cation distribution plays an important role in determining the properties of spinel ferrites. The cations occupy sites where they have higher crystal field

stability energy (CFSE) [26, 27]. The cation distributions lead to different types of spinel ferrites which can be classified as normal, inverse and mixed spinels. The cation distribution of a spinel structure can be expressed by the formula ($M^{2+}_{1-\gamma}$ Fe^{3+})$[M^{2+}_{\gamma}Fe^{3+}_{2-\gamma}]O_4$, where M is one or more divalent elements [28, 29]. The ions in the first set of brackets are confined to the tetrahedral sites, while those in the second are in the octahedral site. The parameter γ is known as the degree of inversion. When $\gamma = 0$, the structure is known as normal spinel. In this case the divalent elements are located in the A sites only, whereas the trivalent elements are located in the B site. When $\gamma = 1$, the divalent elements can occupy half of the B sites and the trivalent elements can equally occupy both A and B sites [30]. This structure is known as the inverse spinel. In some cases spinels can be synthesized with γ values between 0 and 1. This intermediate range of γ values leads to what are known as mixed spinels [31]. However, in all cases the spinel structure is expected to be electrically neutral since the total positive charge (+64 e) balanced by a total negative charge (-64 e) of the oxygen ions [32].

1.3 Synthesis of ferrites

The synthesis method plays a significant role in determining structural, magnetic and electrical properties of ferrites [33]. Solid state reaction by ceramic method [34] and by high energy ball milling [35] are well known conventional methods for the synthesis of ferrite materials. The starting compounds in these methods are usually oxides or carbonates. The ceramic method requires a grinding process and double sintering at a relatively high temperature [36]. Very high temperature sintering can lead to mass loss by evaporation which may change the final chemical composition and intrinsic morphology of the final product. Samples synthesized by ceramic method or high energy ball milling are expected to have a degree of contamination from wear and tear of the grinding surface in contact with the sample [37, 38]. This possible contamination can prevent properties of synthesized samples from different sources to be re-producible. However, there is an advantage in using high energy ball milling technique because of the possibility of producing large quantities of

synthesized samples for a wide range of materials. The wet chemistry methods such as hydrothermal [39], glycol-thermal [40], combustion [41] and sol-gel [42, 43, 44] are also widely used to produce better crystalline ferrite materials at relatively low synthesis temperature. These synthesis methods tend to produce samples with higher purity, chemical homogeneity with small and uniform particle sizes. In the sol-gel method aqueous solutions of metal nitrates are mixed with a gelatine agent (such as polyacrylic acid). Nitric acid can be used in order to adjust the pH of the mixture. The final solution needs to be heated up to evaporate the water. The final gel is calcined at relatively low temperatures [45]. The synthesis of ferrite materials by combustion method requires dissolving of metal nitrate precursors in a urea-water solution [46]. The mixture is heated up until self-ignition starts. The urea in this case acts as a fuel. This synthesis method is usually accompanied with large quantity of smoke. Therefore the synthesis has to be performed under a fume cupboard. The method is considered to be simple and is a quick synthesis technique. The glycol-thermal method is considered to be a suitable technique for the synthesis of nanoferrites at relatively high pressure and low reaction temperature [40]. Metal chlorides or nitrates are used as starting materials in this method. This technique provides nanoparticles with well defined crystalline structure with relatively small particle sizes. The method has been used to produce most of the samples studied in this thesis. A detailed discussion of the glycol-thermal technique is given in chapter 3.

1.4 Magnetic properties

The magnetization of sample arises mainly from magnetic moments of unpaired electron spins in incompletely filled shells of atoms. For spinel oxides the magnetic properties are due to the difference in the magnetic moments of the cations in the sub-lattices (A- and B-sites). The magnetization of spinel ferrites materials can be expressed as $M = M_B - M_A$, where M_B and M_A are the magnetizations of the octahedral (B) and tetrahedral (A) sites respectively [47]. In spinel ferrites, the interaction between the moments are usually mediated by oxygen ions. This is known

as super-exchange interaction [48]. Three types of super-exchange interactions can be identified namely J_{AB} (A-O-B), J_{AA} (A-O-A) and J_{BB} (B-O-B). The strongest exchange interaction is J_{AB} for closely interacting cations with bond angle of 180°. The J_{BB} interaction is weaker followed by J_{AA} [32]. The measuring temperature plays an important role in determining the magnetization of a sample since the spin configuration can be frozen at low temperatures [49]. Evidence of spin freezing can be seen from either zero-field-cooled (ZFC) and field-cooled (FC) magnetization measurements or from the distortion of magnetic hysteresis loops at low temperatures. This can lead to significant changes in magnetization [50]. Furthermore, surface spins may also contribute to increasing the magnetic coercive fields at low temperatures [51]. The reduction in the particle sizes to nanoscale also reveals significant difference in the magnetic properties compared to bulk materials [52]. The magnetization increase drastically at nanoscale when the materials change from the so-called multi-domain to single domain structure [53]. The domain formation and its effect on magnetic properties are discussed in chapter 2.

1.5 Applications of ferrite materials

Technologically, ferrites are well known important materials due to their properties such as high magnetic permeability and low core energy loss [54]. $NiFe_2O_4$ spinel materials for example possess high saturation magnetization [55], low magnetic coercivity, chemical stability and excellent electrochemical performance [56]. $CoFe_2O_4$ ferrites have also attracted the interest of many researchers due to their high coercivity, moderate saturation magnetization, chemical stability, mechanical hardness, large magnetocrystalline anisotropy and magnetostrictive coefficient [57]. These properties make $CoFe_2O_4$ an excellent candidate for many technological applications such as magneto-optic recording medium, high density data storage devices, stress sensor and microwave absorption [58, 59, 60]. $MnFe_2O_4$ is also considered an important material for many application such as microwave applications and electronic devices because of its magnetic permeability and electrical resistivity [61]. The normal spinel $MgFe_2O_4$ ferrite is known to be a soft magnetic material with

n-type semiconductor properties [62]. Magnesium ferrite is also used in different applications such as in heterogeneous catalysis, adsorption, sensors and high-density recording media [63]. $MgFe_2O_4$ plays a role in microwave technology as a phase shifter, isolator and circulator [64]. Ferrites materials also used in biomedical application such as in hyperthermic cancer treatment as thermoseeds [65]. The ferrites can be targeted and be confined only to the infected sites without damaging the healthy cells. Generally, spinel ferrites (XFe_2O_4, $X = Mn^{2+}$, Fe^{2+}, Co^{2+}, Ni^{2+}) can be used as magnetic resonance imaging (MRI) contrast agents [66]. However, for bio-compatibility it is necessary that the ferrite samples should have high saturation magnetization, particles size less than 100 nm and narrow particle distributions [67]. The nanoparticles also need to be coated by suitable surface coating materials such as starch, chitosan, alginate, dextran, and polyethylene-glycol in order to avoid toxicity [68].

1.6 Electrochemical sensors

Magnetic nanoparticle materials are popular to study because they are used in many applications such as biosensors [66], drug delivery [69, 70] and detection of DNA hybridization [71]. For example, Ya *et al.* [72] have reported a novel electrochemical sensor for sensitive determination of paracetamol based on $LaNi_{0.5}Ti_{0.5}O_3/CoFe_2O_4$ nanoparticles. Wang *et al.* [73, 74] have incorporated magnetic nanoparticles to DNA molecules in order to investigate the electron transfer reactions. Chen *et al.* [75] have reported a biosensor for the reduction of H_2O_2 based on Fe_3O_4 nanoparticles. Some more recent the interests also include the determination of drugs in pharmaceutical dosages and in biological fluids using electrochemical sensors [76, 77]. The analysis of biological fluids like blood and urine can therefore be preformed more reliably. This is important in arriving at accurate diagnosis and management of several human disorders.

Electrochemistry is the branch of science that encompasses the interrelation of electrical and chemical effects. It involve several disciplines [78, 79, 80]. It deals with electron-transfer processes, analysis of oxidation-reduction reactions in chemical and

biological systems, catalysis and quantitative measurements of specimens under investigation [81, 82, 83, 84]. Identification and determination of trace amounts of concentrations of an electroactive specimen by electrochemical sensors are now widely used due to their simplicity, faster response, good detectability and relatively low cost compared to other sensors [85]. Electrochemical sensors have many advantages such as good performance in electrolyte sensing, compactness, large dynamic range, high sensitivity and small power requirements [86].

Electrochemistry at solid electrodes is now well-known [87, 88]. The use of chemically modified electrodes has led to the production of other types of electrode systems. This is usually achieved by incorporating an appropriate surface modifier to the electrode. The research on chemically modified electrodes has attracted a lot of interest due to potential applications to electrocatalysis, electrosynthesis and photosensitization [89]. Electrode modification with catalytically active molecules is an active field of research. The electrocatalytic property is considered to be one of the significant features of chemically modified electrodes because of the accelerated transfer of analyte electrons induced by immobilized charge mediators witch now often involve nanoparticles.

Some reviews in the fields of biosensors and electrochemical sensors show that nanomaterials can be used in the modification of electrodes [90, 91]. The introduction of nanoparticles with catalytic properties into electrochemical sensors and biosensors are expected to decrease overpotentials of many analytically important electrochemical reactions, and may cause reversibility of some redox reactions which normally are irreversible at common unmodified electrodes [92]. The simplicity of synthesis and functionalization of nanoparticles makes them suitable for the development and optimization of modified electrodes with specific detection of molecules of particular biological interest [93, 94, 95].

1.7 Motivation of the current work

Several researchers have channeled their efforts to improve and optimize the properties of spinel ferrites [96], [97], [98]. This includes substituting ferrites by various

cations with different valence states and also selecting suitable synthesis techniques. Furthermore, the particle sizes and mono-dispersity of the nanoparticles play significant roles in determining their properties. Among ferrite materials, spinel cobalt ferrite possesses interesting properties which make it a very important system to study. Although this compound has been extensively studied, there are still many other possible substitutions that have not yet been investigated. The present study of spinel cobalt ferrite-based nanoparticles is a contribution to this effort. The intention is to explore novel nanomaterials and provide better explanation for their properties. This kind of study we believe may lead to a better understanding of nanoparticle materials and possible applications. Therefore, we have concentrated on systematic substitutions of Mg, Sr, and Mn into spinel Co-based ferrites. The study comprises of synthesis, structural, magnetic and electrochemical applications of some synthesized nanoparticles.

Double substitutions by equal atomic proportions of elements A and B in the form of compounds of the type $A_{0.5}B_{0.5}Fe_2O_4$ are common. However, some possible substitutions have yet to be investigated.

Among some of the materials synthesized and studied in the present work include $Ba_{0.5}Co_{0.5}Fe_2O_4$. We have now extended the substitutions to three elements in equal atomic proportions. Therefore, we have synthesized and investigated structural and magnetic properties of $(Sr, Ba)_{1/3}Mn_{1/3}Co_{1/3}Fe_2O_4$ ferrite nanoparticles and $Mg_xSr_xMn_xCo_{1-3x}Fe_2O_4$ because properties of such compounds tend differ significantly from those of either AFe_2O_4 or BFe_2O_4. The synthesis of these compound was successfully achieved by glycol-thermal method. We have extended our investigation to include the effect of thermal annealing on structural and magnetic properties of this synthesized nanoparticles. The measuring temperature also plays an important role in determining the magnetic properties so magnetization measurements will be reported from about 2 K to 300 K to take advantage of the mini cryogen free measured system acquired in 2013.

In research of nanomaterials, phase formation sometimes is a challenge and required relatively long time. Therefore, finding a nanocompound has good properties and can easily form well defined crystal structure is interesting to investigate because

of reduction in costs and efforts. In this respect, we have synthesized nanomaterial of TiO and NiO into ferrite spinel structure. The synthesis was achieved by high energy ball milling for milling time of about 90 minutes. The study includes structure, magnetic and electrochemical activity of the synthesized $Ti_{0.5}Ni_{0.5}Fe_2O_4$ nanoparticles.

There is currently a lot of interest in the development and optimization of electrochemical sensors used in a cyclic voltammetry cell for detection of drugs. We have modified glassy carbon electrode (GCEs) by some nanoparticles samples in this study and find good electrochemical response towards potassium ferricyanide $K_3[Fe(CN)_6]$. We have used successfully modified GCEs by $Ba_{0.5}Co_{0.5}Fe_2O_4$ and $Ba_{1/3}Mn_{1/3}Co_{1/3}Fe_2O_4$ nanoparticles in the sensing of ciprofloxacin and didanosine drugs, respectively. In addition we synthesized a NiO-ZrO_2 nanocomposite by high energy ball milling. The intention was to use NiO supported ZrO_2 to enhance the current peak of the modified GCE. This is because the synthesized NiO-ZrO_2 nanocomposite tends to be a good conducting compound. Cyclic voltammetry measurements in this case show high sensitivity, selectivity and a low detection limit of the modified GCE\NiO-ZrO_2 nanocomposite towards Efavirenz an HIV drugs.

1.8 Thesis outline

This thesis consists of 10 chapters. In this chapter we have provided a brief introduction to the structure, synthesis and magnetic properties of spinel nanoferrites. The possible uses of nanoparticles as electrochemical sensors and a motivation for the present work has also been provided. In chapter 2 we introduce the fundamentals of magnetic properties of solids. Chapter 3 is concerned with principles of Mössbauer spectroscopy. The experimental techniques relevant to the present work are given in chapter 4. The results and discussion of the synthesized compounds are presented in chapters 5 to 9. Chapter 10 is reserved for general conclusions derived from the thesis.

Chapter 2

Basic principles of magnetism in solids

2.1 Historical background of magnetism

Magnetism has been known since the ancient Greeks, Chinese and pre-Columbus Americans [99, 100, 101]. The word magnetism itself comes from Magnesia, a region in Macedonia. An early magnet was a natural mineral called lodestone, now known as magnetite (Fe_3O_4) [102, 103]. The first magnetic device called the South Pointer used for navigation, had a centrepiece made from lodestone which was carved into the shape of a Chinese spoon. The magnetic effect of lodestone enabled the construction of compasses which were widely used for navigation by ancient Chinese, Arabs and later by Portuguese mariners. The force of attraction of magnets initially intrigued people and was associate with mysterious powers. In the middle ages (around the 10^{th} century) the lodestone was believed to have the power to heal people from muscle spasms and gout. The ancient Greeks also believed that a magnet possessed a soul because of its ability to move iron pieces. William Gilbert who published the book entitled De Magnete in 1600, was the first scientist to consider the earth as a massive magnet and to provide a credible explanation for magnetism [104].

2.2 Origin of magnetism

It is now well known that magnetic fields arise whenever electric charges move. In atoms, the origin of magnetism is due to the orbital and spin angular momenta of its electrons [104]. The contribution of orbital movement to the atomic magnetic moment can be derived similarly to an electrical circuit as

$$\mu_l = I\pi r^2 = \frac{-e\omega\pi r^2}{2\pi} = \frac{-e\omega r^2}{2}, \tag{2.2.1}$$

where I is the current, μ_l is the orbital magnetic moment, e is the electronic charge, ω is the angular frequency and r is the radius of the electron orbit. The magnitude of the orbital angular momentum $|\vec{l}|$ of an electron with the mass m_e is given by

$$|\vec{l}| = m_e\omega r^2. \tag{2.2.2}$$

Hence, its orbital magnetic moment $\vec{\mu}_l$ can be written as

$$\vec{\mu}_l = \frac{-e}{2m_e}\vec{l}. \tag{2.2.3}$$

Figure 2.1 illustrates the orbital moment $\vec{\mu}_l$ of an electron [104]. Similarly the magnetic moment due to intrinsic spin angular momentum of an electron $\vec{s}$ is given by

$$\vec{\mu}_s = \frac{-e}{m_e}\vec{s}. \tag{2.2.4}$$

It is known from Quantum Mechanics that the z-component of the angular momenta of $\vec{l}$ and $\vec{s}$ are quantized. This leads to

$$\mu_{l_z} = -\frac{e\hbar}{2m_e}m_l = -\mu_B m_l \tag{2.2.5}$$

and

$$\mu_{s_z} = -\frac{e\hbar}{m_e}m_s = -2\mu_B m_s \tag{2.2.6}$$

where the magnetic quantum numbers m_l and m_s take specific values namely $m_l = 0, \pm1, \pm2, \pm3, ...$ and $m_s = \frac{1}{2}, -\frac{1}{2}$ respectively. The natural unit for magnetic

moment is the Bohr magneton μ_B which is defined as

$$\mu_B = \frac{e\hbar}{2m_e}, \tag{2.2.7}$$

where $\hbar = \dfrac{h}{2\pi}$ is the reduced Planck's constant. The total magnetic moment of an atom can be calculated by using the Russell-Saunders coupling scheme and Hund's rules [105].

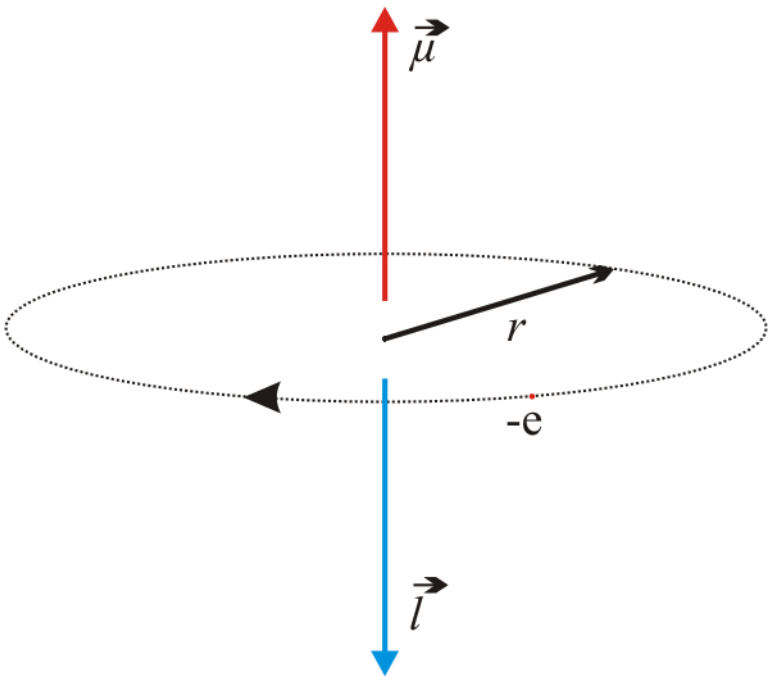

Figure 2.1: Orbital moment. The electron moves in a circular orbit where its quantized angular momentum $\vec{l}$ and magnetic moment $\vec{\mu}$ are oppositely directed.

In this scheme the orbital momenta of all the electrons couple together to form the total orbital momentum

$$\vec{L} = \sum \vec{l}_i. \tag{2.2.8}$$

The spins are also assumed to couple together to give the total spin momentum

$$\vec{S} = \sum \vec{s}_i. \tag{2.2.9}$$

Finally through spin-orbit coupling, $\vec{S}$ and $\vec{L}$ couple together to form total

$$\vec{J} = \vec{L} + \vec{S}. \tag{2.2.10}$$

This leads to the total magnetic moment of an atom in the direction of $\vec{J}$ to be expressed in the form

$$\vec{\mu}_J = -g\mu_B \vec{J}, \tag{2.2.11}$$

where g is known as the Landé g-factor which can easily be deduced to be

$$g = 1 + \frac{J(J+1) + S(S+1) - L(L+1)}{2J(J+1)}. \tag{2.2.12}$$

Magnetic moments are significant in elements with incomplete 3d and 4f shells. This is typically the case in transition metals and rare earth elements.

2.2.1 Magnetization

The magnetization $\vec{M}$ is defined as the total magnetic moment per unit volume usually measured under the influence of an external magnetic field [104]. For a homogeneously magnetised isotropic sample of volume V it is expressed as

$$\vec{M} = \frac{1}{V} \sum_{i=1}^{N} \vec{\mu_i}. \tag{2.2.13}$$

In a non-homogeneous system the magnetization can be expressed as

$$\vec{M} = \sum_{i=1}^{N} \frac{d\vec{\mu_i}}{dV}. \tag{2.2.14}$$

The equations 2.2.13 and 2.2.14 both show the volume dependence of the magnetization. The magnetostriction and thermal expansion effects can change the volume of a sample. In this case the magnetization per unit mass

$$\vec{\sigma} = \frac{1}{m} \sum_{i=1}^{N} \vec{\mu_i}, \tag{2.2.15}$$

is more reliable. The ratio between magnetization of a sample M to a magnetic field B_0 is called the magnetic susceptibility χ of a sample and can be expressed as

$$\chi = \mu_0 \frac{M}{B_0}, \tag{2.2.16}$$

where μ_0 is the magnetic permeability of free space. χ is a useful parameter that expresses the magnetic response of a sample to an applied magnetic field.

2.3 Classification of magnetic materials

From our previous discussions we can see that magnetization of a sample should arise due to the presence of magnetic moments and mutual interaction between them. The arrangement and orientation of magnetic moments can lead to different types of magnetic order in materials such as diamagnetism, paramagnetism, ferromagnetism, antiferromagnetism and ferrimagnetism to name a few.

2.3.1 Diamagnetism

Diamagnetism is a weak phenomena that occurs in all materials. Other magnetic effects may dominate and suppress diamagnetism in a sample. The induced magnetization in diamagnetic materials opposes the external magnetic field. The diamagnetic effect is associated with induced magnetic moments. This effect is small and gives a negative value of the magnetic susceptibility χ [106]. The magnetic susceptibility for the diamgnetic materials [107] can be expressed as

$$\chi = -\mu_0 n \frac{e^2}{6m_e} \sum_i^Z < {r_i}^2 >, \tag{2.3.1}$$

where Z is the atomic number, r_i are the orbital radii of the electrons and n is the number of atoms per unit volume. Possible applications of diamagnetic materials include magnetic field induced alignment of liquid crystals [108]. This can be used to align mesoporous inorganic samples like silica by filling its pores with liquid crystal surfactants. Diamagnetic levitation is also possible in the presence of a very strong applied magnetic field [109]. The magnetization of diamagnetic materials is usually difficult to observe because the effect tends to be small. The magnetic response of a diamagnetic material is illustrated in Figure 2.2 [110]. The figure also shows that

the magnetic susceptibility χ of a diamagnetic material is negative and constant as a function of temperature.

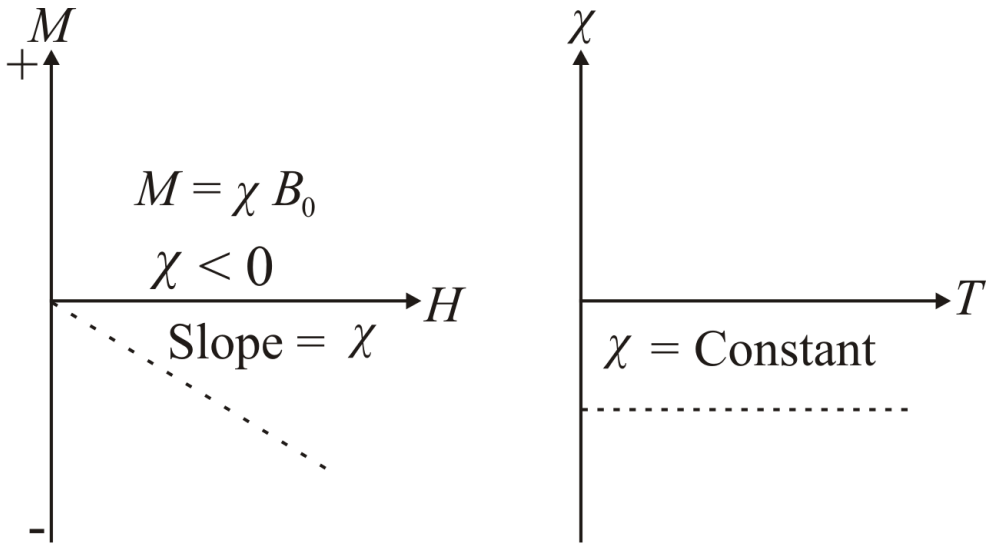

Figure 2.2: Magnetization M dependence on applied magnetic field B_0 and susceptibility χ dependence on measuring temperature T.

2.3.2 Paramagnetism

Randomly oriented magnetic moments are associated with paramagnetic materials. These types of magnetic materials have permanent magnetic moments. However, magnetic moments in paramagnets tend to be non-interacting or very weakly interacting. In fact each atom in a paramagnetic material is assumed to act as a small individual magnet. In the absence of an external magnetic field, a paramagnet shows no magnetization (Figure 2.3). Applying a magnetic field, orients and aligns magnetic moments in the external field direction. The magnetization also depends on temperature. Hence, both external magnetic field and measuring temperature are important factors in determining the magnetization of a paramagnetic material [111].

The classical approach for paramagnetism was derived by Paul Langevin in 1905. This approach considers the non-interacting magnetic moments. The magnetization depends on the external field B_0 and the angle θ of a moment with respect to the

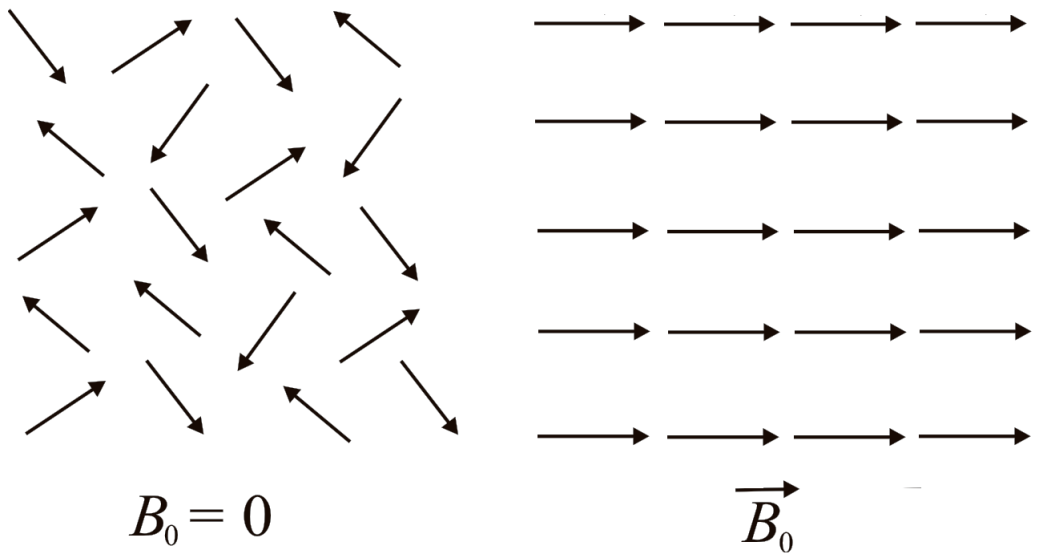

Figure 2.3: Magnetic moments of a paramagnetic material.

direction of B_0 [104]. The quantum approach takes into account quantized orbits and spin contributions to the magnetic moment. The magnetization in this case is described by the Brillouin function instead of the Langevin function. The magnetic energy E_{m_J} of each magnetic moment in a magnetic field B_0 is given as

$$E_{m_J} = -\vec{\mu_J}.\vec{B_0} = -g\mu_B m_J B_0, \tag{2.3.2}$$

where m_J is the magnetic quantum number. The thermal average of each magnetic moment $< \mu_J >$ can be described as

$$< \mu_J > = \sum g m_J \mu_B P(E_{m_J}), \tag{2.3.3}$$

where $P(E_{m_J})$ is the occupation probability of the energy level E_{m_J} which is defined based on the Maxwell-Boltzmann distribution

$$P(E_{m_J}) = \frac{e^{-E_{m_J}/k_B T}}{\sum m_J e^{-E_{m_J}/k_B T}}, \tag{2.3.4}$$

where k_B is the Boltzmann constant. The magnetization for n atoms per unit volume can easily be deduced to be

$$M = ng\mu_B J F(J, x), \tag{2.3.5}$$

where x represents the ratio of the Zeeman energy to the thermal energy

$$x = \frac{g\mu_B J B_0}{k_B T}. \tag{2.3.6}$$

The Brillouin function $F(J,x)$ is expressed as

$$F(J,x) = \frac{2J+1}{2J}\coth\left(\frac{(2J+1)x}{2J}\right) - \frac{1}{2J}\coth\left(\frac{x}{2J}\right). \tag{2.3.7}$$

In the case of $J = \frac{1}{2}$, the magnetization per unit volume for the system with $m_J = \pm\frac{1}{2}$ is given by

$$M = ng\mu_B J \tanh x. \tag{2.3.8}$$

For several experimental situations, the Brillouin function can be approximated by the Taylor series as follows

$$F(J,x) \approx \left(\frac{J+1}{3J}\right)x - \left(\frac{(J+1)[J+1]^2 + J^2}{90J^2}\right)x^3 + ... \tag{2.3.9}$$

In relatively low magnetic fields and at high temperatures (small value of x), $F(J,x) \simeq \frac{J+1}{3J}x$. This leads to the Curie law for susceptibility

$$\chi = \frac{C}{T}, \tag{2.3.10}$$

where C is known as the Curie constant expressed as

$$C = \frac{n\mu_0 g^2 \mu_B^2 J(J+1)}{3k_B}. \tag{2.3.11}$$

The Curie law for non-interacting magnetic moments shows a magnetic susceptibility that depends inversely on temperature. This law is applicable in several rare earth compounds and diluted salts of transition metals. In materials where the interaction between magnetic moments cannot be ignored, the Curie law is replaced by the Curie-Weiss law where

$$\chi = \frac{C}{T - \theta_P}. \tag{2.3.12}$$

In this case, θ_P is called the paramagnetic Curie temperature.

2.3.3 Ferromagnetism

Ferromagnetic materials are associated with spontaneous parallel alignment of magnetic moments. This is associated with strong interaction between magnetic moments via exchange interactions. In ferromagnets, the exchange interaction is positive. The perfect alignment of magnetic moments (Figure 2.4) is presumed at $T = 0$ K. As the temperature increases, the interaction between magnetic moments is overcome by thermal energy which leads to the disorder of magnetic moments. The collapse of the ferromagnet order occurs at the so-called Curie temperature T_C [112]. The magnetic moments of a ferromagnetic material stay ordered below T_C and above T_C Curie-Weiss law is observed.

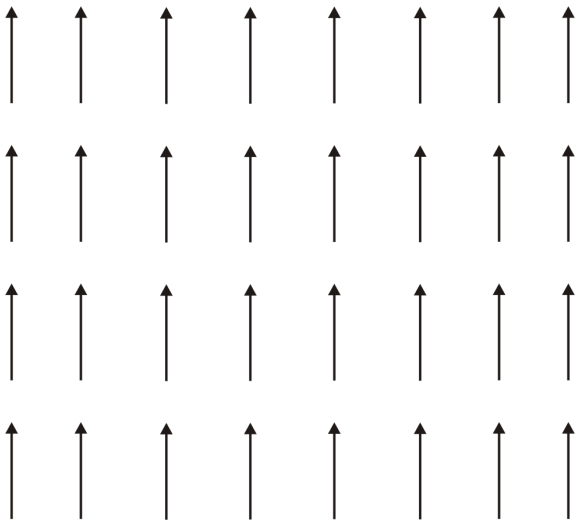

Figure 2.4: Magnetic moments of a ferromagnetic material at $T = 0$ K.

In order to account for the origin of ferromagnetism, in 1907, Weiss proposed an internal magnetic field B_{in} which could be responsible for aligning magnetic moments. In the so-called mean field theory approximation, the internal field is assumed to be

$$B_{in} = \lambda M_S, \tag{2.3.13}$$

where λ is the molecular field coefficient. Justification for this theory was provided by Heisenberg in 1928 [104] who introduced the idea of exchange interactions to

account for the alignment of magnetic moments. In the presence of an external magnetic field B_0 the effective magnetic field on a magnetic moment in a sample can be expressed as

$$B_{eff} = \vec{B}_0 + \lambda \vec{M}_S. \tag{2.3.14}$$

We can now generalise equations 2.3.5 and 2.3.6 for paramagnetism to induced an internal field. Hence, for a system consisting of n magnetic atoms or ions per unit volume the spontaneous magnetization can be given by

$$M_S(B_0, T) = ngJ\mu_B F(J, x), \tag{2.3.15}$$

where x is redefined as

$$x = \frac{g\mu_B J(B_0 + \lambda M_S)}{k_B T}. \tag{2.3.16}$$

In this case, the spontaneous magnetization would still exist even in absence of external magnetic field to give

$$M_S(0, T) = M_S(0, 0)F(J, x), \tag{2.3.17}$$

where $M_S(0,0)$ is the saturation magnetization. The reduced magnetization can be expressed as

$$\frac{M_S(0, T)}{M_S(0, 0)} = \frac{M_S(T)}{M_S(0)} = F(J, x). \tag{2.3.18}$$

From equation 2.3.16 the reduced magnetization can also be expressed as

$$\frac{M_S(T)}{M_S(0)} = (\frac{k_B T}{ng^2\mu_B{}^2\lambda J^2})x. \tag{2.3.19}$$

Figure 2.5 displays the graphical solutions to equations 2.3.18 and 2.3.19 [113]. The straight lines show the magnetization as a function of temperature. However, the last possible solution at the intersection point ($T = T_C$) leads to zero magnetization. The point of intersection between the two curves corresponds to a possible magnetic state of a sample. At $T = T_C$ the intersection occurs only at the origin for which

$M_S(T_C) = 0$. The temperature T_C is called the Curie temperature of the sample. Through this point, the sample transforms from ordered to disordered magnetic state. Near T_C the Brillouin function is approximately $F(J,x) \simeq \frac{J+1}{3J}x$. The tangent to the curve for equation 2.3.18 is the same as the slope of equation 2.3.19. Hence we can easily show that

$$\lambda = \frac{3k_B T_C}{nJ(J+1)g^2\mu_B^2}. \tag{2.3.20}$$

If T_C is known we can easily estimate λ from this equation.

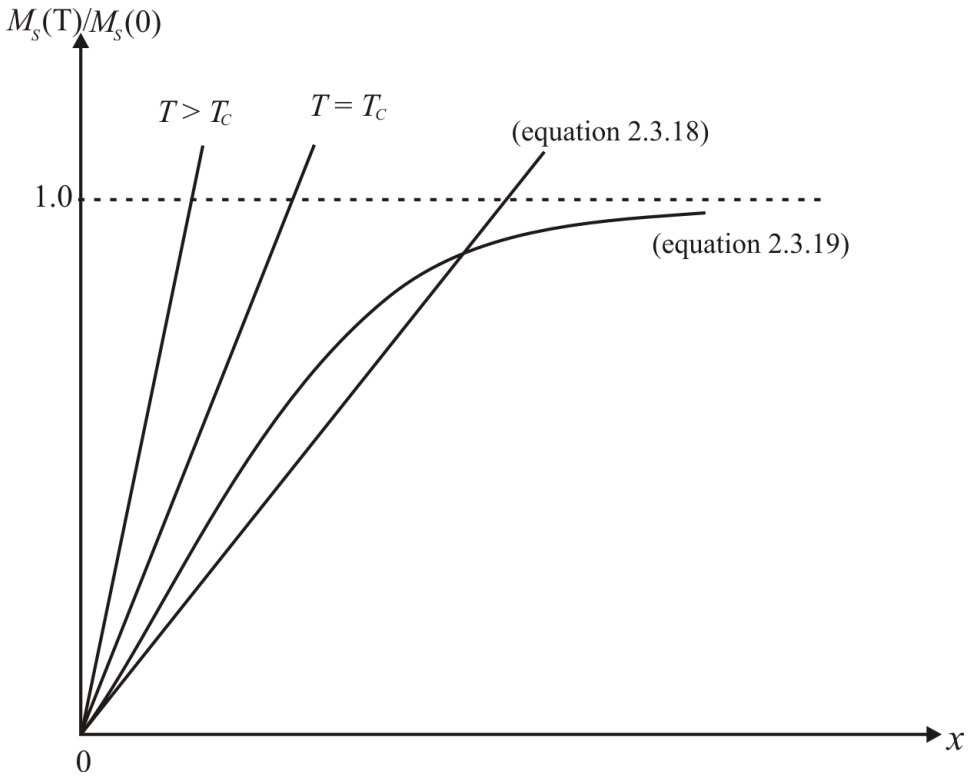

Figure 2.5: Graphical solution of equations 2.3.18 and 2.3.19.

At low temperatures $x \gg 1$ the Brillouin function is approximately

$$F(J,x) \approx 1 - \frac{1}{J}exp(-\frac{x}{J}). \tag{2.3.21}$$

In this case we expect the spontaneous magnetization to vary as

$$\frac{M_S(T)}{M_S(0)} \approx 1 - \frac{1}{J}exp(-\frac{\beta}{T}), \tag{2.3.22}$$

where the parameter β is a constant. What is observed at low temperature is a magnetization that varies according to spin wave excitations given by

$$\frac{M_S(T)}{M_S(0)} = 1 - AT^{3/2} + ... \tag{2.3.23}$$

However, The temperature dependence of the magnetization that tends to be observed over a wide temperature range has the form [114]

$$\frac{M_S(T)}{M_S(0)} = \left(1 - \frac{T}{T_C}\right)^{\frac{1}{2}}. \tag{2.3.24}$$

Above T_C we can easily deduce the Curie-Weiss law for the paramagnetic susceptibility (equation 2.3.12). Experimentally, for many magnetic materials, we find $\theta_P > T_C$.

2.3.4 Antiferromagnetism

Antiferromagnetic materials have equal anti-parallel magnetic moments (see Figure 2.6). This arrangement of magnetic moments leads to zero net magnetization in the absence of an applied magnetic field. This arrangement of the magnetic moments is associated with negative exchange interactions. In this case, the alignment occurs below the so-called Néel temperature T_N. Antiferromagnetic materials can be modelled on the basis of a two sublattice model A and B with saturation magnetization M_A and M_B respectively in opposite directions. At 0 K, the sublattices will have maximum values of saturation magnetizations. The magnetization decreases as the temperature increases. At $T < T_N$, the saturation magnetization is due to the negative interaction between the two sublattices. However, above the Néel temperature, the magnetic moments in sublattices become disordered and show evidence of the paramagnetic state.

Similar to ferromagnetic materials, the mean field theory can be applied to antiferromagnetic materials. The interaction between first and second nearest neighbour magnetic moments creates an internal magnetic field B_{in} in the sublattices

$$B_{in}^A = \lambda_{AA} M_A + \lambda_{AB} M_B, \tag{2.3.25}$$

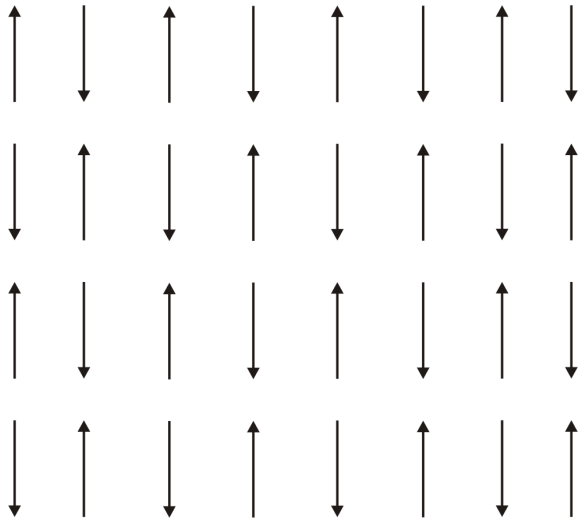

Figure 2.6: Magnetic moments of an antiferromagnetic material.

and

$$B_{in}^{B} = \lambda_{BA} M_A + \lambda_{BB} M_B, \tag{2.3.26}$$

where λ_{AB} and λ_{BA} are the molecular field coefficients of first neighbours. Whilst λ_{AA} and λ_{BB} are the molecular field coefficients of second nearest neighbours. Hence we can expect

$$\lambda_{AB} = \lambda_{BA} = -\lambda_1, \tag{2.3.27}$$

and

$$\lambda_{AA} = \lambda_{BB} = \lambda_2, \tag{2.3.28}$$

where λ_1 and λ_2 are constants. Therefore, equation 2.3.25 and equation 2.3.26 can be written as

$$B_{in}^{A} = M_A(\lambda_1 - \lambda_2), \tag{2.3.29}$$

and

$$B_{in}^{B} = M_B(\lambda_1 - \lambda_2). \tag{2.3.30}$$

The magnetization in the subalttices can be determined to be

$$M_i = \frac{ng\mu_B JB}{2} F(J, x_i), \tag{2.3.31}$$

where i represents the sublattice A or B and

$$x_i = \frac{g\mu_B JB_i^i n}{k_B T}. \tag{2.3.32}$$

Below T_N and in the absence of an applied magnetic field the magnetization of an antiferromagetic material is given by

$$\vec{M}_A + \vec{M}_B = 0. \tag{2.3.33}$$

Therefore, we may rewrite equation 2.3.32 as

$$x_i = \frac{Jg\mu_B}{k_B T}(\lambda_1 - \lambda_2)\vec{M}_i = \frac{J_g \mu_B \lambda M}{k_B T}, \tag{2.3.34}$$

where $\lambda = \lambda_1 - \lambda_2$. The magnetization at sublattices can be expressed as

$$M_i(T) = \frac{n}{2} g\mu_B J F(J, x). \tag{2.3.35}$$

The magnetization becomes zero at $T = T_N$. Hence we can easily show that

$$T_N = \frac{ng^2\mu_B^2 J(J+1)}{2k_B\mu_0}\lambda. \tag{2.3.36}$$

Above T_N the susceptibility of an antiferromagnetic material can be expressed in the form of Curie-Weiss law

$$\chi = \frac{C}{T - \theta_P}, \tag{2.3.37}$$

where the paramagnetic Curie temperature θ_P is negative. Below T_N the sample can respond to an applied magnetic field. However, the direction of the applied magnetic field plays a significant role in determining the resulting magnetization. This leads to parallel and perpendicular susceptibilities $\chi_{\parallel}$ and $\chi_{\perp}$ respectively. The average total magnetic susceptibility for a poly-crystalline sample can be shown to be [104]

$$\chi = \frac{1}{3}\chi_{\parallel} + \frac{2}{3}\chi_{\perp}. \tag{2.3.38}$$

2.3.5 Ferrimagnetism

Ferrimagnetism is associated with unequal magnetic moments that align in anti-parallel directions [115, 112]. This leads to a net magnetization similar to a ferromagnet. Figure 2.7 shows a typical spin alignment for a ferrimagnetic material. Brilliouin function can be also used to calculate magnetization at each sublattice A or B. The net magnetization can be modelled in general as

$$M = M_A - (1 - \lambda)M_B, \tag{2.3.39}$$

where $M_A \neq M_B$ the magnetization for a ferrimagnet. The value of λ decides the magnetic order of a material. Equation 2.3.39 can be used to model ferromagnetism and antiferromagnetism depend on the choice of λ and relative sizes of M_A and M_B.

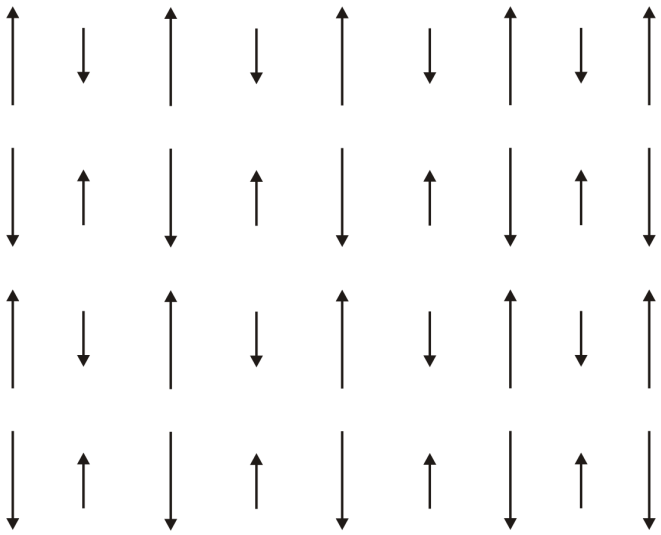

Figure 2.7: Magnetic moments of a ferrimagnetic material.

A ferrimagnet will therefore have a Curie temperature T_C and spontaneous magnetization below T_C. However in some cases, the magnetization becomes zero at a critical temperature known as a compensation temperature T_{comp} (see Figure 2.8 [104]).

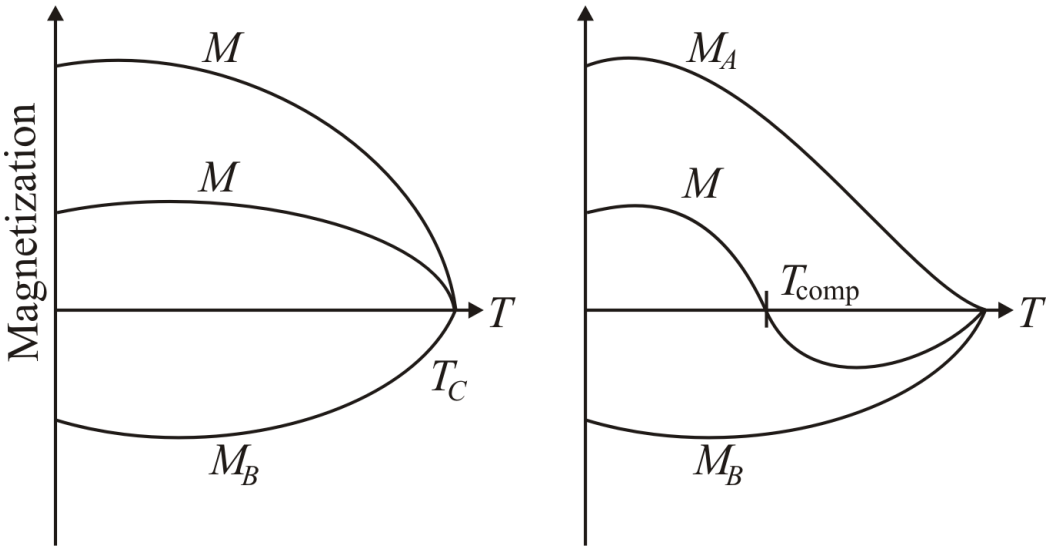

Figure 2.8: Sublattice magnetization of a ferrimagnetic material.

The susceptibility χ of a ferrimagnetic material above T_C follows a modified form of the Curie-Weiss law which can take the form

$$\frac{1}{\chi} = \frac{T - \theta_P}{C_A + C_B} - \frac{C'}{T - \theta'}, \tag{2.3.40}$$

where C_A, C_B, C' and θ' are the microscopic parameters of a ferrimagnetic material.

2.4 Magnetic exchange interactions

The origin of ferromagnetic, antiferromagnetic and ferrimagnetic ordering is therefore due to the magnetic exchange interaction as proposed in the Heisenberg model [116]. In general, magnetic interactions can be classified into dipole-dipole and exchange interactions. Dipole-dipole interaction leads to small magnetic ordering of magnetic moments. Whereas, exchange interactions are responsible for significant ordering of magnetic moments. There are two types of exchange interactions namely direct and indirect exchange interactions.

2.4.1 Dipole-dipole interaction

The interaction energy (E_d) between two magnetic dipoles $\vec{\mu_i}$ and $\vec{\mu_j}$ depends on the distance between them. This can be expressed as

$$E_d = \frac{\mu_0}{4\pi r^3}\left(\vec{\mu_i}.\vec{\mu_j}\frac{3}{r^2}(\vec{\mu_i}.\vec{r})(\vec{r_j}.\vec{r})\right). \tag{2.4.1}$$

We can estimate the strength of the magnetic dipole interaction from equation 2.4.1 by assuming two identical magnetic moments μ_B separated by a ~ 8 Å in nanoferrites. Therefore,

$$|E_d| \simeq \frac{\mu_0\mu_B^2}{2\pi a^3} \sim 3 \times 10^{-24}\text{J}. \tag{2.4.2}$$

Hence the magnetic interactions energy $E_d \sim 3 \times 10^{-24}$ J per atom. The magnetic ordering in ferromagnetic materials is destroyed at the Curie temperature $T_C \sim 10^2$ K. A measure of the strength of magnetic interaction is thermal energy $k_BT_C \sim 1 \times 10^{-21}$ J. Clearly $E_d \ll k_BT_C$. Hence dipole-dipole interactions can not be responsible for collinear arrangement of magnetic moments.

2.4.2 Direct exchange interaction

In the case of magnetic atoms that are close to each other, the interaction between magnetic moments can occur through partially overlapping localised atomic orbitals. This is known as direct exchange interaction. It is an electrostatic effect based on Coulomb interaction and Pauli exclusion principle. We can illustrate the origin of direct exchange interaction by considering the interaction of two electrons that are being shared by two covalently bounded atoms A and B. The total wave function for the two electrons has to be antisymmetric because electrons are fermions. The total wave function consists of the singlet (ψ_S) state and triplet (ψ_T) states defined by

$$\psi_S = [\psi_A(1)\psi_B(2) + \psi_A(2)\psi_B(1)][\alpha(1)\beta(2) - \alpha(2)\beta(1)] \tag{2.4.3}$$

and

$$\psi_T = [\psi_A(1)\psi_B(2) - \psi_A(2)\psi_B(1)] = \begin{cases} \alpha(1)\alpha(2) \\ \beta(1)\beta(2) \\ \alpha(1)\beta(2) + \alpha(2)\beta(1) \end{cases} \tag{2.4.4}$$

where α and β denote spin-up ($m_s = -\frac{1}{2}$) and spin-down ($m_s = \frac{1}{2}$) states. ψ_A and ψ_B are spatial wave functions for each atom. Equations 2.4.3 and 2.4.4 have different spatial wave functions and hence have different energies. The energies of the two possible situations can be obtained from the Hamiltonian $\hat{H}$ as

$$E_S = \int \psi_S^* \hat{H} \psi_S dr_1 dr_2 \tag{2.4.5}$$

and

$$E_T = \int \psi_T^* \hat{H} \psi_T dr_1 dr_2. \tag{2.4.6}$$

Hence the energy difference can be expressed as

$$E_S - E_T = 2 \int dr_1 dr_2 \left[\psi_A^*(1)\psi_B^*(2) V(\vec{r_1}, \vec{r_2}) \psi_A(2)\psi_B(1) \right] = 2J_{12}, \tag{2.4.7}$$

where $V(\vec{r_1}, \vec{r_2})$ is the electrostatic potential energy between the electrons. J_{12} is known as the exchange integral. If $J_{12} > 0$, E_T will be the preferred energy ($E_S > E_T$). This means that spins between the two electrons prefer to be parallel to each other as in ferromagnetic alignment. In the case of $J_{12} < 0$, E_S will be the preferred energy ($E_S < E_T$). This implies anti-parallel spin alignment (antiferromagnetic coupling). In general for several spin $\vec{S_i}$, the energy of interaction between spins can be expressed by the Heisenberg Hamiltonian

$$H_E = -\sum_{i>j} J_{ij} \vec{S_i}.\vec{S_j}. \tag{2.4.8}$$

For a bound state of spins, $H_E < 0$. If $J_{ij} > 0$, the minimum energy occurs for parallel spins (ferromagnetism), while for $J_{ij} < 0$, the minimum energy occurs for antiparallel spins (anti-ferromagnetism). By using the Heisenberg model, the mean

field theory can easily be justified. This is achieved by replacing the spins and H_E by their thermal averages as

$$< H_E> = -2\sum_{i>1} J_{ij} < \vec{S}_i > . < \vec{S}_j >. \tag{2.4.9}$$

For a large number of atoms n per unit volume, the magnetization can be related to the thermal average of the spins where

$$\vec{M}_i = ng\mu_B < \vec{S}_i >. \tag{2.4.10}$$

Equations 2.4.10 can therefore be rewritten as

$$< H_E> = -\sum_{i>1} \left(\frac{2J_{ij}\vec{M}_i}{n^2 g^2 \mu_B^2} \right) . \vec{M}_j = -\vec{B_{int}} . \vec{M}. \tag{2.4.11}$$

For a homogeneously magnetized sample $\vec{M}_i = \vec{M}_j = \vec{M}$. $\vec{B_{int}}$ is an internal magnetic field assumed to exist which can be defined as

$$\vec{B_{int}} = \left(\sum_{i>1} \frac{2J_{ij}}{n^2 g^2 \mu_B^2} \right) . \vec{M} = \lambda \vec{M} \tag{2.4.12}$$

where λ is the molecular field constant. This confirms the mean field theory on the basis of the Heisenberg model.

2.4.3 Indirect exchange interaction

In the case of magnetic moments that are far from each other, interaction between them can occur through intermediary atoms or electrons. This is known as an indirect interaction. If the intermediary is a non-magnetic ion the coupling is called super-exchange interaction. The indirect exchange interaction can also be mediated by the polarization of conduction electrons. This is called the Ruderman-Kittel-Kasuya-Yosida (RKKY) interaction. The exchange integral $J_{eff}(x)$ in this case is long ranged and is an oscillatory function of distance x between spins. A typical form of the effective exchange integral $J_{eff}(x)$ is illustrated in Figure 2.9 [104]. The ferromagnetic or antiferromagnetic depends on the sign of J_{eff}.

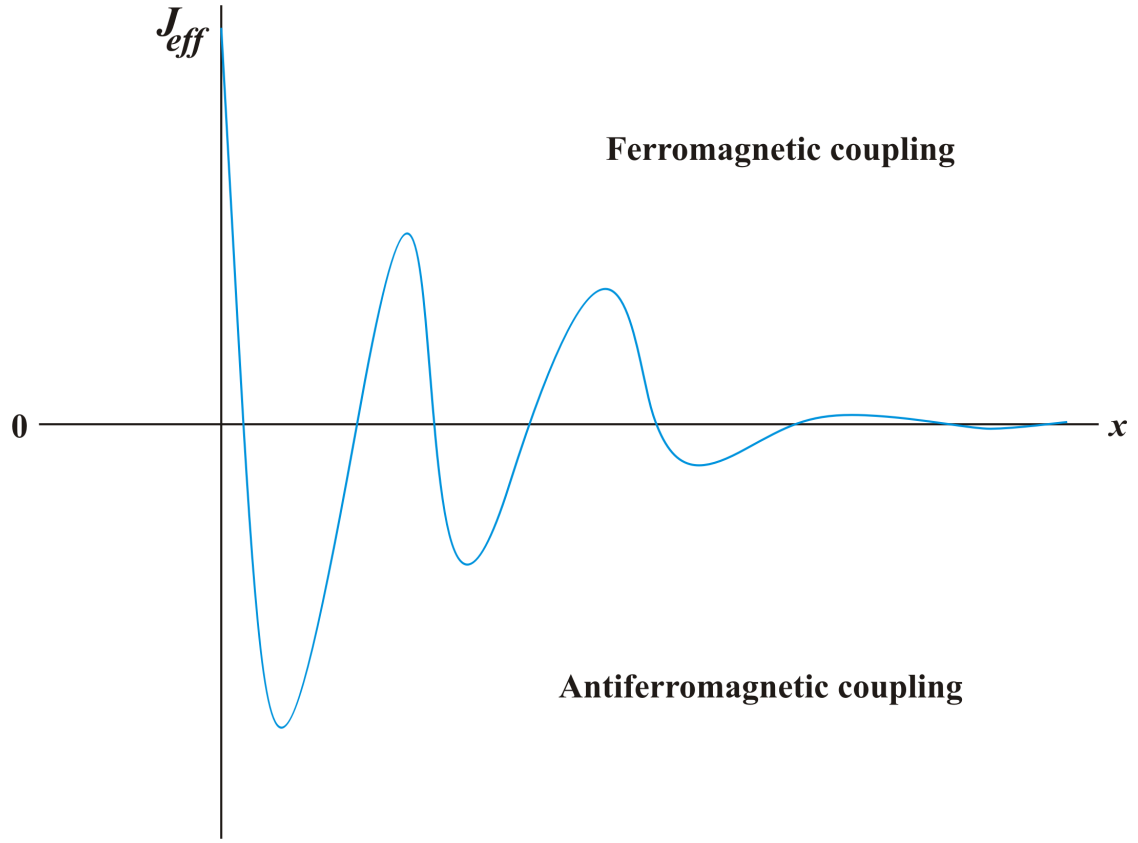

Figure 2.9: Variation of the effective exchange integral as a function of distance between the ions.

2.5 Spin waves

The mean field theory predicts a wrong temperature dependence of the magnetisation at low temperature as expressed by equations 2.3.22 and 2.3.23. The observed decrease in the spontaneous magnetization with increase in temperature is assumed to occur due to the excitation of spin waves. At $T = 0$ K, we assume a perfect alignment of spins $\uparrow\uparrow\uparrow\uparrow\uparrow$ .... $\uparrow\uparrow\uparrow^{i}\uparrow^{i+1}$. For $T > 0$ K, the first excited spin alignment can not be approximated by a reversal of a single spin $\uparrow\uparrow\uparrow\uparrow\downarrow\uparrow\uparrow\uparrow\uparrow$ because this involves significant increase in energy. Experimental results are consistent with gradual spin reversals which have characteristics of waves [117]. Spin waves are quantized spin fluctuations similar to photons or phonons. The quantized spin fluctuations are called magnons. The temperature dependence of the magnetization at low temperature ($T \ll T_C$) due to spin waves excitations can be shown to be

$$M(T) = M_S(0)(1 - AT^{3/2} - CT^{5/2} - ...). \tag{2.5.1}$$

where A and C are the crystal structure parameters [118]. From equation 2.5.1 we can deduce the Bloch $T^{3/2}$ law. A modified Bloch's law given by

$$\frac{M(T)}{M(0)} = \left[1 - \left(\frac{T}{T_0}\right)^{\beta}\right], \tag{2.5.2}$$

is sometimes used to fit the experimental data with T_0 and β as adjustable parameters [119].

2.6 Magnetic domain

In 1907, P. Weiss proposed that ordered spins can form in different regions known as magnetic domains [120]. Figure 2.10 shows different regions of ordered spins in a magnetic sample [23]). The magnetic domains are separated from each other by the so-called domain walls (see Figure 2.11). This involves gradual reversal of the direction of the magnetic moments between two domains. The characteristics of domain walls was first studied by Bloch, Landau and Néel [121]. A Bloch's wall is associated with spins that rotate in parallel to the plane of the wall. A Néel's wall is associated with spins that rotate perpendicular to the plane of the wall [122].

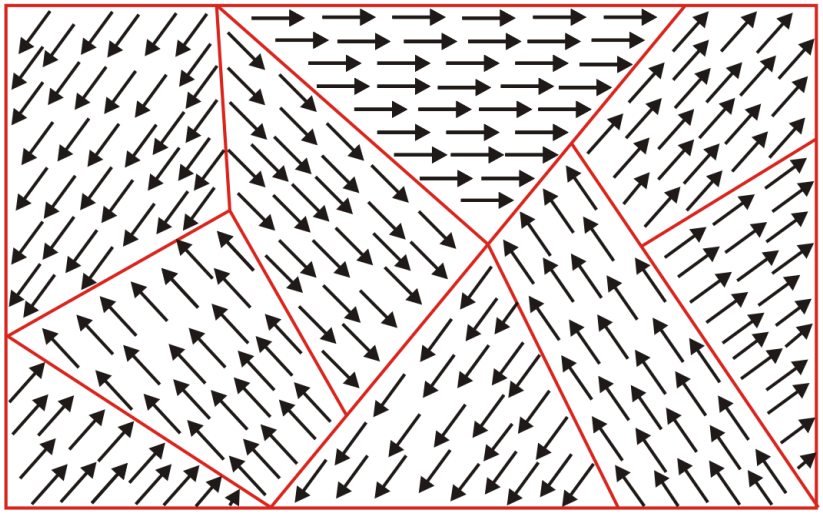

Figure 2.10: Magnetic domains of a ferromagnetic material.

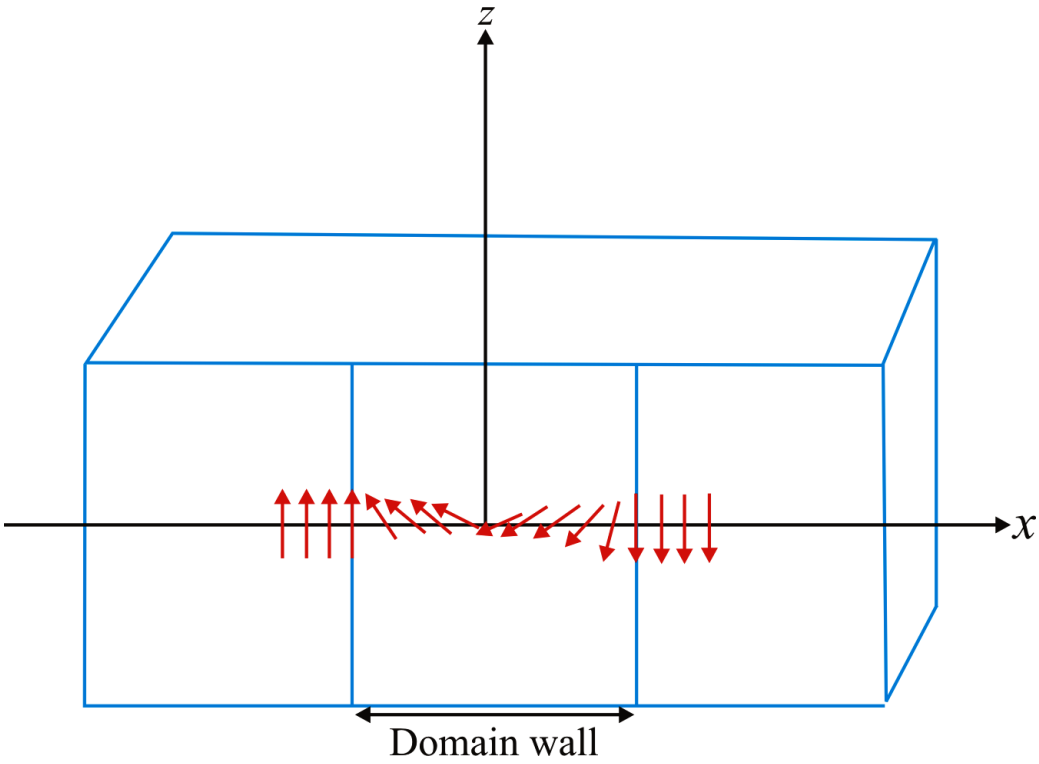

Figure 2.11: Domain wall of a ferromagnet

The formation of magnetic domains is intended to reduce the magnetostatic energy [123]. The discontinuity at the surface of the normal component of magnetization creates free poles. This leads to a demagnetization field given by

$$\vec{B_D} = D\vec{M} \sim \frac{b}{l}\vec{M}, \tag{2.6.1}$$

where D is the demagnetization factor, b and l are the sample's breadth and length respectively. The internal field producing the magnetization is given by

$$\vec{B}_{internal} = \vec{B}_0 - D\vec{M}. \tag{2.6.2}$$

The magnetic energy can be expressed as

$$U_m = -\frac{1}{2}\vec{B}_{internal}.\vec{M} - \vec{B}_0\vec{M}. \tag{2.6.3}$$

In the absence of an applied field, the magnetic energy still exists and is given by the self-energy

$$U_S = \frac{1}{2} D M_S^2, \tag{2.6.4}$$

where U_S is known as the magnetostatic self-energy which is the energy that needs to be minimised for domain to form. The transition from one domain to another through a domain wall occurs by spin flips from directions of easy magnetization. A sudden spin reversal in one step increases the exchange energy by 4 $J_0 S^2$ per atom at the boundary [124]. This is a much larger increase of the exchange energy $J_0 S^2 \pi^2 / N$ for N steps. Therefore, the total wall exchange energy density of the wall per unit area is given by

$$\sigma_{EX} = \frac{\pi^2 J_0 S^2}{N a^2}, \tag{2.6.5}$$

where a is the lattice parameter. As a result of spin-orbital interaction, magnetic moments prefer to align towards particular directions known as easy axes. The energy required to flip the spins from their easy axes is known as the magnetocrystalline anisotropy energy. The anisotropy energy for uniaxial material is given by

$$U_A = K_1 V \sin\theta_i + K_2 \sin^4\theta_i, \tag{2.6.6}$$

where θ_i is the angle between S_i and the easy axes, V is the volume of the sample and K_i is the anisotropy coefficients. K_1 and K_2 are temperature dependent and may also determine if the moments are towards the easy or hard axes [106]. For a simple cubic system the anisotropy energy per unit area of a wall of length Na is given by

$$\sigma_a = K_1 N a. \tag{2.6.7}$$

The increase in magnetic anisotropy energy leads to decrease in domain wall width which increases the exchange energy [125]. The domain structure that forms is intended to minimize both the exchange energy and the anisotropy energy. Below a certain sample size of a few nanometers known as a critical size D_C, the domain wall is difficult to form and the sample can acquire a single domain structure [126]. Nanoferrite materials studied in this thesis tend to fall into this category.

2.7 Magnetic hysteresis loop

To investigate the magnetic response of a sample, it is usually necessary to be subject it to an external magnetic field. A typical hysteresis loop is shown in Figure 2.12. By increasing the external magnetic field, the magnetic moments of a sample can rotate in order to align in the same direction as the applied field. This process increases the sample magnetization. If the field is the sample can be demagnetized by turning the applied field in the opposite direction. The magnetization when the field is reduced to zero is known as the remanence magnetization M_r. The magnetic field required to demagnetize a magnetic sample is known as the coercive field H_C.

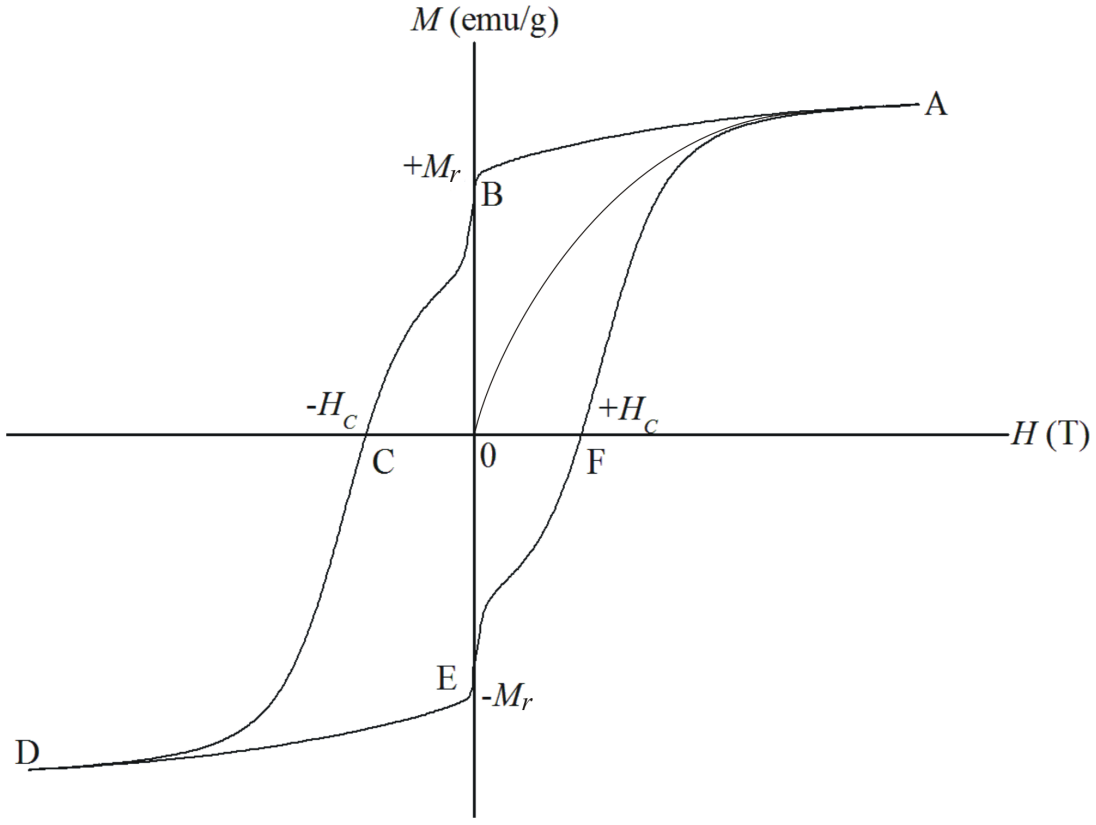

Figure 2.12: Hysteresis loop at 4 K for as-prepared $Ba_{0.5}Co_{0.5}Fe_2O_4$ nanoferrite.

The saturation magnetization can be obtained from the empirical formula given by [127]

$$M(H) = M_S(0)\left(1 - \frac{a}{H} - \frac{b}{H^2} - ...\right) + \chi H, \tag{2.7.1}$$

where χ is the high field susceptibility, a and b are constants. For mono-disperse non-interacting ferri or ferromagnetic ordered particles, the coercive field as a function of measuring temperature can be expressed as [128]

$$H_C(T) = H_C(0)\left[1 - \left(\frac{T}{T_0}\right)^{\alpha}\right]. \tag{2.7.2}$$

where $H_C(0)$ is the coercive field at $T = 0$ K and T_0 is a constant.

The constant α takes the value of 1/2 for an assembly of aligned particles [128]. However, for randomly oriented particles the coercivity follows a T^{α} law as reported by Pfeiffer [129] where α was found to be 0.77.

2.8 Soft and hard magnetic materials

Magnetic materials can be classified based on their response to an applied magnetic field into soft and hard magnetic materials (see Figure 2.13). A soft magnetic material can easily be magnetized and demagnetized [130]. Furthermore, this type of magnetic material has excellent efficiency to concentrate and shape the magnetic flux [131]. The main features of soft magnetic materials include high saturation magnetization and permeability, low coercive field and low energy losses. These properties make soft magnetic materials suitable for different applications in microwave devices, magnetic amplifiers and high frequency devices [132]. A typical soft magnetic material is $NiFe_2O_4$. A magnetic material that does not demagnetized easily is known as a hard magnetic material. Such materials are suitable for permanent magnets because they resist demagnetization. Hard magnetic materials possess high coercive field, high energy product $(BH)_{max}$, low permeability and susceptibility. Hard magnetic materials can also be categorized into conventional materials and high energy materials. Conventional materials have energy product $(BH)_{max}$ of 2-80 kJ/m^3. A typical examples of conventional materials are steel magnets, cunife (Cu-Ni-Fe) and hexagonal ferrites ($BaO\text{-}6Fe_2O_3$). High energy materials have energy products $(BH)_{max}$ of about 80 kJ/m^3. Typical examples of high

energy materials are $SmCo_5$ and $Nd_2Fe_{14}B$ [133].

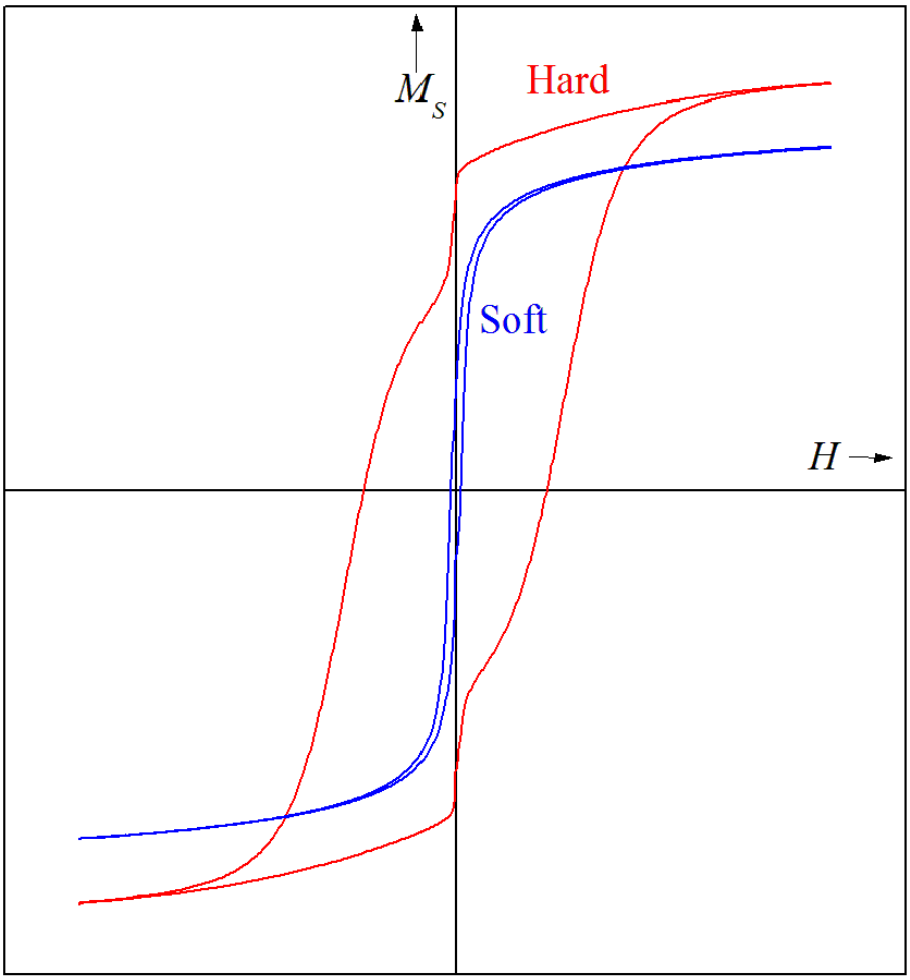

Figure 2.13: Soft and hard magnetic materials of $Ba_{0.4}Co_{0.6}Fe_2O_4$ and $BaFe_2O_4$ respectively, measured at 2 K in the current work.

Chapter 3

Mössbauer spectroscopy

In 1958, Roudolf L. Mössbauer discovered the recoil-free emission of gamma radiation by excited nuclei and its resonant absorption by identical nuclei in their ground states [134, 135]. The Mössbauer effect involves the investigation of the interaction between the nucleus and its local environment through the resonant absorption of gamma (γ) rays. Many isotopes such as ^{57}Fe, ^{61}Ni, ^{119}Sn, ^{151}Eu, ^{161}Dy and ^{191}Ir show the Mössbauer effect [134, 136]. Since a large number of materials in many applications contain iron, ^{57}Fe Mössbauer spectroscopy is more widely used. It is worth mentioning that existence of ^{57}Fe in any natural material with iron is about 2.12 % [104]. Mössbauer spectroscopy can therefore be used to study properties of materials in physics, chemistry, biology and earth sciences [134, 137].

3.1 The Principle of the Mössbauer effect

The general idea of ^{57}Fe Mössbauer spectroscopy is to relate the energy difference between the excited and the ground states of ^{57}Fe nuclei in a substance under investigation. In a ferromagnetic material, the ground state of ^{57}Fe splits into two levels whilst the excited state splits into four levels. This splitting is assumed to be due to the internal magnetic field that arises in a ferromagnetic ordered sample containing iron atoms. If the substance is not magnetic the energy levels only shift without splitting because of the absence of an internal magnetic field. Hence we expect to see evidence of both splitting and shifting of energy levels to occur. By

measuring the differences in the energy levels one can obtain information about the substance that contains ^{57}Fe isotopes. This is achieved by detecting the γ-rays that pass through the material under investigation. The transmitted intensity depends on the resonant emission and absorption of γ-rays. Figure 3.1 shows the emission of γ-rays by a free nucleus and its recoil [136]. The reverse occurs after absorption of a $\gamma-$ray.

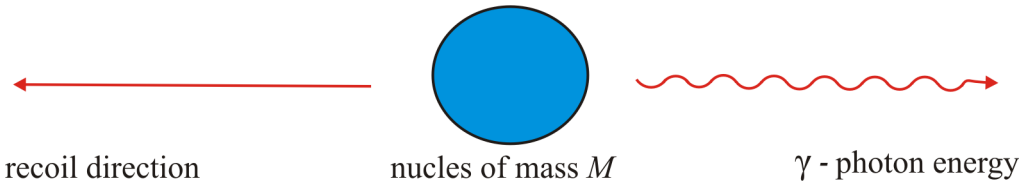

Figure 3.1: Recoil energy loss in free Atoms.

Following after emission or absorption of a $\gamma-$ray, the recoil energy E_R is shown to be

$$E_R = \frac{E_\gamma^2}{2Mc^2}, \tag{3.1.1}$$

where c is the speed of light and M is the mass of the nucleus [138]. In Mössbauer spectroscopy a ^{57}Co source provides $\gamma-$rays. Usually the ^{57}Co isotopes are doped into a non-magnetic Rh matrix which ensures only a shift in the energy levels of ^{57}Co without splitting. If a nucleus that is emitting or absorbing a $\gamma-$ray is bound in a crystal lattice, its recoil energy E_R will be minimized because M in equation 3.1.1 has to be replaced by the mass of the entire crystal. Hence the energy difference between the excited and ground states will be slightly reduced. In Mössbauer spectroscopy, the source of $\gamma-$rays is vibrated in a specific way in order to Doppler shift the energy of the emitted $\gamma-$rays so that they can match the energy difference between the excited and ground states. When a source is moving at a velocity v, the emitted energy of a $\gamma-$ray can be Doppler shifted by

$$\delta E = E_\gamma \frac{v}{c}, \tag{3.1.2}$$

where E_γ is the energy of the $\gamma-$ray. Hence, in order for the resonant absorption to take place in an absorber (or sample of interest), we only need to vibrate the $\gamma-$ray

source with a maximum velocity of about ±10 mm/s. A typical Mössbauer spectrum consists of a plot of transmitted intensities through the absorber as a function of the velocity of the $\gamma-$ray source. The recoilless fraction of the emitted $\gamma-$rays from the source is given by the equation

$$f = exp\bigg(- \frac{E_\gamma^2 < x^2 >}{(\hbar c)^2} \bigg), \tag{3.1.3}$$

where $< x^2 >$ is the mean square thermal displacement of the emitting nucleus in the direction of the $\gamma-$ray [138]. Equation 3.1.3 shows similarity to the Debye model of a solid [138]. Therefore, we may assume that f follows a similar trend. However, note that instead of a single vibration frequency of the lattice atoms, the Debye model assumes a range of possible frequencies from zero up to a maximum cut-off frequency ω_D. Hence, based on the Debye model, the recoilless fraction can be shown to be

$$f = exp\bigg\{ - \frac{3E_R}{2k_B\theta_D} \bigg[1 + 4 \bigg(\frac{T}{\theta_D} \bigg)^2 \int_0^{\frac{\theta_D}{T}} \frac{udu}{e^u - 1} \bigg] \bigg\}, \tag{3.1.4}$$

where k_B is the Boltzmann constant, $u = \hbar\,\omega/(k_B\,T)$ and $\theta_D = \hbar\omega_D/k_B$ is the Debye temperature. The recoilless fraction f is a temperature dependent parameter based on equation 3.1.4. At the lowest temperature ($T = 0$ K), the recoilless fraction is a maximum ($f = 1$) and decreases with increasing T. When the transition energies of the emitter and absorber nuclei match exactly, resonant absorption occurs. In this case the energy difference between the source and absorber can be expressed as

$$E_\gamma = E_{excited} - E_{ground} = E_{excited}^{'} - E_{ground}^{'}, \tag{3.1.5}$$

where $E_{excited}$ and E_{ground} are the excited and ground states respectively. Figure 3.2 illustrates the resonant absorption.

The strength of a Mössbauer signal is associated with the effective thickness t of the absorber [138]

$$t = f_A N_m \sigma \tag{3.1.6}$$

where N_m is the number of Mössbauer nuclei per square centimetre, f_A is the Debye

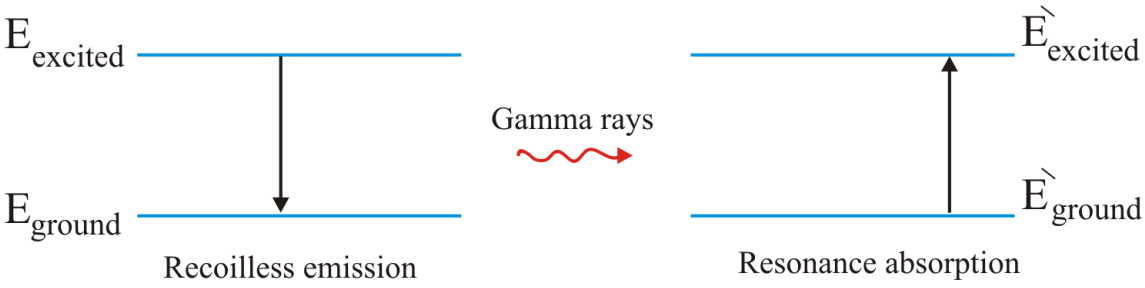

Figure 3.2: Diagram shows the resonant absorption.

factor of the absorber and σ is the resonance cross-section of the Mössbauer isotope. For thin absorbers the variation of σ with E_γ is given experimentally by

$$\sigma_{Exp}(E_\gamma) = \sigma_0 \left[1 + 4 \left(\frac{E_\gamma - E_0}{\Gamma_s - \Gamma_a} \right)^2 \right]^{-1}, \tag{3.1.7}$$

where E_0 is the nuclear transition energy, Γ_s and Γ_a are the widths of the resonant peaks at half maximum of the source and absorber respectively. σ_0 is the total cross-section area for resonant absorption of $\gamma-$rays expressed as

$$\sigma_0 = \frac{\lambda^2}{2\pi} \frac{(1 + 2I_{ex})}{(1 + 2I_g)} \frac{1}{(1 + \phi)}, \tag{3.1.8}$$

where λ is the $\gamma-$ray wavelength, ϕ is the integral conversion coefficient of the gamma rays, I_{ex} and I_g are the nuclear spins for excited and ground states respectively [136].

According to the Heisenberg uncertainly principle, the uncertainty in energy corresponding to the energy spread Γ of gamma rays with nuclear life time τ is given by

$$\Gamma \approx \frac{\hbar}{\tau}. \tag{3.1.9}$$

Resonant absorption does not take place if $E_R > \Gamma$. However, by Doppler shifting of the γ-ray energy resonant absorption can occur. As stated earlier this is achieved by vibrating the γ-ray source as demonstrated in Figure 3.3 [139].

The radioactive source ^{57}Co decays to the excited state $I_{ex} = 5/2$ of ^{57}Fe isotope by nuclear electron capture (EC). This state in not stable and the ^{57}Fe nucleus can

subsequently decay directly to the ground state I_g of ^{57}Fe with a probability of 9% or to the excited state $I_{ex} = 3/2$ with probability 91% as shown in Figure 3.4 [140]. The decay from $I_{ex} = 3/2$ to $I_{ex} = 1/2$ produces γ-rays with energies 14.4 keV which are associated with ^{57}Fe Mössbuer spectroscopy.

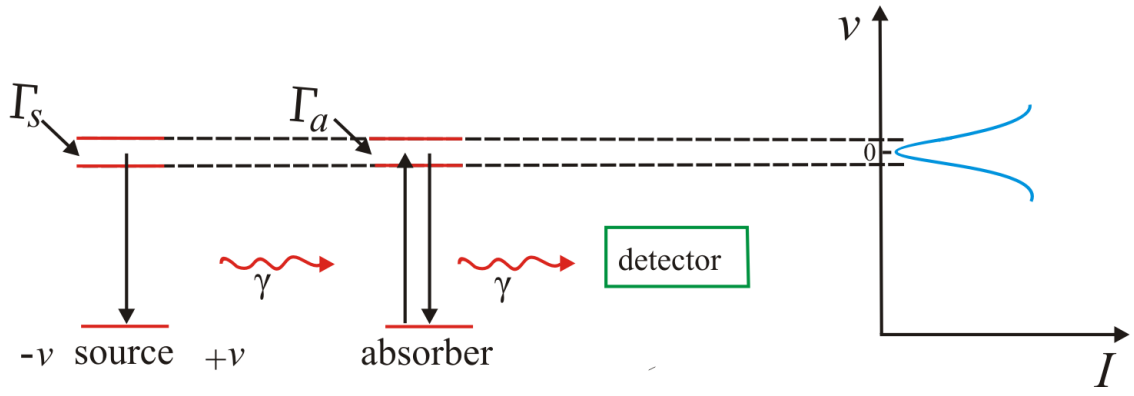

Figure 3.3: Mössbauer spectrum measurement.

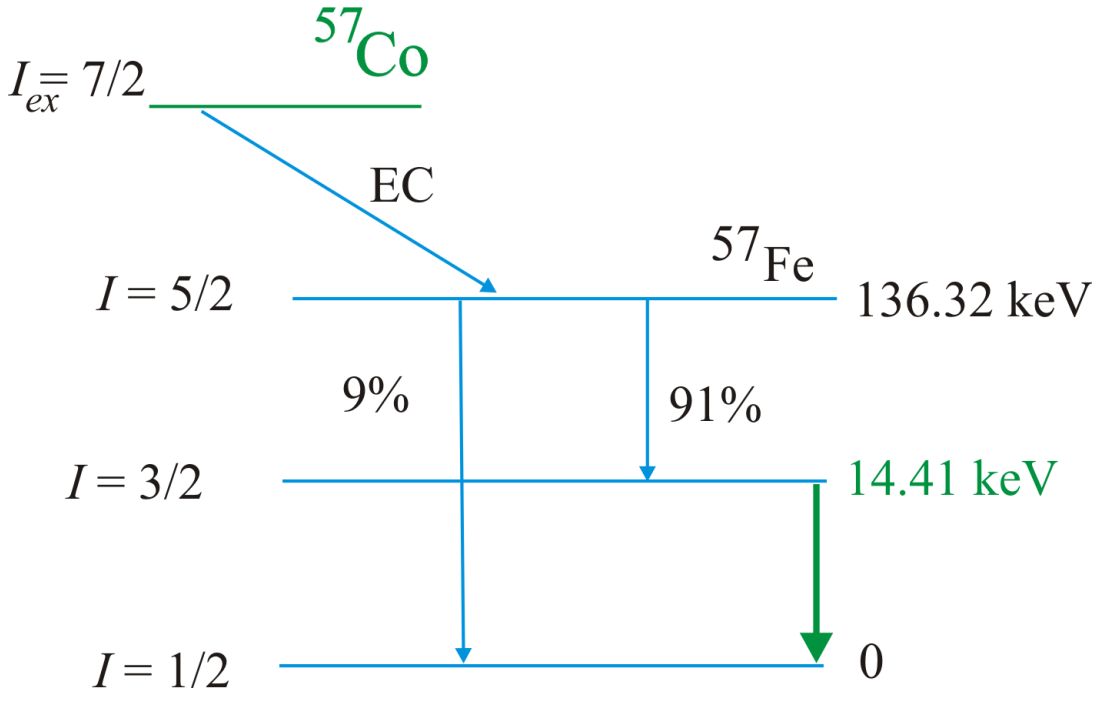

Figure 3.4: Schematic demonstration of ^{57}Co nuclear decay.

3.2 Hyperfine interactions

Magnetic and electrostatic interactions between a nucleus and its environment are known as hyperfine interactions. The energy states of a nucleus can split in the case of a magnetic environment due to an internal magnetic field. Electrostatic interactions cause energy shifts only in the case of non-magnetic environments. Hyperfine interactions show the effects of both electronic and magnetic states of a material such as electron distribution, valence state, defects, internal spin reorientations, magnetic order, spins configuration, spin transition and magnetic relaxation. This information can be obtained from the so-called hyperfine parameters such as isomer shift δ, quadrupole splitting Δ and magnetic hyperfine interactions H.

3.2.1 Isomer shift

The electrostatic interaction between nuclear charge and electronic charge is known as isomer shift. Nuclei of the same mass and charge but with different nuclear states are known as isomers, hence the name isomer shift because this effect depends on the difference in the nuclear radii of the ground and isomeric excited states [140]. Isomer shift is related to s-electron density due to changes in the valence electrons which lead to a change in the Coulomb interaction. This causes a shift in the nuclear states to occur. Figure 3.5 [138], shows centroids of Mössbauer spectra that are shifted from zero velocity due to isomer shifts.

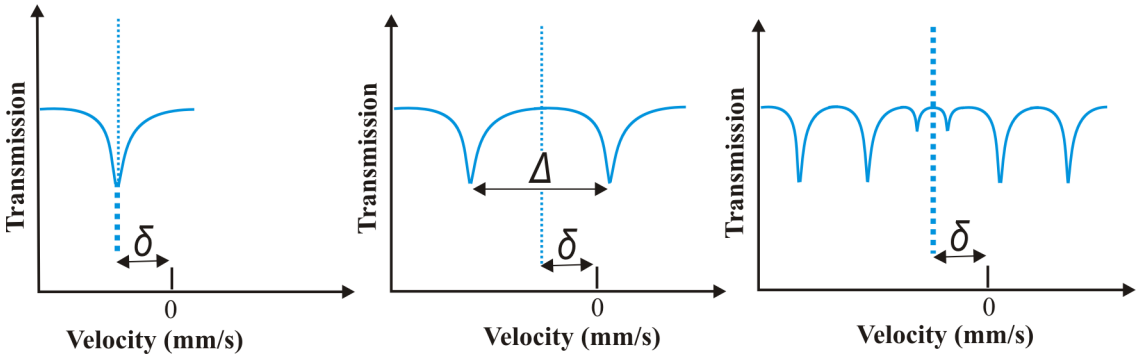

Figure 3.5: Isomer shifts in nuclear states.

The isomer shift occurs in the absorber energy levels and gives information about electron distribution, valence state and spin state coordination. In ^{57}Fe Mössbauer spectroscopy the isomer shift of values for Fe^{2+} ions are in the range 0.6-1.7 mm/s, whereas for Fe^{3+} ions they are in the range 0.1-0.5 mm/s [141]. Isomer shifts are associated with the electronic charge density $|\psi(0)|^2$ at the nucleus [142]. However, isomers shifts are different for different charge distributions since the radii of the two charge distributions in the excited and ground states tend to be different. Based on energy difference between excited and ground states, the isomer shift can be shown to be

$$\delta = \Delta E_A - \Delta E_S = \frac{Ze^2}{10\varepsilon_0}\left[|\psi(0)|_A^2 - |\psi_S(0)|_S^2\right]\left(R_e^2 - R_g^2\right). \tag{3.2.1}$$

R_e and R_g are the nuclear radii of ^{57}Fe in the excited and ground state respectively and ε_0 is the permittivity of free space. The isomer shift can also be expressed by velocity units usually in mm/s based on equations 3.1.1 and 3.2.1 to give

$$\delta = \frac{Ze^2c}{10\varepsilon_0 E_\gamma}\left[\psi(0)_A^2 - \psi_S(0)_S^2\right]\left(R_e^2 - R_g^2\right). \tag{3.2.2}$$

3.2.2 Quadrupole splitting

A non-spherical nucleus of charge e with spin $I > 1/2$ has a quadrupole moment $\vec{Q}$ which is expressed as

$$Q = \frac{1}{e}\int \rho(r)(3z^2 - r^2)dr. \tag{3.2.3}$$

The interaction between Q and electric field gradient (EFG), $\bigtriangledown\vec{E}$ is known as the quadrupole interaction [140]. Figure 3.6 [138], shows the effect of the electric quadrupole interaction with the nuclear charge which leads to the so-called quadrupole splitting in the Mössbauer spectrum.

The quadrupole interaction is given by the Hamiltonian

$$H_Q = \vec{Q}.\vec{\nabla}E. \tag{3.2.4}$$

The eigenvalues of equation 3.2.4 are given by

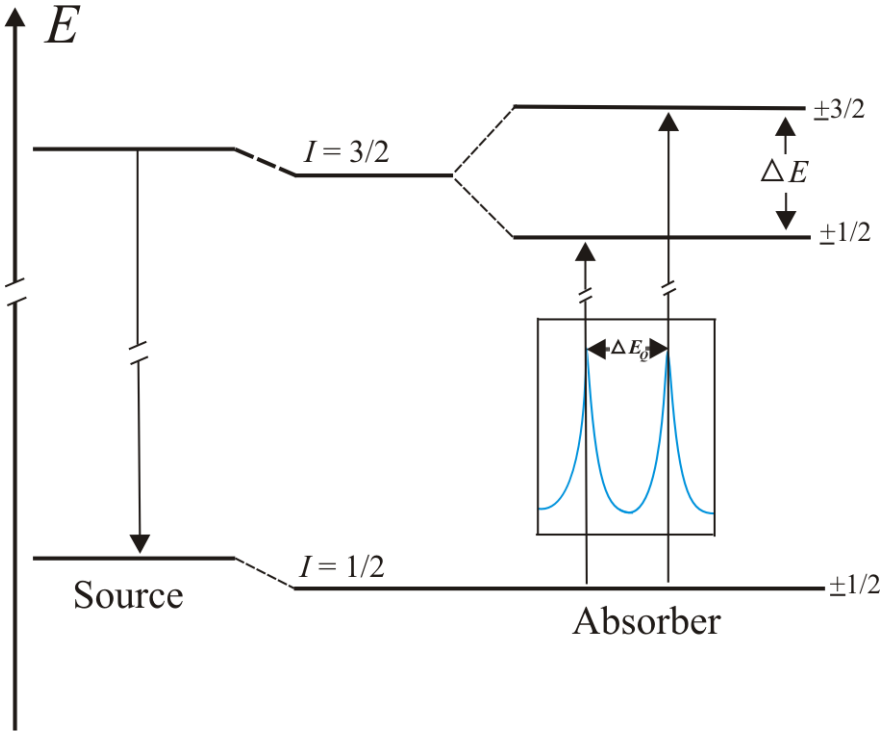

Figure 3.6: Effect of the electric quadrupole interaction leads to splitting in Mössbauer spectrum.

$$E_Q = \frac{eQV_{zz}}{4I(2I-1)}(3m_I^2 - I(I+1))\left(1+\frac{\eta^2}{3}\right)^{\frac{1}{2}}, \tag{3.2.5}$$

where $V_{zz} = \partial V/\partial Z^2$ is the principal axis component of the electric field gradient, m_I is the magnetic quantum number and η is an asymmetry parameter of the electric field given by

$$\eta = \frac{V_{xx} - V_{yy}}{V_{zz}}, \qquad 0 \leq \eta \leq 1. \tag{3.2.6}$$

In the case of EFG being axial (i.e, $V_{xx} = V_{yy}$), $\eta = 0$ equation 3.2.5 can be written as

$$E_Q = \frac{eQV_{zz}}{4I(2I-1)}(3m_I^2 - I(I+1)). \tag{3.2.7}$$

The quadrupole interaction causes a split in the excited state $m_I = 3/2$ of ^{57}Fe isotopes while, the ground state $I = 1/2$ remain unsplit because of lack of quadrupole moment. The splitting of the excited state $I = 3/2$ creates double degenerate

substates due to the m_I^2 dependence of the quadrupole energies

$$\begin{aligned} E_Q(\pm 3/2) &= 3eQV_{zz}/12, \\ E_Q(\pm 1/2) &= -3eQV_{zz}/12. \end{aligned} \tag{3.2.8}$$

The transition from $I = 3/2$ to $I = 1/2$ appears as a doublet in the Mössbauer spectrum (see Figure 3.6) which is separated by the quadrupole splitting [143]

$$\Delta E_Q = E_Q(\pm 3/2) - E_Q(\pm 1/2) = \frac{eQV_{zz}}{2}. \tag{3.2.9}$$

The quadrupole splitting can provide information about the sample such as charge symmetry around the nucleus [142], charge distribution [144] and defects [145].

3.2.3 Magnetic hyperfine interaction

In the case of magnetic dipole interaction, the splitting of the spectrum occurs due to the interaction of nuclear magnetic dipole moments $\vec{\mu}$ with the magnetic field $\vec{H}$ [140]. Nuclear levels with spin $I = 0$ have no Zeeman splitting because their magnetic moment is zero. However, a nucleus in a state with spin quantum number $I > 0$ has a magnetic dipole interaction give by the Hamiltonian

$$H_d = -\vec{\mu}.\vec{H} = -g_N \mu_N \vec{I}.\vec{H}, \tag{3.2.10}$$

where g_N is the nuclear Landé $g-$factor, μ_N is the nuclear Bohr magneton. Therefore, the energy levels can be expressed as

$$E_m = -\frac{\mu H m_I}{I} = g_N \mu_N H m_I, \tag{3.2.11}$$

where m_I is the spin quantum number. Figure 3.7 shows the Zeeman effect in ^{57}Fe [138]. The magnetic field leads to the splitting of the nuclear levels that have spins I to $2I+1$. The splitting is equally spaced into nondegenerate sub-levels [136]. Zeeman splitting with the selection rules $\triangle m_I = 0, \pm 1$ causes six possible transitions which appear as a sextet in the Mössbauer spectrum. The splitting of the sub-levels is $g_N \mu_N H$. The magnetic hyperfine fields provide information about magnetic

moments, magnetic order and spin configurations. As a function of temperature, the magnetic hyperfine fields can also give information about magnetic relaxation.

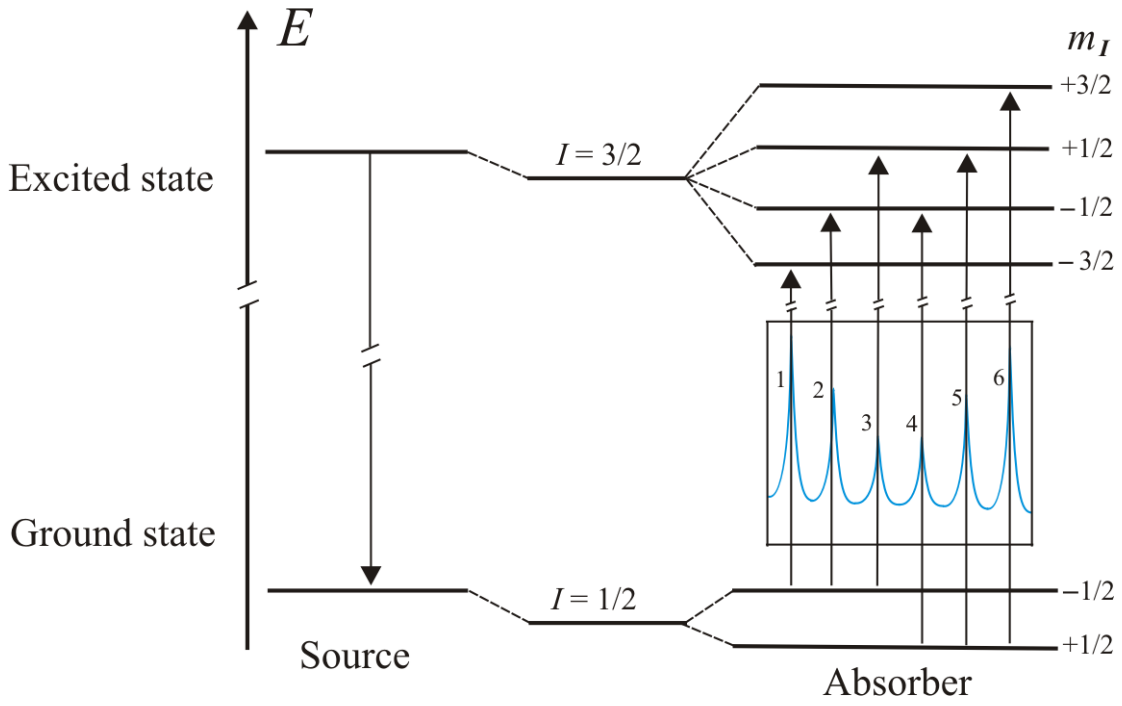

Figure 3.7: Effect of the magnetic dipole interaction in ^{57}Fe Mössbauer spectrum.

Chapter 4

Experimental techniques

This chapter provides a discussion about experimental techniques which were used in this thesis. Two synthesis techniques were used namely glycol thermal and high energy ball milling. The spinel phase was identified by X-ray diffraction of powdered samples. The morphology was studied by high resolution transmission electron microscopy and high resolution scanning electron microscopy. The surface area measurements were carried out by the Brunauer-Emmet-Teller (BET) technique. A mini cryogen free measurement system and a vibrating sample magnetometer were used to investigate the magnetization behaviour of the synthesized nanoparticles. The magnetic properties were also studied by ^{57}Fe Mössbauer spectroscopy measurements which also provided information about site occupation at tetrahedral and octahedral sites of the spinel structure. The electrochemical activity in the present work was studied by cyclic voltammetry measurements.

4.1 Synthesis and structural techniques

4.1.1 Glycol-thermal

The glycol-thermal method was used to synthesize compounds in a closed system using glycol ethylene as a synthesis medium. The confined closed system helps to raise the reactor's pressure. The glycol thermal technique has the advantage of achieving relatively high pressures and low synthesis temperature (T = 200 °C). The

starting materials can be high purity metal nitrates or chlorides as in the present case namely $MgCl_2.6H_2O$: 99%, $SrCl_2.6H_2O$: 99%, $MnCl_2.6H_2O$: 99%, $CoCl_2.4H_2O$: 98%, $BaCl_2.6H_2O$: 99% and $FeCl_2.6H_2O$: 99% purchased from Sigma-Aldrich. The stoichiometric amount of starting materials was mixed in 400 mL of deionised water and homogenized using a magnetic stirrer. Drops of ammonium hydroxide were used to precipitate the mixture and to adjust the pH of the mixture to about 9. The mixture was washing continuously using deionized water over a Whatman glass microfibre filter (GF/F) until all the chlorides were removed. The presence of chloride was detected by adding a standard solution of silver nitrate to the filtered water. The clean precipitate was added to 200 mL of glycol ethylene that was thereafter transferred into a Watlow series stirred pressure reactor shown in Figure 4.1.

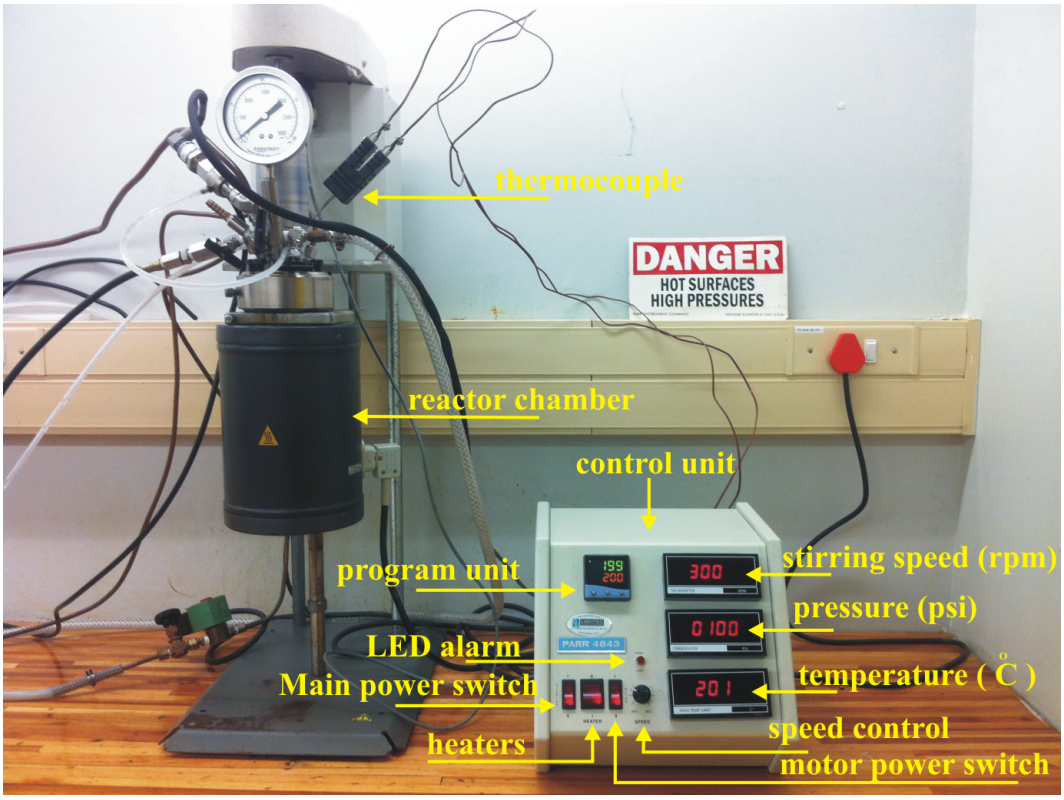

Figure 4.1: PARR 4843 stirred pressure reactor, Condensed Matter Physics Laboratory, Westville campus.

The reactor was programmed (see Table 4.1) to run for 6 hours at $T = 200$ °C and stirring speed of 300 rpm. Figure 4.2 shows a typical operation schedule of

the PARR 4843 stirred pressure reactor. As the reactor's temperature increases the pressure also increases until it reaches certain level and stabilizes. Any overshoot in the pressure can be reduced through the pressure relief valve. The cooling system of the Watlow stirred pressure reactor is based on tap water flowing through it. This was adjusted to a slow flow rate in form of drops of water at the outlet hose end. The control unit has a circuit breaker that stops the heating program when a fault is detected as indicated by red LED light. Common faults include too high or too low water flow rate or wetting of the heating chamber due to water leaks.

Table 4.1: Programme for PARR 4843 temperature controller.

General set up				
Program configuration				
level 1	level 2	level 3	level A	level C
tune: off	SP1.P: 97	SP1.d: ssd	An.hi: 997	Addr: 0
bAnd: 99	hAnd: off	SP2.d: rLK	An.Lo: 0	bAud: 9600
int.t: 4.8	PL.1: 100	Burn: uP.SC	hi.in: 50.0	dAtA: 18nl
aEr.t: 100	PL.2: 100	rEU.d: lr.2d	lo.10.0	abuC: off
aAC: 1.5	SP2.A: Cool	rEU.L: in.2n	dECP: 0000	
CyC.t: 20	SP2.b: none	SPAn:0.0	SP3.A: none	
oFSt: 0	diSP: 1o	2Ero: 0.0	SP3.b: none	
SP.LK: off	hi.SC: 800	ChEK: off	SET.3: 0	
SEt.2: 0	LO.SC:0	rEAd: UAro, 0.0	hK5.3: 2.2	
Bnd.2: 2.0	inPt: tCL	tECh: CtA, 0.0	brn.3: UP.SC	
CYC.2: on.off	unit: psi	UEr: 954.0	rEU.3: 3d	
		rSEt: none		
Level P				
ProG 1	SEG 1	SEG 2	SEG 3	SEG 4
Run: (on or off)	Type: Spr	Type: Soak or	Type: Spr	Type: Soak
FAiL: rSET, ConT	Sprr: 200 °C	Step or Loop or	SPrr: 200 °C degree	Sin: 10 min
or hold	t.SP: 150 °C	CALL or E.op	t.SP: 25 °C	E.oP: none
St.U: PU	hb.U: off	Edit: dEL	hb.U: off	
or SP	and E.oP: none	or inS	E.oP: none	
SPru: hour		Sint: 360 min		
or 60 s		E.op: none		

The product after synthesis in the reactor was washed over a GF/F filter with 200 mL of ethanol. The sample was dried using a 200 W infrared light for about 24 hours. Finally, the dried sample was homogenized using an agate mortar and pestle. All the samples synthesized by glycol-thermal technique in this thesis were produced under similar conditions.

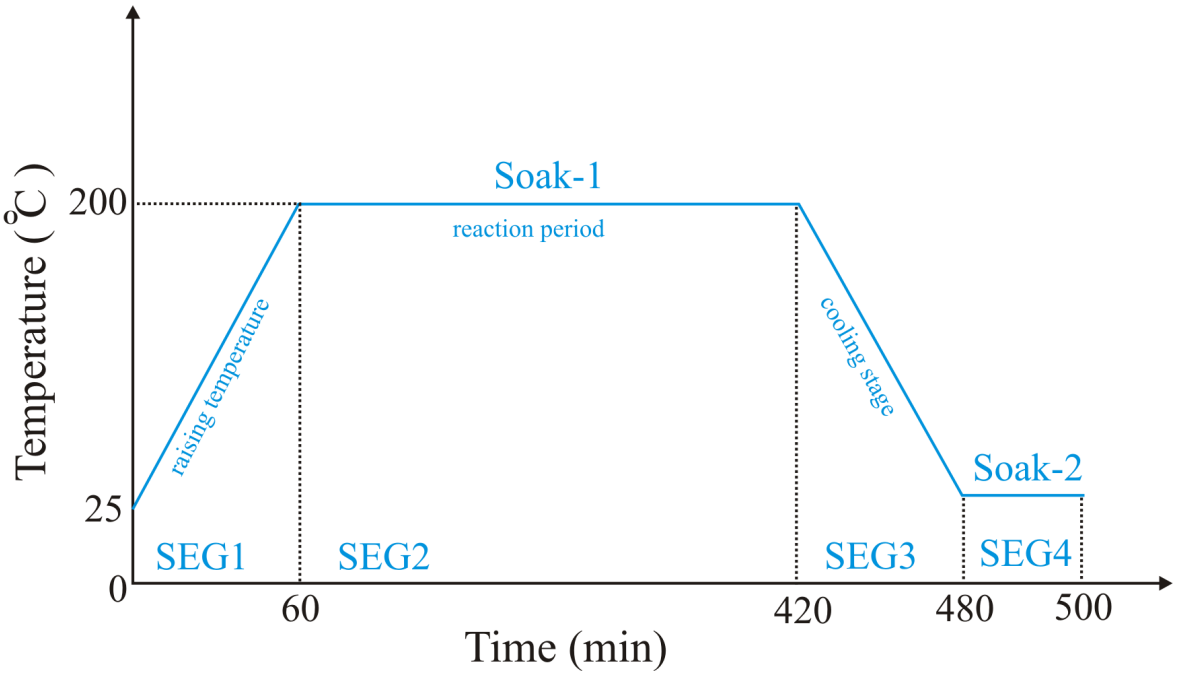

Figure 4.2: Schedule illustrates the operation of PARR 4843 controller.

4.1.2 High-energy ball milling

Nanoparticle ferrites can also be produced by mechanical milling of metal oxides. In this case the required stoichiometric amount of the metal oxides to produce a desired compound are weighted and put into grinding jars with hardened stainless steel balls. Phase formation can be affected by many factors such as stoichiometry, milling time, rotation speed, ball to mass ratio and milling environment. A Retsch planetary ball milling (type PM 400 MA) shown in Figure 4.3 was used to synthesize some of the samples. The collision between stainless steel balls provides high energy which can break the oxide bonds and force the phase to form. The steel vial (jar) covers

are designed in such way as to ensure proper tight fitting. However, some of these covers are designed in order to allow synthesis in other supplying atmospheres such as argon. The Retsch PM 400 MA has four milling stations. Hence for rotational balance two or four samples can be milled at same time. The control unit allows for the adjustment of milling time, rotational speed and rotational direction (clockwise or anticlockwise).

Figure 4.3: Retsch planetary ball milling (type PM 400 MA), Condensed Matter Physics Laboratory, Westville campus.

In the present work high-energy ball milling was used to synthesize the NiO-ZrO_2 nanocomposite and $Ti_{0.5}Ni_{0.5}Fe_2O_4$ nanoparticles samples. The ball to sample mass ratio was 10 : 1. The starting materials NiO: 99%, ZrO_2: 99%, TiO_4: 99% and Fe_3O_4: 95% supplied by Sigma-Aldrich. The samples were milled for 10 hours in air under a rotational speed of 300 rev/min.

4.1.3 X-ray diffraction

In crystalline solid materials the periodic distribution of the atoms act as diffraction gratings. The atomic spacing $d \approx 1$ Å hence, the X-rays with wavelength $\lambda \approx 1$ Å can be diffracted by the crystal and provide information about its crystallography. Therefore, X-ray diffraction (XRD) is a technique in which the X-rays is used in order to determine the crystal structure of materials. Figure 4.4 shows schematic diagram of incident monochromatic beam of X-rays on crystalline sample.

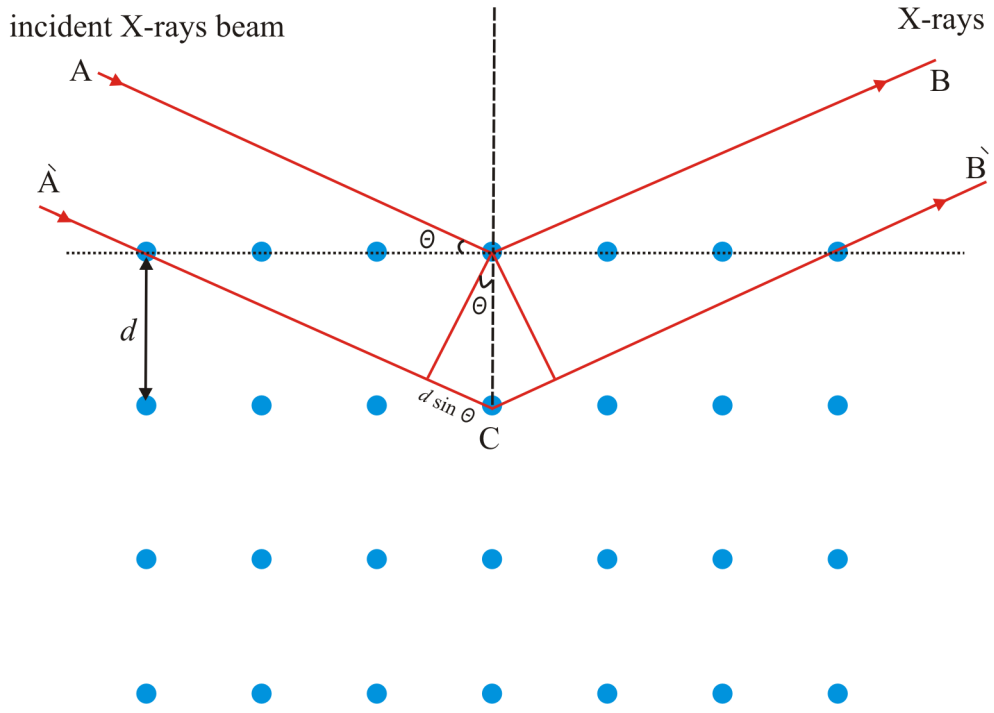

Figure 4.4: Schematic illustration of the principle of X-rays diffraction.

Reflected X-rays can interfere constructively whenever the optical path difference is an integer multiple of the wavelength. This leads to the diffraction condition

governed by Bragg's law [146]

$$n\lambda = 2d\sin\theta, \tag{4.1.1}$$

where n is an integer number and θ is the angle between the incident beam and the scattering plane. The relation between d and the lattice parameter a of a cubic crystalline system can be expressed by

$$d(h,k,l) = \frac{a}{\sqrt{h^2+k^2+l^2}}, \tag{4.1.2}$$

where h, k and l are Miller indices of a particular plane [146]. The crystallite sizes D can be estimated from the XRD pattern through the Scherrer's equation

$$D = \frac{K\lambda}{W_{hkl}\cos\theta}, \tag{4.1.3}$$

where $K \approx 0.9$ is known as the crystal shape factor and W_{hkl} is the line broadening of the diffraction peaks at full width at half-maximum (FWHM). The X-ray densities ρ_{XRD} of a cubic spinel can be calculated to be

$$\rho_{XRD} = \frac{8M}{N_A a^3}, \tag{4.1.4}$$

where M is the molecular weight of the sample and N_A is the Avogadro's number. The microstrain of the synthesized sample can be given as [147]

$$\varepsilon = \frac{W_{hkl}}{4\tan\theta}. \tag{4.1.5}$$

The microstrains can also be deduced from Williamson plots [148]. The percentage porosity $P(\%)$ of a sample can be calculated from the formula

$$P(\%) = \left(1 - \frac{\rho_{Bulk}}{\rho_{XRD}}\right) \times 100. \tag{4.1.6}$$

The bulk density ρ_{Bulk} in this case can be obtained from a suitable pellet of a powdered sample.

Figure 4.5 shows the Phillips XRD diffractometer Model: PANalytical, EMPYREAN that was used for structure determination. The instrument uses a CoKα radiation source (λ = 1.7903 Å). The XRD measurements were carried out in the range: 10 $\leq 2\theta \geq$ 80. A typical sample size for XRD measurements was about 0.25 g.

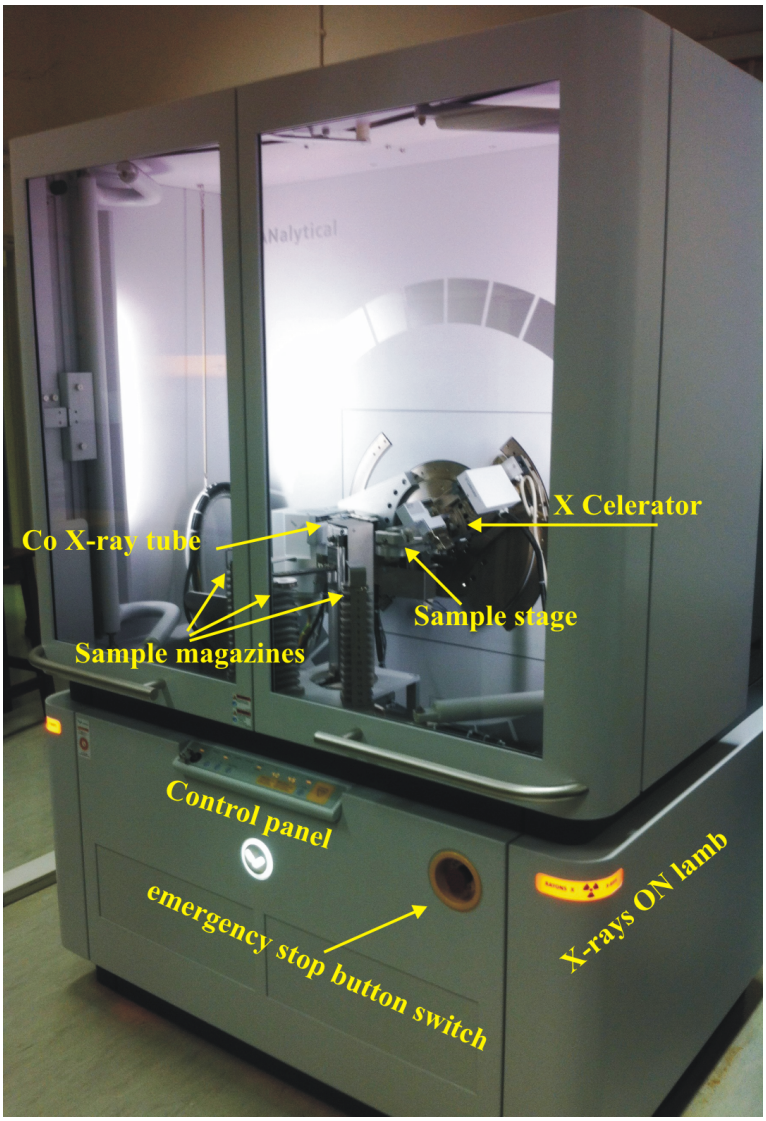

Figure 4.5: Empyrean PANalytical X-rays diffractometer cabinet, Geology Westville campus.

4.1.4 High resolution transmission electron microscopy and scanning electron microscopy

High resolution transmission electron microscopy (HRTEM) is a powerful technique to study the crystallographic structure of nanoparticles. The formation of nanoparticle images in the HRTEM measurements is due to the interaction between the incident electron beam and the sample. Figure 4.6 shows a Joel-2100 high resolution transmission electron microscope. The sample size required in HRTEM measure-

ment is about 0.0002 g dispersed in ethanol and then vibrated for 2 minutes in a 80 Hz Watt transistorized sonic cleaner. The HRTEM sample holder is immersed into the dispersed sample and then transferred to HRTEM in order to perform the measurements. HRTEM images can provide information about the crystalline quality and particle sizes.

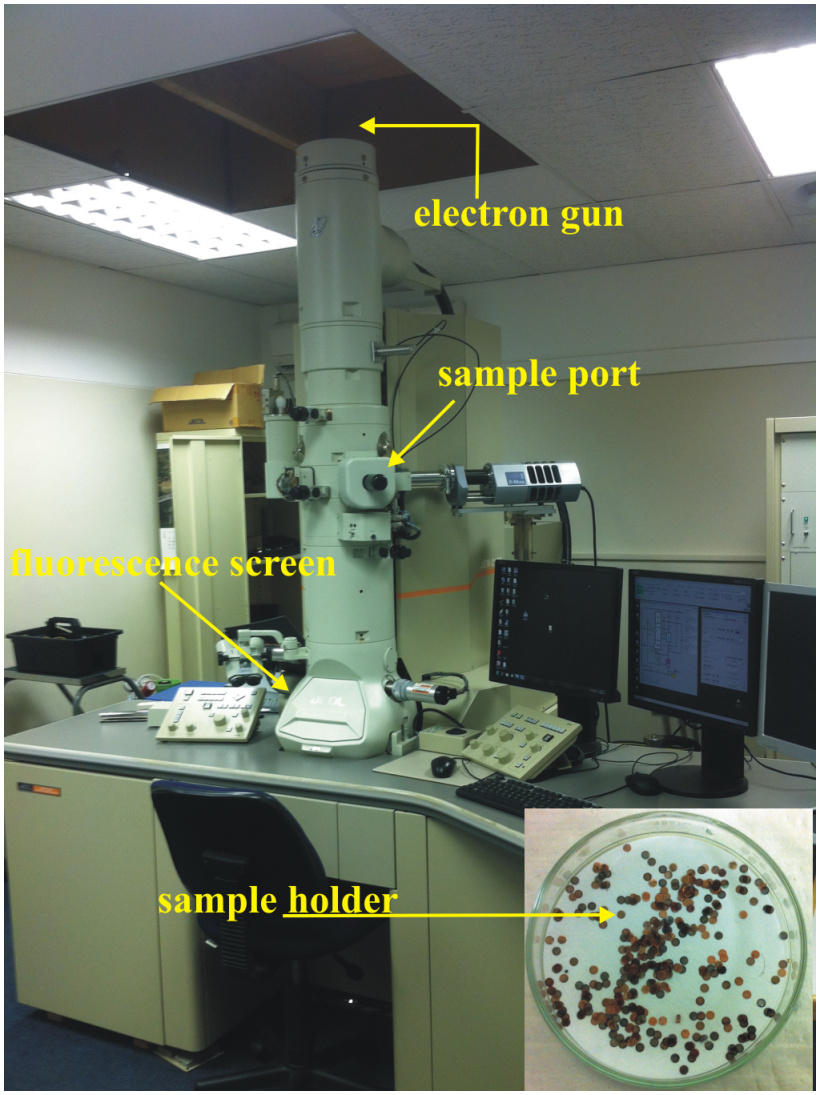

Figure 4.6: Joel-JEM-2100 high resolution transmission electron microscope, Westville campus.

High resolution scanning electron microscopy (HRTEM) uses a beam of electrons that can be reflected mainly from surface of the sample. This technique therefore, provides information about the surface morphology of a sample. The sample prepa-

ration in this case is critical and requires dispersion of the powdered sample on a double sided adhesive of carbon tape and coated with gold by using a Quarum coater type: Q 150 ES shown in Figure 4.7. The purpose of coating by gold is to increase the conductivity to obtain better resolution of surface images. Other elements such as carbon and platinum can also be used for coat samples. HRSEM measurements were performed on a Zeiss ultra high resolution scanning electron microscope shown in Figure 4.8. A scale of 200 nm was gave better image resolution for the samples studied in this thesis. The energy dispersive X-rays (EDX) measurements were also carried out on the same instrument. The EDX measurements provide information about elemental compositions as well as elemental distributions (mapping) on the sample surface. The EDX analysis was performed out using the AZtech software.

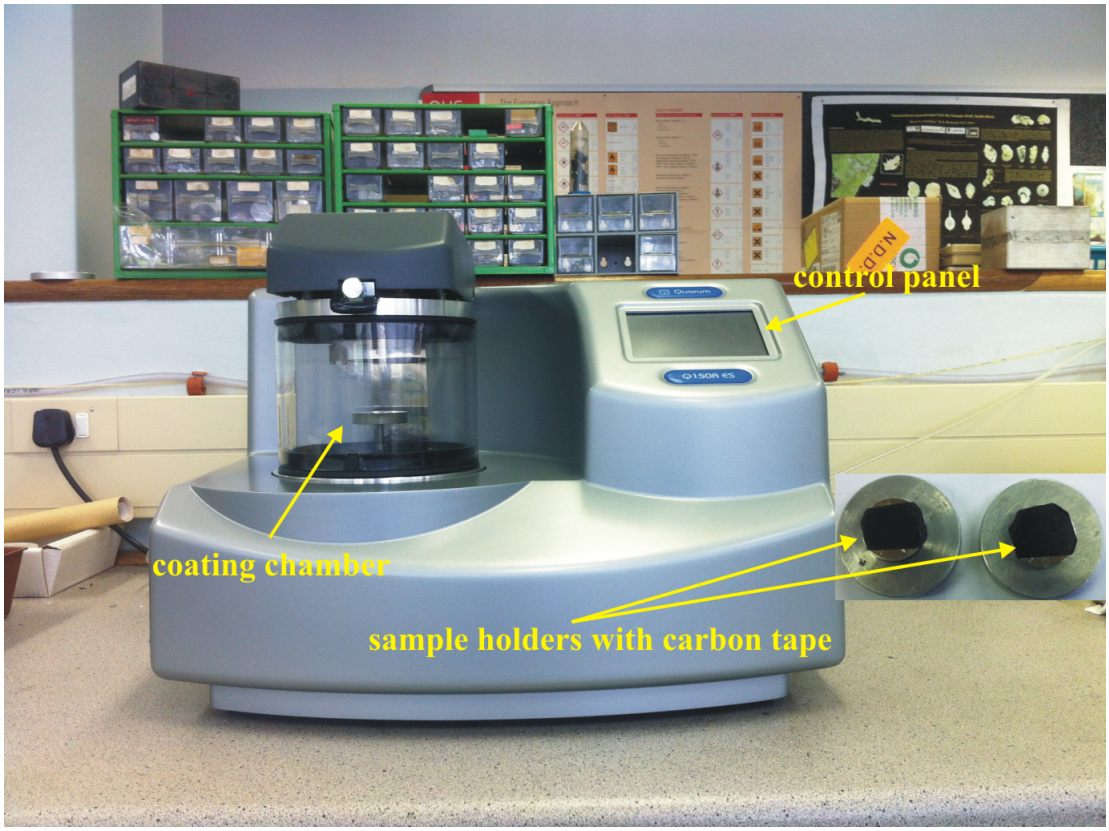

Figure 4.7: Quarum coater type: Q 150 ES, EM Unit Westville campus.

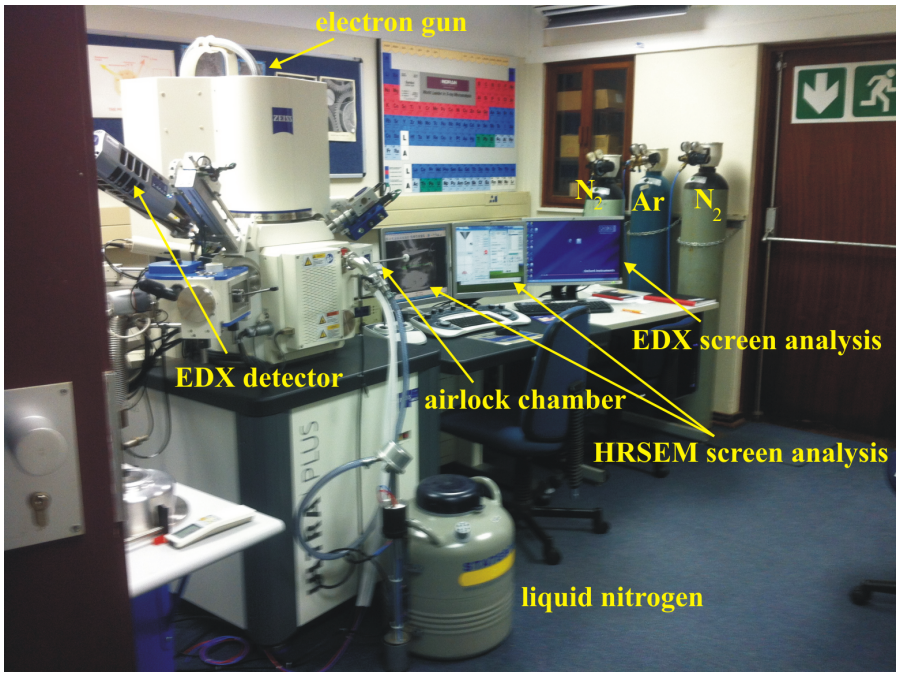

Figure 4.8: Zeiss ultra plus high resolution scanning electron microscope, EM Unit Westville campus.

4.1.5 Brunauer-Emmet-Teller and Barrett-Joyner-Halenda measurements

The Brunauer-Emmet-Teller (BET) method can be used to obtain surface areas of the particles in powdered sample. This technique gives information about the porosity of a sample in terms of pore volume and pore size distribution. The BET isotherm hysteresis loops are obtained by measuring the adsorption-desorption of nitrogen gas in the particle surfaces. Adsorption of nitrogen gas occurs by increasing the relative pressure P/P_0 at the constant liquid nitrogen temperature of 77 K and by decreasing P/P_0 desorption takes place. Materials can in general be classified based on adsorption isotherms into six categories [149]. The samples synthesized in this thesis were classified as type IV mesoporous materials. The sample size used to perform BET surface area measurement is about 0.2 g. The sample initially has to be degassed by nitrogen gas overnight at 200 °C using a micrometrics FlowPrep 060 Sample Degas System. The purpose of degassing by nitrogen gas is to dry and remove the moisture from the sample. The texturel and porosity characteristics of

the synthesized nanoparticles were investigated using a micrometrics Tristar II 3020 instrument using liquid nitrogen as the analysis gas at 77 K as shown in Figure 4.9.

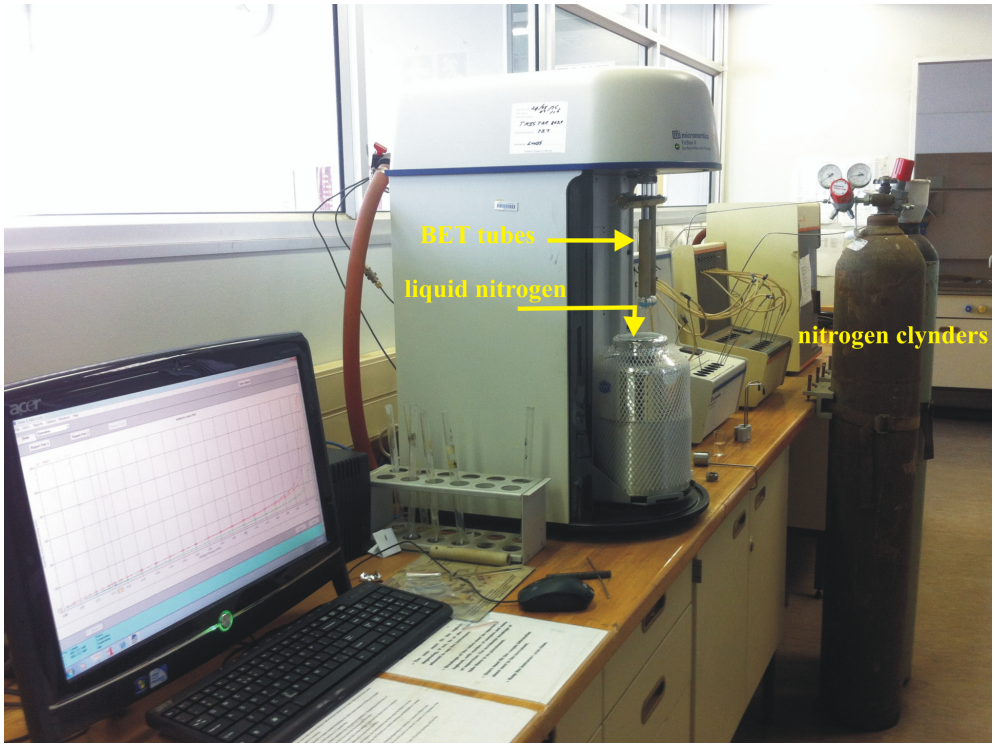

Figure 4.9: Micrometrics tristar II 3020 surface area and porosity, School of Chemistry and Physics, Westville campus.

4.1.6 Inductively coupled plasma optical emission spectrometer

Inductively coupled plasma optical emission spectrometer (ICP) is a technique which is used for elemental analysis of a sample. The technique can detect very low concentration of part per million (ppm) of elemental composition of a sample. The principle of elemental identification in ICP technique is based on detection of spontaneous photons that emitted from ionized sample. The sample ionized by an external magnetic field. The heat causes by the ionized sample (plasma) is cooled by argon gas. ICP is a suitable technique toward liquid samples. Therefore even a solid sample has to be in a solution form. That is why digestion process of the sample under investigation is a crucial matter in preforming ICP measurements. The digestion

process depends on nature of the sample. However, the digestion can be in open vessel (such as hotplate) or closed vessel (such as microwave). A solid sample can be dissolved in acid such as HNO_3, HCL, HF or H_2SO_4 for digestion process. In this thesis 0.0142 g of $Ti_{0.5}Ni_{0.5}Fe_2O_4$ was digested in 10 mL nitric acid on hotplate for 30 min. The vials were washed properly with double satire water to ensure better cleaning procedures. The digested sample was diluted in 100 mL of double satire water. The standard solutions of 1000 ppm were purchased from DLD Scientific South Africa. Different concentrations of the standard solution were diluted in 50 mL double stair water. The calibration solution of 50 mL was prepared by diluted 10 mL of nitric acid with double stair water. The prepared sample, standard and calibration solutions were transferred to ICP-OES Optima 2100 as shown in Figure 4.10. The ICP-PES system consist optical emission spectroscopy Optima 2100 DV, Autosampler: AS93 plus, computer with widows operation system for the analysis, chiller system type: PolyScieno No 772025 and extractor to ensure that the metal vapour does not contaminate the measurement room.

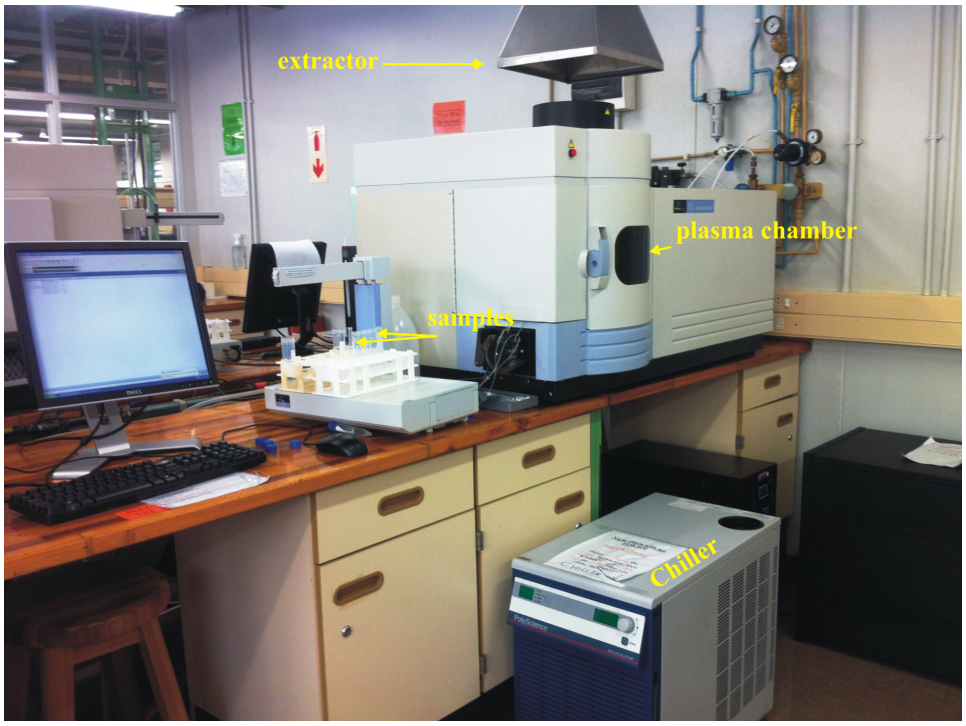

Figure 4.10: ICP optical emission spectrometer Optima 2100 DV, School of Chemistry and Physics Westville campus.

4.2 Magnetic measurements

The magnetic properties of the compounds were determined by a LakeShore model 735 vibrating sample magnetometer (VSM), mini-cryogen free measurement system (CFMS) and by ^{57}Fe Mössbauer spectroscopy (MS) in transmission geometry. The basic operation of the VSM, CFMS and MS are presented below.

4.2.1 LakeShore model 735 vibrating sample magnetometer

A vibrating sample magnetometer (VSM) is used to measure the magnetization of a sample as a function of magnetic field and temperature. The principle of VSM is based on Faraday's law, expressed as

$$\frac{d\Phi}{dt} = -E, \tag{4.2.1}$$

where Φ is the magnetic flux and E is the induced voltage in the pick-up coils that depends on the magnetic state of a sample. The magnetic properties can be studied by measuring the magnetic moment of the sample. The magnetization of the sample is proportional to the induced voltage. The change in flux is caused by vibrating the sample at fixed frequency. Figure 4.11 shows a LakeShore model 735 VSM. The system consists of a LakeShore model 362 power supply, model 735 VSM controller, model 340 temperature controller, model 450 Gaussmeter, vibrating head, Janis helium cryostat, Neslab ThermoFlex 2500 chiller and an EM4-HVA electromagnet. The VSM measurement components are connected via PCI-GPIB cables to a National Instruments IEEE-488 interface card in a computer. The magnetizations were calibrated with respect to a spherical standard nickel sample with a saturation magnetization of 54.8 emu/g in an applied external magnetic field of 5000 Oe. The calibration procedure also includes positioning of the nickel sample at the center of pick-up coils. This can be achieved by using the gears that attached to the VSM head. A typical sample size for magnetization measurement is about 0.025 g, the maximum applied field on this system is 14 kOe. The LakeShore model 735 provides the magnetic parameters value directly into a Text Document file.

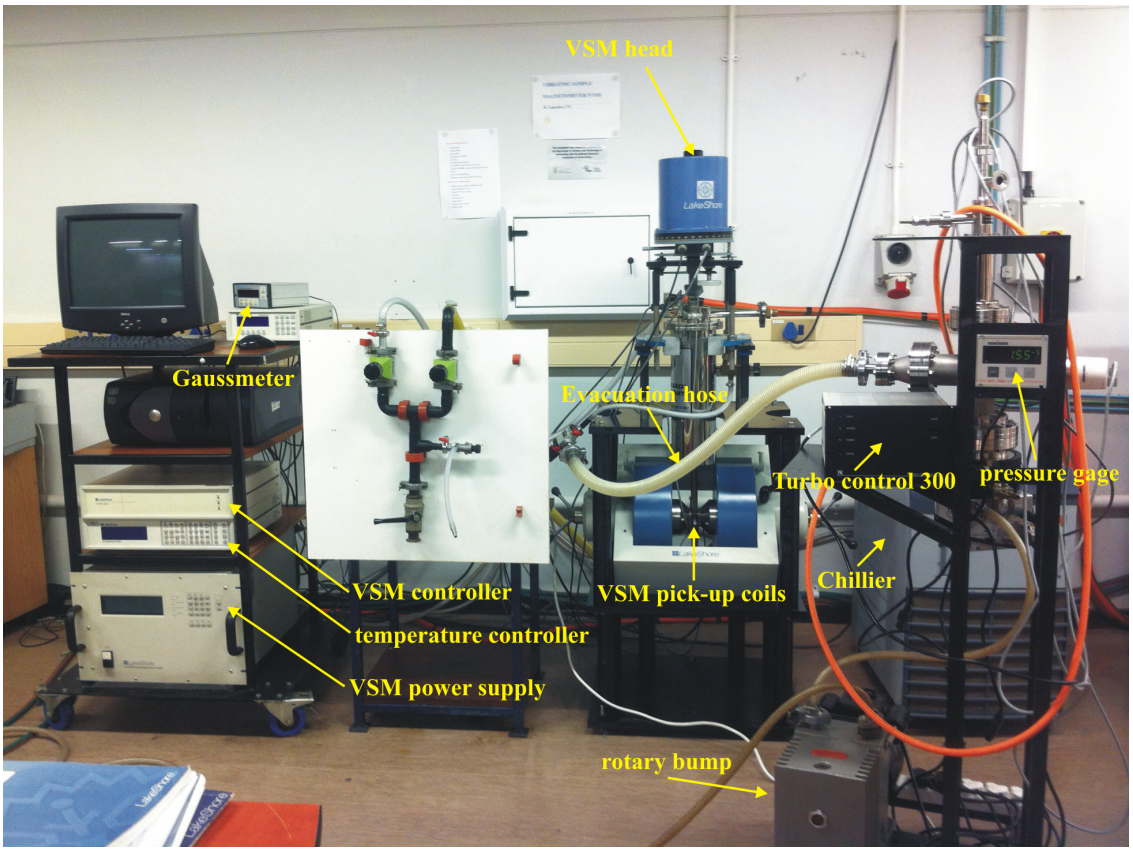

Figure 4.11: LakeShore model 735 vibrating sample magnetometer (VSM), Condensed Matter Physics Laboratory, Westville campus.

4.2.2 Mini cryogen free measurement system

The mini cryogen free measurement system (CFMS) was purchased from Cryogenic Ltd, UK. The system consists of a number measurement options namely vibrating sample magnetometer (VSM), AC susceptibility, resistivity and Hall effect measurements. The hardware for the system includes the cry-cooler system (cold head unit, compressor and water chiller), superconducting magnet, cryostat, variable temperature insert (VTI) and an electronics rack (for various components and desktop computer). In addition two vacuum pumps are available for evacuation of the sample space and for circulating the helium gas. The CFMS has capabilities for measurement from 1.6 K to 700 K in magnetic fields of up to 5 Tesla. Figure 4.12 shows the CFMS that we have used for magnetization measurement which has only exploited the VSM option on the system.

Figure 4.12: Mini cryogenic free VTI system, Condensed Matter Physics Laboratory, Westville campus.

The water chiller is a type TAE EVO 020 unit which consists of a refrigeration compressor, condenser, evaporator, tank, pump and electronic controller. It is important to address some technical issues associated with the chiller. We have experienced refrigerant low pressure and flow meter alarm condition. The refrigerant low pressure occurs when the refrigerant gas is lost through a leak. This appears as a code A02 alarm accompanied by the sound of a buzzer. The water chiller stops when refrigerant gas pressure falls to 1.7 bars. The water chiller can be reset by raising the gas pressure to 2.7 bars using refrigerant gas type R407C to a charge of 1.95 kg.

Since ordinary tap water is used in this chiller, dirt and some precipitates are expected to accumulate in the water tank and hoses. Thus regular flushing of the chiller is required.

In the case of a flow meter alarm, the electronic controller displays a A08 warning code accompanied by the sound of the buzzer. The top cover of the chiller should be opened in order to reset the thermal protection device by pressing it for 5 seconds. A green light comes on indicating a successful reset procedure. Table 4.2 shows the access to the function menu for the display, reset and historic alarms.

Table 4.2: The functions menu for display, reset and historic alarms.

Function menu			
Display AlrM	Reset AlrM	Display historic AlrM	Reset AlrM historic
1- Press "M"	1- Press "M"	1- Press "M"	Press "M"
2- Press ⇑ or ⇓	2- Select "ALrm"	2- Press ⇑ or ⇓	2- Select "ALoG"
to select ALrM	3- Press "SET"	to select "ALoG"	3- Press "SET"
3- Press "SET"	4- "rSr": can be reset,	3- Press "SET"	4- Inside "ALoG"
4- Press ⇑ or ⇓	"No": can not reset	4-Press ⇑ or ⇓	enter the password
to scroll all alarms	5- Press ⇑ or ⇓	to scroll all alarms	5- "ArSt" flashes
5- Press "M" for	to scroll all alarms	5- Press "M" for 5 sec	confirms the resetting
30 sec to exit.	6- When "rSt" displays	30 sec to exit.	
	press "SET"		
	7- Press "M" for.		
	30 sec to exit		

The continuous closed-cycle refrigeration of the CFMS is provided by the crycooler system type: SRP-062. The compressor is connected to the water chiller through water hoses for cooling. The cold head unit and the compressor unit are connected by flex lines which include a filter unit on one the lines. The compressor is responsible for providing high pressure helium gas to the cold head unit through the helium gas supply connectors. At low gas pressure (noted from the supply and return pressure gauges), the compressor does not work. In this case it is necessary to refill the compressor by helium gas to the admissible range as indicated in Figure 4.13. It is very important to know that damage can occurs if the pressure gas varies from the operation range. Every 30000 hours the filter unit has to be replaced. The cold head unit requires maintenance every 20000 operating hours.

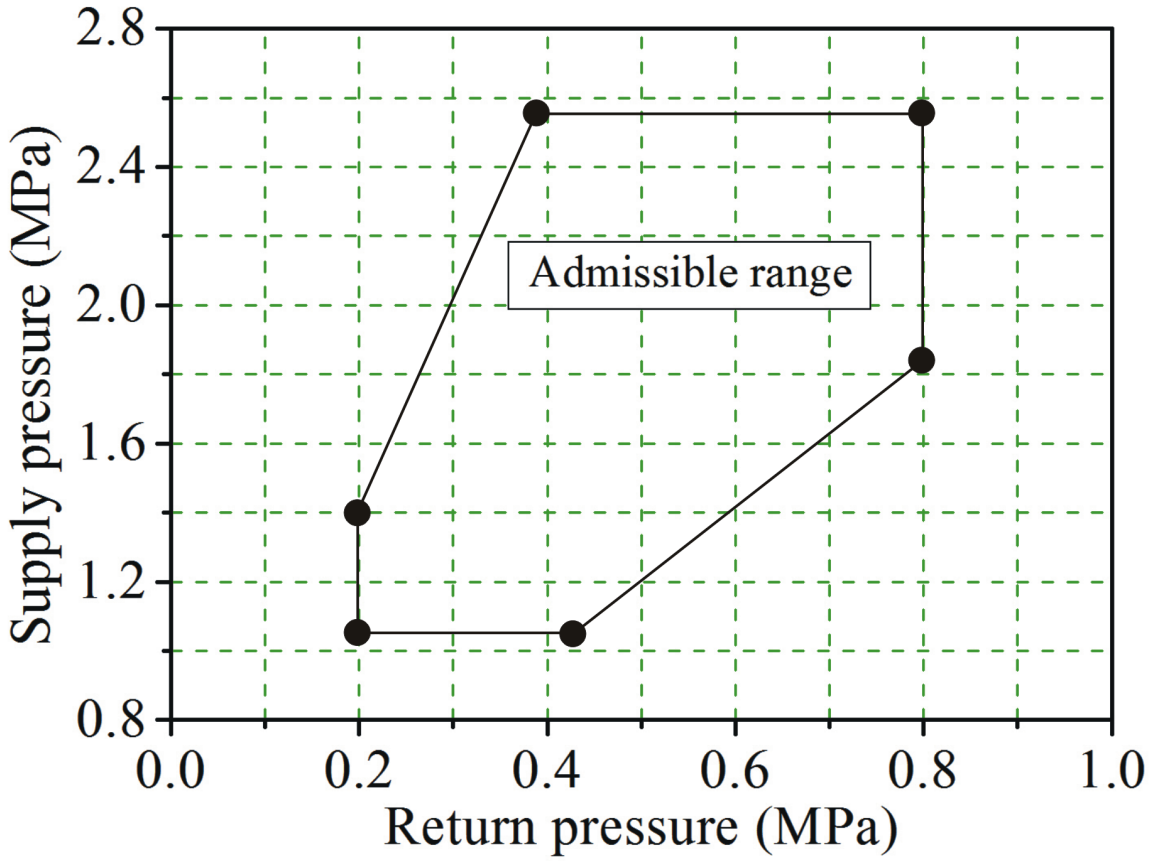

Figure 4.13: Admissible operation range for return and supply pressure.

The CFMS uses the LabeVIEW graphical program as the software interface for

the system. For magnetization measurements the system needs to be calibrated by standard yttrium iron garnet of a spherical sample. The sample preparation for measurement consists of placing about 0.005 g of the sample into a Perspex cone sample holder. A small piece of cotton wool was used to secure the powdered sample in order to avoid torques on the sample during magnetization measurements. This Perspex cone was attached and fixed properly using Kapton tape at a position of 20 mm in a straw of length 80 mm as shown in Figure 4.14. An adaptor was fixed at the other end of the straw and screwed to the CFMS probe. The probe was loaded into the CFMS sample space using the sample load option in the software window. This procedure requires the helium exchange gas cylinder to be opened. The Load sample instructions have to be followed precisely.

Figure 4.14: CFMS VSM probe attached to a sample.

For all measurements, centring of the sample also plays an important role in obtaining the best signal sensitivity and a good measurements curve. To get a magnetic signal from the sample a magnetic field of 0.1 T is applied. The VSM rod is lowered slowly while monitoring the changes in the magnetic response on a graphical display of moment versus time. The lowering is stopped at the highest magnetic moment obtained. The auto-centering option from control window is used to determine the sensitivity accuracy. The recommended sensitivity value is about ± 0.5. For the magnetic samples that investigated here a sensitivity accuracy value of ± 1 was also acceptable. The sample is finally secured in the optimum position. Magnetic measurements are initiated through a programmed sequence of commands from the control window.

4.2.2.1 Evacuation procedure

The continuous operation of the CFMS over a few weeks can lead to the formation of ice in the sample space, loss of the low pressure in the vacuum chamber and VTI circuit. Therefore, it is important to evacuate the vacuum chamber and VTI circuit regularly. The CFMS system need to be warmed up to room temperature and that usually takes about 3 days. Every time that the CFMS is warmed up to room temperature the vacuum chamber should also be evacuated. To evacuate the vacuum chamber, the airlock hose has to be disconnected from its original position and connected to the vacuum pumping port. The recommended vacuum chamber pressure should be below 10^{-4} mbar. Since no pressure gauge is available using the rotary pump, the vacuum chamber is normally evacuated overnight. The vacuum pump valve is closed after the evacuation procedures. The airlock hose is re-connected to the helium inlet through a special adaptor. VTI circuit is also evacuated overnight to ensure that all the contaminations in VTI system and charcoal filter are removed.

4.2.2.2 Recharging the dump

The helium dump is the main storage chamber for helium gas. The dump which has an oil free pump is connected to exhausted release valve. To ensure complete evacuation of the dump, the helium airlock hose is connected directly to the dump exhaust and pumped out by a rotary pump. The helium inlet hose is connected to helium gas cylinder of purity of 99.999% purchased from Afrox, South Africa. To fill up the dump, the exhaust valve is closed and the helium cylinder is opened to allow the helium gas to fill up the dump. The helium cylinder is closed after the dump pressure reaches about -0.5 bar. The dump is re-filled with helium gas and re-evacuated and the above process is repeated 3 times to ensure only uncontaminated fresh helium gas finally occupies the helium dump. The dump is finally recharged to about 0.25 bar with fresh helium gas. The exhaust valve is closed while the helium inlet and airlock hoses are re-connected to their original positions. Switch-on and shut-own procedures are specified in CFMS manual.

4.2.3 Mössbauer spectroscopy measurements

Most of the samples studied in this work contain Fe atoms. We have therefore used ^{57}Fe Mössbaue spectroscopy (MS) measurements to supplement the magnetization measurements. MS provides information of the magnetic order and the distribution of the cations in the tetrahedral and octahedral sites. Two spectrometers are available, one with a cryostat and the other with a Mössbauer furnace. Each consists of a power supply, MR-351 Mössbauer drive unit, spectroscopic CANBERRA amplifier, IIFAST ComTec pre-amplifier, LND INC 45431 proportional counter radiation detector (activated by 1800 V), ORTEC MCS-pci^{TM} data acquisition card and multichannel analyser software version 2.13 installed in a desktop computer. Figure 4.15 shows Mössbauer spectroscopy set-ups. The ORTEC MCS-pci^{TM} data acquisition card does not have a default pulse height analysis (PHA) mode. The option for single channel analyser (SCA) sweep through the 512 channels, one at time, exists which allows for a somewhat slow identification and selection of the 14.4 keV Mössbauer peak. A standard 99.5% pure iron foil of thickness of about 0.025 mm was used at room temperature to generate the spectrum for velocity calibration at a particular maximum velocity setting of the source. A typical sample size for our absorber was about 0.10 grams spread uniformly on a 13 mm diameter sample holder. in plastic sample holder and fixed properly by a small piece cotton wool. The sample was positioned in between the detector and a 25 mCi ^{57}Co radioactive source. The source was vibrated at constant acceleration. A typical detected γ rays spectrum was recorded for at least 12 hours after which the data was ready for analysis in order to extract the Mössbauer parameters.

4.3 Sentro Tech high temperature tube furnace

Thermal annealing of the synthesized samples were carried out in a Sentro Tech type: STT-1600C-3-24 high temperature tube furnace shown in Figure 4.16. The furnace uses $MoSi_2$ heating elements, B-type thermocouples, Yudian 30 segment programmable temperature controller and Eurotherm over-temperature controller. The maximum operating temperature of the furnace is 1600 °C. The furnace allows

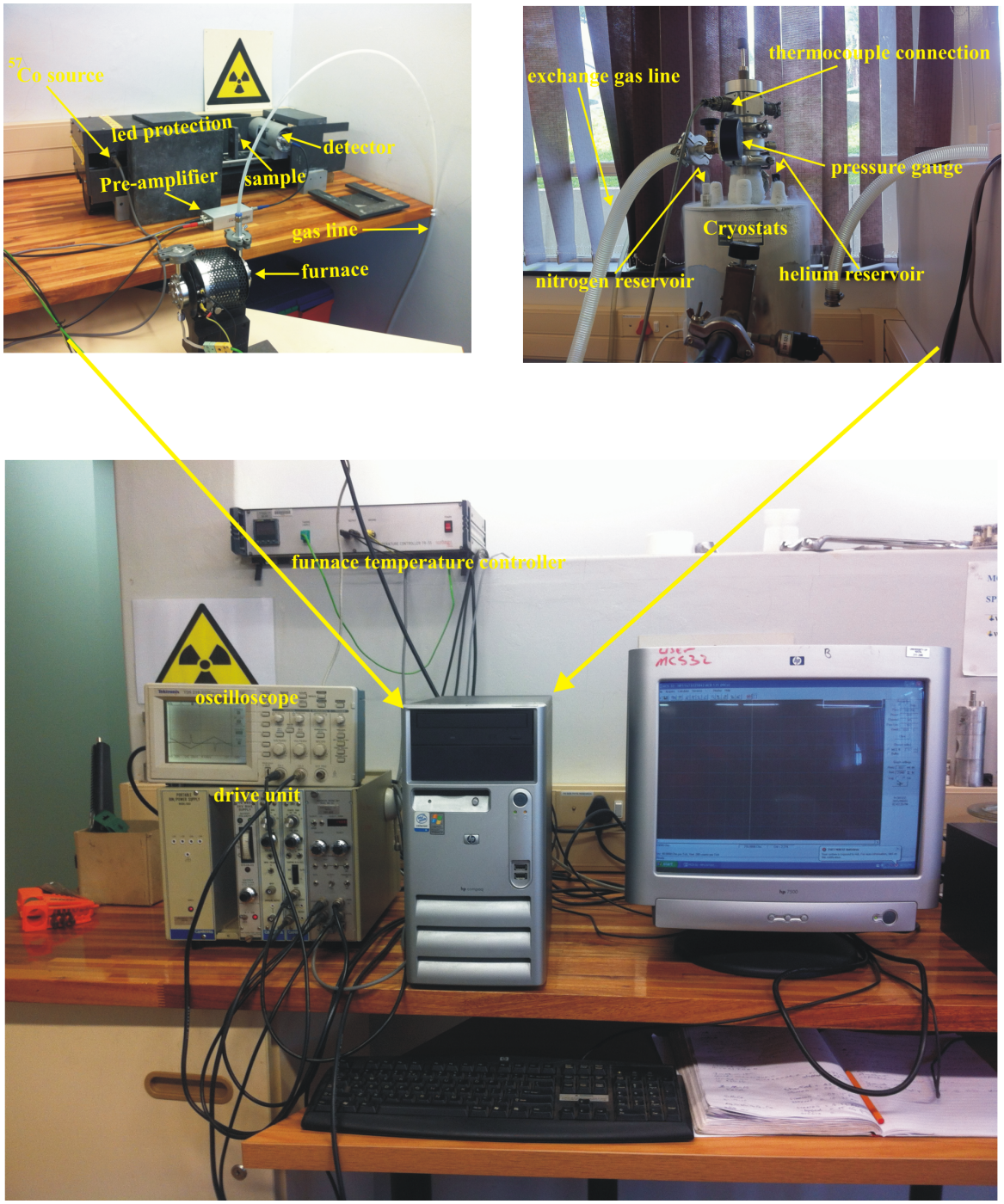

Figure 4.15: Mössbauer spectroscopy set up, Condensed Matter Physics Laboratory, Westville Campus.

for annealing in air or flowing argon gas atmosphere.

Figure 4.16: Sentro Tech type: STT-1600C-3-24 high temperature furnace, Condensed Matter Physics Laboratory, Westville Campus.

4.4 Electrochemical measurements

4.4.1 Voltammetric equipment

The voltammetric measurements were performed on an electrochemical analyser CH instrument model: 800B Series. This facility consists of a three electrode electrochemical cell namely Ag/AgCl reference electrode, a platinum counter electrode and glassy carbon working electrode (GCE) shown in Figure 4.17. The GCE electrode needs to be cleaned thoroughly by polishing using 0.5 mm alumina slurry on a polishing cloth. The electrode is also thoroughly rinsed with double-distilled water and dried in air. A small amount of a sample of about 0.5 mg was diluted in 0.001 L of dimethylformamide (DMF) solvent. A small drop of the diluted sample of DMF

was deposited into the surface of the cleaned GCE. The modified GCE was dried for 10 minutes in a pre-heated oven at 100 °C. The active surface areas of the bare and modified GCE can be obtained from cyclic voltammograms (CVs) in the presence of 1.0 mM of $K_3[Fe(CN)^6]$ solution at different scan rates.

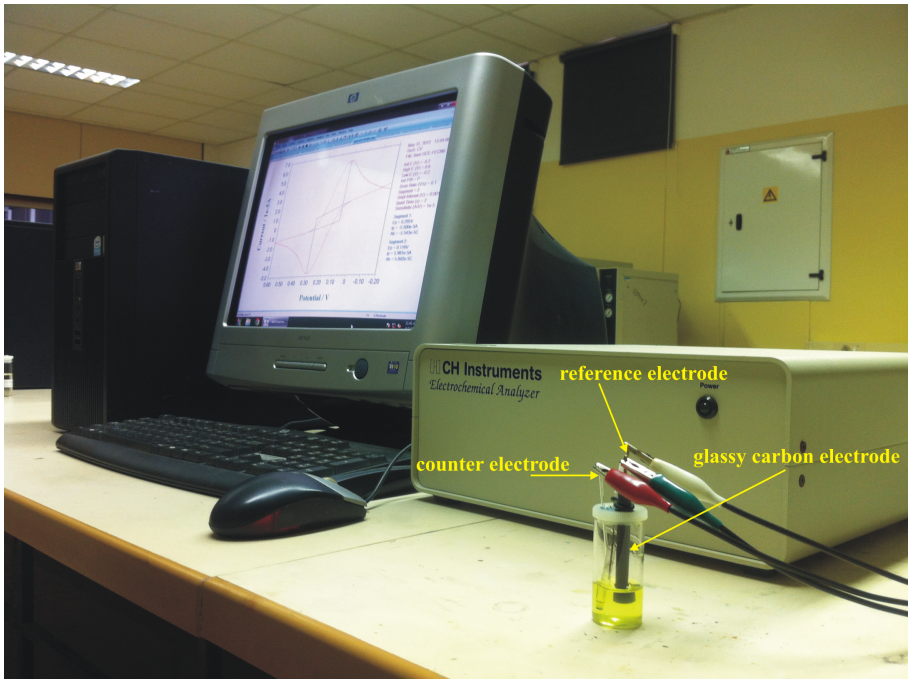

Figure 4.17: Cyclic voltammetric set-up, Department of Pharmaceutical Chemistry, Westville Campus.

4.4.2 Electrochemical analysis

The electrochemical cell is used to investigate the chemical response of an analyte by measuring the voltage (potential) and/or current signals [150]. Three electrodes are conventionally employed in electrochemical set-up which comprises of a working electrode, reference electrode and an auxiliary electrode [150]. Electroanalytical methods are commonly used due to their relatively cheap instrumentation, high accuracy, precision, sensitivity, rapid analysis time and ability to simultaneously determine various analytes in a solution [151, 152]. Furthermore, electroanalytical analysis has a feature of direct analysis of a sample without tedious and long preparative procedures [153]. The technique is widely used for analysis of drugs

in pharmaceutical formulations and biological samples. Electrochemical techniques mainly include cyclic voltammetry and chronocoulometry [154]. Cyclic voltammetry is powerful, simple and rapid method for characterizing the electrochemical activity of an analytes which can be electrochemically oxidized or reduced [155]. The electrochemical reactions can be described at least in part by the Nernst equation [156] expressed as

$$E = E^0 - \frac{RT}{nF} \ln\left(\frac{C_R}{C_O}\right), \tag{4.4.1}$$

where E^0 is the redox potential. The Nernst equation describes the relation between potential of an electrode and concentrations C_O and C_R of two species O and R which are involved in the redox ($O + ne^- \longleftrightarrow R$) reaction at the electrode surface.

In cyclic voltammetry, the potential of a working electrode is changed gradually (in Volts/second) and then reversed to the initial potential. Simultaneously, the curve of measured current versus applied potential is recorded. This curve (as shown in Figure 4.18) is known as a cyclic voltammogram [157].

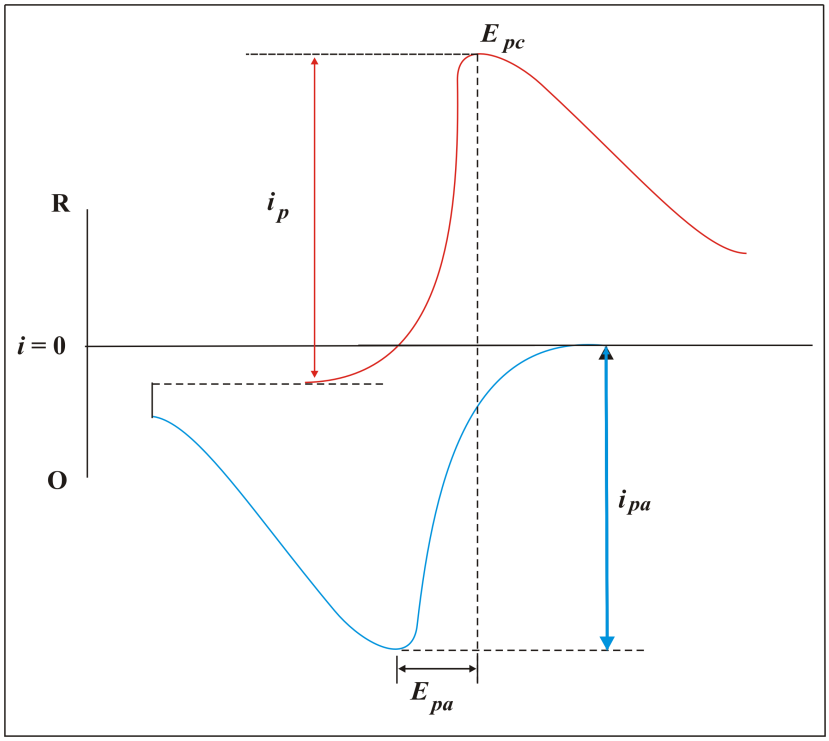

Figure 4.18: Theoretical cyclic voltammogram for a reversible case.

In the case of a reversible system the peak current (in amperes) i_p at 298 K is given by Randles-Sevcik equation [158]

$$i_p = 2.69 \times 10^5 n^{3/2} A D^{1/2} C v^{1/2}, \tag{4.4.2}$$

where A is the surface area of working electrode in cm^2, n is the number of electrons transferred in the electrochemical process, D (in $cm^2\ s^{-1}$) is the diffusion coefficient, C (in mol cm^{-3}) is the concentration of the electroactive species and v is the scan rate (in V s^{-1}). The diffusion coefficient of the electroactive species can be determined from equation 4.4.2. For specimens where the diffusion coefficient is already known, the slope obtained from the plot of i_p verses $v^{1/2}$ can provide information about the redox process [159].

In the case of irreversible processes, individual peaks are reduced in size and are widely separated. The peak current is given by [160]

$$i_p = 2.99 \times 10^5 n(\alpha n)^{1/2} A D^{1/2} C v^{1/2}. \tag{4.4.3}$$

For an irreversible electron transfer, E_P is expressed by the Laviron's equation

$$E_p = E^0 + \left[\frac{2.303RT}{\alpha nF}\right] \log \left[\frac{RTk^0}{\alpha nF}\right] + \left[\frac{2.303RT}{\alpha nF}\right] \log v, \tag{4.4.4}$$

where α is the transfer coefficient, k^0 is the standard heterogeneous rate constant of the reaction and E^0 is the formal redox potential [161]. The value of αn can be calculated from slope of the plot of E_p verses log v by considering $T = 298$ K, $R = 8.314$ J/K mol and $F = 96480$ C/mol. The value of n can therefore be calculated since the parameter α is known to be

$$\alpha = \frac{47.7}{E_p - E_{p/2}}, \tag{4.4.5}$$

where $E_{p/2}$ is the half-peak potential [162].

The electrochemical process can be adsorption or diffusion controlled. Adsorption-controlled electrochemical process takes place when i_p is proportional to v whilst, if i_p is proportional to $v^{1/2}$ suggests diffusion-controlled electrochemical process [163]. This is can further be confirmed by plotting $\log i_p$ versus $\log v$ that exhibits a straight

line graph with a slope of 0.5 for ideal diffusion and 1.0 for adsorption-controlled process [164]. The effect of pH on electro-oxidation or reduction of an analyte can be investigated by plotting E_p versus pH. The value of the slope reveals the characteristics of the electrode in terms of the number of electrons and protons which are involved in the reaction process [165].

Chapter 5

Structural and magnetic properties of $CoFe_2O_4$ nanoferrite simultaneously and symmetrically substituted by Mg, Sr and Mn

5.1 Introduction

Spinel nanoferrites are amongst the most studied materials with interesting optical, magnetic and electrical properties [166]. By changing the divalent elements at the tetrahedral and octahedral sites, the magnetic properties can be tuned. $CoFe_2O_4$ ferrite has been widely studied and is known for its good magnetostriction properties, high magneto-crystalline anisotropy and moderate saturation magnetization. These features make $CoFe_2O_4$ a popular and interesting system to study. This is further encouraged by multiple substitutions of Co and Fe ions in the system. Jigajeni *et al* [167] have reported that $Mn_{0.2}Mg_{0.3}Co_{0.7}Fe_{1.8}O_4$ is a good candidate for magnetoelectric applications which show favorable values of resistivity, saturation magnetization and coercive field. Abdallah *et al* [168, 169] have reported the synthesis and the magnetic properties of $(Mg, Sr)_{0.2}Mn_{0.1}Co_{0.7}Fe_2O_4$. These results show enhancement in the magnetic properties compared to the parent $Mn_{0.3}Co_{0.7}Fe_2O_4$

sample. Therefore, simultaneous and symmetrical stoichiometric samples with Mg, Sr and Mn could be interesting to synthesize and study. As compared to the reported results in references [168, 169, 170], a new compound of $Mg_{0.1}Sr_{0.1}Mn_{0.1}Co_{0.7}Fe_2O_4$ shows a relatively large lattice parameter, high magnetic internal hyperfine fields, slightly smaller grain size, significantly larger coercive field at 300 K and at 2 K. Sr and Mg have similar electronic configurations but differ in atomic sizes. This may also have important implications on the properties. Therefore, in this chapter we have discussed simultaneous substitutions of Co by Mg, Sr and Mn in $CoFe_2O_4$ for a series of samples with equal atomic proportions of substituting elements. The aim is to investigate how structural and magnetic properties change due to the symmetry in the stoichiometry of the substituting elements.

5.2 Experimental details

A series of $Mg_xSr_xMn_xCo_{1-3x}Fe_2O_4$ nanoferrites (for $x = 0$, 0.1, 0.2, 0.3, 1/3) were synthesized by the glycol-thermal method. The starting materials were $CoCl_26H_2O$: 98% , $FeCl_36H_2O$: 99%, $MnCl_24H_2O$: 99%, $MgCl_26H_2O$: 99% and $SrCl_26H_2O$: 99%. The synthesis procedures were described in chapter 4. The phase and structural characterization of the samples were studied by a Phillips X-ray diffractometer Model: PANalytical, EMPYREAN using CoK_α radiation. The morphology of the nanoparticles was investigated by a high-resolution transmission electron microscope (HRTEM) (type: Jeol_JEM-1010). The microstructure of the samples was investigated by a high-resolution scanning electron microscope (HRSEM) (Ultra Plus ZEISS-FEG HRSEM instrument). The iron distribution was investigated by room temperature ^{57}Fe Mössbauer spectroscopy measurements. Room temperature magnetic measurements were first investigated by magnetization measurement on a LakeShore vibrating sample magnetometer (VSM). Further measurements were performed on the the mini cryogenic free measurement system (CFMS).

5.3 Results and discussion

5.3.1 Structural and morphology investigations

Figure 5.1 shows XRD patterns of the as-prepared samples of $Mg_xSr_xMn_xCo_{1-3x}Fe_2O_4$ series. The patterns indicate that single-phase spinel structure was obtained for all the samples. The highest intensity peak corresponds to (311) planes. The broadening of the peaks indicated small particle sizes. The average particle sizes were calculated using equation 4.1.3. The lattice parameters a were calculated using the equations 4.1.1 and 4.1.2. The XRD densities of the samples ρ_{XRD} were calculated using equation 4.1.4. The results show reduction of ρ_{XRD} with increasing value of x. This is associated with the decrease in the Co content and molecular weight M_0 (Table 5.1). We have therefore, plotted ρ_{XRD} versus M_o. Good correlation between ρ_{XRD} and M_o is observed as shown in Figure 5.2. The microstrain ε values were deduced from the Williamson-Hall Plots as shown in Figure 5.3 [171]. The calculated values of a, D and M_0, ρ and ε are also presented in Table 5.1. The lattice parameter and the density of the sample at $x = 0$ were found to be similar to the reported values of 8.383 Å and 5.29 g cm^{-3} respectively, for a $CoFe_2O_4$ sample [172]. However, there is no significant changes in the lattice parameters after substitution of Co except for the sample at $x = 1/3$ which shows a relatively higher lattice parameter. The calculated microstrains do not show large variation with composition. The average strain value obtained is 0.0017±0.0002. This reflects similar microstructure environments with strains induced by similar synthesis conditions. The microstructure and the surface morphology were studied by HRTEM and HRSEM respectively. Figure 5.4 shows typical HRTEM micrographs which appear to show nearly spherical nanoparticles with some agglomeration known to enhance magnetic interactions between nanoparticles [173]. The boundaries between the crystallites are clearly distinct. The values of the particle sizes estimated from the images are also given in Table 5.1 and are consistent with the estimates from the XRD. HRSEM surface morphologies of the as-prepared $Mg_xSr_xMn_xCo_{1-3x}Fe_2O_4$ which also support the observations from HRTEM are shown in Figure 5.5. Figure 5.6 shows the EDX analysis spectrum for the $CoFe_2O_4$ sample. All the peaks are associated with the expected elemental

compositions (Figure 5.6 (a)). The elemental distributions are presented in Figure 5.6 (b). The elemental mapping measurements show homogeneous elemental distribution along the sample surface.

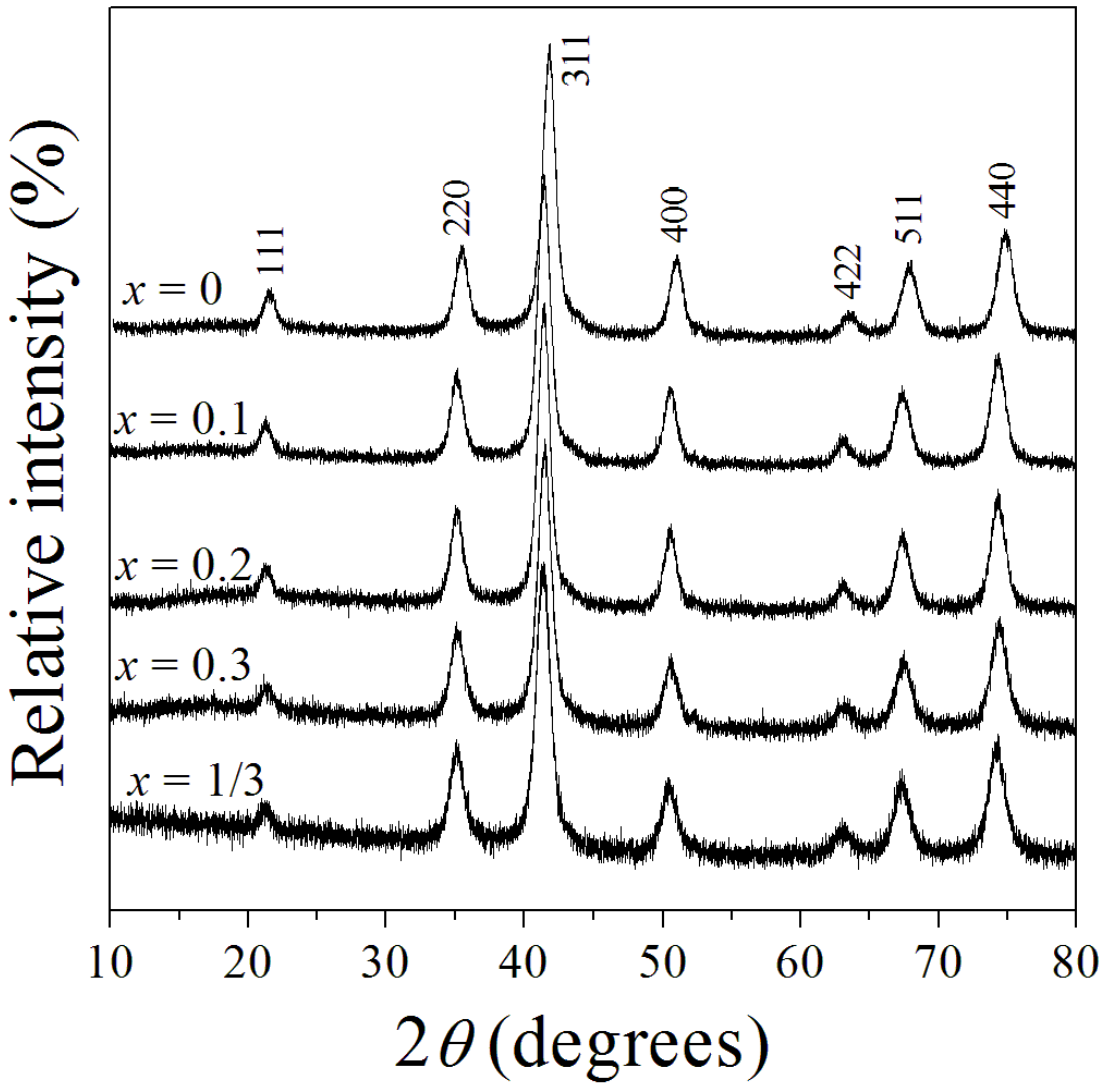

Figure 5.1: XRD patterns for the as-prepared samples of $Mg_xSr_xMn_xCo_{1-3x}Fe_2O_4$ nanoparticle ferrites.

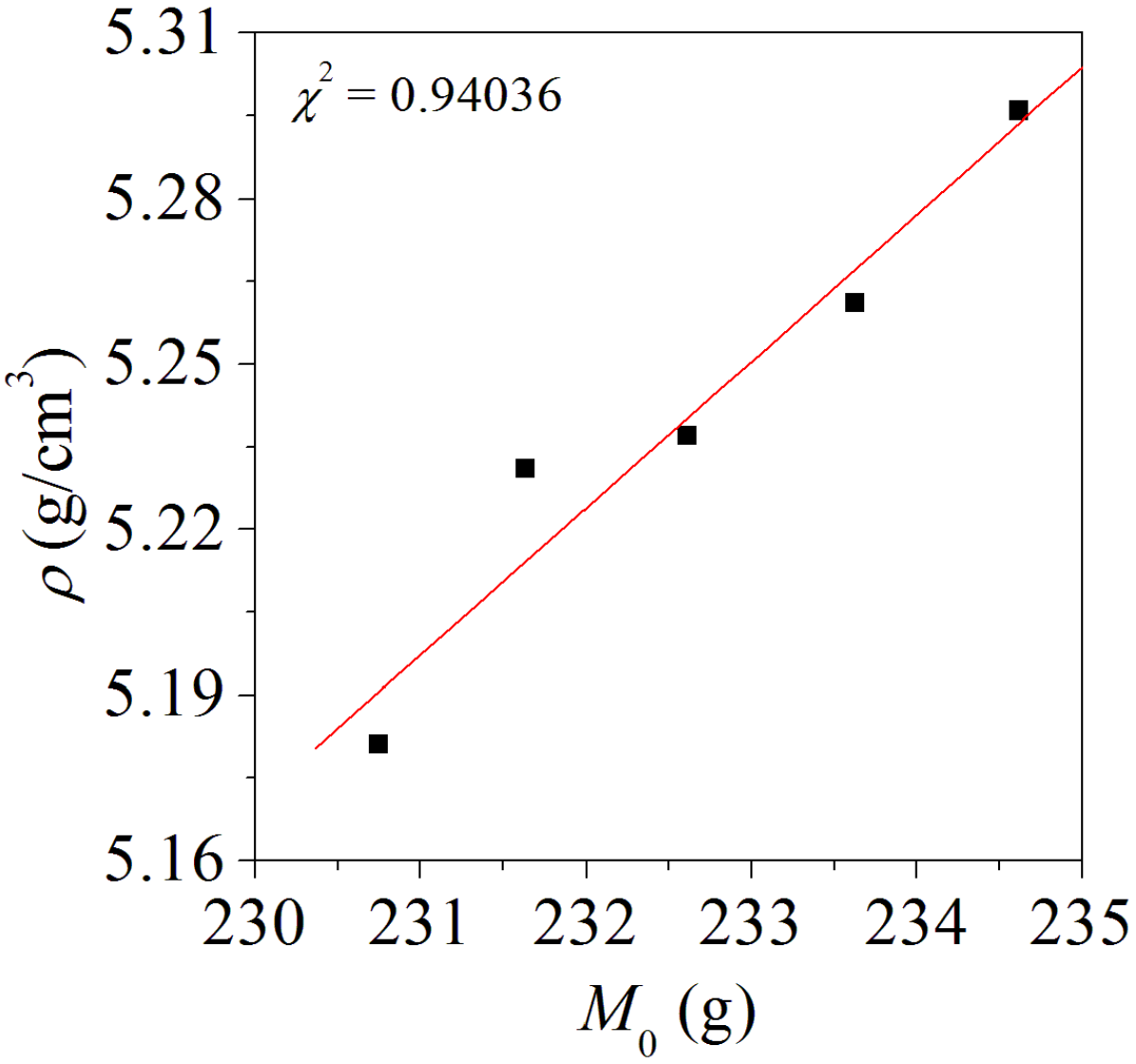

Figure 5.2: Variation of samples density with molecular weight of the as-prepared $Mg_xSr_xMn_xCo_{1-3x}Fe_2O_4$ nanoparticle ferrites.

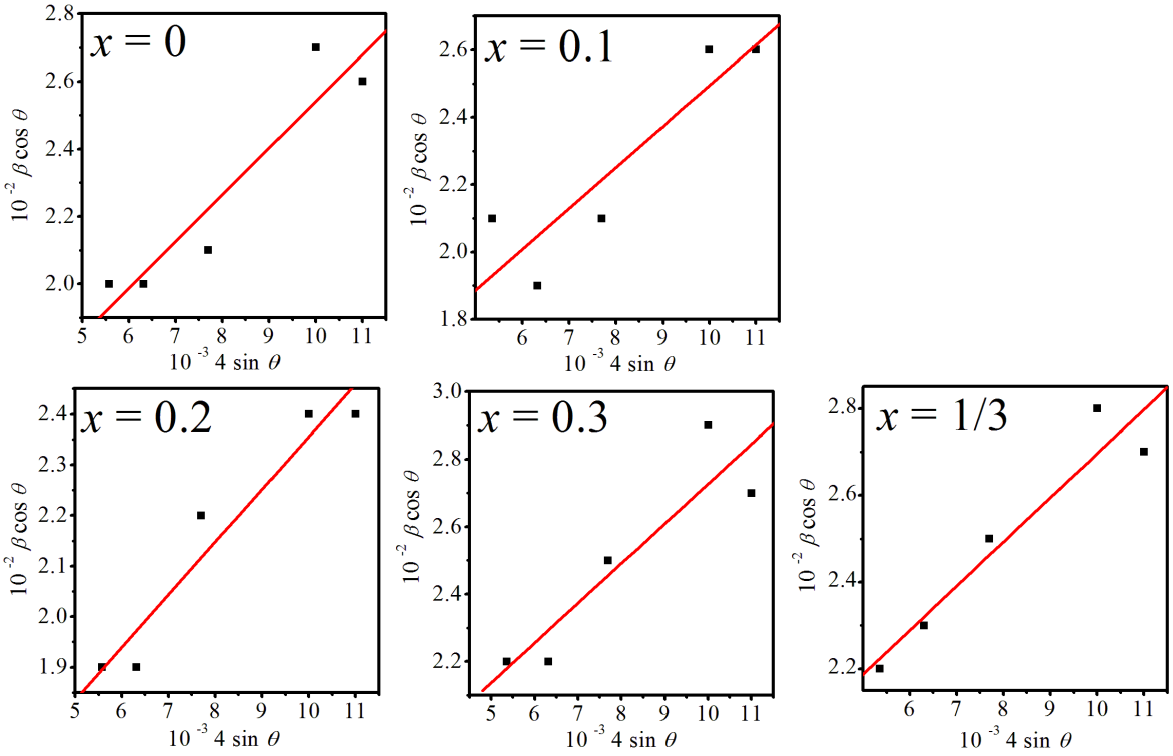

Figure 5.3: Williamson plot for the as-prepared $Mg_xSr_xMn_xCo_{1-3x}Fe_2O_4$ samples.

Table 5.1: The lattice parameters (a), crystallite sizes (D), HRTEM particle sizes (D_{HRTEM}), X-ray densities and microstrains (ε) of the as-prepared $Mg_xSr_xMn_xCo_{1-3x}Fe_2O_4$ compounds.

x	$a(\AA)$	D_{XRD}(nm)	D_{HRTEM}(nm)	ρ_{XRD}(g/cm^3)	ε	M_0
	$\pm$0.003	$\pm$0.01	$\pm$2	$\pm$0.001	$\pm$0.0004	(g)
0.0	8.380	8.27	9	5.296	0.0020	234.62
0.1	8.387	8.91	8	5.261	0.0017	233.63
0.2	8.387	8.34	9	5.237	0.0015	232.61
0.3	8.379	8.28	7	5.231	0.0019	231.64
1/3	8.395	8.20	8	5.1181	0.0016	230.75

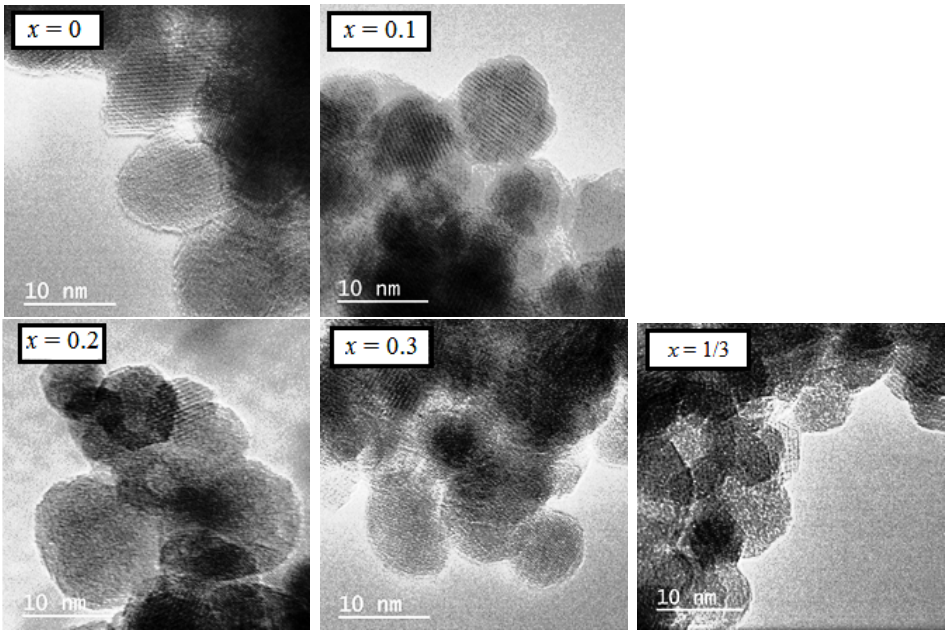

Figure 5.4: HRTEM micrographs for the as-prepared $Mg_xSr_xMn_xCo_{1-3x}Fe_2O_4$ samples.

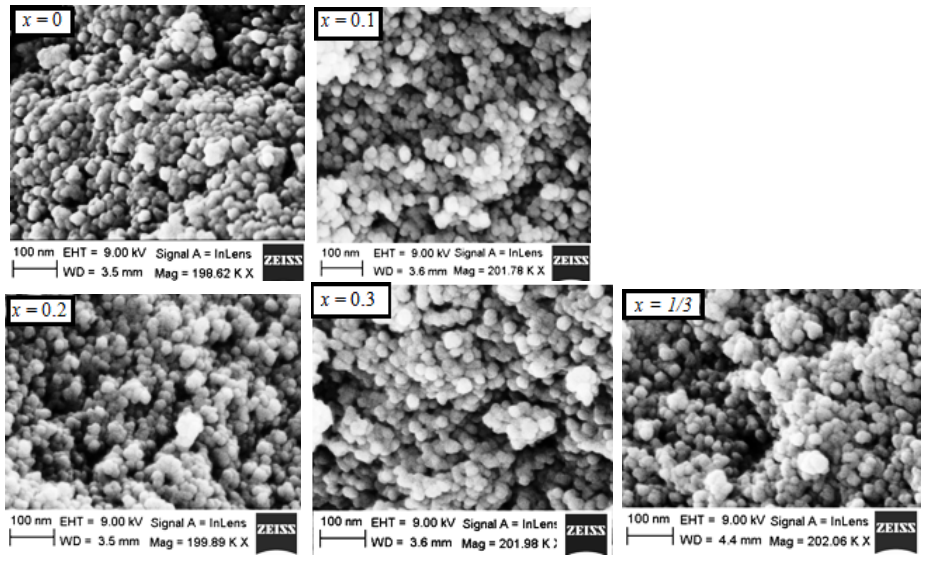

Figure 5.5: HRSEM micrographs for the as-prepared $Mg_xSr_xMn_xCo_{1-3x}Fe_2O_4$ samples.

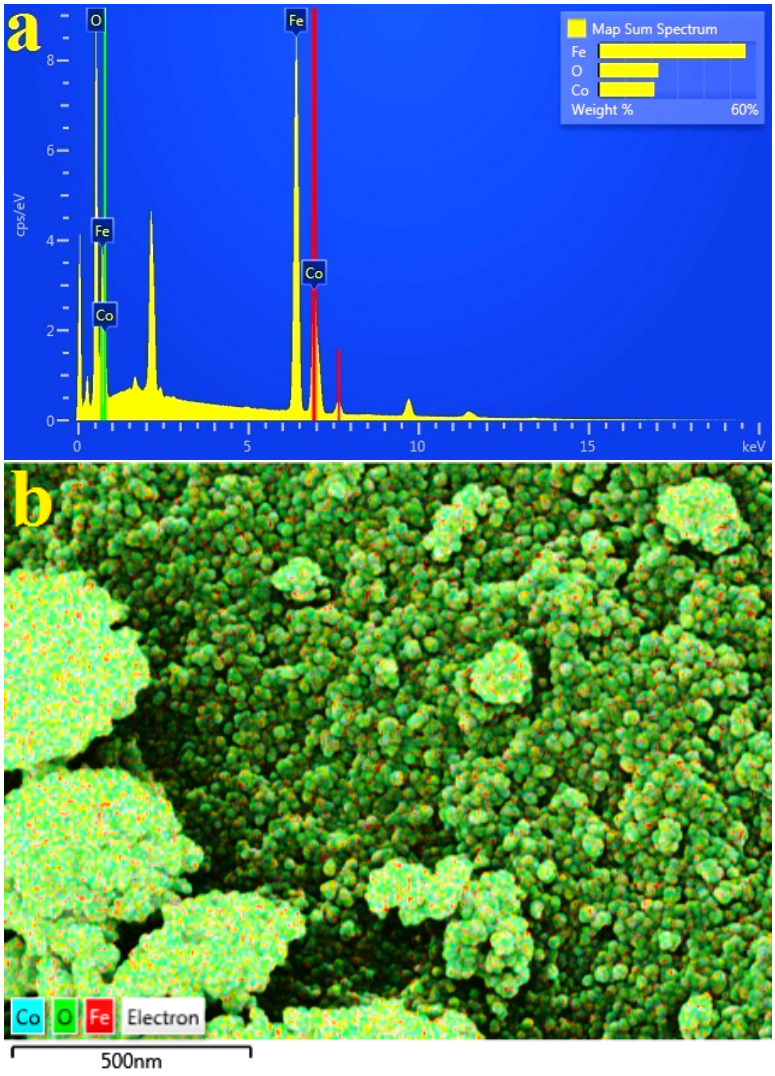

Figure 5.6: (a) EDX spectra of the elemental composition, and (b) the distribution of the elements for sample $CoFe_2O_4$.

5.3.2 Magnetic measurements

5.3.2.1 Mössbauer measurements

Figure 5.7 illustrates the room temperature Mössbauer spectra for the as-prepared $Mg_xSr_xMn_xCo_{1-3x}Fe_2O_4$ samples. The samples show distinct Zeeman sextets except $x = 1/3$ which is revealed magnetic relaxation. The two Zeeman sextets are attributed to iron ions on tetrahedral (A) and octahedral (B) sites were used to fit the Mössbauer data. The results of the hyperfine parameters are presented in

Table 5.2. The values of hyperfine fields (H) are high as expected and are associated with superexchange interaction between atomic moments. Larger values of hyperfine magnetic fields are assigned to the B-sites [167, 174]. We observed that the increase in x values from 0.1 up to 1/3 causes a decrease in H values. Figure 5.8 shows the variation of the H_A and H_B with x. We suspect that the decreases in H is associated with the decline in Co content. The line widths Γ also appear to change with respect to the increase in x. This reflects the effect of the substitutions on the magnetic ordering of the samples. The maximum line width broadening is found for the sample at $x = 1/3$. All isomer shift values are associated with Fe^{3+} ions [175] and show no significant change with composition. This shows that the s-electrons are not significantly affected by substitution Mg, Sr, Mn and Co atoms.

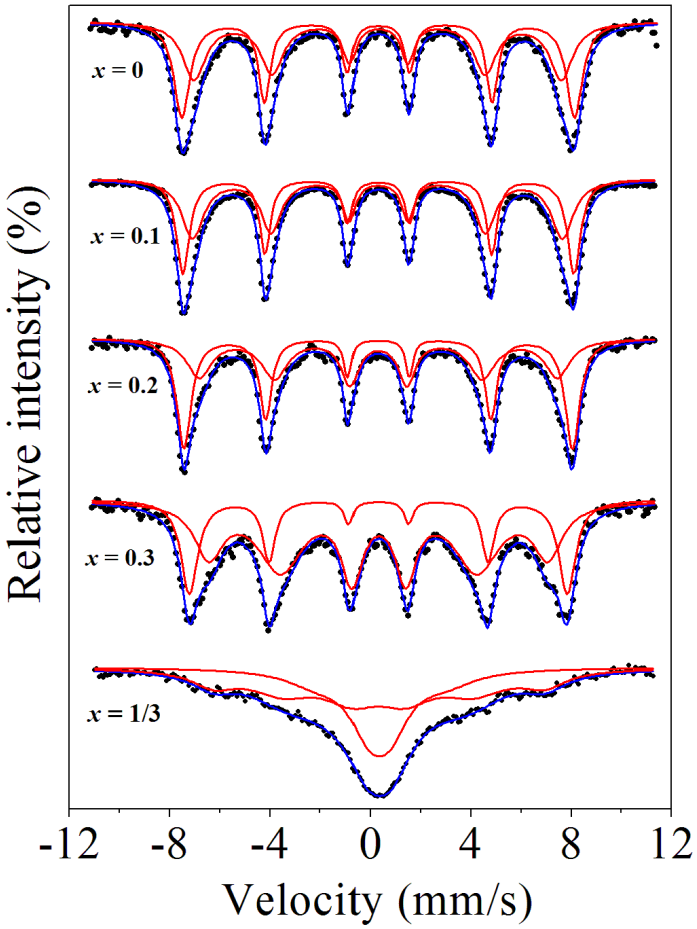

Figure 5.7: Mössbauer spectra for the as-prepared $Mg_xSr_xMn_xCo_{1-3x}Fe_2O_4$ samples measured at room temperature.

Table 5.2: Isomer shifts (δ), hyperfine magnetic fields (H), line widths (Γ) and Fe^{3+} fraction population (f) on A-site and B-site for the as-obtained $Mg_xSr_xMn_xCo_{1-3x}Fe_2O_4$ samples.

x	δ(mm/s)		H(kOe)		Γ(mm/s)		f(%)	
	δ_A	δ_B	H_A	H_B	Γ_A	Γ_B	f_A	f_B
	±0.03	±0.04	±9	±4	±0.09	±0.08	±3	±7
0.0	0.31	0.31	453	485	0.32	0.24	50	50
0.1	0.30	0.31	457	483	0.30	0.23	53	47
0.2	0.31	0.31	442	480	0.42	0.17	49	51
0.3	0.32	0.32	419	467	0.55	0.21	70	30
1/3	0.38	0.34	161	409	0.94	1.35	47	53

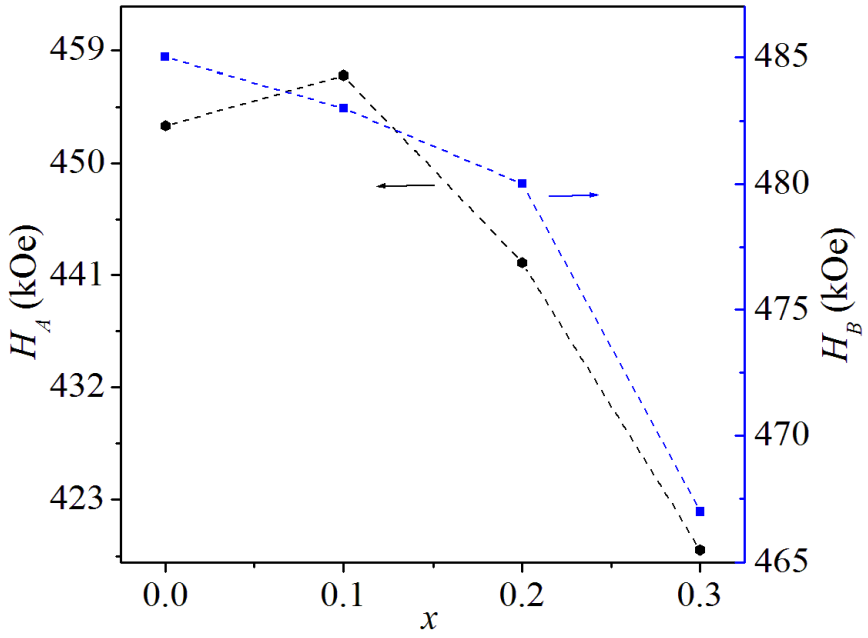

Figure 5.8: Variation of hyperfine interactions field H_A and H_B as a function of x for the as-prepared $Mg_xSr_xMn_xCo_{1-3x}Fe_2O_4$ samples measured at room temperature.

5.3.2.2 Room temperature magnetic measurements

Figure 5.9 shows the hysteresis loops of the as prepared $Mg_xSr_xMn_xCo_{1-3x}Fe_2O_4$ measured at an applied field of about 14 kOe at 300 K. Slightly substituting Co by Mg, Sr and Mn atoms significantly increases the value of the magnetization from

32.79 emu/g to 76.61 emu/g for $x = 0.1$. There after the magnetization decreases with increasing x to 32.87 emu/g when $x = 1/3$. Room temperature magnetic properties can be explained in terms of cation distribution [166] based on super-exchange interaction between A and B sites. The increases in the magnetization can be attributed to the magnetic moments of 5 μ_B Mg or Mn with addition of Mn favouring a more negative exchange interaction. The results also show that the coercive field decreases with increase in x reflecting the decline in the Co atoms which are associated with high uniaxial anisotropy [176]. Table 5.3 shows magnetic parameters deduced from the magnetization measurements at room temperature. The values of M_R/M_s indicate the hysteresis loop squareness [173].

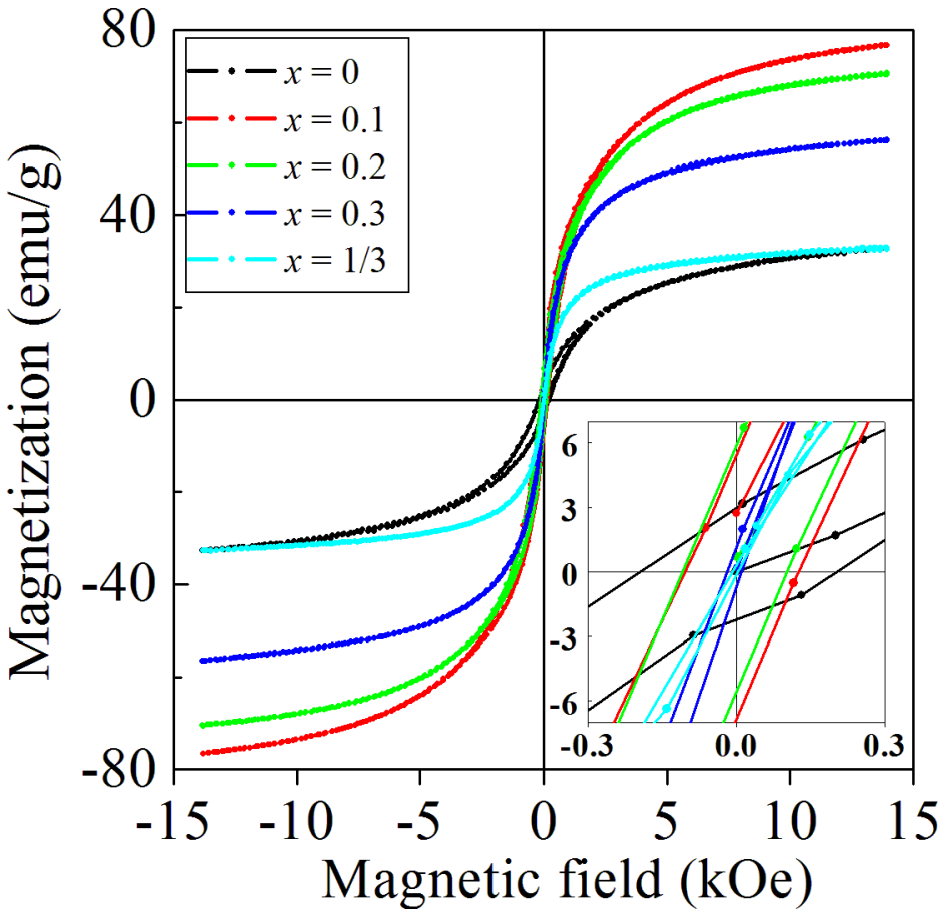

Figure 5.9: Room temperature hysteresis loops of $Mg_xSr_xMn_xCo_{1-3x}Fe_2O_4$ as-prepared. The inset shows magnified view of M-H curves.

Table 5.3: Magnetic parameters of the as-prepared $Mg_xSr_xMn_xCo_{1-3x}Fe_2O_4$ measured at 300 K in maximum applied field of 14 kOe.

x	H_C(Oe)	M_s(emu/g)	M_r(emu/g)	M_R/M_s	n_B (μ_B)
	±0.5	±0.1	±0.01	±0.001	±0.01
0.0	198.2	33.0	2.59	0.078	2.37
0.1	115.0	77.0	6.14	0.077	3.18
0.2	106.0	71.0	5.73	0.081	2.94
0.3	15.3	57.0	0.97	0.017	2.34
1/3	6.0	33.0	0.24	0.007	1.36

5.3.2.3 Magnetic measurements using the mini CFMS

Figure 5.9 reveals the magnetization of the as-prepared $Mg_xSr_xMn_xCo_{1-3x}Fe_2O_4$ samples did not saturate under external magnetic fields of up to 14 kOe. Hence, the samples were further investigated using the cryogen free measurement system CFMS at maximum applied field of 50 kOe. The effect of the measuring temperature on the magnetic properties of the synthesized samples have also been studied in the temperature range from 2 K up to 300 K. Figures 5.10 and 5.11 clearly show the hysteresis loops of the as-prepared samples. Full saturation of the magnetization especially at 2 K is not achieved even up to 50 kOe. This is attributed to significant canting of spins. However, we can deduce reliable values of the saturation magnetizations of the samples by fitting the equation 2.7.1 to the initial magnetization data. The magnetic parameters of the as-prepared $Mg_xSr_xMn_xCo_{1-3x}Fe_2O_4$ samples measured in external magnetic fields of 50 kOe at 300 K are shown in Table 5.4. Significant changes with composition are observed for the coercive field (H_C) and saturation magnetization (M_S). The remanent magnetization (M_r), squareness ratio (M_R/M_S) and magnetic moment (n_B) do not significantly change with composition, x. The magnetic moments were calculated from maximum magnetizations M_S (in emu/g) using the formula $n_B = M_0 \times M_S/5585$ [177], where M_0 is the molecular weight of the sample. We found good correlation between the saturation magnetizations and particle sizes as indicated by the plot in Figure 5.12.

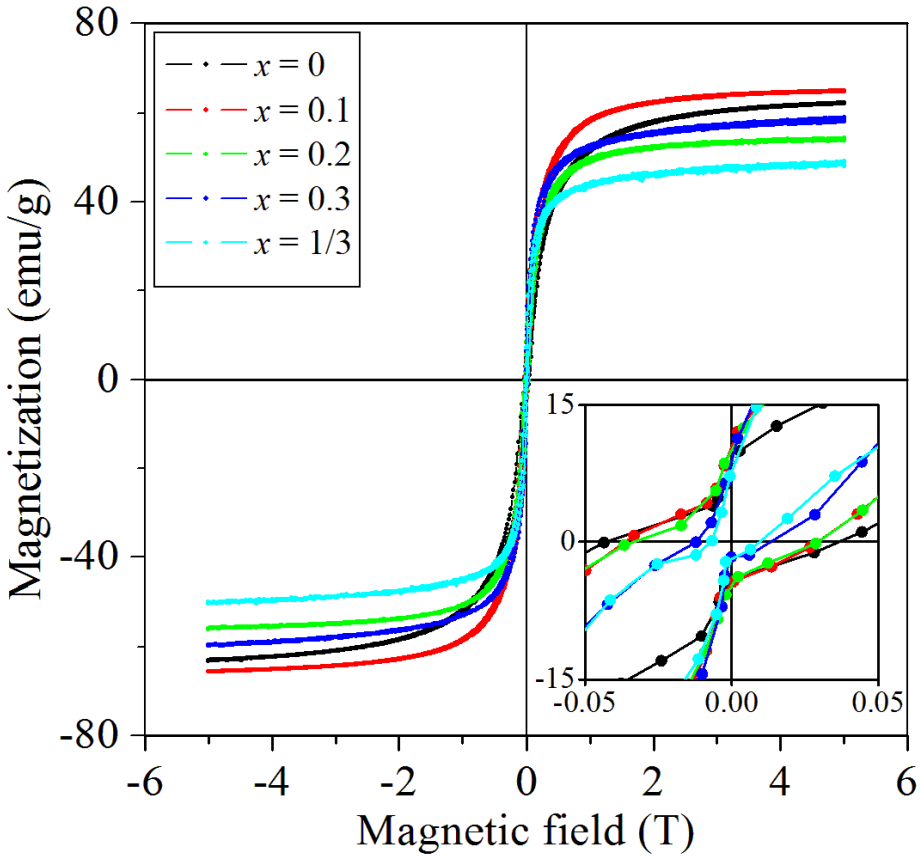

Figure 5.10: Hysteresis loops of the as-prepared $Mg_xSr_xMn_xCo_{1-3x}Fe_2O_4$ measured at room temperature in external applied fields of up to 5 T. The inset shows the magnification around the origin.

The hysteresis loops obtained at 2 K (Figure 5.11) show the sample at $x = 0.1$ has a higher coercive field. Lower coercivity values are obtained for other samples. Some distortion of the hysteresis loops are also observed for the sample with $x = 0$, 0.1 and 0.2. We suspect this to be caused by the decoupling between the hard and soft magnetic phases. Upadhyay *et al.* [178] have explained similar behaviour in term of freezing of disordered spins. No distortion of the loops are observed for the samples with $x = 0.3$ and 1/3. Based on hysteresis loops recorded at 300 K (in Figure 5.10) and those recorded at 2 K (in Figure 5.11), we observed significant increases in coercive fields with decrease in temperature. The highest increase in the coercive field at 2 K is obtained for the sample at $x = 0.1$. The least increase is for $x = 1/3$.

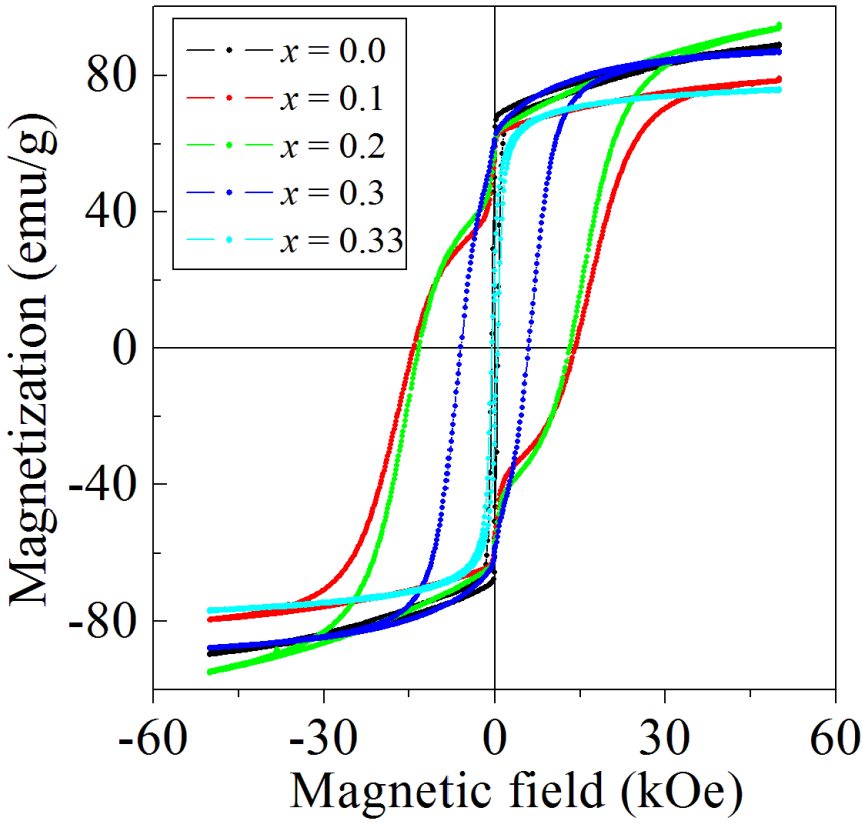

Figure 5.11: Typical hysteresis loop measured at 2 K of $Mg_xSr_xMn_xCo_{1-3x}Fe_2O_4$ as-prepared samples.

Table 5.4: Magnetic parameters of the as-prepared $Mg_xSr_xMn_xCo_{1-3x}Fe_2O_4$ samples measured at 300 K in maximum applied field of 50 kOe.

x	H_C(Oe)	M_S(emu/g)	M_r(emu/g)	M_R/M_S	$n_B(\mu_B)$
	±0.5	±0.5	±1	±0.001	±0.01
0.0	398.0	67.3	8	0.119	2.80
0.1	351.0	68.1	10	0.147	2.90
0.2	318.2	75.0	10	0.133	3.10
0.3	142.0	61.3	9	0.147	2.30
1/3	84.0	56.2	9	0.160	2.30

Figure 5.13 shows the variation of the maximum energy product $(BH)_{max}$ and the saturation magnetization M_S as a function of Co contents at 2 K. The $(BH)_{max}$ increases to the maximum value of 1679 kJ.m^{-3} at the sample with $x = 0.1$ and then

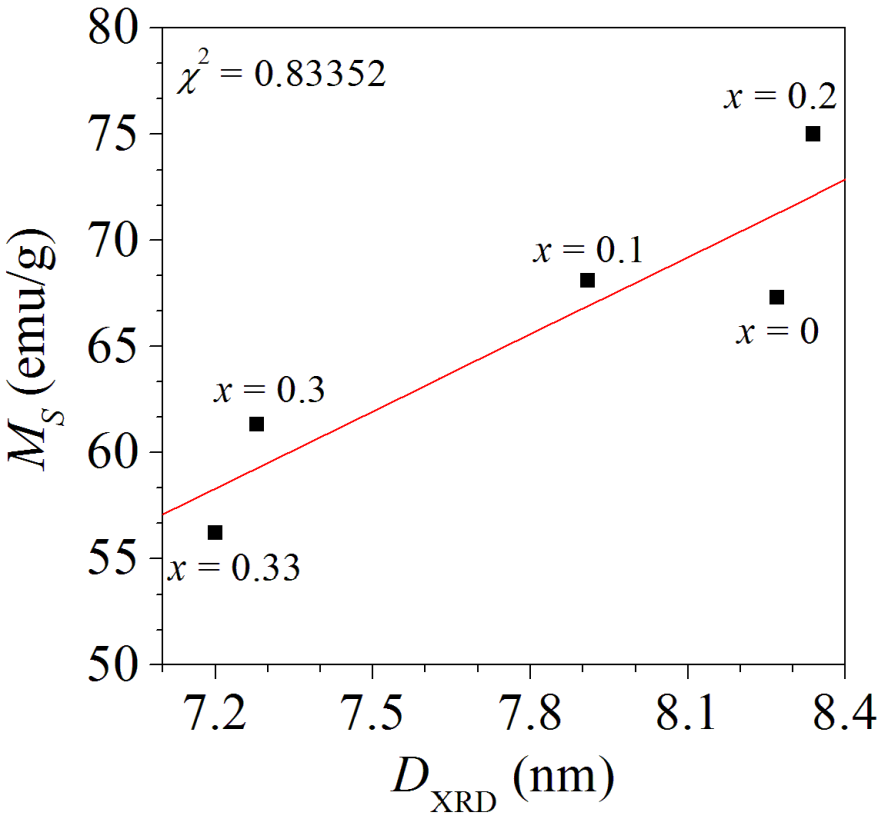

Figure 5.12: Changes of the saturation magnetization at room temperature with the XRD particles sizes of the as-prepared $Mg_xSr_xMn_xCo_{1-3x}Fe_2O_4$.

decreases dramatically to reach 3 kJ.m^{-3} for the sample $x = 1/3$ due to reduced anisotropy. The saturation magnetization increases to reach the maximum value of 75.03 emu/g at $x = 0.2$ and then deceases up to 56.17 emu/g for $x = 1/3$.

Figure 5.14 shows the temperature dependent saturation magnetization fitted to the modified Bloch's law in equation 2.5.2. The Bloch exponent $\beta = 3/2$ is valid for bulk ferromagnetic and ferrimagnetic materials at low temperatures. For nanoparticles, β is larger than 1.5 due to the finite size effect [179]. Table 5.5 shows the fit parameters to the data in Figure 5.14 with correlation coefficients of at least 0.998. We find values of β greater than 1.5 which are an indication of the confinement effects of the spin-wave spectra of magnetic nanoparticles. Simultaneous substitution of Co by Mg, Sr and Mn is accompanied by an initial enhancement of the magnetization $M_S(0)$ and the parameter T_0. The increase in the magnetization at low temperature can be attributed to the shell spin moment contributions at

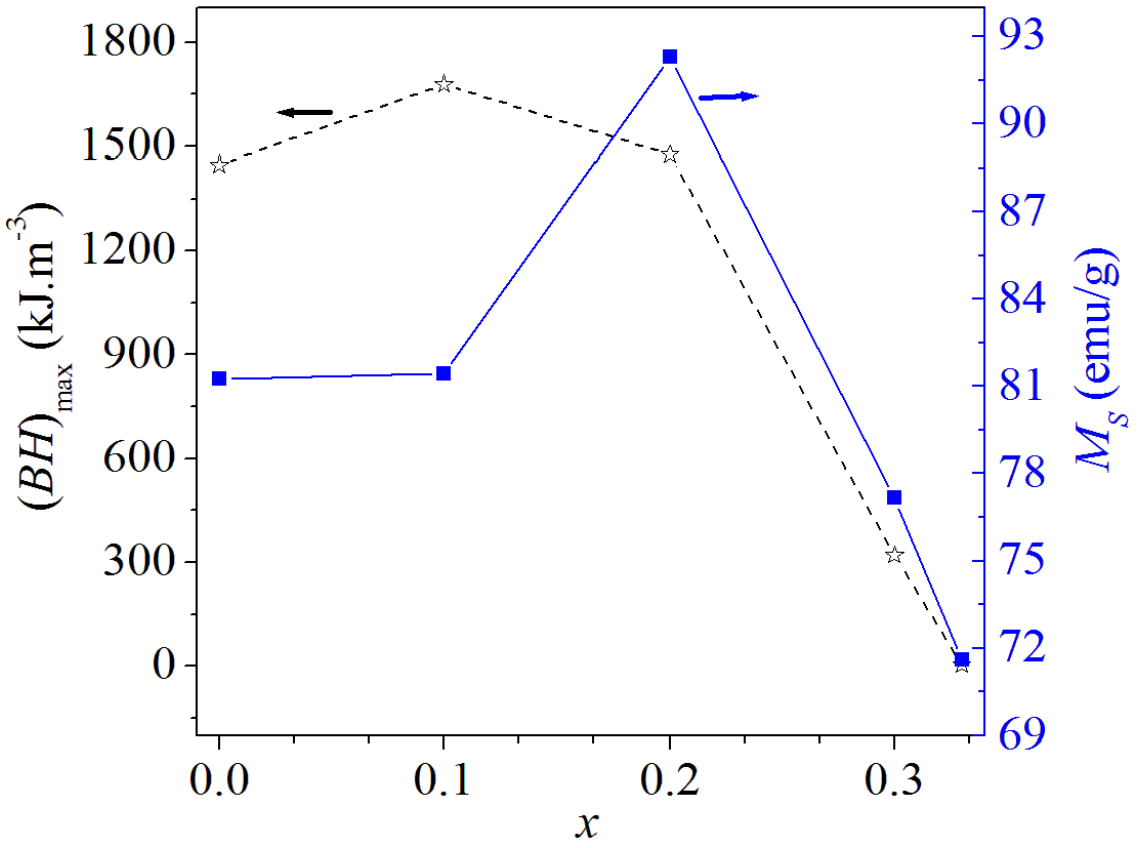

Figure 5.13: Variation of the maximum energy product $(BH)_{max}$ and the saturation magnetization with the cobalt content measured at 2 K.

low temperature [180]. The temperature-dependent measurements of the hysteresis loops reveal significant increases in coercive fields at lower temperatures as shown in Figure 5.15. This is associated with the freezing of the blocked moments across the anisotropy barriers [181]. The variation of the coercive field with temperature was found to follow Kneller's formula (see equation 2.7.2). In Figure 5.15 we show the best fit curves to the low temperature coercive field data based on Kneller's formula. The insets in Figure 5.15 show that the coercivity decreases almost linearly with T^{α} at lower temperatures. The fit parameters to the data are given in Table 5.6. For non-interacting single domain particles with uniaxial symmetry the exponent α is known to take a value of 0.5 and in the present case this is associated with the sample without Co content ($x = 1/3$). The coercive fields for samples at $x = 0$, 0.1, 0.2, 0.3 were found to follow T^{α} law with $\alpha = 0.77$ which indicates the case of an

assembly of randomly oriented particles [129]. Figure 5.16 shows the fit parameters plotted as a function of composition. Both $H_C(0)$ and T_B decrease significantly with increase in x for $Mg_xSr_xMn_xCo_{1-3x}Fe_2O_4$ nanoferrites.The inset also shows the existence of a strong correlation between $H_C(0)$ and T_B (with $\chi^2 = 0.99$).

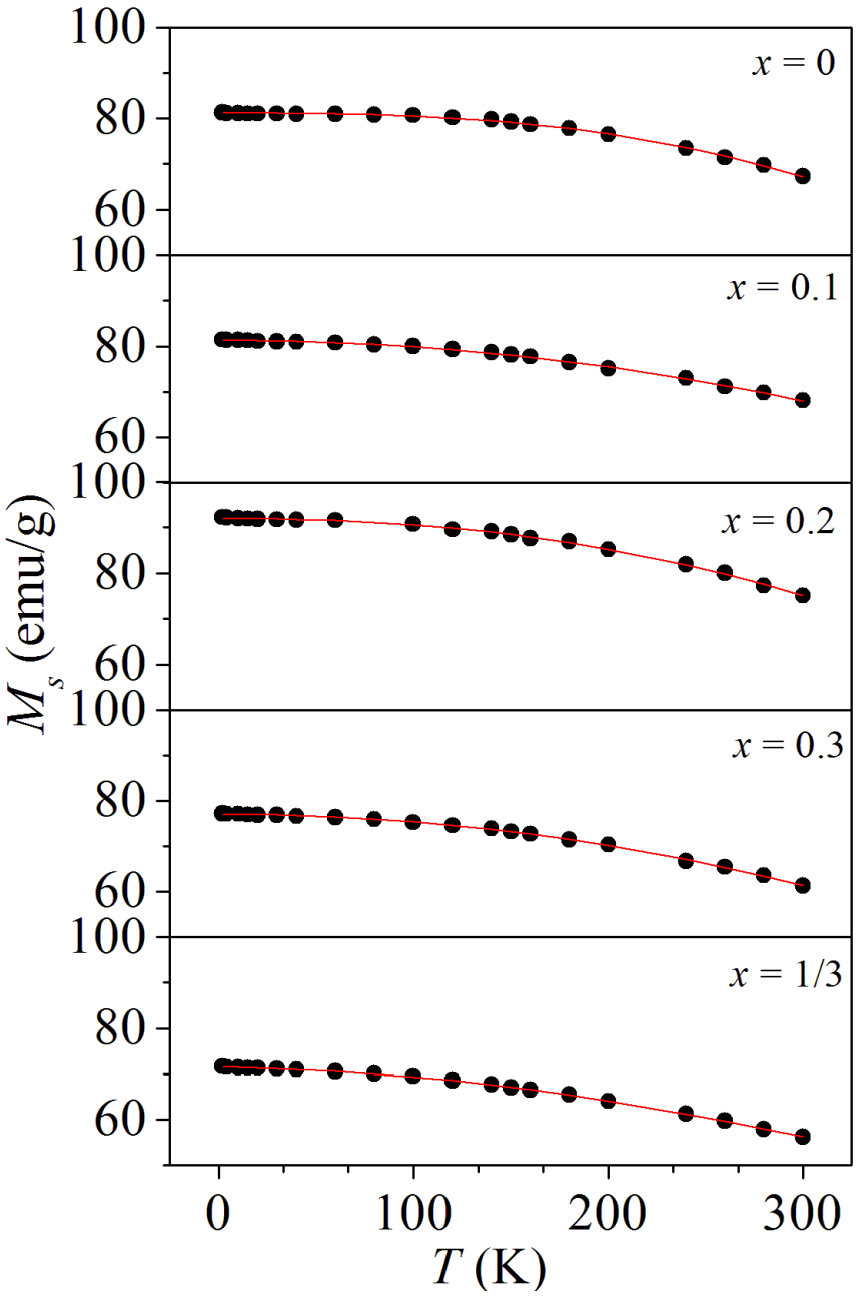

Figure 5.14: Temperature-dependence of saturation magnetization. The solid lines are the fitting curve according to the modified Bloch's law.

Table 5.5: The saturation magnetization $M_S(0)$ at 0 K, temperature at which the saturation magnetization is zero (T_0), Bloch exponent β and the fit curves accuracy (χ^2) for $Mg_xSr_xMn_xCo_{1-3x}Fe_2O_4$ samples.

x	$M_S(0)$(emu/g)	T_0(K)	β	χ^2
	± 0.1	± 9	± 0.04	
0.0	81.2	564	2.80	0.99879
0.1	81.3	730	2.03	0.99895
0.2	94.0	631	2.27	0.99880
0.3	77.0	566	2.04	0.99931
1/3	71.4	704	1.81	0.99972

The sample with $x = 0.2$ shows a much higher saturation magnetization and coercivity compared to $Mg_{0.2}Mn_{0.1}Co_7Fe_2O_4$ and $Sr_{0.2}Mn_{0.1}Co_7Fe_2O_4$ which have been reported in reference [170]. Table 5.7 shows the comparison values of M_S (emu/g) and H_C (kOe) at 300 K (RT) and 4 K (LT) between the present work and that reported in reference [170].

Table 5.6: The coercivity at $T = 0$ $H_C(0)$, blocking temperature (T_B), Kneller's constant (α) and the fit curves accuracy (χ^2) for $Mg_xSr_xMn_xCo_{1-3x}Fe_2O_4$ samples.

x	$H_C(0)$(kOe)	T_B(K)	α	χ^2
	± 0.1	± 4	± 0.06	
0.0	13.8	217	0.77	0.99484
0.1	14.9	215	0.77	0.99340
0.2	14.2	211	0.77	0.99023
0.3	6.0	135	0.77	0.99754
1/3	0.6	97	0.50	0.98363

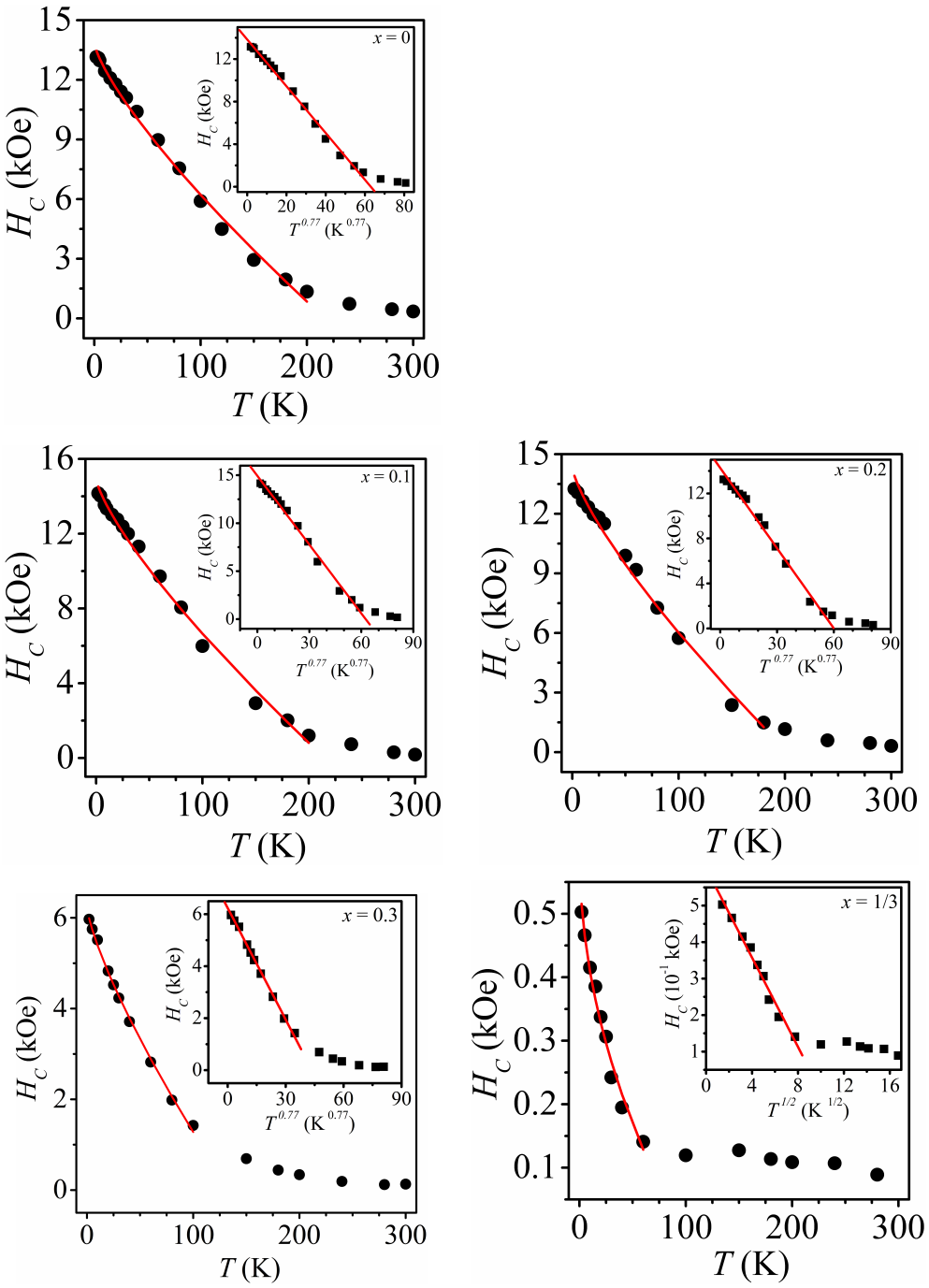

Figure 5.15: Temperature dependence of coercivity for $Mg_xSr_xMn_xCo_{1-3x}Fe_2O_4$ samples. The solid line is the fit curve according to the Kneller's law. The inset shows H_C(T) to obey a T^{α} dependence.

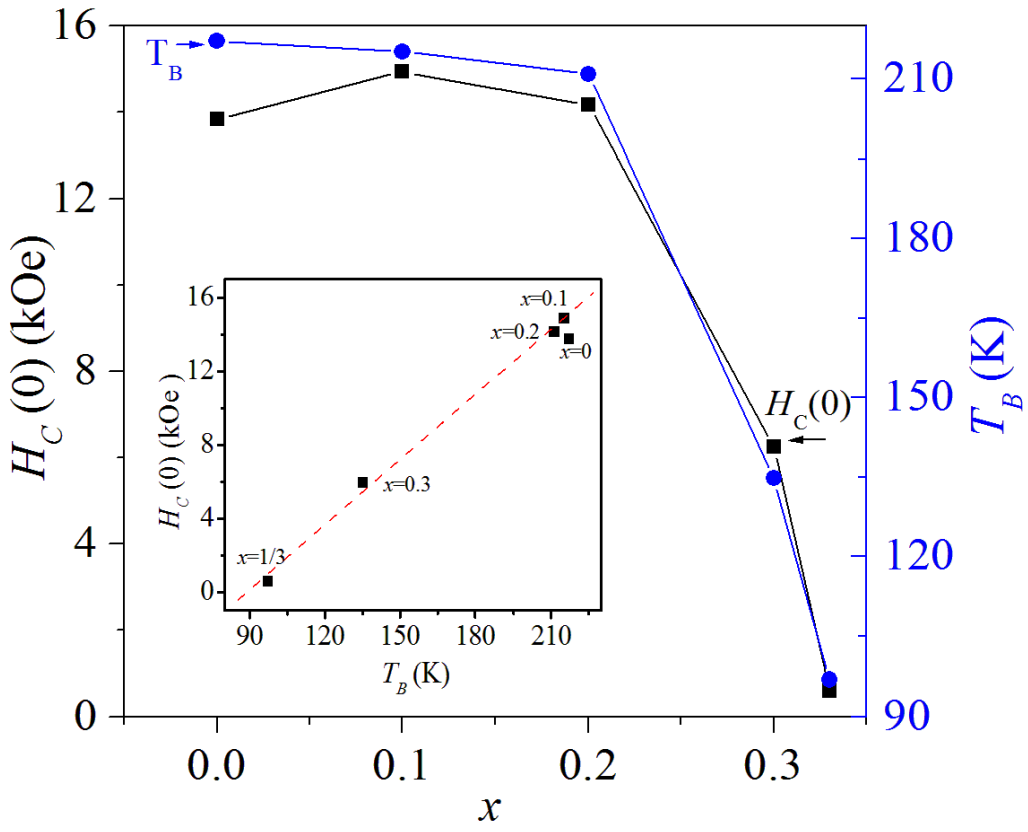

Figure 5.16: Variation of the $H_C(0)$ and T_B with the cobalt content for the as-prepared samples of $Mg_xSr_xMn_xCo_{1-3x}Fe_2O_4$. The inset shows the $H_C(0)$ versus T_B.

Table 5.7: Comparison values of M_S (emu/g) and H_C (kOe) at 300 K (RT) and 4 K (LT) for the present work and previous work.

Sample	M_S(emu/g)		H_C(kOe)		Ref
	RT	LT	RT	LT	
	±0.3	±2	±0.01	±0.01	
$Mg_{0.2}Sr_{0.2}Mn_{0.2}Co_{0.4}Fe_2O_4$	75.0	92.1	0.32	12.30	Present work
$Mg_{0.2}Mn_{0.1}Co_7Fe_2O_4$	49.9	89.2	0.18	10.70	[170]
$Sr_{0.2}Mn_{0.1}Co_7Fe_2O_4$	40.9	84.8	0.20	3.00	[170]

5.4 Conclusion

XRD patterns of $Mg_xSr_xMn_xCo_{1-3x}Fe_2O_4$ (x = 0, 0.1, 0.2, 0.3, 1/3) indicate that the simultaneous substitution of Co by Mg, Sr and Mn was achieved. Single phase nearly spherical spinel nano-crystallites with sizes from about 8 nm were synthesized. The temperature dependent measurements show interesting trends in the saturation magnetization and coercive field. The Bloch law was fitted successfully to the magnetization data over the entire temperature range while Kneller's law fits the experimental data in the range $T<T_B$. Distorted hysteresis loops and enhancement of the coercive fields are also observed at low temperatures for samples with x = 0, 0.1, 0.2. Significant correlation between coercive fields and the blocking temperatures are observed in the present series of compounds with increase in x. The reduction in cobalt content reduces both $H_C(0)$ and T_B .

Chapter 6

Temperature dependence of coercive field and magnetization of $Sr_{1/3}Mn_{1/3}Co_{1/3}Fe_2O_4$ ferrite nanoparticles

6.1 Introduction

Spinel ferrite nanoparticles can be considered to be important materials for possible applications for recording media, telecommunications, magneto-optic devices, microwave components, high frequency devices, catalysts and biomedical applications [182]. The studies of these materials tend to concentrate on the optimization of the properties by looking for the best substitutions or doping with suitable elements into either the tetrahedral (A) or octahedral (B) sites of the spinel structure. In normal spinels, divalent elements prefer A sites while trivalent elements prefer B sites. The resulting properties are known to depend strongly on elemental compositions, synthesis method and route, particle size distribution and particle morphologies [183]. The measuring temperature also plays an important role in revealing the intrinsic magnetic properties of the compounds.

A typical spinel ferrite can be specified by the formula $M\mathrm{Fe_2O_4}$ where M may represent one or more different metal ions $M1$, $M2$, $M3$,... . Several studies have been reported in the literature that involve double substitutions of two different metal ions ($M1$ and $M2$) at equal atomic proportions namely $(M1)_x\ (M2)_{1-x}\mathrm{Fe_2O_4}$ where $x = 0.5$ [184, 185, 186]. These compounds are considered to be at an interesting composition midway between $(M1)\mathrm{Fe_2O_4}$ and $(M2)\mathrm{Fe_2O_4}$ which can exhibit new and unique properties. In addition, properties for $x < 0.5$ and $x > 0.5$ can differ significantly [184]. Hence the focused attention on the compositions at $x = 0.5$. The common feature of these mixed compounds $(M2)_{0.5}(M2)_{0.5}\mathrm{Fe_2O_4}$ is symmetry with regards to equality in the number of atoms ($M1$ and $M2$) that can compete for occupation of the tetrahedral and octahedral sites in the spinel structure. We have therefore extended these studies to simultaneous substitutions involving three different metal ions ($M1$ = Sr, $M2$ = Mn and $M3$ = Co) at the unique composition $(M1)_{1/3}(M2)_{1/3}(M3)_{1/3}\mathrm{Fe_2O_4}$ which belongs to a class of materials that have not yet been widely studied.

$\mathrm{CoFe_2O_4}$ ferrites have been widely investigated and found to exhibit interesting magnetic properties such as high coercive field and moderate magnetization [187]. Substitutions by Mn atoms cause the properties to change. Materials with larger magneto-mechanical quality and higher sensitivity to stress are obtained [188]. In reference [169], a study of simultaneous substitution by Mn and Sr was undertaken to produce successfully $\mathrm{Mn_{0.1}Sr_{0.2}Co_{0.7}Fe_2O_4}$ ferrite nanoparticles, the results showed enhanced properties. The aim was to investigate the effect of the larger Sr on the Mn-Co ferrite. In the present chapter we have produced a novel ferrite nanoparticle compound, $\mathrm{Sr_{1/3}Mn_{1/3}Co_{1/3}Fe_2O_4}$ which possesses equal stoichiometry with respect to Sr, Mn and Co substitutions in the spinel structure. The primary focus is on the magnetic properties induced by the simultaneous substitutions.

6.2 Experimental details

The $\mathrm{Sr_{1/3}Mn_{1/3}Co_{1/3}Fe_2O_4}$ ferrite nanoparticles were produced by glycol-thermal technique using a Watlow series model PARR 4843 stirred pressure reactor. The

synthesis procedures have been discussed in chapter 4. The phase and structural characterizations of the sample was obtained by a Phillips X-ray diffractometer type Model: PANalytical, EMPYREAN using CoKα radiation. The morphology and micro-structure of the nanoparticles were investigated by high-resolution transmission electron microscope (HRTEM) (type: Jeol_JEM-1010) and high-resolution scanning electron microscope (HRSEM) (Ultra Plus ZEISS-FEG HRSEM instrument). The synthesized elemental compositions were identified by energy-dispersive X-ray spectroscopy (EDX). The textural and porosity characteristics of the nanoparticles were investigated using a micrometrics tristar II 3020 instrument using liquid N_2 as the analysis gas at liquid N_2 temperature. A mini cryogen free measurement system was used to perform low temperature magnetization measurements from 4 to 300 K in magnetic fields of up to 50 kOe.

6.3 Results and discussion

The XRD peaks are shown in Figure 6.1. The peaks are indexed and identified as a corresponding to single phase spinel structure. No impurities peaks are observed in the XRD peaks. The highest peak intensity in Figure 6.1 is the (311) peak which was used to calculate the lattice parameter a using the equations 4.1.1 and 4.1.2. The average crystallite size was calculated using equation 4.1.3. The microstrain was determined using the Williamson-Hall plot [148] as shown in Figure 6.2. The scattering of the points around the linear fitting line in Figure 6.2 suggests that the sample has homogenous microstrain. The obtained values of the lattice parameter, crystallite size and microstrain for the as-prepared $Sr_{1/3}Mn_{1/3}Co_{1/3}Fe_2O_4$ are found to be 0.841±0.003 nm, 9.26±0.02 nm and 0.0014±0.0002 respectively.

The morphology of the $Sr_{1/3}Mn_{1/3}Co_{1/3}Fe_2O_4$ ferrite nanoparticles was investigated using HRSEM and HRTEM. Figure 6.3 (A) shows that the particles have spherical shape with some evidence of agglomeration. Typical transmission electron microscopy images for the as-prepared $Sr_{1/3}Mn_{1/3}Co_{1/3}Fe_2O_4$ are shown in Figure 6.3 (B). The particle size was also estimated from the HRTEM image to be about 8±2 nm. The HRTEM image shows well resolved crystalline structure for the sam-

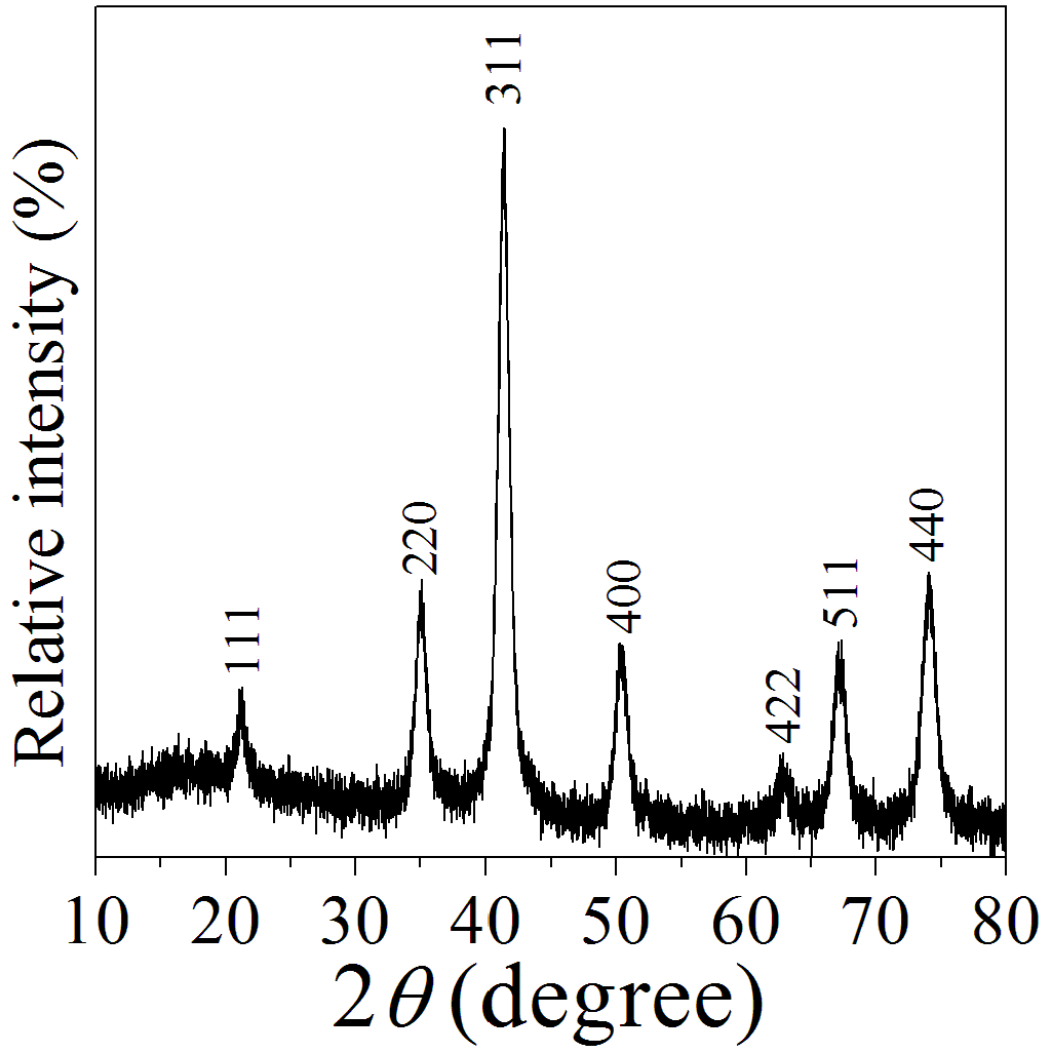

Figure 6.1: X-ray diffraction patterns for as-prepared of $Sr_{1/3}Mn_{1/3}Co_{1/3}Fe_2O_4$ ferrite nanoparticles.

ple under investigation since the lattice fringes appear clearly in Figure 6.3 (B). The HRTEM results are in agreement with the XRD results in terms of particle size and structure. The results of the elemental compositions obtained by a typical EDX scan are shown in Figure 6.4. This qualitatively confirms the presence of the expected elements in the sample.

The texture and porosity characteristic of the as-prepared nanoparticle $Sr_{1/3}Mn_{1/3}Co_{1/3}Fe_2O_4$ ferrite was determined by N_2 adsorption-desorption isotherm study. The results obtained in Figure 6.5 indicate that the material can be classified as a mesoporous sample, as shown by the type IV hysteresis loop [189]. Figure

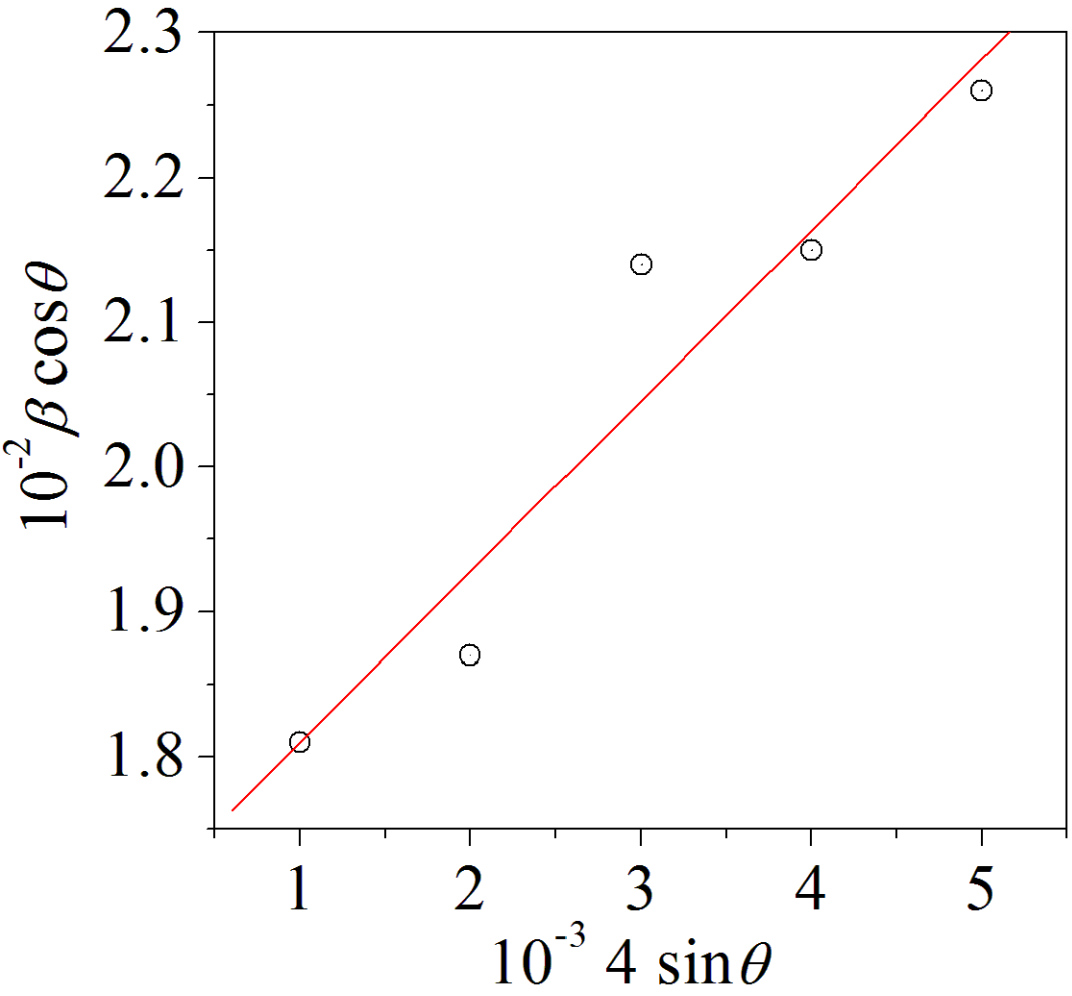

Figure 6.2: Williamson-Hall plot of $\beta\cos\theta$ Vs $4\sin\theta$ for $Sr_{1/3}Mn_{1/3}Co_{1/3}Fe_2O_4$ ferrite nanoparticles.

6.5 also shows that the adsorption of nitrogen gas by the sample increased from 30 cm^3/g to 180.4 cm^3/g when the relative pressure P/P_0 changes from 0.03 to 1.0. The pore size range is wide, since the gap between the adsorption and desorption is rather wide. Furthermore, the pores of the sample tend to be empty as shown by the low P/P_0 onset point. The surface area of the material was determined by Brunauer-Emmett-Teller (BET) surface area measurements to be 109.3 m^2/g. This is expected, since related materials (in terms of structure) are reported to have similar surface area [190]. The Barrett-Joyner-Halenda (BJH) pore size distribution measurements show that most of the pore diameters are located below 50 nm (see inset in Figure 6.5). This is additional evidence of mesoporous structure for our sample [191].

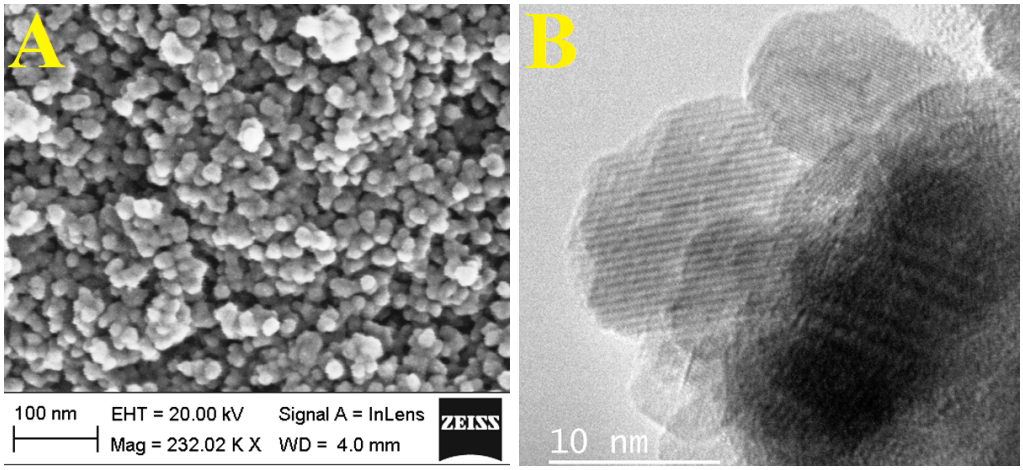

Figure 6.3: HRSEM (A) and HRTEM (B) images for $Sr_{1/3}Mn_{1/3}Co_{1/3}Fe_2O_4$ ferrite nanoparticles.

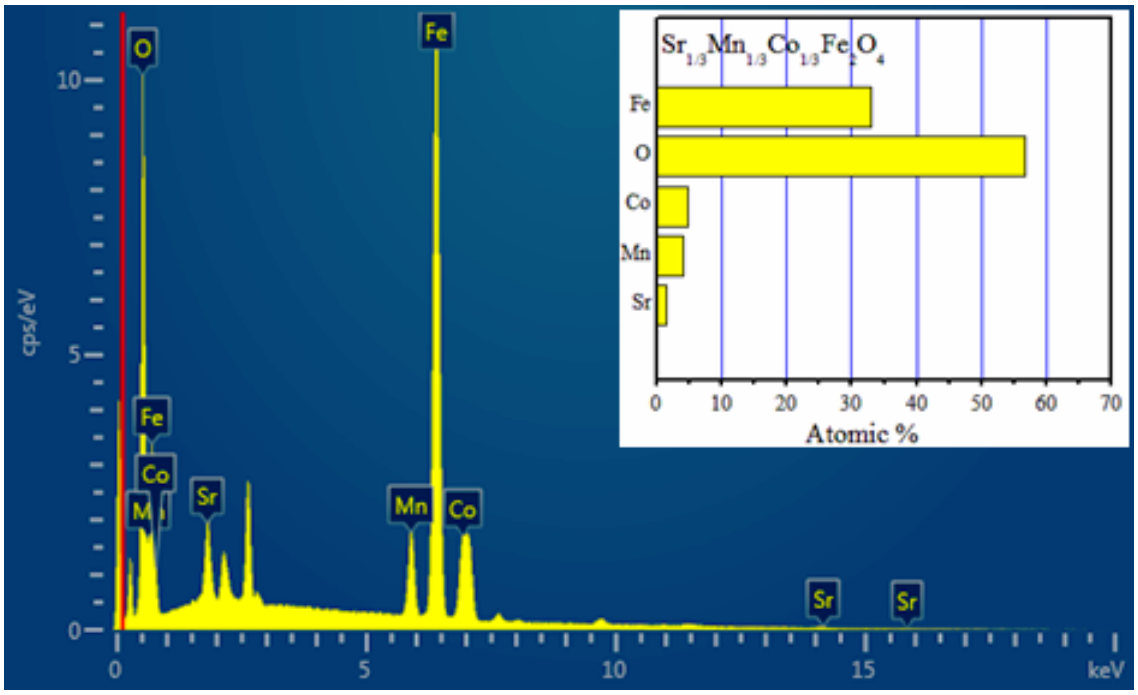

Figure 6.4: EDX measurement of the as-prepared $Sr_{1/3}Mn_{1/3}Co_{1/3}Fe_2O_4$ sample.

6.3.1 Magnetic measurements

Figure 6.6 displays M-H curves as a function of measuring temperature in the range of 4 to 300 K. Saturation magnetizations M_S were calculated from the empirical expression 2.7.1 given in reference [104]. M_S increases as the temperature decreases.

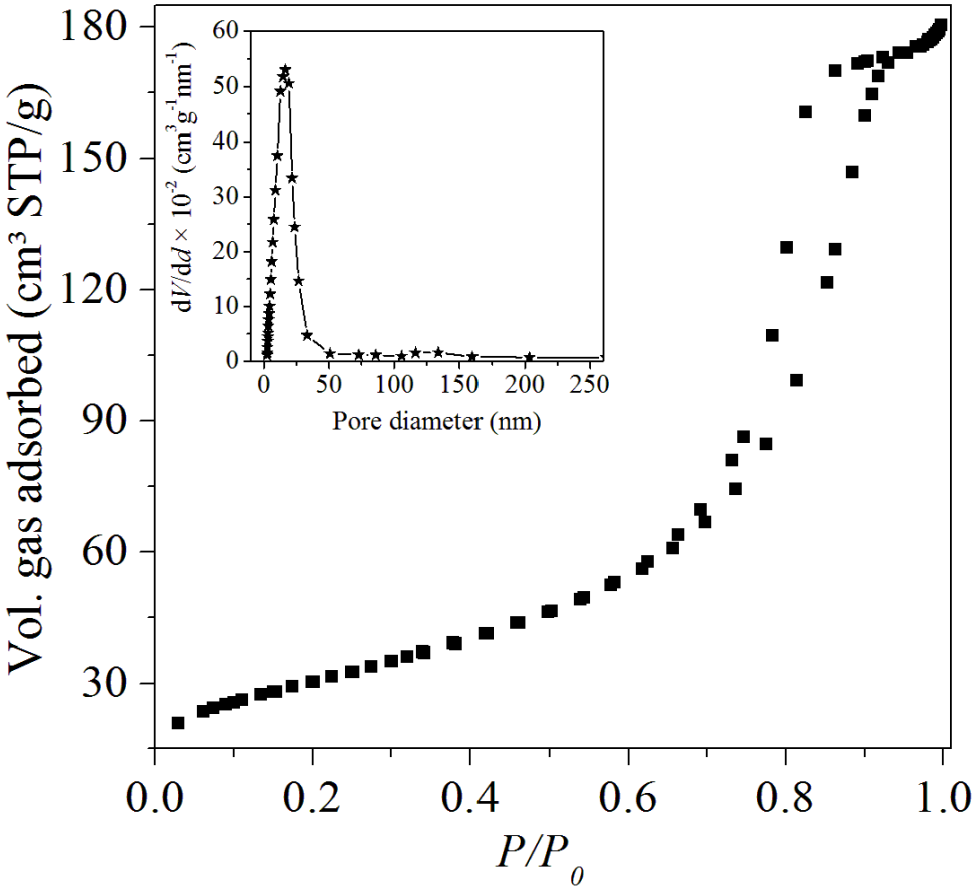

Figure 6.5: N_2 gas adsorption isotherms for as-prepared $Sr_{1/3}Mn_{1/3}Co_{1/3}Fe_2O_4$ sample ferrite nanoparticle. The inset shows the pores size distribution.

Figure 6.6 also reveals distortion in the loops (near zero field) which appear to become more prominent in the temperature range below 100 K. This distortion in the loops is related to the spin freezing phenomena [169] due to significant time dependence of the remnant magnetization. Systematic increases in the coercivity have been observed as the temperature decreases indicating that the material becomes magnetically harder at lower temperature. The values of the coercive fields change from 0.20±0.01 kOe at 300 K to 11.24±0.02 kOe at 4 K. The coercive field is a sensitive property to the temperature of a sample. More magnetic moments are frozen into anisotropic directions at lower temperature. As the temperature increases, the value of the coercive field decreases [192]. The temperature dependency of the coercivity can be explained based on the effects of thermal fluctuations of the

blocked moments across anisotropy barriers [193]. Figure 6.7 shows the variation of coercivity with measuring temperature. The spin freezing effect is dominant at low temperature particularly below the blocking temperature T_B. This can arise due to exchange coupling between the core and surface spins. The temperature dependence of the coercive field in this case can be expressed in terms of Kneller's law expressed by equation 2.7.2 [192]. In the present case Kneller's law appears to fit the experimental data in Figure 6.6 well below about 200 K. The fit parameters $H_C(0)$ and T_B to Kneller's law in Figure 6.7 are 14.0±0.3 kOe and 223±9 K respectively. The inset in Figure 6.7 depicts a linear variation of $H_C(0)$ with $T^{1/2}$ as expected with a high correlation coefficient of 0.99398.

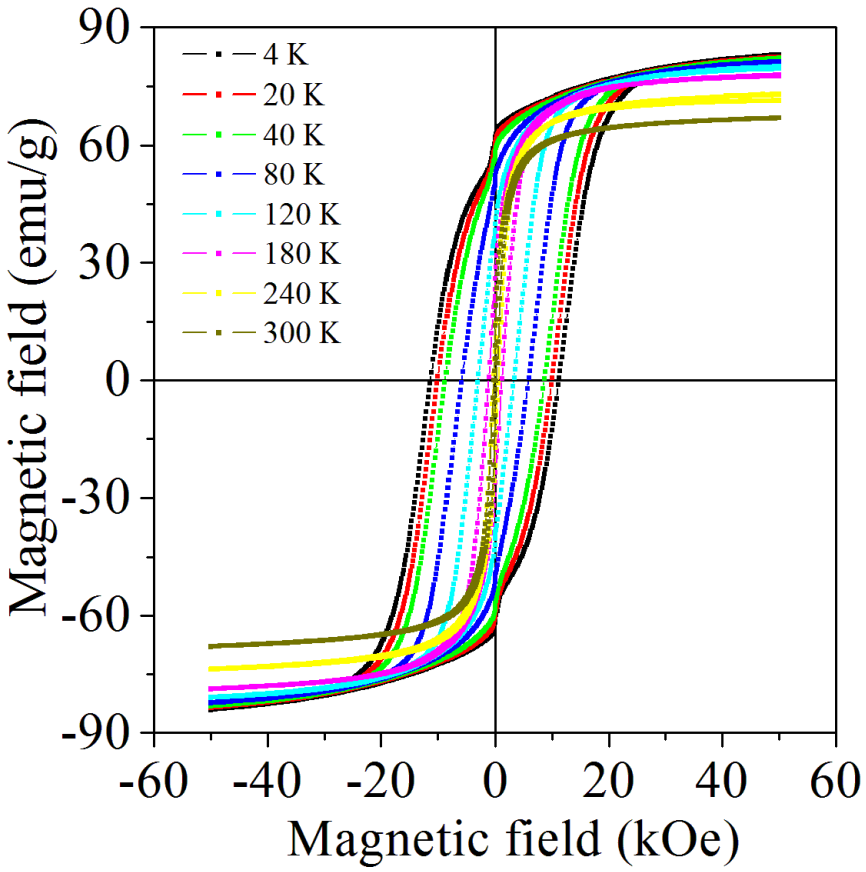

Figure 6.6: Hysteresis loops of $Sr_{1/3}Mn_{1/3}Co_{1/3}Fe_2O_4$ ferrite nanoparticles as a function of measuring at various temperatures in the range 4 to 300 K in the external magnetic field up to ±50 kOe.

The variation of the remanent magnetization (M_r) and the reduced remanent

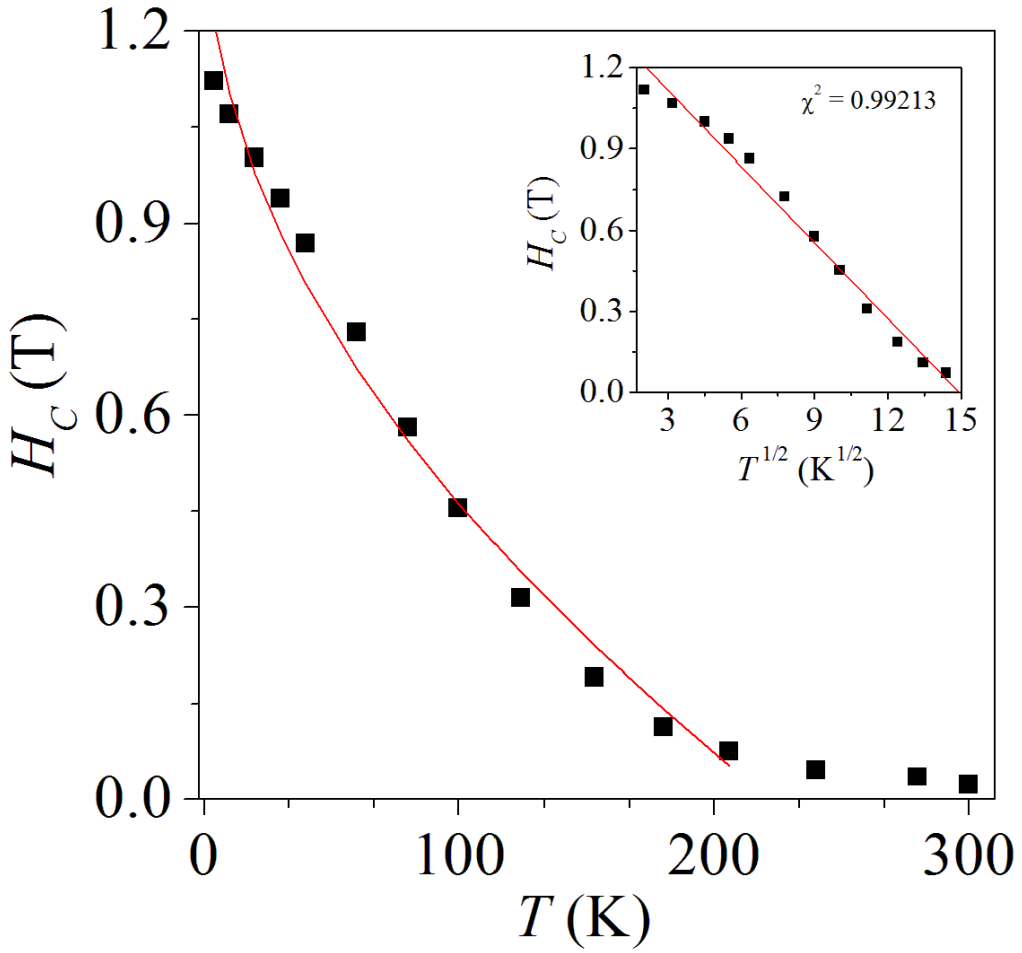

Figure 6.7: Coercivity temperature dependence for as-prepared $Sr_{1/3}Mn_{1/3}Co_{1/3}Fe_2O_4$ ferrite nanoparticles. The red line shows the fit curve according to modified Kneller's law. The straight red line in the inset shows the $T^{1/2}$ dependence.

magnetization (M_r/M_S) with temperature are shown in Figure 6.8. Both M_r and M_r/M_S decrease as the temperature increases indicating that the magnetic anisotropy strength reduces at higher temperature [194]. For non-interacting single domain particles with randomly oriented easy axes M_r/M_S takes a value of 0.5 for uniaxial anisotropy and 0.832 for cubic anisotropy according to the Stoner-Wohlfarth theory [195]. The inset in Figure 6.8 shows that the values of M_r/M_S for our sample exceed 0.5 but is less than 0.832. This implies both cubic and uniaxial anisotropy.

Figure 6.9 shows the temperature dependence of the saturation magnetization

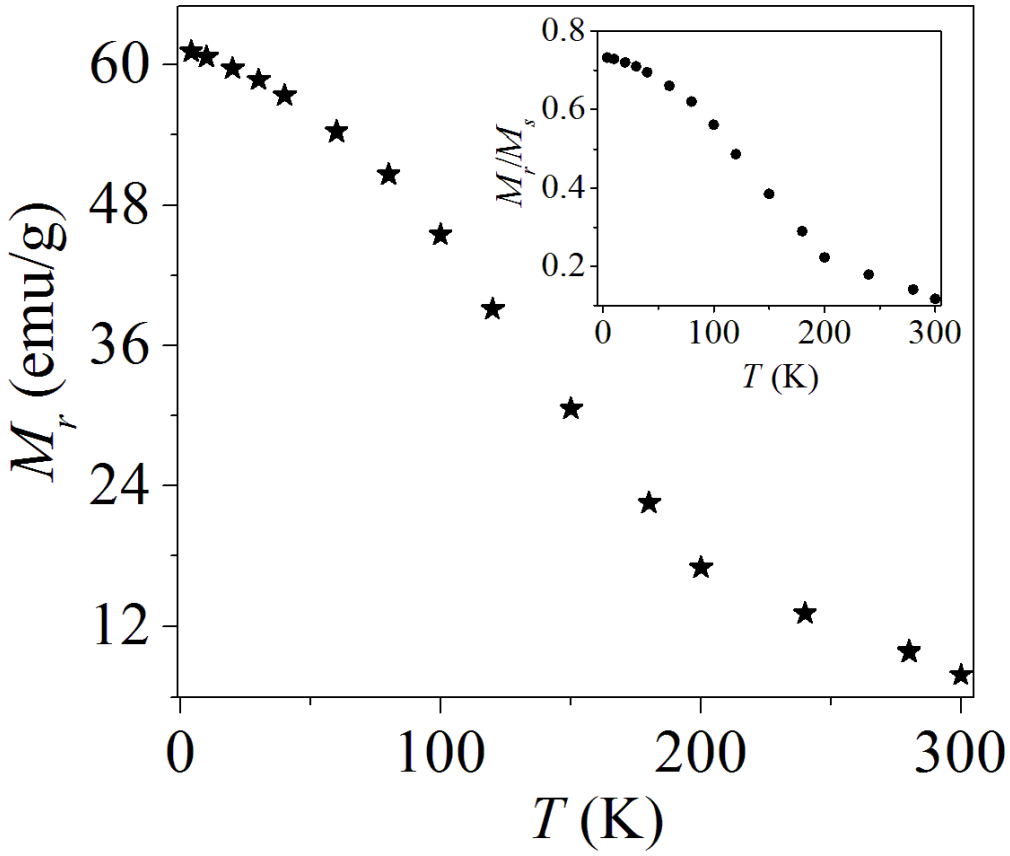

Figure 6.8: Variation of the remanence magnetization (M_r) with the measuring temperature of $Sr_{1/3}Mn_{1/3}Co_{1/3}Fe_2O_4$ ferrite nanoparticles. The inset shows the variation of the reduced remanence magnetization (M_r/M_s) with the measuring temperature.

$M_S(T)$ which we attribute to spin wave excitations. Below the Curie temperature the magnetization is usually described in terms of the Bloch's law following equation 2.5.2 [196]. It is well known for bulk materials that the exponent takes the value of 3/2. However, due to the finite size effect of the nanoparticles, the magnetization tends to deviate from pure Bloch's law [197]. In Figure 6.9 there is a slight increase in the magnetization below about 40 K. This increase is attributed frozen surface spins [198]. The best fit to the data in Figure 6.9 is the so-called modified Bloch's law expressed as follows

$$M_S(T) = M_S(0)[1 - (T/T_0)^{\beta} + Aexp(T/T_f)] \tag{6.3.1}$$

where A and T_f are experimental parameters which depend on the nanoparticle size. The parameter A represents the contribution from surface spins to the magnetization M_S [198]. The results extracted from the fit in Figure 6.9 are presented in Table 6.1.

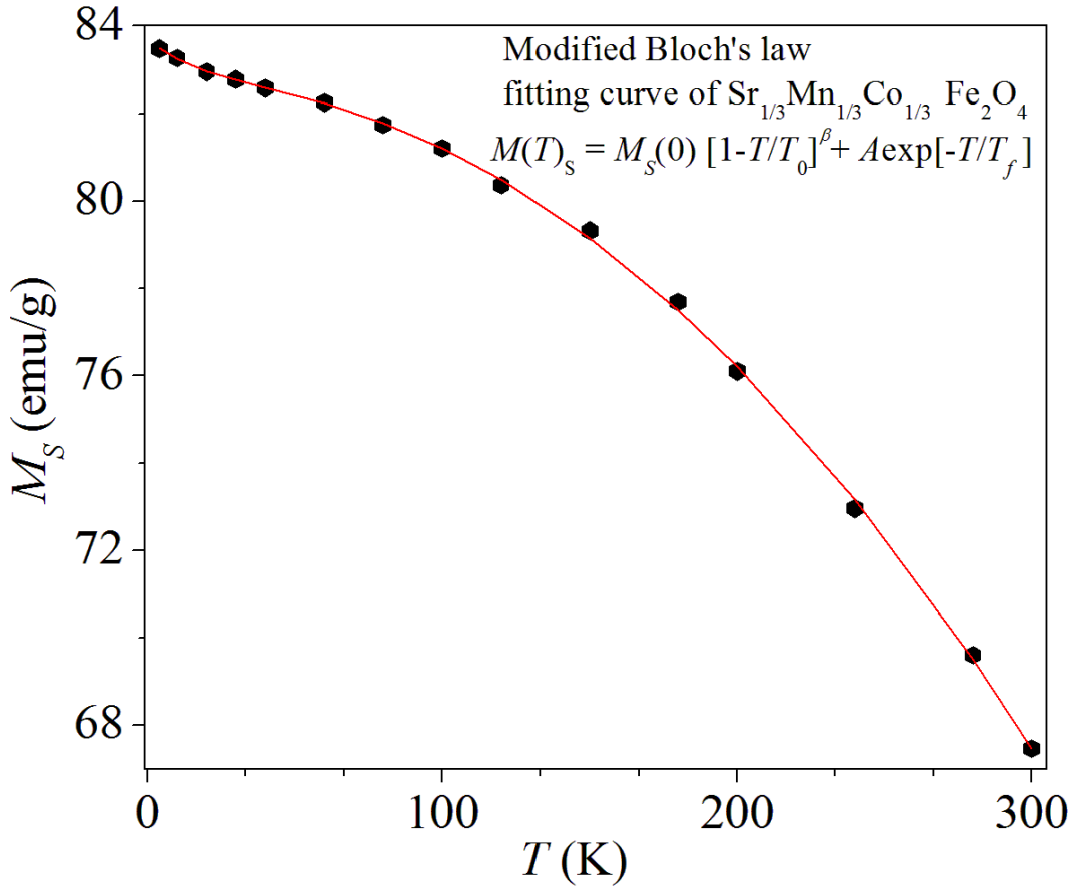

Figure 6.9: Magnetization temperature dependence for $Sr_{1/3}Mn_{1/3}Co_{1/3}Fe_2O_4$ ferrite nanoparticles. The red line shows the fit curve according to Bloch's model.

Table 6.1: The fitting parameters based on the modified Bloch's law model for the as-prepared $Sr_{1/3}Mn_{1/3}Co_{1/3}Fe_2O_4$ ferrite nanoparticles.

Parameter	$M_S(0)$ ± 0.1 (emu/g)	T_0 ± 13 (K)	β	A ± 0.06 (emu/g)	T_f ± 1 (K)	χ^2
Value	82.7	672	2	0.96	17	0.9996

6.4 Effect of annealing process on structure and magnetic properties of $Sr_{1/3}Mn_{1/3}Co_{1/3}Fe_2O_4$ ferrite nanoparticles

6.4.1 Structural investigation of $Sr_{1/3}Mn_{1/3}Co_{1/3}Fe_2O_4$ ferrite nanoparticles annealed at different temperatures

We have studied the influence of annealing temperature on the structure and magnetic properties of the $Sr_{1/3}Mn_{1/3}Co_{1/3}Fe_2O_4$ ferrite nanoparticles initially synthesized at 200 °C. Figure 6.10 shows X-ray diffraction (XRD) results of the $Sr_{1/3}Mn_{1/3}Co_{1/3}Fe_2O_4$ samples annealed at different temperatures (T_A) of 300 °C, 400 °C, 500 °C and 600 °C. It is clear that the spinel phase structure collapses at T_A = 600 °C. We suspect the additional peaks that appear at 600 °C to be due to an impurity phase such as α-Fe_2O_4 [57]. We have investigated the microstrain of the annealed samples based on the Williamson-Hall plot as shown in Figure 6.11. The values of the lattice parameter a, crystallite sizes D_{XRD} and lattice-strain ε for the as-prepared and the annealed samples of $Sr_{1/3}Mn_{1/3}Co_{1/3}Fe_2O_4$ at different temperatures are given in Table 6.2. The crystallite sizes increase from 9.3±0.1 nm to 20.6±0.1 nm with increase in annealing temperature from 200 °C to 500 °C, respectively. The microstrain ε values decrease from 0.0014±0.0002 to 0.0009±0.0002 as T_A increases from 200 °C to 500 °C respectively. We attribute decreases in ε value to the reduction of defects and internal stresses [199]. The lattice parameter decreased slightly after annealing at T_A = 300 °C and subsequently increased with increasing T_A. That the as-prepared sample appears to be more strained due to the initial synthesis condition. Hence, annealing temperature might lead initially to internal thermal relaxation that causes drop in lattice parameter followed by an increase. Figure 6.12 shows the variation of crystallite sizes D and microstrain ε with annealing temperature. The morphology of the annealed samples was studied by HRSEM (Figure 6.13) and HRTEM (Figure 6.14). The images show increases in particle sizes as annealing temperature increases. However, the annealed nanoparticles appear to have regular shape and good particles distribution.

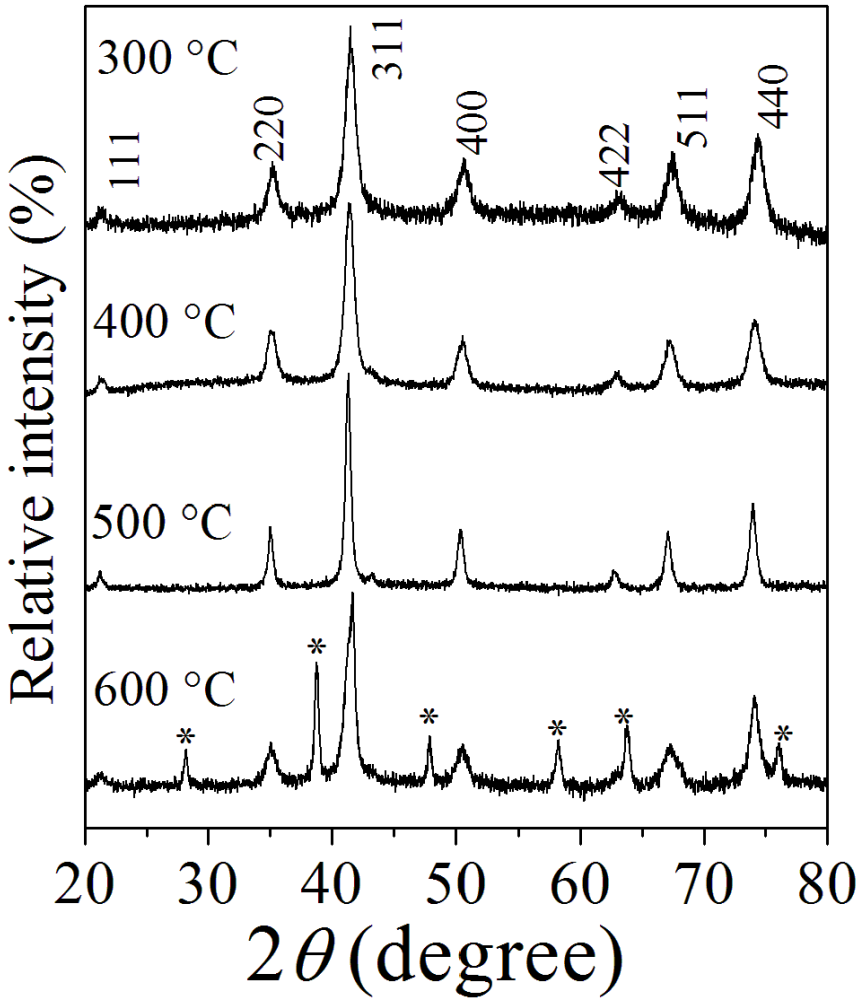

Figure 6.10: XRD patterns for $Sr_{1/3}Mn_{1/3}Co_{1/3}Fe_2O_4$ ferrite nanoparticles annealed at different temperatures.

Table 6.2: Annealing temperatures T_A, Lattice parameters a, XRD crystallite sizes and microstrains ε for the annealed $Sr_{1/3}Mn_{1/3}Co_{1/3}Fe_2O_4$ ferrite nanoparticles.

T_A	$a(\AA)$	D_{XRD}(nm)	ε
	± 0.01	± 0.1	± 0.0003
200 °C	8.41	9.3	0.0014
300 °C	8.37	10.2	0.000948
400 °C	8.39	11.4	0.000945
500 °C	8.41	20.7	0.000900

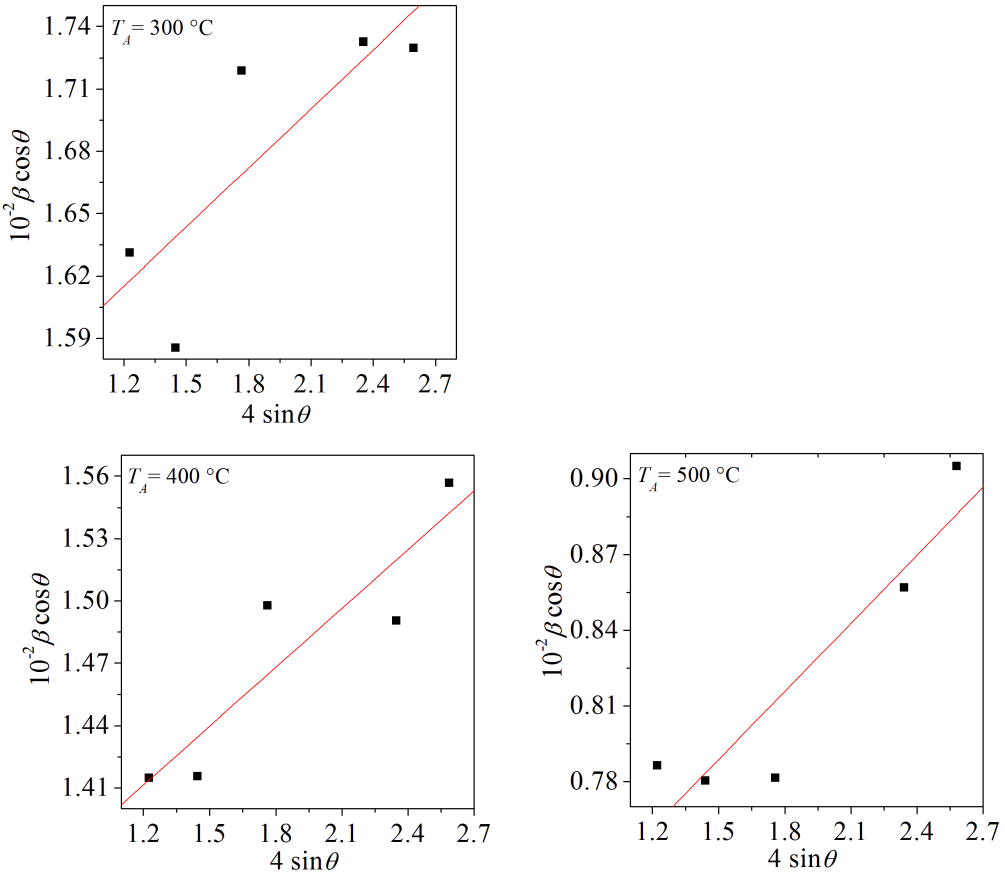

Figure 6.11: Williamson-Hall plot of $\beta\cos\theta$ versus 4sinθ for $Sr_{1/3}Mn_{1/3}Co_{1/3}Fe_2O_4$ ferrite nanoparticles.

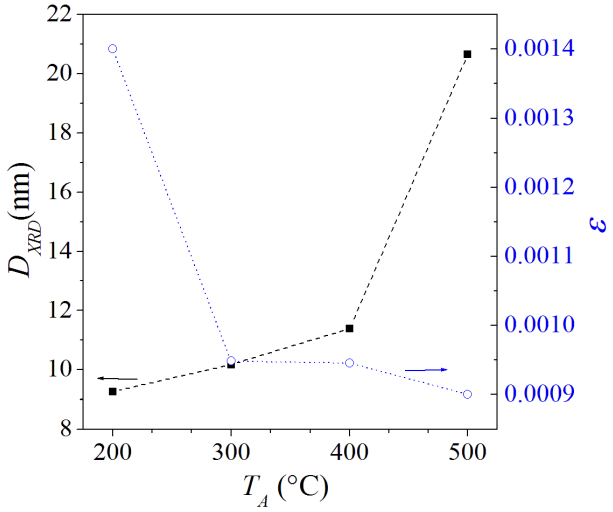

Figure 6.12: Variation of crystallite sizes and microstrain with annealing temperature for $Sr_{1/3}Mn_{1/3}Co_{1/3}Fe_2O_4$ ferrite nanoparticle.

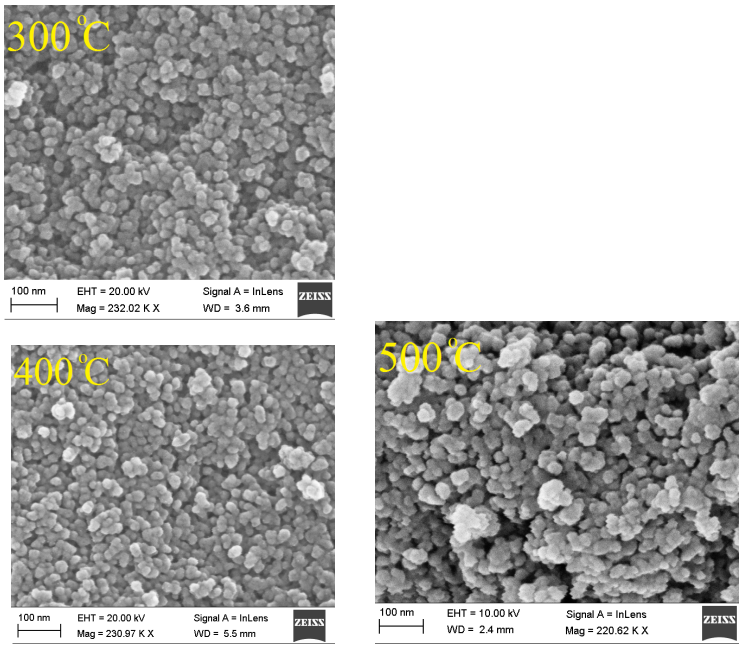

Figure 6.13: HRSEM images for $Sr_{1/3}Mn_{1/3}Co_{1/3}Fe_2O_4$ ferrite nanoparticles annealed at different temperatures.

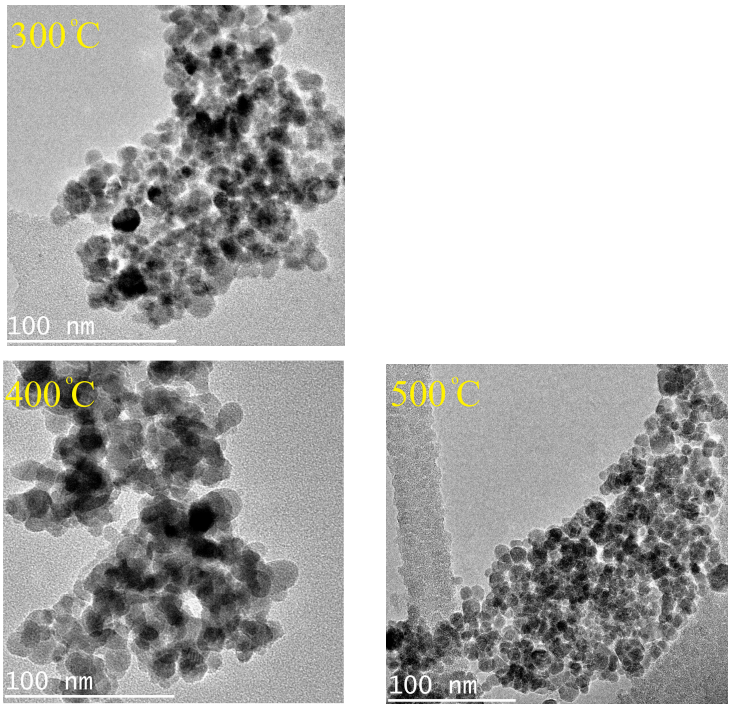

Figure 6.14: HRTEM images for $Sr_{1/3}Mn_{1/3}Co_{1/3}Fe_2O_4$ ferrite nanoparticles annealed at different temperatures.

6.4.2 Magnetic study of $Sr_{1/3}Mn_{1/3}Co_{1/3}Fe_2O_4$ nanoparticles ferrite annealed at different temperatures

Figure 6.15 shows room temperature ^{57}Fe Mössbauer spectra for the as-prepared and samples annealed $Sr_{1/3}Mn_{1/3}Co_{1/3}Fe_2O_4$ ferrite nanoparticles at different temperatures. The spectra were fitted with two Zeeman sextets this associated with Fe ions in tetrahedral A and octahedral B sites. The magnetic hyperfine parameters deduced from the fitted spectra are presented in Table 6.3. The obtained values of isomer shifts δ show only Fe^{3+} ions. This implies that annealing process does not change the oxidation state of Fe ions. The isomer shifts change only slightly with increasing in T_A. The values of magnetic hyperfine fields are high indicative of strong super-exchange interaction between magnetic moments. On A site we observed an initial reduction at T_A = 300 °C followed by increase in H_A at higher T_A. At octahedral B site, H_B increases from 475±2 to 487±1 kOe as the annealing temperature T_A increases from 200 °C to 500 °C respectively. Figure 6.16 shows the variations of magnetic hyperfine fields with annealing temperature T_A.

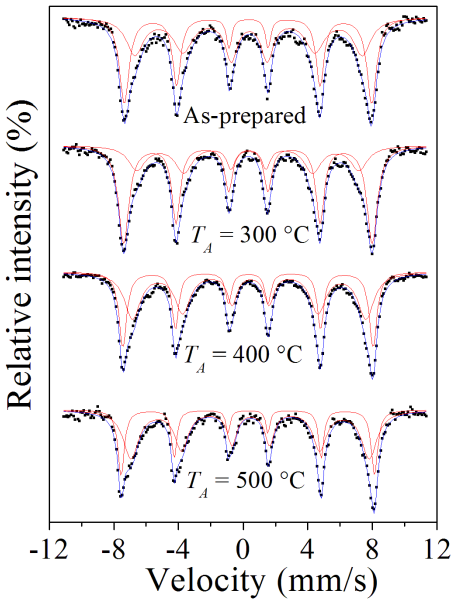

Figure 6.15: Room temperature ^{57}Fe Mössbauer spectra for the as-prepared and samples annealed at different temperatures of $Sr_{1/3}Mn_{1/3}Co_{1/3}Fe_2O_4$ ferrite nanoparticles.

Table 6.3: Annealing temperatures T_A, Isomer shifts (δ), hyperfine magnetic fields (H), line widths (Γ) and Fe^{3+} fraction population (f) on A-site and B-site for the as-prepared and samples annealed at different temperatures of $Sr_{1/3}Mn_{1/3}Co_{1/3}Fe_2O_4$ ferrite nanoparticles.

T_A	δ(mm/s)		H(kOe)		Γ(mm/s)		f(%)	
	δ_A	δ_B	H_A	H_B	Γ_A	Γ_B	f_A	f_B
	±0.02	±0.02	±6	±2	±0.08	±0.1	±5	±7
200 °C	0.36	0.32	436	475	0.46	0.20	53.2	46.8
300 °C	0.31	0.31	426	477	0.32	0.29	34.2	65.8
400 °C	0.42	0.31	448	480	0.37	0.23	59.1	40.9
500 °C	0.45	0.29	457	487	0.36	0.15	67.5	32.5

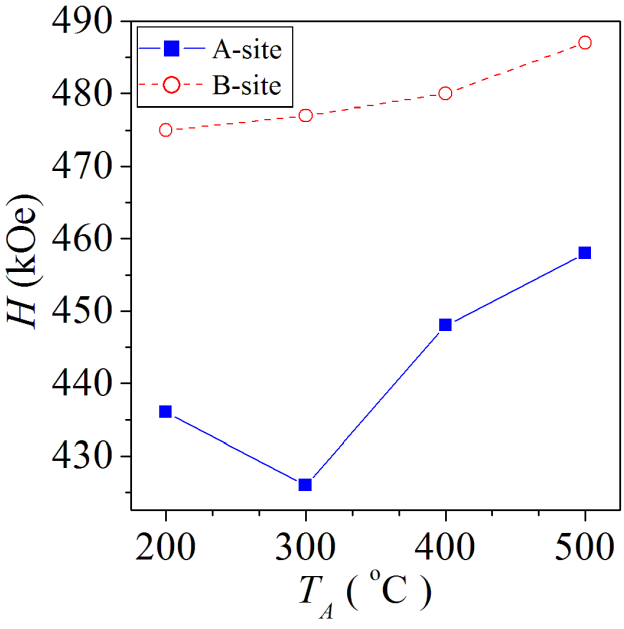

Figure 6.16: Variation of H_A and H_B with T_A for $Sr_{1/3}Mn_{1/3}Co_{1/3}Fe_2O_4$ ferrite nanoparticles.

Figure 6.17 shows room temperature M-H loops for the as-prepared and for annealed samples. The magnetic parameters M_S, H_C, M_r and M_r/M_S are presented in Table 6.4. The magnetization increased from 67.5±0.4 to 71.94±0.4 emu/g as the annealing temperature increased from 200 °C to 500 °C and the corresponding

coercive fields increased from 0.24±0.03 to 9.2±0.03 kOe respectively. Figure 6.18 shows variation of M_S and H_C with T_A measured at 300 K.

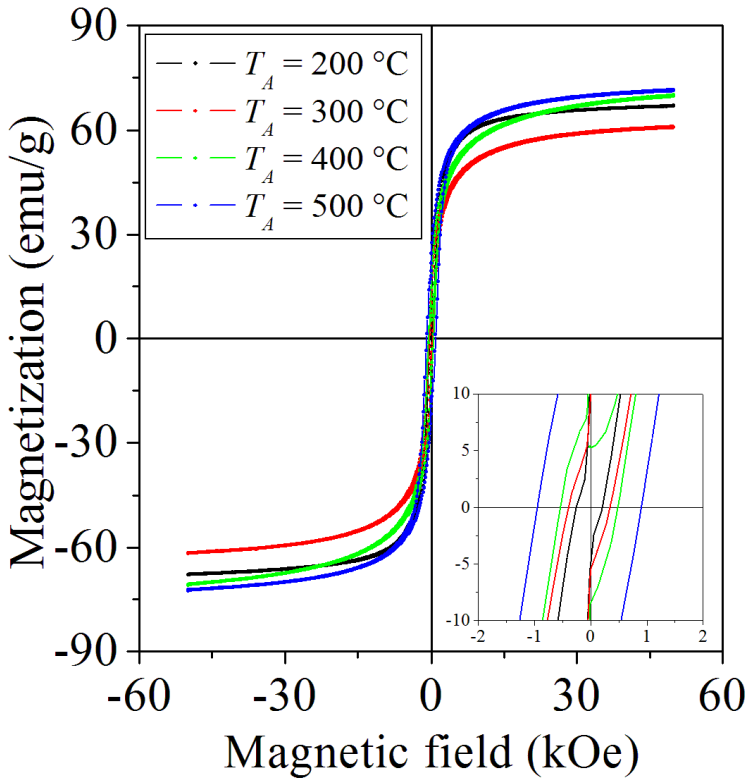

Figure 6.17: Room temperature hysteresis loops for the as-prepared and samples annealed at different temperatures of $Sr_{1/3}Mn_{1/3}Co_{1/3}Fe_2O_4$ ferrite nanoparticles. The inset shows the magnification around the origin.

Table 6.4: Magnetic parameters obtained at room temperature for the as-prepared and samples annealed at different temperatures (T_A) of $Sr_{1/3}Mn_{1/3}Co_{1/3}Fe_2O_4$ ferrite nanoparticles.

T_A	M_S(emu/g) ±0.4	H_C(kOe) ±0.02	M_r(emu/g) ±3	M_r/M_s
200 °C	67.46	0.24	8	0.12
300 °C	61.29	3.88	8	0.13
400 °C	70.39	5.10	12	0.17
500 °C	71.94	9.22	20	0.28

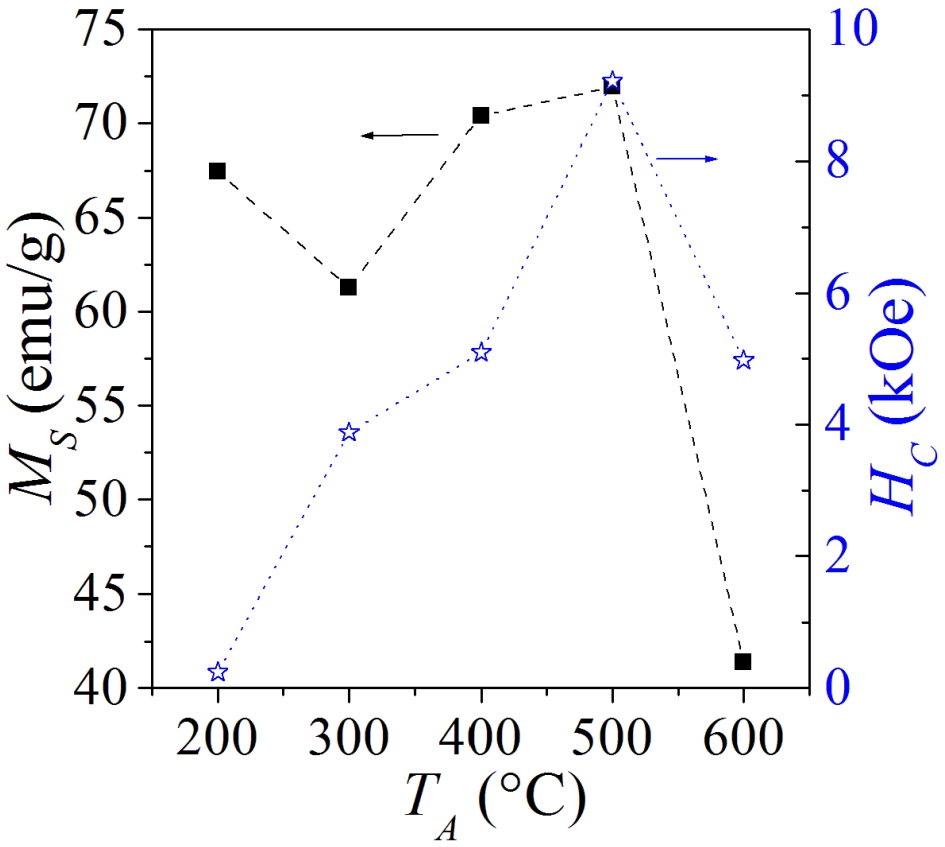

Figure 6.18: Variation of M_S and H_C with T_A for $Sr_{1/3}Mn_{1/3}Co_{1/3}Fe_2O_4$ ferrite nanoparticles measured at 300 K.

6.5 Conclusion

The $Sr_{1/3}Mn_{1/3}Co_{1/3}Fe_2O_4$ nanoferrite was successfully produced by glycol thermal method. The simultaneous substitution of Sr, Mn and Co leads to a slight increase in the lattice parameter from 0.836±0.001 nm (for $Sr_{0.2}Mn_{0.1}Co_{0.7}Fe_2O_4$ [169]) to 0.841±0.003 nm. The BET and BJH measurements show high surface area property. The temperature dependence of the saturation magnetization follows the modified Bloch's law. Evidence of spin freezing has been observed as indicated by some distortion in the magnetic hysteresis loops and increased coercivity at lower temperature. The temperature dependence of the coercive fields follow Kneller's law below about 200 K. We have also found significant increases in the coercive field at room temperature from 0.045 kOe (for $Mn_{0.1}$ $Sr_{0.2}Co_{0.7}Fe_2O_4$ [169]) to 0.20±0.01 kOe in the current compound. At 4 K the coercive field increased from 3.0 kOe to 11.24±0.02

kOe and corresponding crystallite sizes increased from 8.06±0.01 nm to 9.26±0.02 nm. We can attribute the increase in crystallite size to the increase in coercive fields. The sample is highly affected by the annealing temperature and the crystallite sizes increase from 9.3±0.1 nm to 20.6±0.1 nm for samples annealed at 200 °C and 500 °C respectively. The annealed samples show mono-dispersive characteristics indicated by HRSEM and HRTEM images. Increasing the annealing temperature affects the s-electrons, but does not change the oxidation states of Fe atoms as confirmed by isomer shift values. Thermal annealing increases the coercive field significantly from 0.24±0.03 to 9.2±0.03 kOe after annealing at 200 °C and 500 °C respectively which we associate with increase in crystallite sizes for single domain particles.

Chapter 7

Synthesis and characterization of $Ba_{0.5}Co_{0.5}Fe_2O_4$ nanoparticle ferrites: Application as electrochemical sensor for ciprofloxacin

7.1 Introduction

Cobalt based ferrites have emerged as attractive materials due to their interesting physical, chemical, magnetic and electrical properties. Spinel structured cobalt ferrite ($CoFe_2O_4$) possesses significant properties such as large anisotropy, high coercive field, moderate saturation magnetization, chemical stability and good electrical conductivity [200]. These properties provide applications of $CoFe_2O_4$ in various fields such as electronics, photomagnetism, catalysis, ferrofluids, in cancer therapy as well as agents for molecular magnetic resonance imaging [201]. More recently, $CoFe_2O_4$ nanoparticles have been utilized in the area of electroanalysis due to their appreciable electrocatalytic activity, high surface area and low cost of production [202, 203]. The effect of different elements on the characteristics of $CoFe_2O_4$ have been well ex-

plored in the past [204]. However, investigation of substituted $CoFe_2O_4$ by various other elements still remains a subject of popular investigation. Barium ferrites have been found to possess numerous applications in magnetic storage media, catalysis, permanent magnets, pigments, magneto-materials and for the absorption of electromagnetic waves [205]. Due to large atomic size (atomic radius ∼2.78 Å) and high chemical reactivity of barium (Ba) as compared to cobalt (Co) (atomic radius ∼1.67 Å), we envisaged substituting Co with Ba in order to form $Ba_{0.5}Co_{0.5}Fe_2O_4$ nanoparticles, and subsequently investigate the effect of the Ba atom on the ferrite structure and its electrochemical properties. A suitable synthesis route was required in order to minimise the lattice deformation that could occur due to the size mismatch between Co and Ba. The glycol thermal technique was chosen for the synthesis of the nanoparticles because of the relatively low reaction temperature of the technique [206].

Ciprofloxacin,(1-cyclopropyl-6-fluoro-1,4-dihydro-4-oxo-7-(1-piperazinyl) -3-quinoline carboxylic acid (Figure 7.1), is a second-generation fluoroquinolone drug employed for treatment of different kinds of bacterial infections in the body [207, 208]. It is also used for treating people having anthrax infection after inhalational exposure [209].

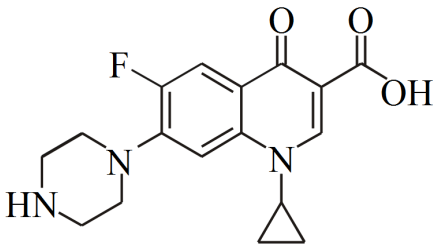

Figure 7.1: Scheme illustrates the chemical structure of CFX.

Adverse effects of the drug include swelling or tearing of a tendon, especially the Achilles' tendon of the heel, toxic epidermal necrolysis, Stevens-Johnson syndrome, aggravation of muscle weakness in patients having neurological disorder myasthenia gravis leading to breathing problems, agranulocytosis, thrombocytopenia and myelosuppression [210, 211, 212, 213]. An overdose of ciprofloxacin results in severe hepatotoxicity [214]. Thus, it is essential to quantify ciprofloxacin (CFX) in human

plasma/serum/urine to monitor drug accumulation in patients with hepatic dysfunction or for diagnosis of CFX poisoning in severe overdose victims. CFX analysis also plays a critical role in drug quality control. Hence, there is a need to develop reliable, sensitive, simple and rapid methods for the determination of CFX in pharmaceutical preparations and body fluids. Many methods such as spectrophotometry, fluorometry, high-performance liquid chromatography and voltammetry have been reported for the analysis of CFX [215, 216, 217, 218, 219, 220]. Electrochemical analytical methods have attracted considerable attention in the field of drug analysis, with the last few decades having witnessed modification of the electrode surface using a variety of nanomaterials for effective determination of the electroactive species of interest. Literature survey reveals that $CoFe_2O_4$ nanoparticle modified electrodes have been considerably used in electroanalysis. Malviya *et al.* [221] fabricated a polypyrrole and $CoFe_2O_4$ nanoparticle composite electrode and employed it as an electrocatalyst for the reduction of oxygen. $CoFe_2O_4$ spinels were synthesized and reported to demonstrate electrocatalytic activity towards reduction of oxygen and nitric oxide [222]. Later, a β-cyclodextrin-cobalt ferrite nanocomposite based electrochemical sensor was fabricated for the successful detection of catechol [202]. Paracetamol was also determined voltammetrically using $CoFe_2O_4$ and Ni- substituted $CoFe_2O_4$ nanoparticle modified glassy carbon electrode [223, 224]. However, to the best of our knowledge, there is no report on the synthesis of $Ba_{0.5}Co_{0.5}Fe_2O_4$ nanoferrite and investigation of its electrochemical sensing property. Thus, the present chapter aims to synthesize $Ba_{0.5}Co_{0.5}Fe_2O_4$ ferrite nanoparticles by glycol thermal method and to develop a sensitive electrochemical sensor for CFX based on the novel $Ba_{0.5}Co_{0.5}Fe_2O_4$ nanoparticles modified glassy carbon electrode (nano $Ba_{0.5}Co_{0.5}Fe_2O_4$/GCE).

7.2 Experimental details

$Ba_{0.5}Co_{0.5}Fe_2O_4$ nanoferrite was synthesized by the glycol-thermal method in a Watlow series model PARR 4843 stirred pressure reactor. The starting materials were high purity metal chlorides. The synthesis procedures were discussed in chapter 4.

The phase and structural characterizations of the sample were obtained on a Phillips X-ray diffractometer type Model: PANalytical, EMPYREAN using CoKα radiation. The morphology and micro-structure of the nanoparticles were investigated on a high-resolution transmission electron microscope (HRTEM) (type: Jeol_JEM-1010) and high-resolution scanning electron microscope (HRSEM) (Ultra Plus ZEISS-FEG HRSEM instrument). The textural and porosity characteristics of the nanoparticles were investigated using a micrometrics Tristar II 3020 instrument using liquid N_2 as the analysis gas at 77 K. CFX and potassium ferricyanide were purchased from Sigma-Aldrich, USA. Other chemicals used for voltammetric experiments were of analytical reagent grade and used without further purification. A stock solution (1.00×10^{-3} M) of CFX was prepared by dissolving the drug in double distilled water. The studies were conducted in 0.1 M phosphate buffer solution (PBS) at pH 7.2. Prior to each experiment, pure N_2 was purged into the solution containing CFX for 5 minutes. All the electrochemical measurements were performed using an electrochemical analyzer (Model 800B Series, CH Instruments, Inc.) as shown in chapter 4. A three-electrode system was employed, which consisted of a reference electrode (Ag/AgCl), a counter electrode (platinum wire) and a working electrode. The working electrode was glassy carbon electrode (GCE), $CoFe_2O_4$ nanoparticles modified GCE (nano $CoFe_2O_4$/GCE) or $Ba_{0.5}Co_{0.5}Fe_2O_4$ nanoparticles modified GCE (nano $Ba_{0.5}Co_{0.5}Fe_2O_4$/GCE). Cleaning of the GCE was discussed in chapter 4. A 2.0 mg mL^{-1} suspension of $CoFe_2O_4$ or $Ba_{0.5}Co_{0.5}Fe_2O_4$ nanoparticles in water was prepared. 5.0 μL of the respective suspension was cast onto the surface of the cleaned GCE surface and dried to constitute nano $CoFe_2O_4$/GCE and nano $Ba_{0.5}Co_{0.5}Fe_2O_4$/GCE, respectively.

7.3 Results and discussion

7.3.1 Characterization of $Ba_{0.5}Co_{0.5}Fe_2O_4$ nanoparticles

Figure 7.2 confirms the single phase structure of the synthesized novel $Ba_{0.5}Co_{0.5}Fe_2O_4$ ferrite nanoparticles with no impurity peaks. The peaks were indexed to the cubic spinel structure of $CoFe_2O_4$ (JCPDS file No. 22-1086) [55]. The lattice parameter

a was calculated using equation 4.1.1 [146]. The average crystallite size was calculated using the Scherrer's equation 4.1.3. The microstrain was determined using the formula 4.1.5. The calculated values of the lattice parameter, crystallite size and microstrain for the as-prepared $Ba_{0.5}Co_{0.5}Fe_2O_4$ were found to be 0.838±0.003 nm, 7.4±0.1 nm and 0.0016±0.0001, respectively.

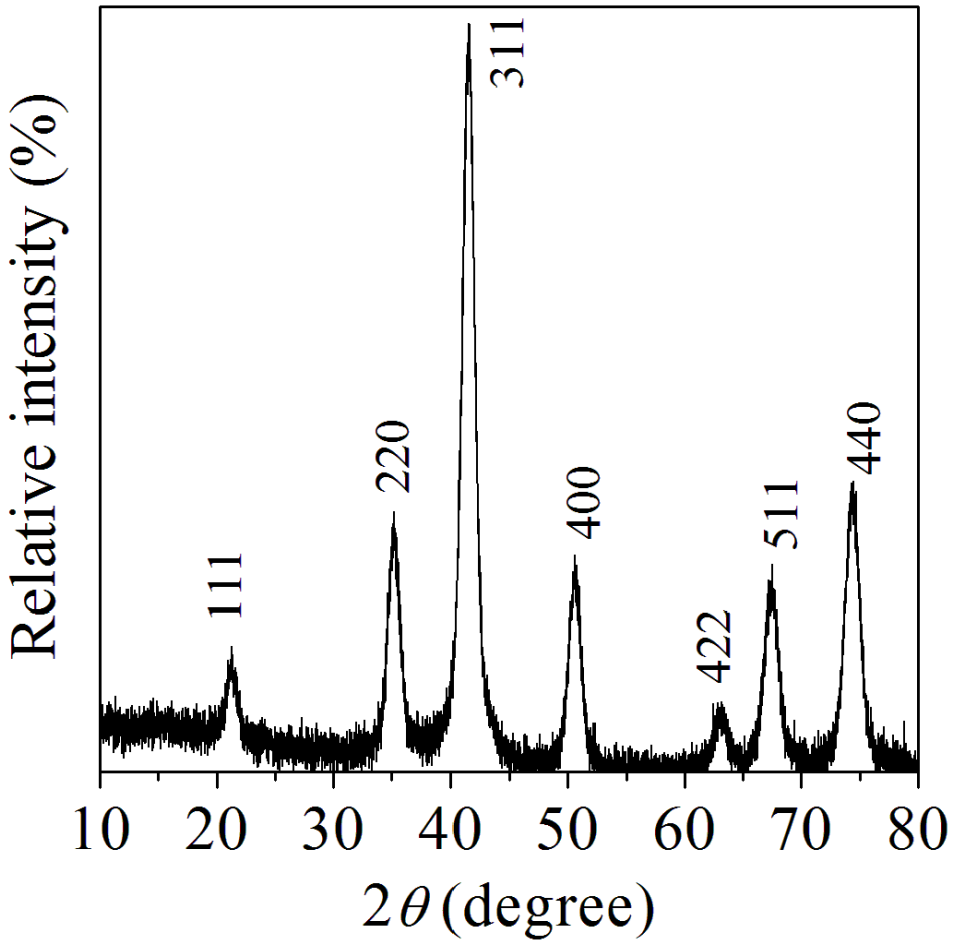

Figure 7.2: X-ray diffraction patterns for the as-prepared $Ba_{0.5}Co_{0.5}Fe_2O_4$ ferrite nanoparticles.

The effect of incorporating Ba into $CoFe_2O_4$ on the morphology was studied by high resolution transmission electron microscopy (HRTEM) and the high resolution scanning electron microscopy (HRSEM), as shown in Figure 7.3. The lattice fringes are well defined suggesting well-formed crystalline structure of the nanoferrite particles, as displayed in Figure 7.3 (A). Furthermore, a high magnification image scale of

10 nm shows that the particles tend to have almost spherical shapes. The HRTEM results were found to be in good agreement with the XRD data. In both techniques evidence of crystallinty is observed. The HRTEM image was also used to deduce the particle size that was calculated to be 7±2 nm. This value is close to the crystallite size calculated from XRD results. The HRSEM image display the surface morphology of the particles as depicted in Figure 7.3 (B). No significant difference in the shape of the particles was noted and on average the particles are homogeneously distributed.

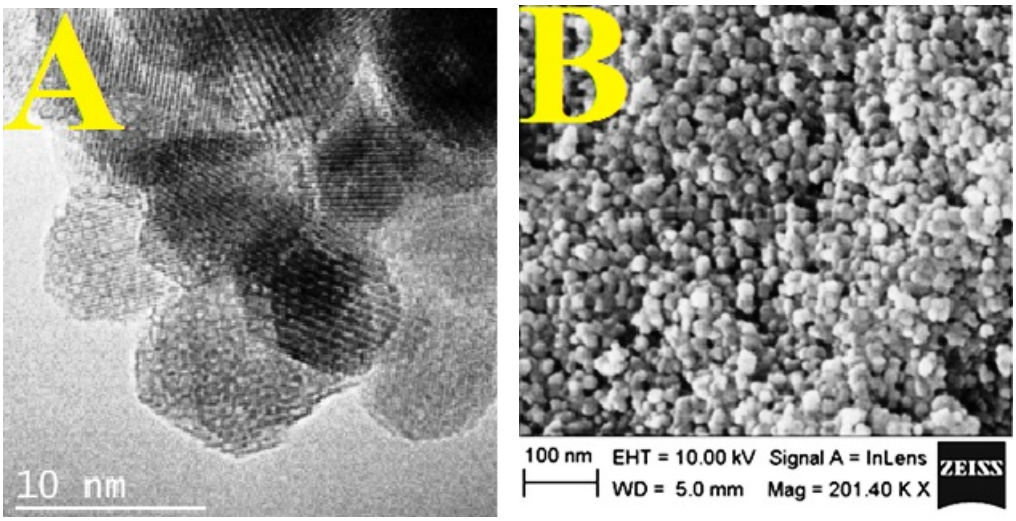

Figure 7.3: HRTEM (A) and HRSEM (B) images for the as-prepared $Ba_{0.5}Co_{0.5}Fe_2O_4$ ferrite nanoparticles.

The Brunauer-Emmet-Teller (BET) surface area measurement of the nanoferrite sample showed a high value of 137 m^2/g. N_2 adsorption-desorption measurement was used to investigate the textural and character of the pores of the synthesized $Ba_{0.5}Co_{0.5}Fe_2O_4$ sample. At a relative pressure (P/P_0) of 3%, the adsorption of N_2 increased from 25.4 cm^3/g to reach its maximum value of 152.2 cm^3/g at P/P_0 of 100%. As the relative pressure reduces, the desorption isotherm decreases but follows a new path that is different from the adsorption one and shows a hysteresis loop due to the condensation of the N_2 in the sample pores [190]. Moreover, below P/P_0 ∼50% the adsorption and desorption branches join together to form a reversibility curve. Since the hysteresis loop covered a wide range of P/P_0 values, the pores are

expected to be large [225].

Furthermore, the gap between the adsorption and desorption paths in Figure 7.4 are wide and can be associated with wide pore sizes. The sample pores appear to be empty up to $P/P_0 \sim 0.5$. Figure 7.4 also depicts type IV isotherm hysteresis loop that indicates the onset of mesoporous property of the $Ba_{0.5}Co_{0.5}Fe_2O_4$ sample [189]. The distribution of the pores in the sample was investigated by the Barrett-Joyner-Halenda (BJH) measurement, as shown in the inset of Figure 7.4, with most of the points in BJH plot located in the range between 3-30 nm, which strongly hints towards mesoporous property of the sample [191]. In addition, the sharpness of the peak indicates homogeneous porosity of the sample.

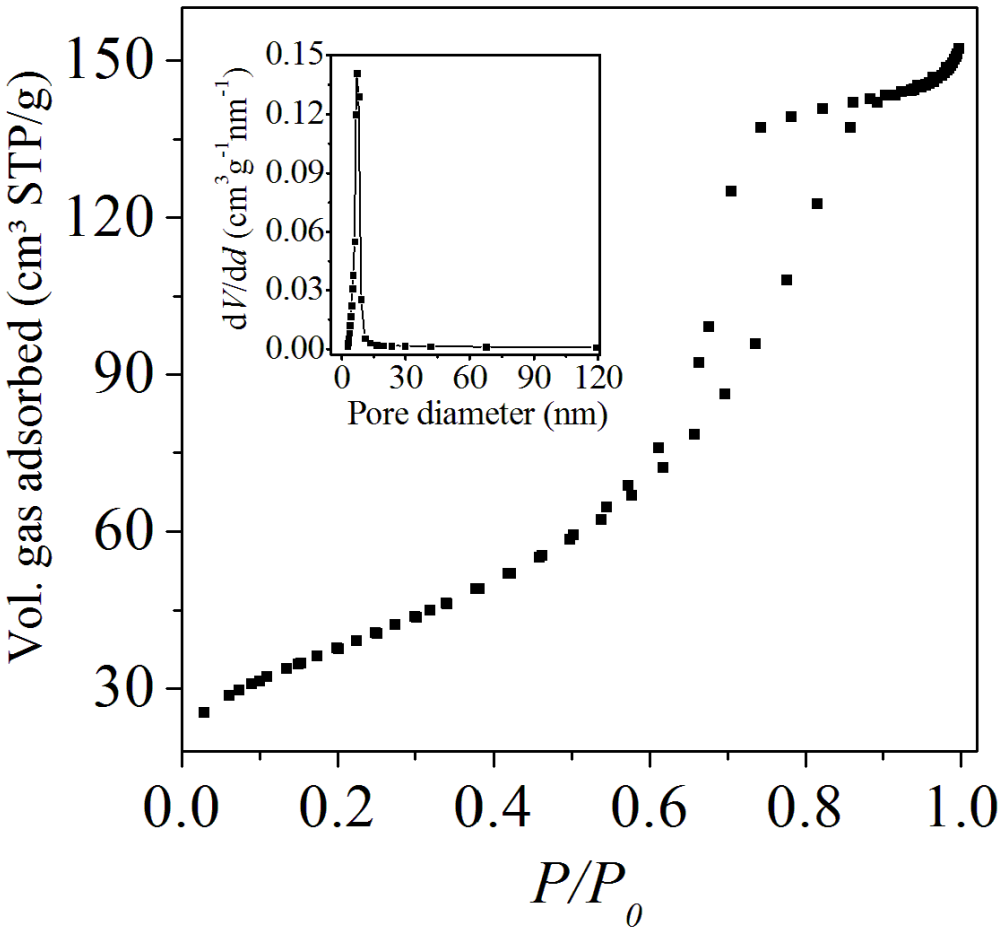

Figure 7.4: N_2 gas adsorption isotherms for the as-prepared $Ba_{0.5}Co_{0.5}Fe_2O_4$ ferrite nanoparticles. The inset shows the pore size distribution.

7.3.2 Magnetic measurements

Figure 7.5 shows the room temperature Mössbauer spectra for the as-prepared $CoFe_2O_4$ and $Ba_{0.5}Co_{0.5}Fe_2O_4$ nanoparticles. Two sextets associated with Zeeman splitting have been used to fit the spectra. The $CoFe_2O_4$ is included as a reference. The sextets indicate the ordered magnetic state of a sample. The best fit parameters to the data are give in Table 7.1. The values of the isomer shift decrease after doping with Ba only in the A site, indicating the increase in the s-electrons on that site due to the presence of Ba atoms. Because of the large bond separation between Fe^{3+} ions and O^{-2} ions on octahedral site and reduced orbital overlapping, the value of the isomer shift in the tetrahedral (A) site is lower than on the octahedral (B) site [226]. Evidence of the existence of Fe^{3+} ions can be proved from isomer shift values which are in the range of 0.1-0.5 mm/s [227]. The values of the hyperfine fields from $CoFe_2O_4$ to $Ba_{0.5}Co_{0.5}Fe_2O_4$ decreased from 454 to 443 kOe at A site and from 485 to 478 kOe at B site for the $CoFe_2O_4$ and $Ba_{0.5}Co_{0.5}Fe_2O_4$, respectively. However, the values of the hyperfine fields are still high as expected, due to super-exchange interaction between the atoms [228]. The values of line widths ω hardly change on the A site but change significantly from 0.24 to 0.31 mm/s on the B site indicating wide broadening in the octahedral site. Furthermore, the values of Fe^{3+} fraction population f increased at A site to 55%, whilst at B site it decreased to 45%. The f values of the parent material ($CoFe_2O_4$) are at 50% for both sites (as reported in chapter 5). Therefore, the values of line width and f show that the Ba atoms have higher preference for the octahedral sites.

Figure 7.6 shows typical M-H loops for the as-prepared $Ba_{0.5}Co_{0.5}Fe_2O_4$ sample. The magnetic measurements were carried out in external magnetic fields of ± 50 kOe. The magnetic hysteresis loops were measured at different temperatures in the range of 4 to 300 K. Full saturation of the magnetization is not achieved especially at low temperature which we attribute to spin canting effect. The magnetizations obtained at 300 K and at 4 K at the highest applied field were 69.4 ± 0.3 emu/g and 84.3 ± 0.5 emu/g, respectively. The coercive field increases from 0.20 ± 0.03 kOe to 13.00 ± 0.06 kOe between 300 K and 4 K respectively. The hysteresis loops in Figure 7.6 show that the sample becomes magnetically harder at lower temperature associ-

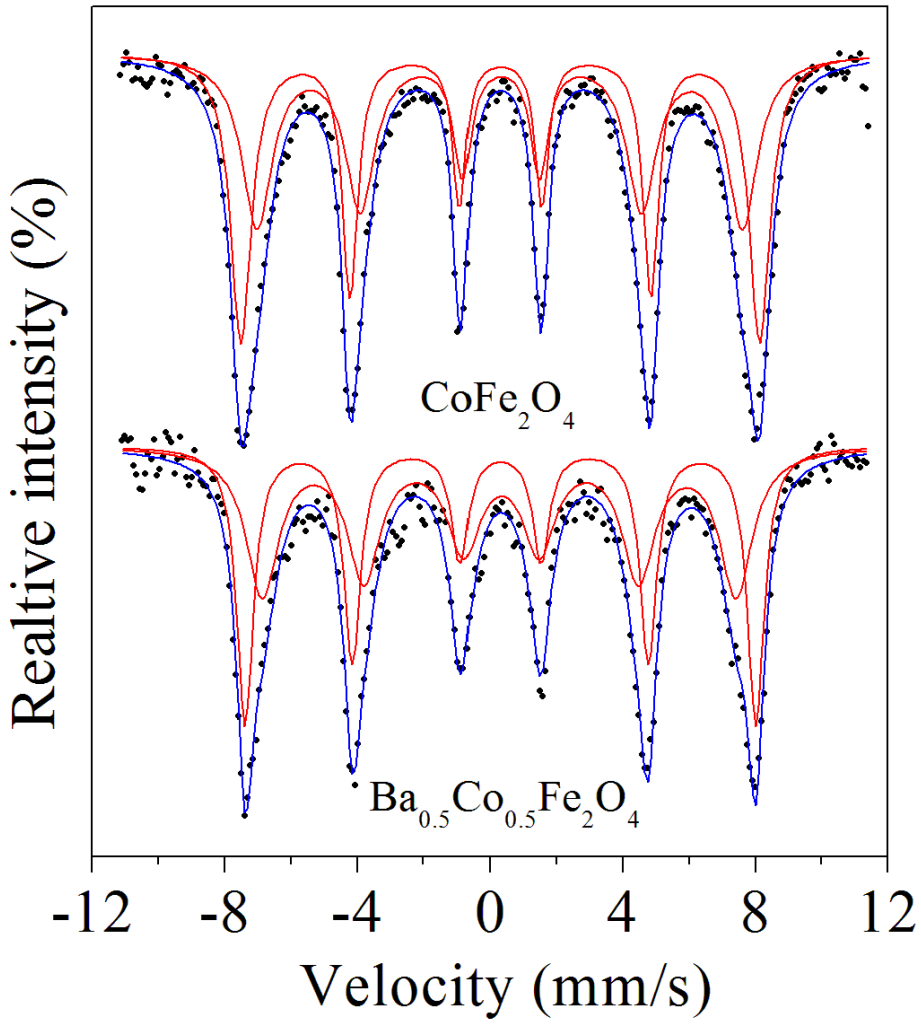

Figure 7.5: Room temperature Mössbauer spectra of $CoFe_2O_4$ and $Ba_{0.5}Co_{0.5}Fe_2O_4$ ferrite nanoparticles.

Table 7.1: Isomer shifts (δ), hyperfine magnetic fields (H), line widths (Γ) and Fe^{3+} fraction population (f) on A-site and B-site for the as-prepared $CoFe_2O_4$ and $Ba_{0.5}Co_{0.5}Fe_2O_4$ samples.

Sample	δ(mm/s)		H(kOe)		Γ(mm/s)		f(%)	
	δ_A	δ_B	H_A	H_B	Γ_A	Γ_B	f_A	f_B
	±0.03	±0.01	±7	±2	±0.07	±0.05	±1	±2
$CoFe_2O_4$	0.31	0.31	453	485	0.32	0.24	50	50
$Ba_{0.5}Co_{0.5}Fe_2O_4$	0.30	0.31	443	478	0.30	0.31	55	45

ated with spin freezing effect. Below 80 K we see clear distortions in the hysteresis loops which become more prominent at lower temperature. This distortion can be explained in terms of a combination of soft and hard magnetic phases. Disorder of the spins in surface layers of the nanoparticles can be responsible for the hysteresis loop distortions [229].

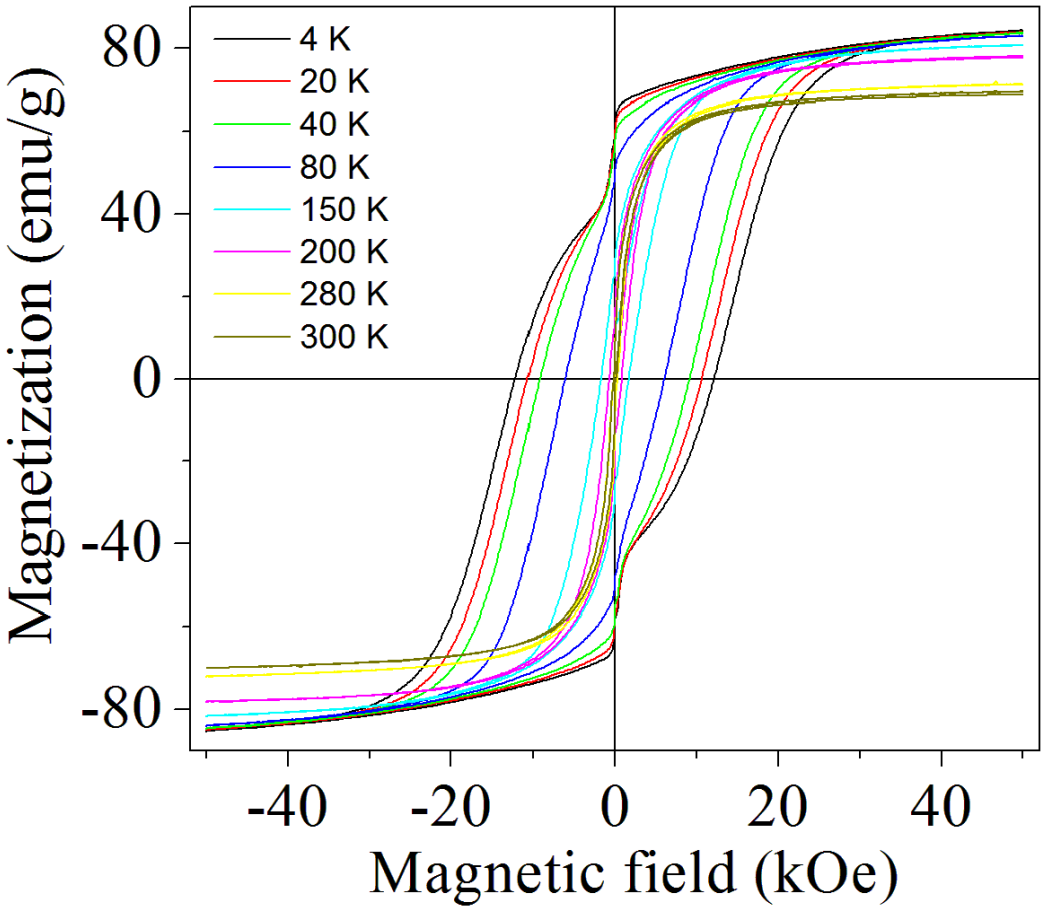

Figure 7.6: Hysteresis loops for as-prepared $Ba_{0.5}Co_{0.5}Fe_2O_4$ ferrite nanoparticles measured at different temperature.

Zero field cooling (ZFC) and field cooling (FC) magnetization measurements were performed using the mini cryogenic free magnetization measurement system. The sample was first cooled to 2 K in zero field and the measurements obtained while raising the temperature to 300 K. Similarly, FC measurements were obtained after cooling the sample in magnetic fields of 1 kOe and 10 kOe. Figure 7.7 shows ZFC and FC of the as-prepared $Ba_{0.5}Co_{0.5}Fe_2O_4$ ferrite nanoparticles. The ZFC and

FC curves separate at a finite temperature around 289 K and 200 K as shown in Figure 7.7 at 1 kOe and 10 kOe, receptively. Clearly, the blocking temperature T_B values decreased at higher field cooling. The separation between ZFC and FC are known to be associated with magnetic anisotropy barriers [230].

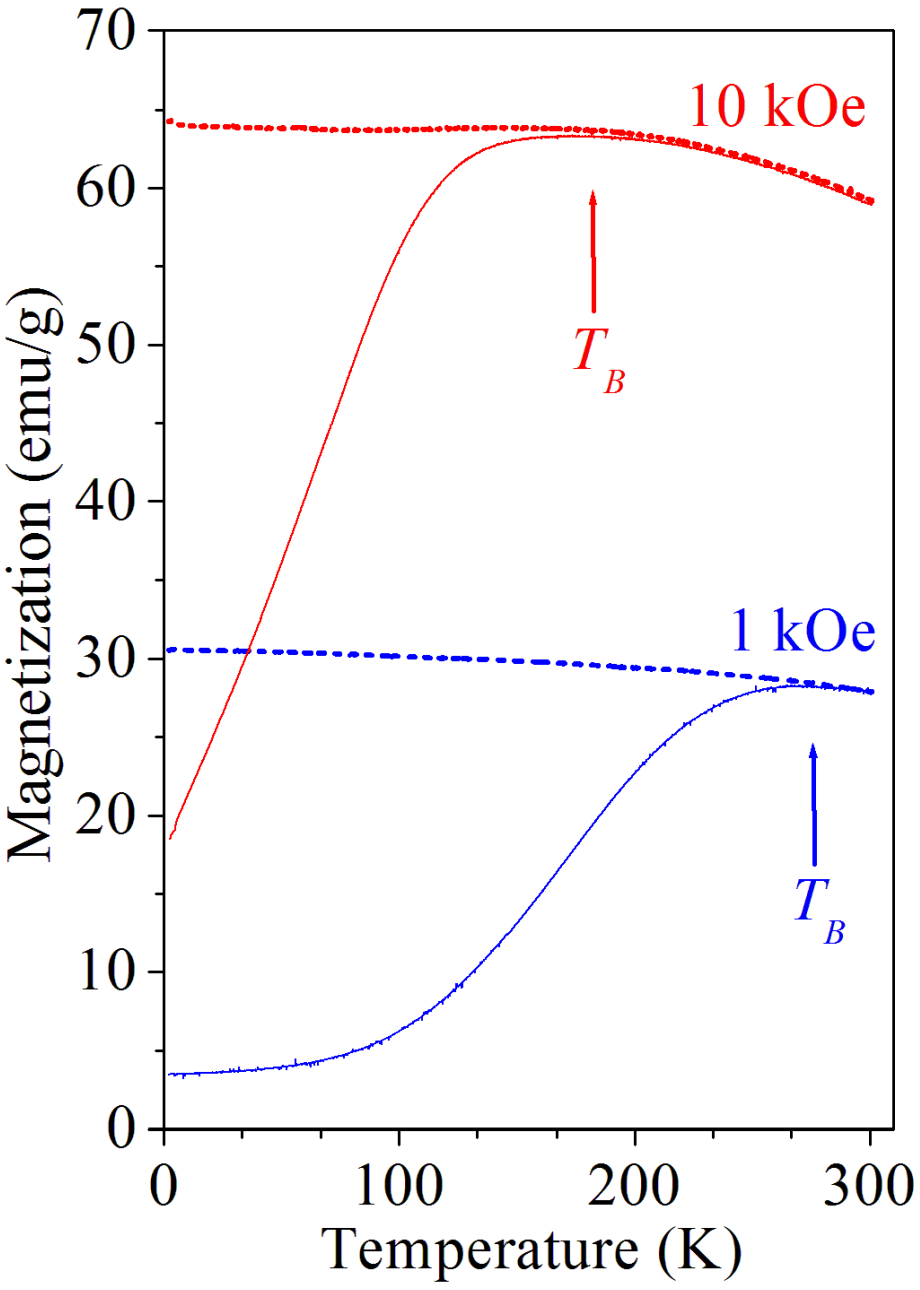

Figure 7.7: ZFC and FC measured at 10 kOe and 1 kOe for as-prepared $Ba_{0.5}Co_{0.5}Fe_2O_4$ ferrite nanoparticles.

7.4 Influence of annealing process on the structure and magnetic behavior of $Ba_{0.5}Co_{0.5}Fe_2O_4$ nanoparticles

The influence of annealing temperature on the structure and magnetic properties of $Ba_{0.5}Co_{0.5}Fe_2O_4$ ferrite nanoparticles was also investigated. Different batches of the sample were annealed at different temperatures (300 °C, 400 °C, 500 °C, and 600 °C) under flowing argon gas (purity: 99.999 %). Figure 7.8 shows the XRD patterns as a function of synthesis and annealing temperatures. The position of the peaks are indexed according to the spinel structure of $CoFe_2O_4$ (JCPDS file No. 22-1086).

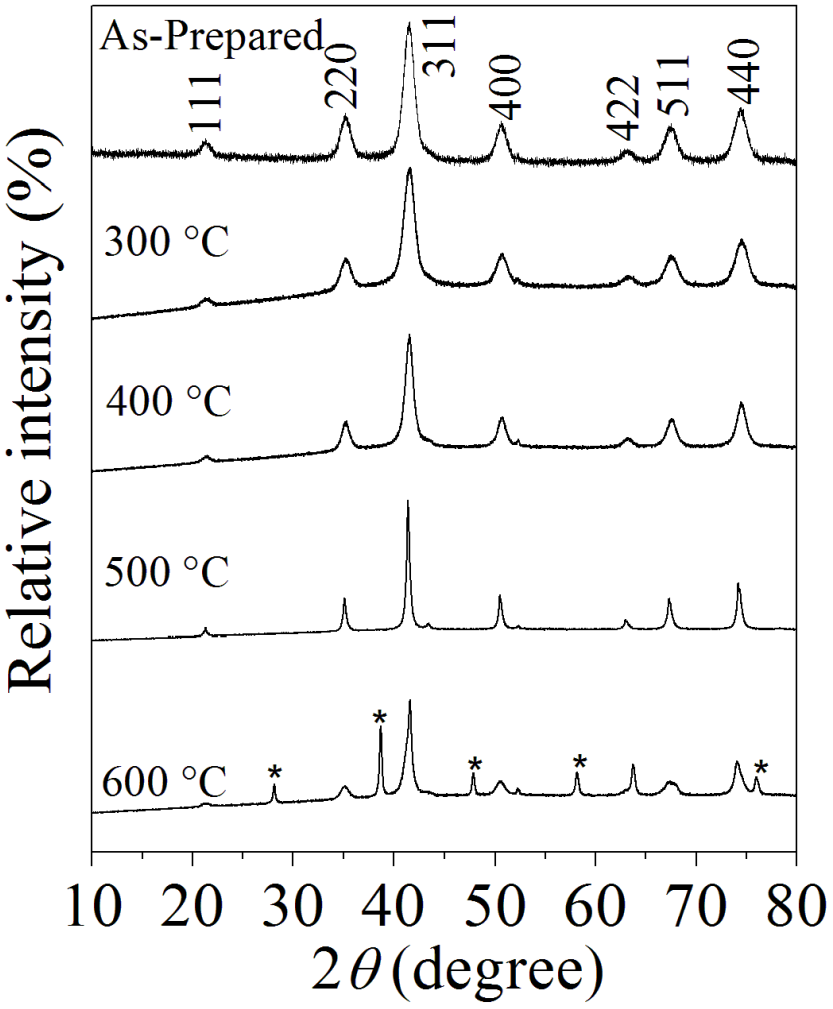

Figure 7.8: XRD patterns for $Ba_{0.5}Co_{0.5}Fe_2O_4$ nanoparticle ferrites.

The peaks become sharper as the temperature increases up to 500 °C. This indicates an increase in the particle sizes and enhanced crystallinity. At 600 °C additional peaks appear which are suspected to be due secondary phases such as of α-Fe_2O_4 [57]. The lattice parameter a were calculated using Bragg's equation 4.1.1. The average XRD crystallite sizes D_{XRD} was calculated using Scherrer's equation 4.1.3. The XRD densities of the samples ρ_{XRD} were calculated using the equation 4.1.4. The microstrains ε were determined using the equation 4.1.5. The calculated values of a, D_{XRD}, ρ_{XRD}, HRTEM particle sizes D_{HRTEM} and ε for as-prepared $Ba_{0.5}Co_{0.5}Fe_2O_4$ and the annealed samples at different temperatures are given in Table 7.2.

Table 7.2: Lattice parameters a, XRD crystallite sizes D_{XRD}, HRTEM particle sizes D_{HRTEM}, X-ray densities and microstrains ε for the annealed $Ba_{0.5}Co_{0.5}Fe_2O_4$ nanoparticle ferrites.

T_A (°C)	a(Å) ±0.01	D_{XRD}(nm) ±0.01	ρ_{XRD}(g/cm^3) ±0.001	D_{HRTEM}(nm) ±3	ε ±0.0002
200	8.379	7.40	6.183	10	0.0016
300	8.366	7.68	6.212	13	0.0006
400	8.367	10.79	6.210	15	0.0005
500	8.389	27.05	6.161	21	0.0003

After annealing at T_A = 300 °C, the lattice parameter decreased slightly and subsequently increased with further annealing to 500 °C. This can be explained as a result of higher surface defects at low annealing temperature and subsequent increase in particle size and crystallinity expected at higher T_A [231, 232, 232]. Since the Ba atom is relatively larger (atomic radius 2.78 Å) than Co atom (atomic radius 1.67 Å), suspected defects in the sample could be caused be Ba atoms which may initially substitute at the tetrahedral site. Figure 7.9 shows the variation of the crystallite size and the microstrain with annealing temperature. The crystallite size increases from 7.4±0.1 nm to 27±0.2 nm with increase in annealing temperature from 200 °C to 500 °C, respectively. The microstrain values decrease from 0.0016±0.0001 to 0.0004±0.0001 as T_A increases which we attribute to the reduction of defects and

internal stress relaxation [199].

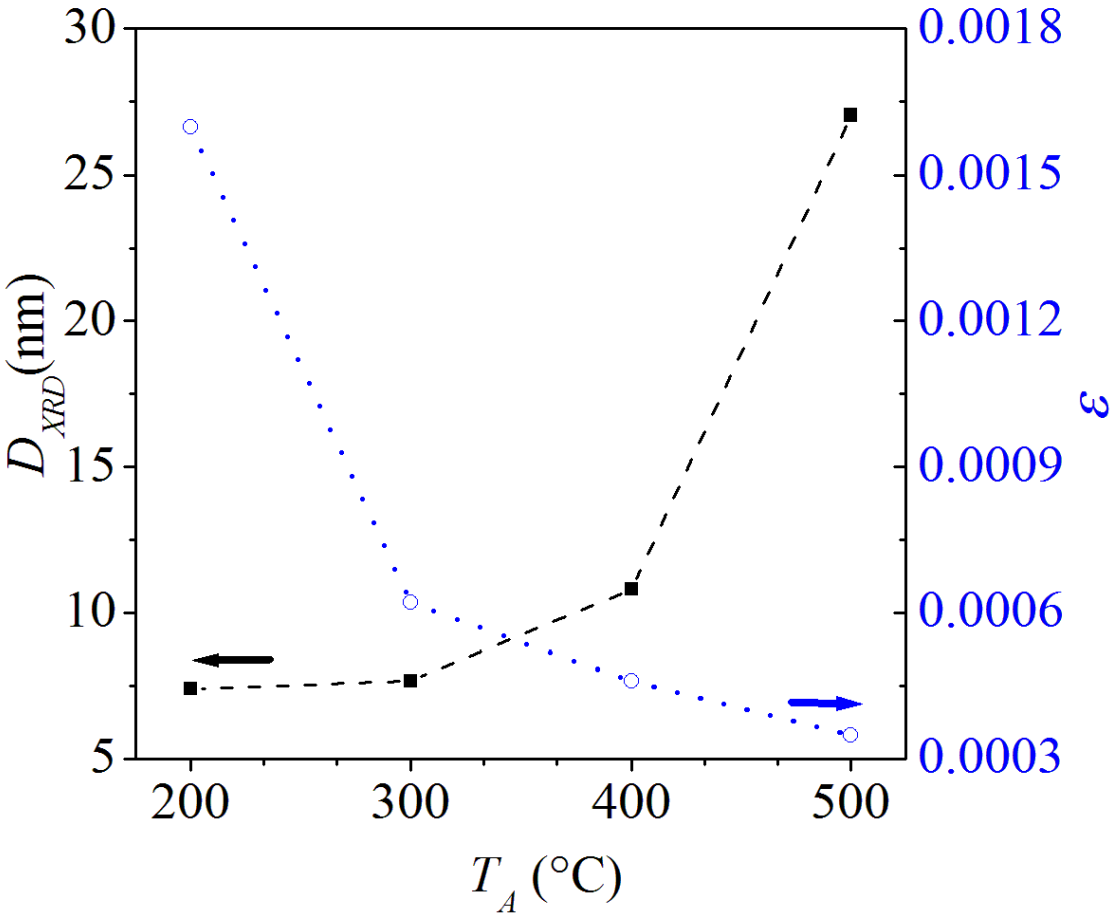

Figure 7.9: Variation of crystallite size and the microstrain with annealing temperature for $Ba_{0.5}Co_{0.5}Fe_2O_4$ nanoparticle ferrites.

The effect of the annealing temperature on the morphology of $Ba_{0.5}Co_{0.5}Fe_2O_4$ nanoparticle ferrites was studied through HRSEM and HRTEM images which show quasi-spherical-like shaped nanoparticles. The increase in the particle sizes due to increases in T_A is observed in the images presented in Figures 7.10 and 7.11. The nanoparticles appear to be uniformly distributed. Figure 7.11 shows crystalline enhancements of the nanoparticles defined by lattice fringes. The particle sizes calculated using HRTEM images are also presented which show an increase with T_A.

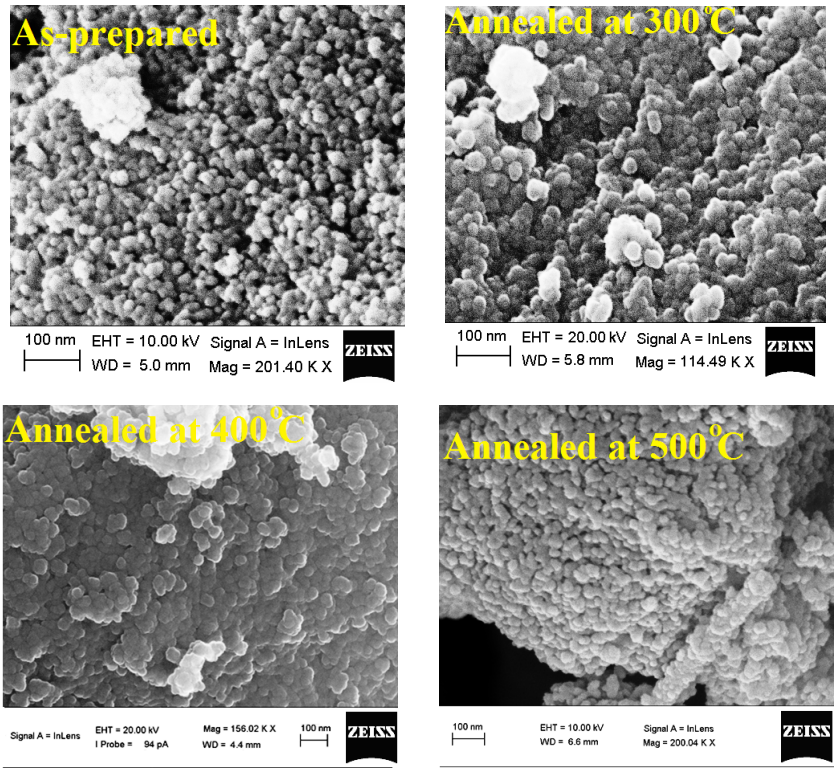

Figure 7.10: HRSEM images for the as-prepared $Ba_{0.5}Co_{0.5}Fe_2O_4$ samples annealed at different temperatures.

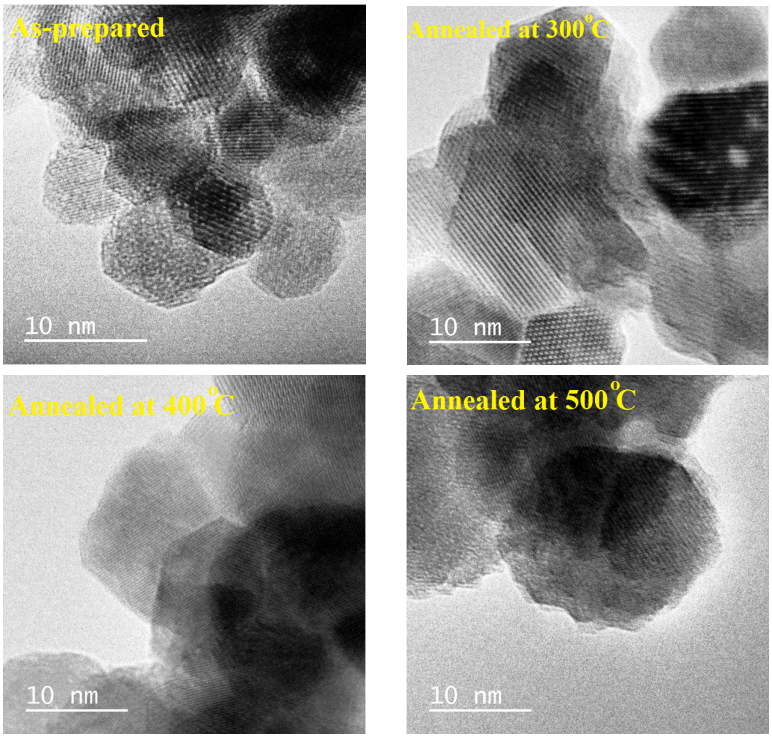

Figure 7.11: HRTEM images for the as-prepared $Ba_{0.5}Co_{0.5}Fe_2O_4$ samples annealed at different temperatures.

Figure 7.12 shows room temperature Mössbauer spectra for the $Ba_{0.5}Co_{0.5}Fe_2O_4$ samples which were fitted by two sextets corresponding to the presence of Fe^{3+} ions at the tetrahedral A and octahedral B sites [233]. Significant changes in the hyperfine parameters given in Table 7.3 are observed. The isomer shift values obtained from the fitting curves confirm the presence of only Fe^{3+} ions [227]. The orbital overlapping of Fe^{3+} on B site is smaller compared to A site, thus, the bond separation is anticipated to be larger at B site. Hence, the value of the isomer shift at B site is expected to be larger than an A site [226] as observed in Table 7.3. The changes in the isomer shift values with T_A indicate that the s-electrons in the sample are hardly affected by temperature [234]. The values of the hyperfine fields are due to the super-exchange interaction between the atomic moments [228]. The higher values of the hyperfine fields correspond to the B site while the lower value is associated with A sites. Hyperfine field values appear to increase with increasing T_A which we relate to the increase in the particle sizes [235]. The hyperfine fields increase and reach the highest values of 479 kOe and 514 kOe at A and B sites, respectively after annealing at 500 °C. The variation of hyperfine fields at tetrahedral site H_A and octahedral site H_B with the annealing temperature T_A are presented in Figure 7.13. A significant changes in the line widths occur only after annealing the sample at 300 °C. No significant changes occur at higher annealing temperature. The calculated values of the isomer shift (δ), hyperfine field (H), line width (Γ) and the Fe^{3+} site fraction populations (f) are also given in Table 7.3.

The magnetization measurements consisted of isothermal initial magnetization curves and hysteresis loops. The hysteresis loop measurements are presented in Figure 7.14. The saturation magnetization (M_S) were determined from initial magnetizations by fitting an empirical law of approach to saturation presented elsewhere [236]. The results deduced from the hysteresis loops and initial magnetization curves at 300 K are presented in Table 7.4. In Figure 7.15 we show the influence of annealing temperature on the deduced M_S and coercive fields H_C based on the magnetization measurements at 300 K. The results show significant correlation between M_S or H_C with T_A. The saturation magnetization M_S decreases as T_A increases up to 600 °C.

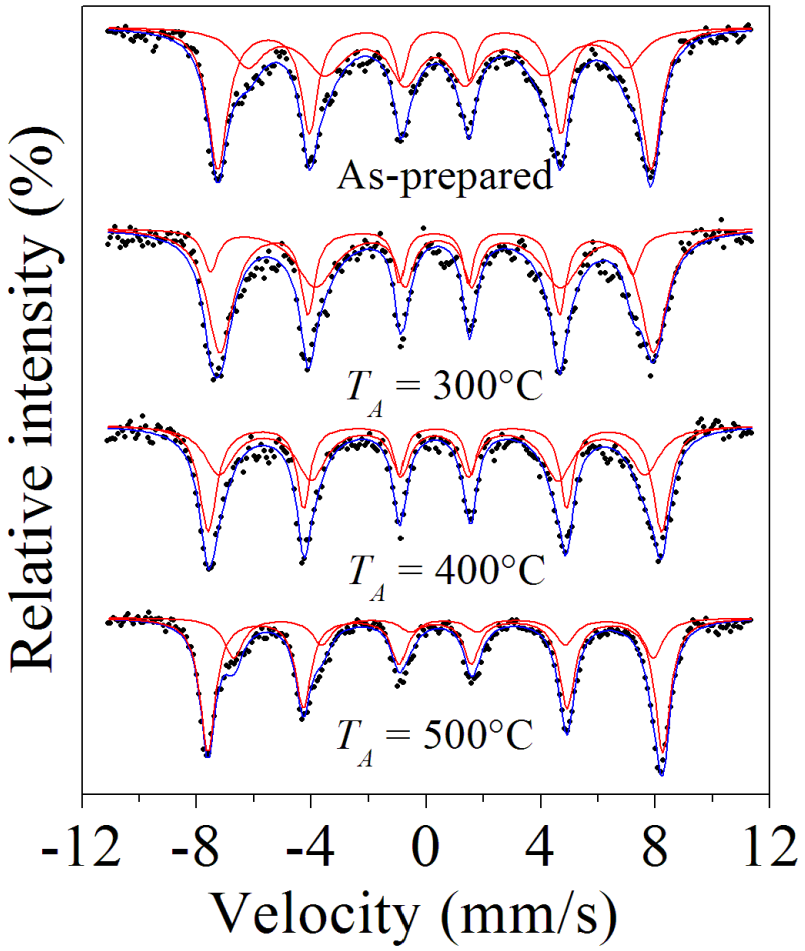

Figure 7.12: Mössbauer spectra for $Ba_{0.5}Co_{0.5}Fe_2O_4$ ferrite nanoparticles measured at room temperature.

Table 7.3: Isomer shifts (δ), hyperfine magnetic fields (H), line widths (Γ) and Fe^{3+} fraction population (f) on A-site and B-site for $Ba_{0.5}Co_{0.5}Fe_2O_4$ ferrite nanoparticles.

Sample	δ(mm/s)		H(kOe)		Γ(mm/s)		f(%)	
	δ_A	δ_B	H_A	H_B	Γ_A	Γ_B	f_A	f_B
	±0.03	±0.04	±9	±4	±0.09	±0.08	±3	±7
200 °C	0.30	0.31	443	478	0.60	0.31	54.5	45.5
300 °C	0.14	0.32	457	469	0.34	0.22	42.8	57.2
400 °C	0.26	0.32	461	490	0.36	0.23	51.7	48.3
500 °C	0.30	0.36	479	514	0.33	0.17	61.5	38.5

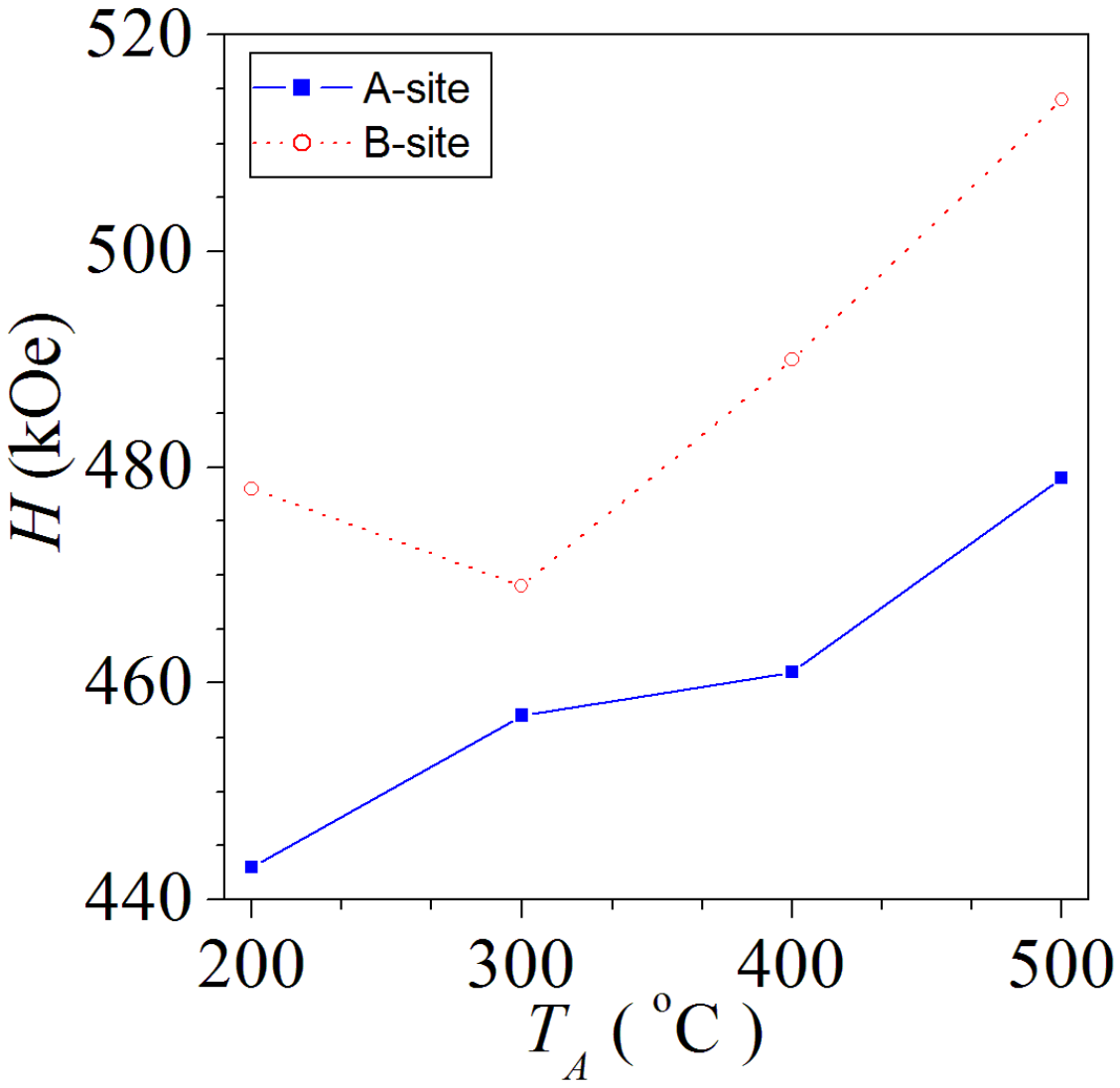

Figure 7.13: Variation of H_A and H_B with T_A for $Ba_{0.5}Co_{0.5}Fe_2O_4$ ferrite nanoparticles measured at room temperature.

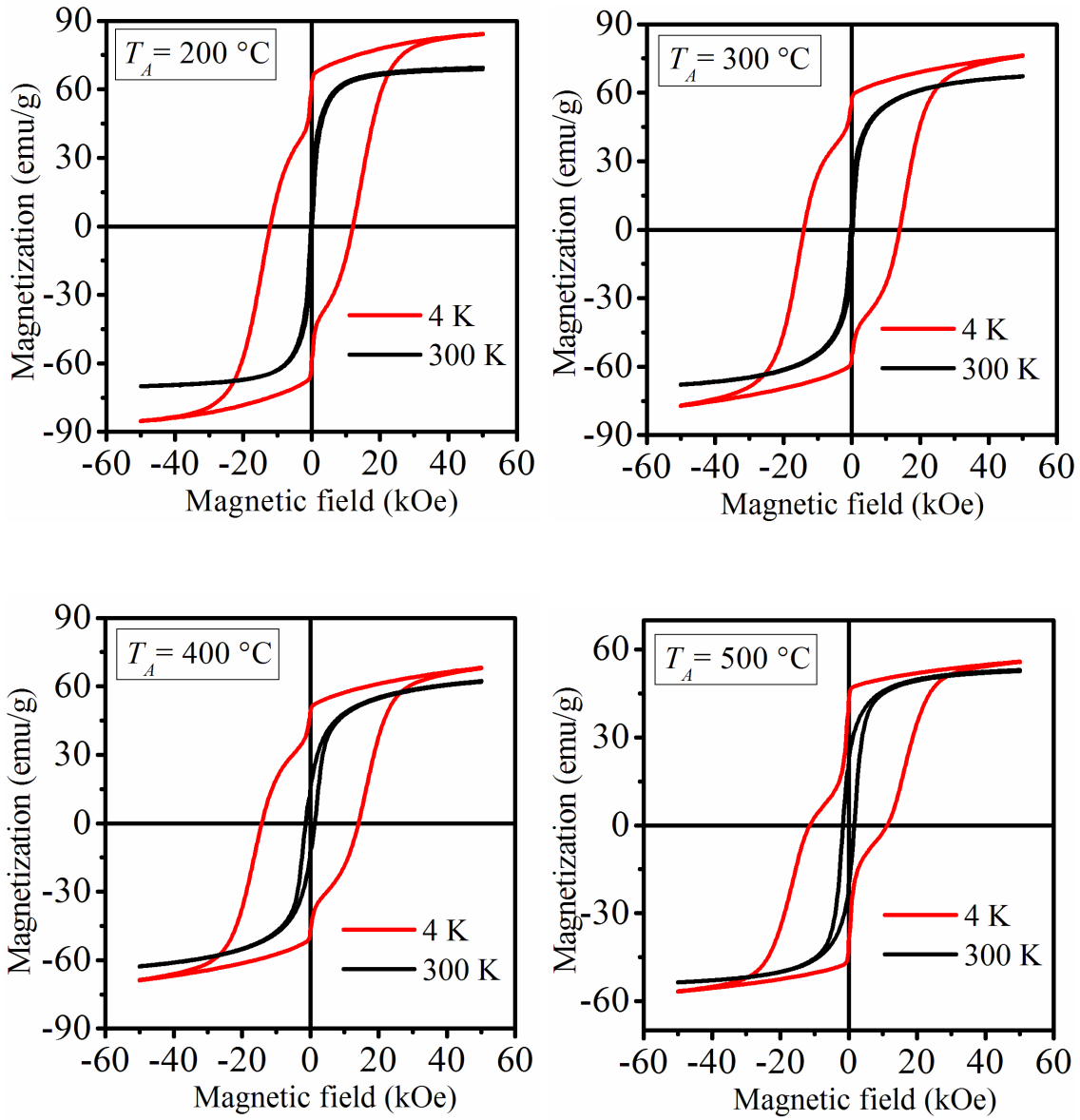

Figure 7.14: *M-H* loops at 4 K (in red) and 300 K (in black) for $Ba_{0.5}Co_{0.5}Fe_2O_4$ ferrite nanoparticles.

Table 7.4: Saturation magnetization (M_S), coercive field (H_C), remnant magnetization (M_R) and squareness of magnetization loops (M_R/M_S) for $Ba_{0.5}Co_{0.5}Fe_2O_4$ measured at 300 K.

T_A	M_S(emu/g) ±0.4	H_C(Oe) ±2	M_R(emu/g) ±1	M_R/M_S
200 °C	69.5	153	7	0.09
300 °C	66.7	779	14	0.20
400 °C	61.3	923	12	0.18
500 °C	53.2	1642	21	0.39
600 °C	39.6	802	8	0.01

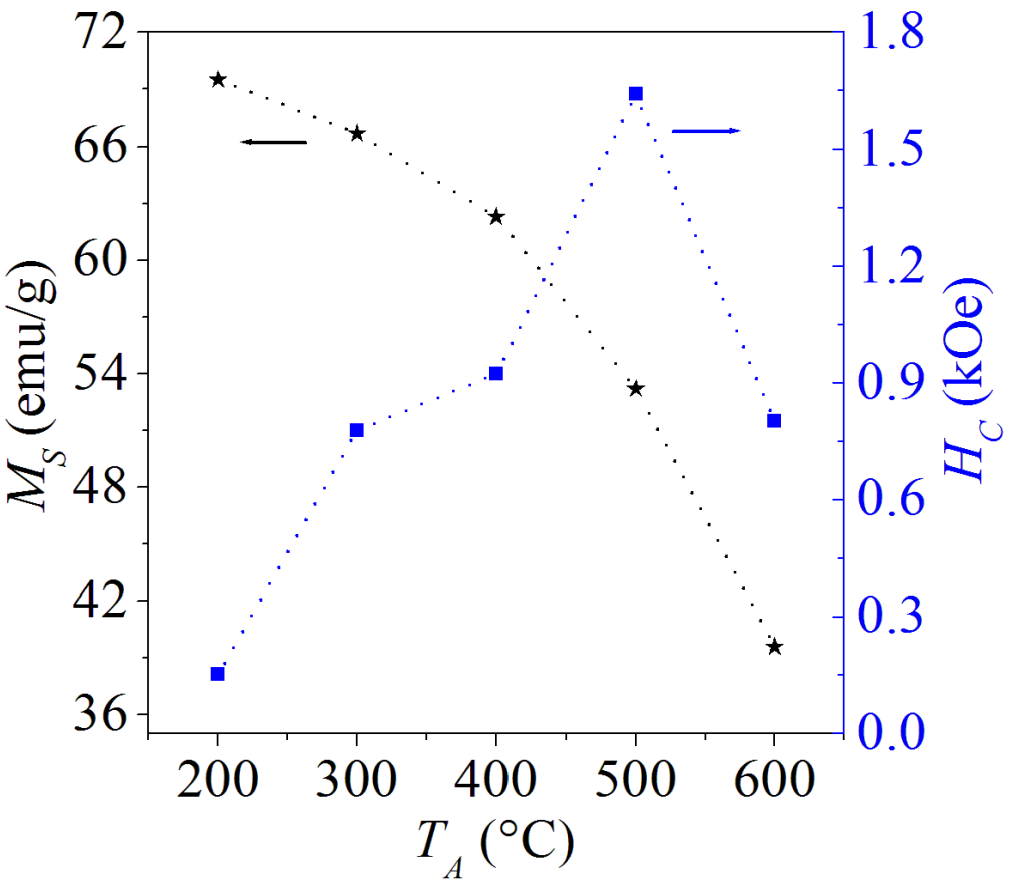

Figure 7.15: Effect of T_A on H_C and M_S at 300 K for $Ba_{0.5}Co_{0.5}Fe_2O_4$ ferrite nanoparticles.

The decrease in M_S can be attributed to changes in the degree of inversion (transfer of Fe^{3+} ions between A and B sites) with increase in particle size [42]. In addition, uncompensated surface spins for smaller particles can cause reduction in the magnetization with increasing T_A [237]. The coercivity on the other hand, increases as T_A increases and reaches a maximum at 500 °C. This is in line with transformation from single to multi-domain structure for which H_C may rise to a maximum value at a critical particle size. The decrease in H_C for $T_A = 600$ °C can be associated with the onset of an impurity and bulk phases as indicated in the corresponding XRD pattern in Figure 7.8. The magnetization measurements also reveal the sensitivity of the properties on the measuring temperature. Figure 7.14 shows that the magnetizations measured at 4 K are much larger than at 300 K. This is attributed to contributions of the surface spins at low temperature which become less important with increase in T_A or particle size [238]. The hysteresis loops also show significant increases in the H_C and remanence magnetization (M_r) at 4 K which we associate with spin freezing effects. Some distortion of the hysteresis loops showing significant time dependence of M_r at 4 K are observed. Distortions in the hysteresis loops can arise in a magnetic material with mixed soft and hard magnetic phases with surface spin canting [229]. In Figure 7.16 we show the temperature dependence of the coercive fields $H_C(T)$ for the as-synthesized and annealed samples. For relatively wide range of measuring temperature as shown in Figure 7.16, we find that the coercive fields decrease almost linearly with increasing measuring temperature. The data were fitted according to the equation $H_C(T) = H_C(0)[1 - (T/T_B)]$. This is associated with random distribution of easy axes [174]. A linear fall off $(1-(T/T_B))$ for coercive fields has also been observed in Fe_2O_3 nanoparticles [239]. The extrapolated results from fitted curves are reported in Table 7.5. The coercive fields at $T = 0$ are found to increase by increasing the annealing temperature T_A as shown in Figure 7.17. This might be associated with the increase in particle sizes. The blocking temperature T_B also increases by increasing the annealing temperature T_A as shown in the inset of Figure 7.17 .

The temperature dependence of the remanence $M_r(T)$ is shown in Figure 7.18. In the Stoner-Wohlfarth model the squareness ratio M_r/M_S is 0.5 for non-interacting

single-domain particles with randomly oriented easy axes. The particles are assumed to interact via magnetostatic interaction when M_r/M_S is less than 0.5. The exchange interaction is assumed to dominate when the ratio M_r/M_S exceeds 0.5. M_r/M_S of 0.83 has been reported to represent particles with cubic anisotropy [240]. The inset in Figure 7.18 shows clearly that M_r/M_S values for the present set of samples are greater than 0.5 at low temperatures which signifies tendency towards cubic anisotropy, and existence of stronger exchange interactions.

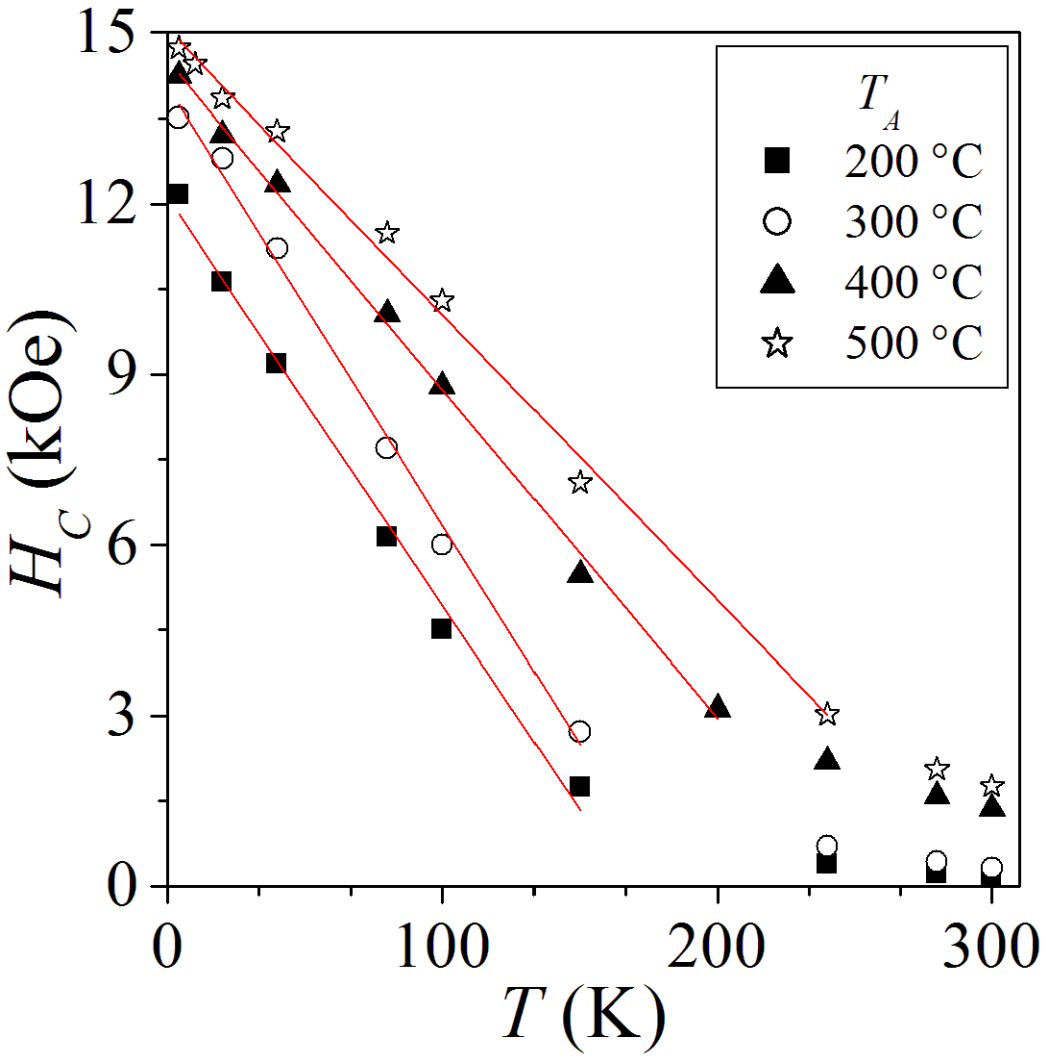

Figure 7.16: Temperature dependence of coercive fields ($H_C(T)$) for as-prepared and annealed samples of $Ba_{0.5}Co_{0.5}Fe_2O_4$ ferrite nanoparticles.

Table 7.5: The fitting parameters of coercive fields temperature dependence of the as-prepared and annealed samples of $Ba_{0.5}Co_{0.5}Fe_2O_4$ ferrite nanoparticles.

T_A	$H_C(0)$ (kOe) ±0.2	T_B (K) ±5	χ^2
200 °C	12.1	168	0.9934
300 °C	14.1	182	0.9955
400 °C	14.5	250	0.9976
500 °C	15.1	300	0.9952

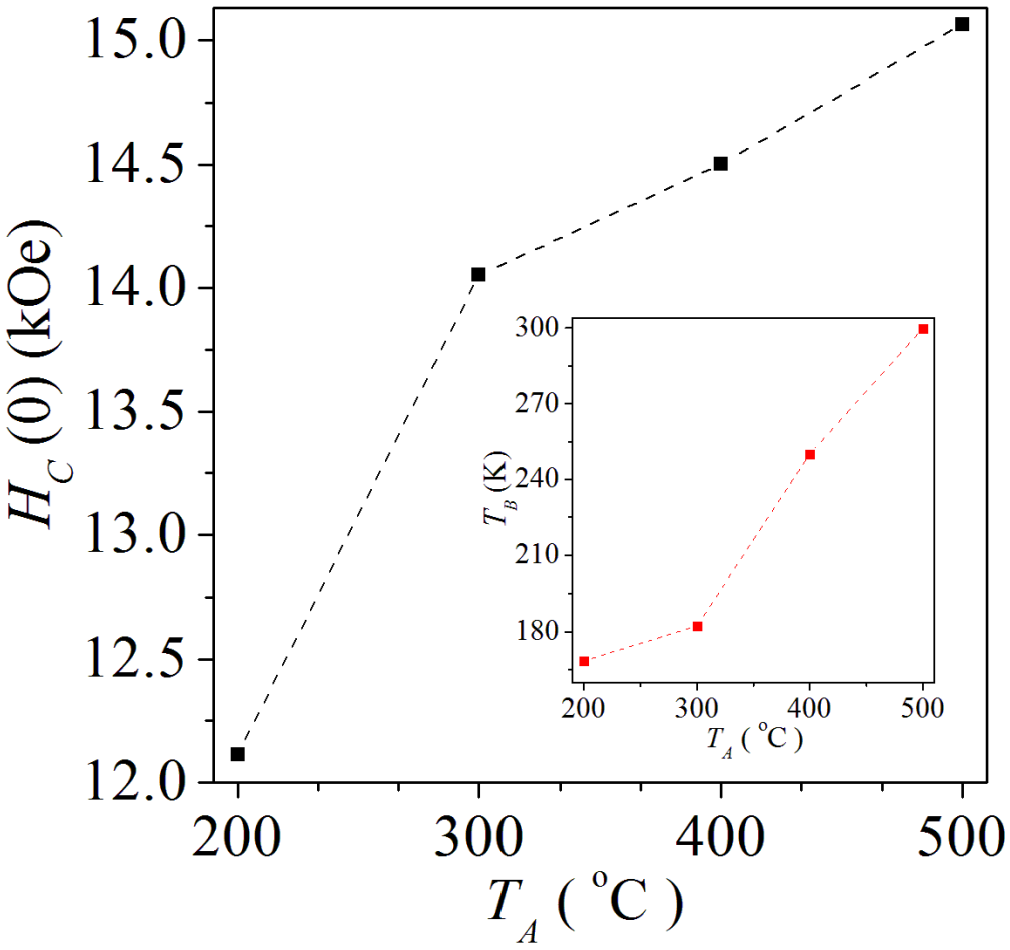

Figure 7.17: Variation of coercive fields $H_C(0)$ with the annealing temperature T_A for as-prepared and annealed samples of $Ba_{0.5}Co_{0.5}Fe_2O_4$ ferrite nanoparticles.

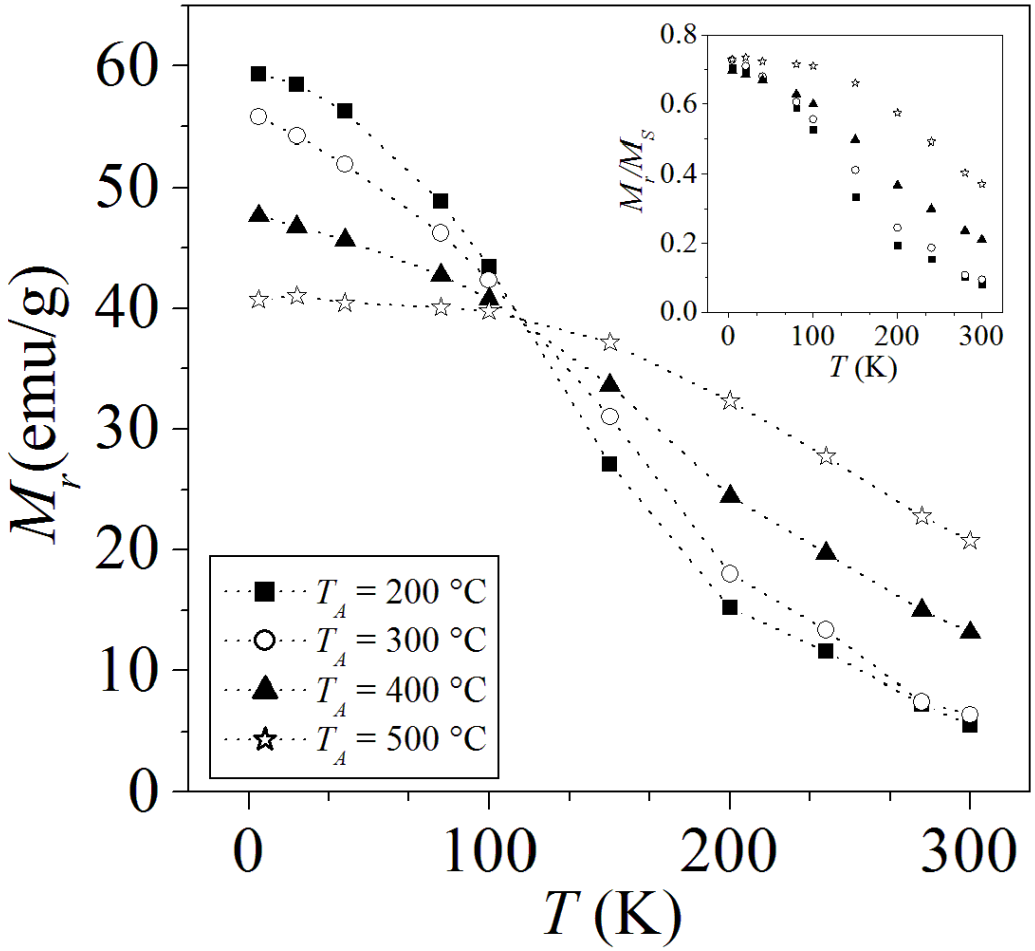

Figure 7.18: Temperature dependence of $M_r(T)$ for the $Ba_{0.5}Co_{0.5}Fe_2O_4$ samples. The inset shows the variation of M_r/M_S.

7.4.1 Electrochemical characterization

To investigate the electrochemical activity of the modified electrodes, $CoFe_2O_4$/GCE and $Ba_{0.5}Co_{0.5}Fe_2O_4$/GCE were characterized by cyclic voltammetry (CV) using K_3[Fe(CN)6] as the redox probe. Cyclic voltammograms (CVs) recorded in the presence of 1 mM K_3[Fe(CN)6] in 0.1 M KCl solution showed well-defined redox peaks (as depicted in Figure 7.19), with an improved voltammetric response observed at the modified electrodes as compared to bare GCE. Compared to nano $CoFe_2O_4$/GCE, the nano $Ba_{0.5}Co_{0.5}Fe_2O_4$/GCE exhibited superior electrochemical behavior with an increased peak current and a reduced peak separation potential, suggesting the enhanced catalytic activity of the $Ba_{0.5}Co_{0.5}Fe_2O_4$ nanoparticles.

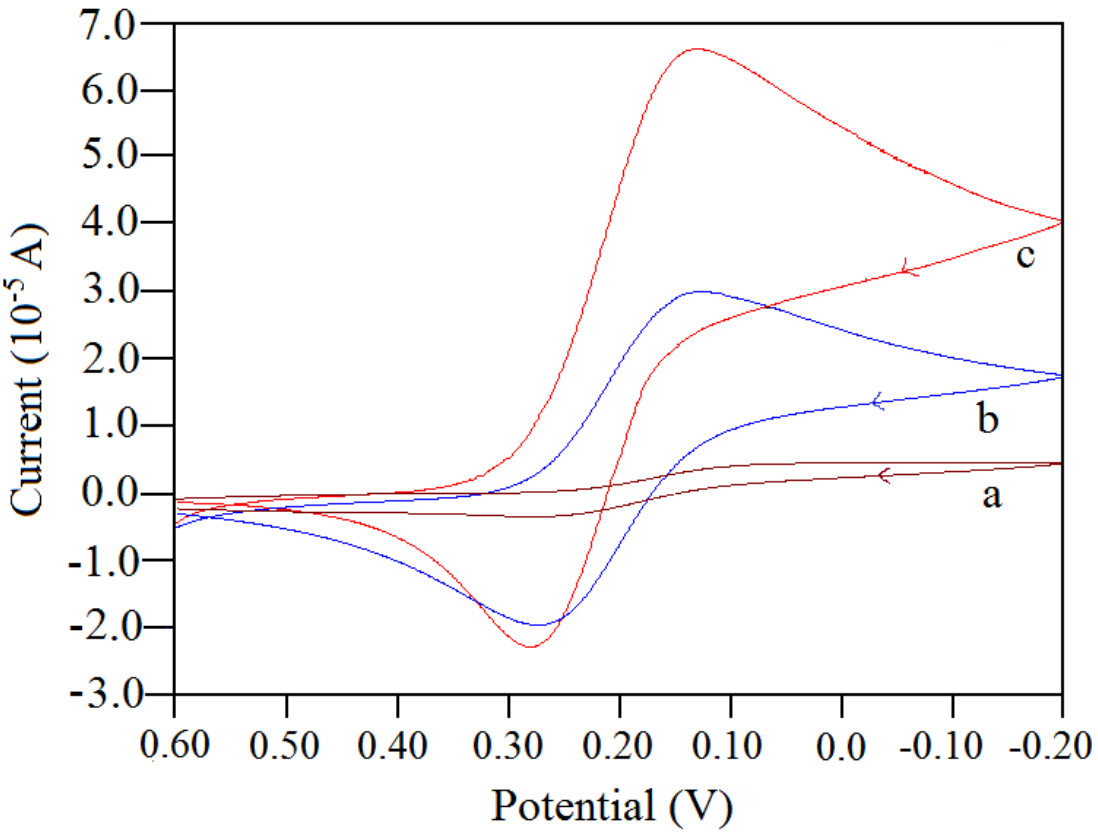

Figure 7.19: Cyclic voltammograms of 1.0 mM $K_3[Fe(CN)_6]$ in 0.1 M KCl solution at bare GCE (a), nano $CoFe_2O_4$/GCE (b) and nano $Ba_{0.5}Co_{0.5}Fe_2O_4$/GCE (c) at 5 mV/s.

In order to demonstrate that the $Ba_{0.5}Co_{0.5}Fe_2O_4$ nanoparticles improve the surface area and conductivity of the electrode, the active surface area (A) of GCE, nano $CoFe_2O_4$/GCE and nano $Ba_{0.5}Co_{0.5}Fe_2O_4$/GCE was measured by recording CVs in 1.0 mM K_3[Fe(CN)6] solution at various scan rates (Figure 7.20) and using equation $i_p = 2.69\times10^5 n^{3/2} A D^{1/2} C v^{1/2}$. Taking into account the diffusion coefficient $D = 7.6 \times 10^{-6}$ cm^2 s^{-1} for $[Fe(CN)_6]^{3-}$ [241], slope of the i_{pa} versus $v^{1/2}$ plot (inset of Figure 7.20), A was calculated to be 0.069 cm^2, 0.583 cm^2 and 0.652 cm^2 for GCE, nano $CoFe_2O_4$/GCE and nano $Ba_{0.5}Co_{0.5}Fe_2O_4$/GCE, respectively. The electroactive surface area of nano $Ba_{0.5}Co_{0.5}Fe_2O_4$/GCE is almost 10 times larger compared to the unmodified electrode, indicating superior conductivity of the $Ba_{0.5}Co_{0.5}Fe_2O_4$ nanoparticles.

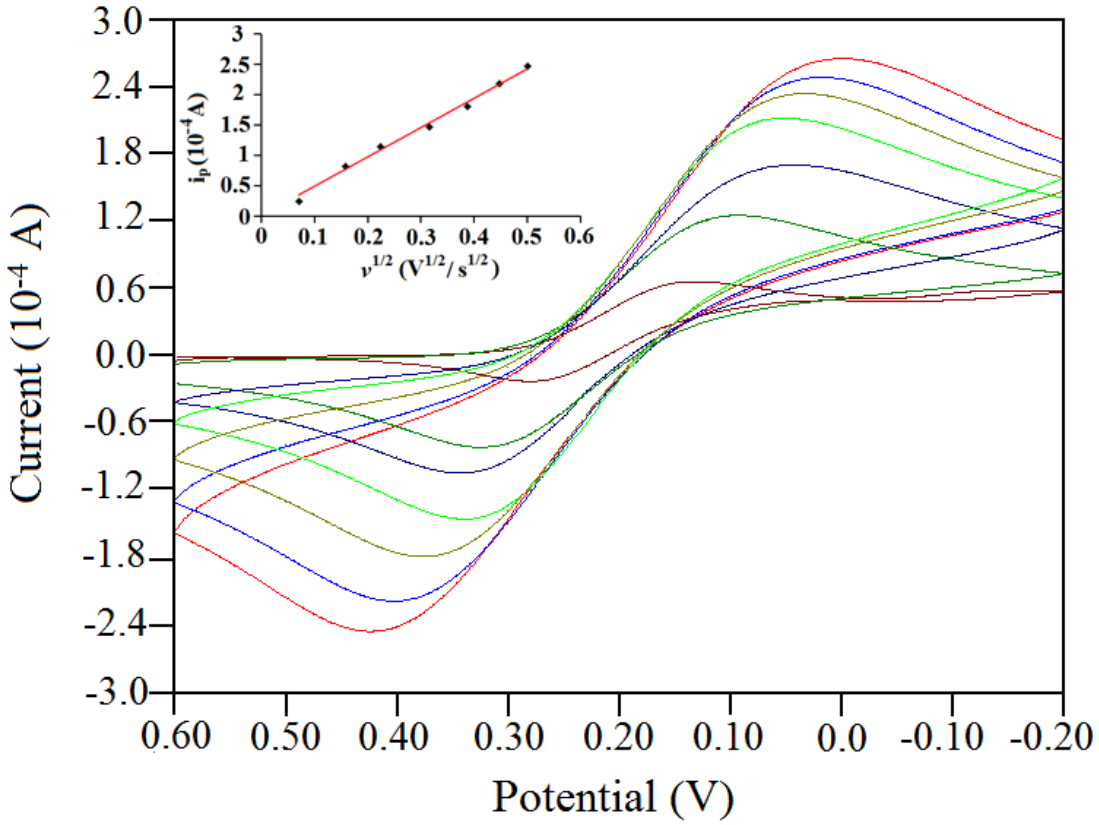

Figure 7.20: Cyclic voltammograms of 1.0 mM $K_3[Fe(CN)_6]$ in 0.1 M KCl solution at nano $Ba_{0.5}Co_{0.5}Fe_2O_4$/GCE at scan rates 5-250 mVs^{-1} (Inset shows plot of scan rate versus peak current).

7.4.2 Electrochemical behavior of CFX

The electrochemical behavior of the ciprofloxacin (CFX) was investigated at bare GCE, $CoFe_2O_4$/GCE and $Ba_{0.5}Co_{0.5}Fe_2O_4$/GCE in presence of 0.3 mM CFX in 0.1 M phosphate buffer solution (PBS) using CVs (Figure 7.21). A very weak oxidation peak at $\sim$ 1.1 V was observed at bare GCE (curve a, brown). Under similar conditions, at nano $CoFe_2O_4$/GCE, the peak potential was found to shift negatively to 1.0 V (curve b, green) accompanied by an enhanced peak current. However, this peak was broad and not very distinct. On the other hand, the voltammogram for nano $Ba_{0.5}Co_{0.5}Fe_2O_4$/GCE exhibited a well defined oxidation peak at 0.9 V (curve c, red). The decrease in the peak potential and the increased anodic peak current suggest that the synthesized nanoparticles effectively catalyze the electrochemical oxidation

of CFX. The electrocatalytic activity of the nano $Ba_{0.5}Co_{0.5}Fe_2O_4$/GCE was ascribed to an improved electron transfer rate, which we associate with the high surface area and significant electrical conductivity of the $Ba_{0.5}Co_{0.5}Fe_2O_4$ nanoparticles. Porosity in nanoparticles leads to exposure of the analyte to more active surface sites and an increase in mass transport [242]. Thus, it also contributes to the enhanced electrocatalytic efficiency of the nanoparticles. Hence, nano $Ba_{0.5}Co_{0.5}Fe_2O_4$/GCE was chosen for further electrochemical studies on CFX. No peaks were observed in the reverse scan showing the irreversible nature of the electrooxidation process.

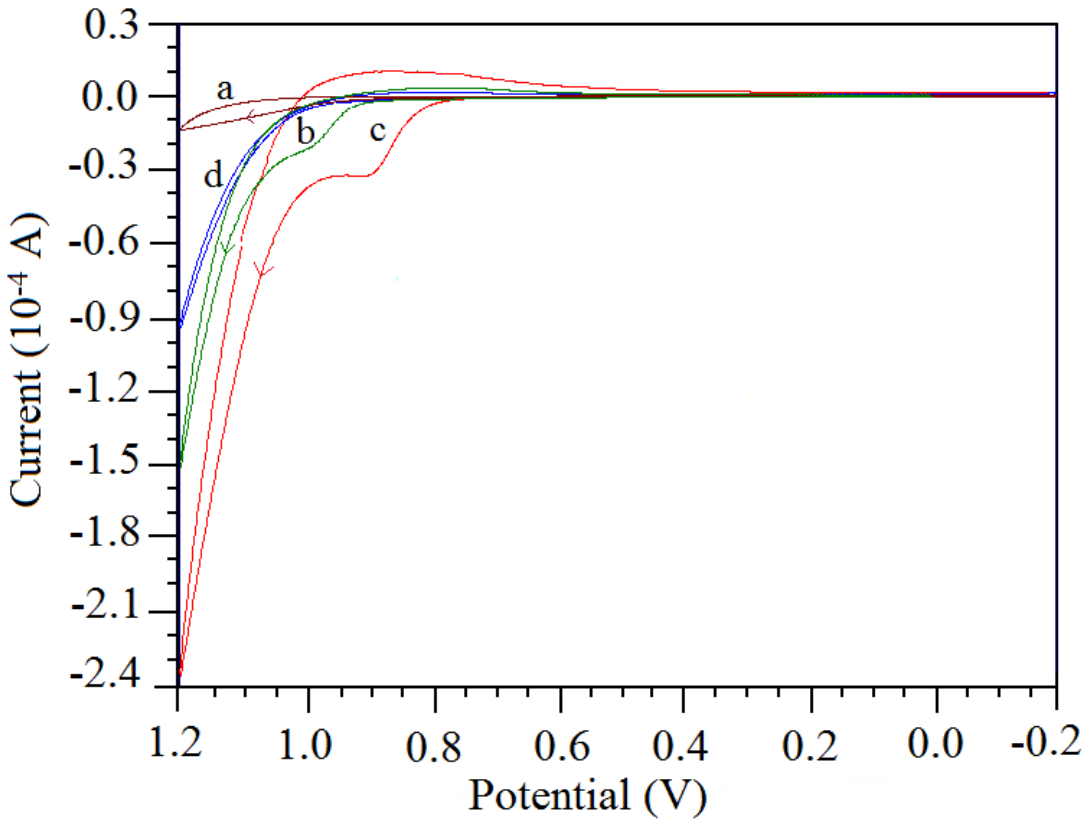

Figure 7.21: Typical cyclic voltammograms observed in presence of 0.3 mM CFX in 0.1 M PBS (pH 7.2) at (a) bare GCE, (b) nano $CoFe_2O_4$/GCE, (c) nano $Ba_{0.5}Co_{0.5}Fe_2O_4$/GCE and (d) in absence of CFX in 0.1 M PBS (pH 7.2) at nano $Ba_{0.5}Co_{0.5}Fe_2O_4$/GCE.

The effect of scan rate on the peak current was examined to identify the nature of the electrochemical process taking place at the electrode surface. The voltammetric behavior of 0.3 mM CFX in 0.1 M PBS (pH 7.2) was observed at various scan rates

(5 mV/s to 200 mV/s) using cyclic voltammetry to check whether the oxidation process at the modified electrode was diffusion or adsorption controlled. A linear relationship was observed between the peak current (i_p) and the square root of scan rate ($v^{1/2}$) with a correlation coefficient of 0.9966, suggesting that the oxidation of CFX at nano $Ba_{0.5}Co_{0.5}Fe_2O_4$/GCE was a diffusion-controlled process (Figure 7.22 A) with the equation expressed as $i_p = (0.52\pm0.01)v^{1/2}$ - (0.2±0.1). The presence of a non-zero y-axis intercept indicates the presence of some associated adsorption at the electrode surface [243]. A linear relationship between i_p and log v (Figure 7.22 B) was observed corresponding to the equation $i_p = (0.54\pm0.01)$log v - (0.39±0.01) with a correlation coefficient of 0.9987. A slope of 0.54±0.01 was obtained, which is close to the theoretical value of 0.5 expected for an ideal reaction for a diffusion-controlled electrode process [244], thus confirming that the oxidation process was diffusion controlled.

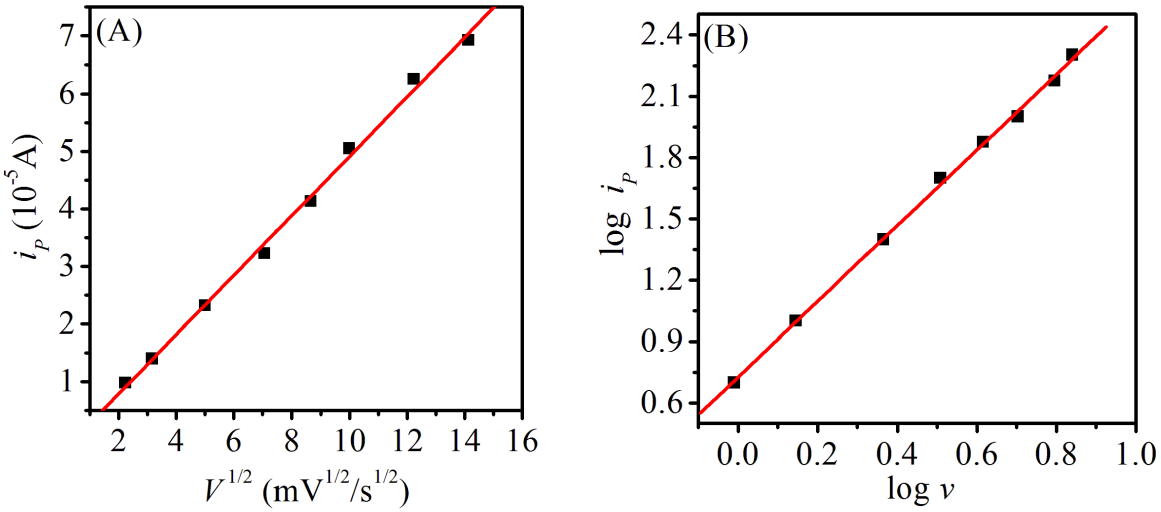

Figure 7.22: (A) Variation of peak current (i_p) with square root of scan rate (v$^{1/2}$) and (B) Dependence of logarithm of peak current on the logarithm of scan rate for 0.3 mM CFX in 0.1 M PBS (pH 7.2) at nano $Ba_{0.5}Co_{0.5}Fe_2O_4$/GCE.

Furthermore, the peak potential (E_p) was found to shift towards more positive values with an increase in the scan rate indicating the irreversible nature of the electrochemical process. On plotting E_p (in V) versus log v, a linear plot with the equation $E_p = (0.033\pm0.003)$ log v + (0.845±0.001) and a correlation coefficient of

0.9995 was obtained (Figure 7.23), which shows that the electrochemical reaction is followed by an irreversible chemical step [245].

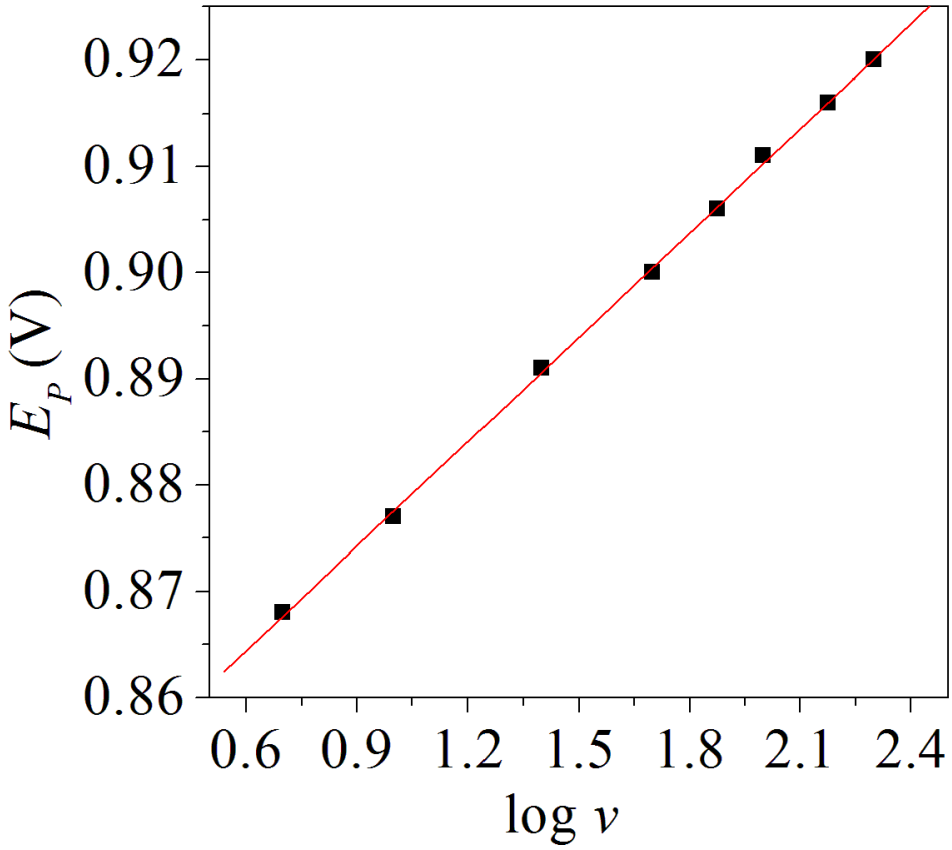

Figure 7.23: Dependence of peak potential on the logarithm of scan rate for 0.3 mM CFX in 0.1 M PBS (pH 7.2) at nano $Ba_{0.5}Co_{0.5}Fe_2O_4$/GCE.

According to Laviron [161], the E_p for an irreversible electron transfer can be expressed by the equation 4.4.4 where $E_p = E^0 + \left[\frac{2.303RT}{\alpha nF}\right] \log \left[\frac{RTk^0}{\alpha nF}\right] + \left[\frac{2.303RT}{\alpha nF}\right] \log v$. From the slope of E_p versus log v plot, the value of αn can easily be calculated. Here, the slope is 0.033±0.003 V. Considering $T = 298$ K, $R = 8.314$ J/K mol, and $F = 96480$ C/mol, αn is calculated to be 1.8. This value is then employed to calculate n using the equation 4.4.5 [162]. The number of electrons exchanged n is found to be 2, indicating that two electrons were involved in the oxidation of CFX at the nano $Ba_{0.5}Co_{0.5}Fe_2O_4$/GCE. In order to investigate the effect of pH on the electrooxidation of CFX, CVs were recorded at a fixed concentration of the drug in pH range 3.0-10.0 (0.1M PBS). The peak potential (E_p) was found

to shift linearly to a less positive value with increase in the solution pH. The dependence of E_p (in V) on pH is expressed by the equation E_p = 1.3154 - 0.0606 pH with a correlation coefficient of 0.9839. The slope of 60.6 mV indicates that equal numbers of protons and electrons participated in the electrochemical process. Thus, the study confirms that the electrooxidation of CFX involves two protons and two electrons, as shown in Figure 7.24 [219].

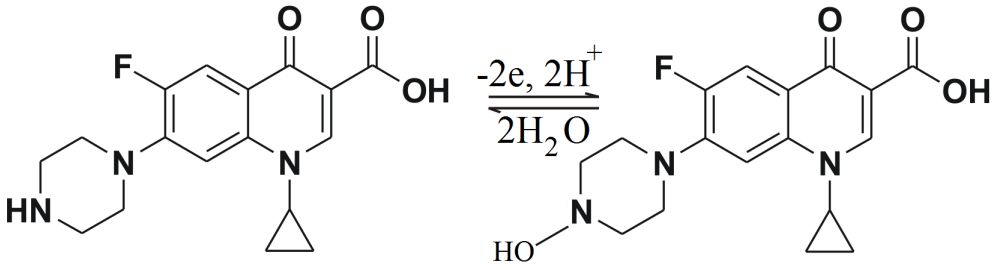

Figure 7.24: Scheme illustrates electrooxidation mechanism of CFX.

Quantitative evaluation of an analyte is based on the linear correlation between the observed peak current and the analyte concentration. The calibration curve for CFX was obtained using linear sweep voltammetry (LSV). The oxidation peak current (peak height) was found to be proportional to CFX concentration in the range 1.0×10^{-8} M to 0.5×10^{-3} M as shown in Figure 7.25 and the linear equation is $i_p(10^{-5}\text{ A}) = 10.23C$, where C is the concentration of CFX (in mM). The detection limit (LOD) and limit of quantification (LOQ) was found to be 0.58×10^{-8} M and 1.95×10^{-8} M, respectively.

In order to assess the specificity of the sensor towards CFX, the effect of excipients on the voltammetric response of the drug was investigated. Samples containing 0.01 mM CFX and different concentrations of the excipients (starch, colloidal anhydrous silica, cellulose and magnesium stearate) were analysed using the proposed procedure. The voltammetric response of CFX in the presence of excipients was compared with that of the pure drug. The assay result did not display any change, showing that the proposed sensor has good selectivity for CFX determination. To check the reproducibility of the nano $Ba_{0.5}Co_{0.5}Fe_2O_4$/GCE, a series of four electrodes fabricated in a same manner were employed for the detection of 0.01 mM

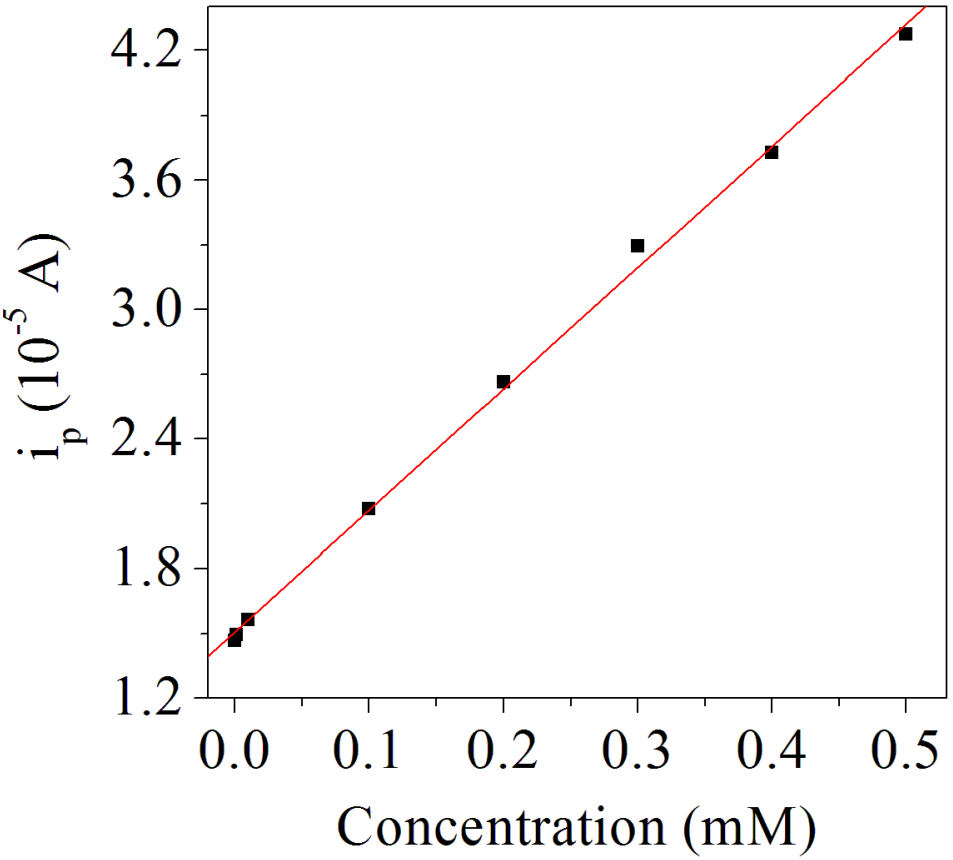

Figure 7.25: Observed dependence of peak current (i_p) on CFX concentration at pH 7.2 (0.1 M PBS) at nano $Ba_{0.5}Co_{0.5}Fe_2O_4$/GCE.

CFX in 0.1 M PBS (pH 7.2). A relative standard deviation (RSD) of the peak current values obtained at the four electrodes was 3.3%, suggesting good reproducibility of the proposed electrode. To evaluate the precision of the method, the analytical performance was observed for six repeated measurements of 0.01 mM CFX solution. A RSD of 2.4% confirmed the good precision of the method. The LSV response of the modified electrode was also investigated after 7 days for the same drug concentration, during which the peak current did not vary much indicating appreciable stability of the nano $Ba_{0.5}Co_{0.5}Fe_2O_4$/GCE.

In order to investigate the feasibility of the developed procedure, the proposed method was successfully applied for direct analysis of the drug in different pharmaceutical preparations without the need for sample pretreatment or time-consuming extraction steps prior to the analysis. The quantity of CFX was determined in two

different formulations, i.e. Ciprodac 500 (Mfd. by Cadila Pharmaceuticals Ltd.) and Ciprocore (Mfd. by Core Healthcare). The tablets were weighed, grinded in a mortar and the obtained powder was dissolved in double distilled water. The sample solution was further diluted so that the concentration of CFX was in the working range and the solution was then directly used for voltammetric analysis. The amount of CFX obtained by the proposed method in different pharmaceutical formulations was compared with the stated amount. The results, summarized in Table 7.6, show that the drug content for both assayed tablets fall within the claimed amount indicating good agreement with the proposed voltammetric method. Hence, the method can be used efficiently for CFX determination in commercial pharmaceutical dosage forms.

Table 7.6: Determination of CFX in different pharmaceutical formulations using nano $Ba_{0.5}Co_{0.5}Fe_2O_4$/GCE.

Sample	Stated content (mg/tablet)	Detected content* (mg/tablet)	R.S.D	LOD (M)	LOQ (M)
Ciprodac 500	500	503.5	0.6%	6.0×10^{-9}	2.0×10^{-8}
Ciprocore	500	506.5	1.3%	6.3×10^{-9}	2.1×10^{-8}

*Amount found represents the average of three observations.

The electroanalytical performance of the present method for $Ba_{0.5}Co_{0.5}Fe_2O_4$/GCE was compared with that of voltammetric methods reported (since 2007 to present) for CFX quantification, as summarized in Table 7.7. It can be seen from the table that the proposed method is superior to previously reported electrochemical methods, in terms of linear concentration range and detection limit. The ease of preparation of the modified electrode, simplicity of the procedure, low cost of analysis, good reproducibility, remarkable detection limit and analytical applicability of the proposed method offers a promising substitute to the frequently reported chromatographic methods for determination of CFXs.

Table 7.7: A comparison of analytical parameters for voltammetric determination of CFX at various modified electrodes.

Electrode	Linear Concentration Range (M)	LOD (M)	LOQ (M)	Ref.
$MgFe_2O_4$-Multi-walled carbon nanotubes modified GCE.	0.1×10^{-6} to 1.0×10^{-3}	0.1×10^{-7}	0.8×10^{-7}	[219]
Carbon paste electrode (CPE) in presence of sodium dodecyl benzene sulphonate.	8.0×10^{-8} to 5.0×10^{-6}	2.0×10^{-8}	-	[246]
CPE in presence of cetyl trimethylammonium bromide.	1.0×10^{-7} to 2.0×10^{-5}	5.0×10^{-8}	-	[247]
Multi-walled carbon nanotubes modified GCE.	1.0×10^{-7} to 7.5×10^{-5}	3.0×10^{-8}	-	[248]
GCE.	1.0×10^{-6} to 4.0×10^{-5}	1.3×10^{-7}	4.3×10^{-7}	[249]
Multi-walled carbon nanotubes modified GCE.	3.0×10^{-6} to 1.2×10^{-3}	0.9×10^{-6}	-	[250]
Tyrosine modified CPE.	0.2×10^{-4} to 0.8×10^{-4}	4.5×10^{-6}	-	[251]
Hanging mercury drop electrode (HMDE).	1.5×10^{-7} to 4.5×10^{-7}	-	3.0×10^{-8}	[252]
β-cyclodextrin-l-arginine. modified CPE.	0.5×10^{-7} to 1.0×10^{-4}	0.1×10^{-7}	-	[253]
Co/TiO_2/CPE.	0.1×10^{-6} to 0.7×10^{-4}	0.3×10^{-7}	-	[254]
Glassy carbon paste electrode.	3.0×10^{-8} to 2.3×10^{-6}	3.3×10^{-8}	2.7×10^{-8}	[255]
Boron-doped diamond electrode.	1.0×10^{-6} to 1.0×10^{-4}	3.3×10^{-7}	1.0×10^{-6}	[256]
dsDNA modified GCE.	1.0×10^{-6} to 1.0×10^{-5}	1.0×10^{-6}	-	[257]
HMDE.	3.0×10^{-7} to 2.0×10^{-6}	7.0×10^{-9}	-	[258]
Poly(alizarin red)/graphene composite film modified GCE.	0.4×10^{-7} to 1.2×10^{-4}	0.1×10^{-8}	-	[259]
Nano $Ba_{0.5}Co_{0.5}Fe_2O_4$/GCE (Proposed method).	1.0×10^{-8} to 0.5×10^{-3}	5.8×10^{-9}	1.9×10^{-8}	Present work

7.5 Conclusion

The Ba atoms were successfully incorporated into the spinel structure by the chemical route using the glycol thermal process. The XRD pattern suggests that $Ba_{0.5}Co_{0.5}Fe_2O_4$ ferrite nanoparticles were produced without any impurity. The images obtained from HRTEM and HRSEM display cubic shape-like particles with well defined crystalline structure, in support of the XRD results. The nanoparticles exhibited a high surface area and showed high mesoporous character, as confirmed by BJH test. Furthermore, the electrochemical sensing behavior of the novel nanoparticles was demonstrated by successful exhibition of the electrocatalytic activity of the nano $Ba_{0.5}Co_{0.5}Fe_2O_4$/GCE towards CFX oxidation, suggesting that the nanoparticles promote a higher rate of electron transfer. The proposed method was found to be simple, accurate, precise, specific and inexpensive for the determination of CFX in bulk as well as in tablet dosage forms. Thus, it is expected that the synthesized novel nanoferrites can lead to the development of a new group of electrochemical sensors. The influence of the annealing at different temperatures on the structure and the morphology of the samples was investigated by XRD, HRSEM and HRTEM. Increasing T_A leads to enhanced sample crystallinity up to 500 °C. An additional phase appears at $T_A = 600$ °C. The hyperfine parameters obtained from Mössbauer spectrum show that the samples are sensitive to T_A. The magnetic measurement at 300 K revealed a decrease of the saturation magnetization with increasing T_A, whereas the coercivity increased as T_A increased up to 500 °C. The magnetization as a function of measuring temperature shows evidence of spin freezing at low temperature. Based on equation 2.7.2 the temperature dependence of the coercive field for $Ba_{0.5}Co_{0.5}Fe_2O_4$ nanoferrites follows Kneller's law with $\alpha = 1$. Thermal annealing appears to affect the inversion of ions between on A and B sites, and leads to transformation from single domain to multi-domain structures.

Chapter 8

Simultaneous substitution of Ba, Mn and Co into Fe_3O_4 spinel structure: magnetic and electrochemical sensing properties of the synthesized nanoparticles towards didanosine (DDI), an anti-HIV drug

8.1 Introduction

Nanomaterials have emerged as active materials to study by researchers because of their properties due to surface area, catalytic effects and quantum size effect [260]. Recent years have also witnessed an upsurge in the study of spinel nanoferrites (SNPs) for their theoretical interests and numerous potential applications

in diverse fields such as ferrofluids, magneto-optics, spintronics, medical diagnostics, information storage systems, microwave absorbers and manufacturing anodes for batteries [229]. The magnetic properties of SNPs can be tuned by substituting different elements at spinel sub-lattices [261]. Several factors, such as purity, homogeneity and microstructure are known to affect the magnetic properties of these ferrites [262]. A number of methods for synthesis of SNPs have been reported. Some of these methods are hydrothermal, co-precipitation, electrospinning, sol-gel, combustion and conventional ceramic techniques [263]. However, the easiness and higher control of particle sizes by wet chemistry method makes this method preferable compared to solid state reaction techniques [264]. SNPs have also been found to exhibit advantages towards electrochemical detection in a wide range of analytes due to their distinctive electrical and catalytic properties [223, 265]. Research is in progress to improve their electrochemical sensing ability to the maximum possible extent. Adding dopants to ferrites is shown to vary their electronic conductivity and thus extending their application in the field of electroanalysis [266].

In this chapter, we have synthesized novel single phase spinel structured $Ba_{1/3}Mn_{1/3}Co_{1/3}Fe_2O_4$ ferrite nanoparticles and investigated the structure and properties of the nanomaterial obtained. The presence of magnetic ions in the sample has led us to investigate its magnetic properties. Literature survey reveals that iron-based magnetic nanoparticles can act as excellent materials for electrode modification in electroanalysis owing to their unique properties such as large surface area and high surface energy [267, 268]. Magnetic nanoparticles have also been found to function as electron-conducting pathways allowing rapid transfer of electrons between the redox system and the electrode surface [269, 270]. This information motivated us to study the electrochemical properties of the newly synthesized magnetic $Ba_{1/3}Mn_{1/3}Co_{1/3}Fe_2O_4$. The work further investigates the electrochemical sensing ability of the synthesized nanoparticles towards didanosine (DDI), an anti-HIV drug.

Didanosine (2',3'-dideoxyinosine, DDI) (Figure 8.1) is a purine nucleoside analogue, which is used to treat human immunodeficiency virus (HIV) infection as part of highly active antiretroviral therapy (HAART) [271]. Approved in 1991 by the Food and Drug Administration (FDA), it belongs to a class of antiretroviral drugs

called nucleoside reverse transcriptase inhibitors (NRTIs) [272].

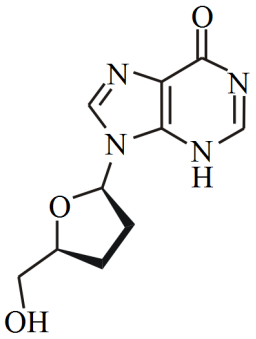

Figure 8.1: Scheme illustrates the chemical structure of didanosine.

Adverse effects of the drug include peripheral neuropathy, pancreatitis, retinal changes, optic neuritis and lactic acidosis [273]. Determination of DDI is very important for quality control and obtaining the optimal therapeutic drug concentration. A number of analytical methods have been reported for the estimation of the drug, with the majority of them involving high-performance liquid chromatography and spectrophotometric techniques, which are expensive as well as time-consuming [274, 275, 276, 277]. Due to their high sensitivity, specificity, low cost of instrumentation and simplicity, the electroanalytical methods have proved to be expedient for quantitative analysis of several drugs in bulk, pharmaceutical formulations and biological fluids. However, to date, very few voltammetric methods have been reported for DDI determination. Ozoemena *et al.* [278] fabricated electrochemical sensors, based on metallopthalocyanine (MPc, M = Co, Fe) complexes impregnated carbon paste electrode to determine the drug. Later, Farias *et al.* [279] developed an adsorptive stripping method for the quantification of DDI at a mercury film electrode. Metal ferrite nanoparticles therefore show promising application in the field of electroanalysis [223]. Hence, in the present study, a novel electrochemical sensor based on the $Ba_{1/3}Mn_{1/3}Co_{1/3}Fe_2O_4$ nanoparticles modified glassy carbon electrode was developed for sensitive determination of DDI. The electrochemical behavior of the drug was studied using cyclic voltammetry (CV) and the modified electrode was validated for quantification of the drug in human urine samples.

8.2 Experimental details

$Ba_{1/3}Mn_{1/3}Co_{1/3}Fe_2O_4$ nanoparticles were synthesized by the glycol-thermal method in a Watlow series model PARR 4843 stirred pressure reactor. The synthesis details were provided in chapter 4. The phase and structural characterization of the sample was conducted using a Phillips X-ray diffractometer (Model: PANalytical, EMPYREAN) using CoKα radiation ($\lambda = 1.7903$ Å). The morphology and microstructure of the nanoparticles were investigated by high-resolution transmission electron microscopy (HRTEM) (Jeol_JEM-1010) and high-resolution scanning electron microscopy (HRSEM) (Ultra Plus ZEISS-FEG HRSEM instrument). The textural and porosity properties of the nanoparticles were investigated using a micrometrics tristar II 3020 instrument, with liquid N_2 as the analysis gas. A mini cryogen free magnetization measurement system (supply by Cryogenic Ltd, UK) was used to perform low temperature magnetization measurements from 4 to 300 K in magnetic fields of up to 50 kOe. For the electrochemical experiments, DDI and potassium ferricyanide were obtained from Sigma-Aldrich, USA. All other chemicals used were of analytical reagent grade and purchased from Merck (Pty) Ltd, South Africa. A stock solution (2.00×10^{-3} M) of DDI was prepared in double distilled water and stored in a dark place, when not in use. Phosphate buffer solution (PBS; $\mu = 0.2$ M) at various pH values was used as a supporting electrolyte. Pure nitrogen gas was purged into the DDI containing solution for at least 3 minutes before each experiment. The electrochemical measurements were performed on an electrochemical analyzer (Model 800B Series, CH Instruments, Inc.) and conducted in a single-compartment three-electrode glass cell, which consisted of a reference electrode (Ag/AgCl), a counter electrode (platinum wire) and a working electrode (a bare/modified glassy carbon electrode). For sample preparation, the urine samples (obtained from laboratory personnel) were diluted 100 times by phosphate buffer of pH 7.2. The dilution process helps in reducing the matrix effect [280]. The drug was then quantified in spiked human urine samples using cyclic voltammetry (CV).

Before fabrication of the modified electrode, the glassy carbon electrode (GCE) was cleaned by polishing with 0.05 micron alumina slurry on a polishing cloth for

about 30 seconds. The electrode was then rinsed thoroughly with double-distilled water and dried in air. A 0.5 mg/mL suspension of $Ba_{1/3}Mn_{1/3}Co_{1/3}Fe_2O_4$ nanoparticles in dimethyl formamide was prepared. 10.0 μL of the suspension was then cast onto the cleaned electrode surface and dried to constitute $Ba_{1/3}Mn_{1/3}Co_{1/3}Fe_2O_4$/GCE. The active surface area of bare and modified GCE was measured by recording CVs in 1.0 mM $K_3[Fe(CN)_6]$ solution at different scan rates and using equation 4.4.2 [281]. The active surface area was found to be 0.070 cm^2 and 0.218 cm^2 for bare GCE and $Ba_{1/3}Mn_{1/3}Co_{1/3}Fe_2O_4$/GCE, respectively.

8.3 Results and discussion

8.3.1 Characterization of $Ba_{1/3}Mn_{1/3}Co_{1/3}Fe_2O_4$ nanoparticle ferrites

Figure 8.2 depicts X-ray powder diffraction (XRD) patterns of $Ba_{1/3}Mn_{1/3}Co_{1/3}Fe_2O_4$ nanoparticles. The XRD pattern shows a well-defined spinel structure with no impurity peaks. The lattice parameter a was calculated using equations 4.1.1 and 4.1.2. The average crystallite size was determined using the Scherrer's equation 4.1.3. The microstrain was determined using a Williamson-Hall plot, as displayed in Figure 8.3. The distribution of the data points reflects the homogeneity of the microstrain. The lattice parameter, crystallite size and microstrain for the as-prepared $Ba_{1/3}Mn_{1/3}Co_{1/3}Fe_2O_4$ nanoparticles were found to be 0.839±0.003 nm, 8.37±0.06 nm and 0.0015±0.0001, respectively.

Figure 8.4 shows images of the as-prepared $Ba_{1/3}Mn_{1/3}Co_{1/3}Fe_2O_4$ nanoparticles, captured via high resolution transmission electron microscopy (HRTEM) and high resolution scanning electron microscopy (HRSEM). The images in (Figure 8.4A and 8.4B) show quasi-spherical like shapes which are mono-dispersived. The lattice fringes are well-defined (as seen in Figure 8.4 A), thus the particles exhibit well-formed crystalline structure. The marked spacing of 0.252 nm is anticipated to reflect 311 planes. The average particle sizes are found to be 9±2 nm. Figure 8.4C shows that the particles are well-dispersed. The HRTEM and HRSEM images in

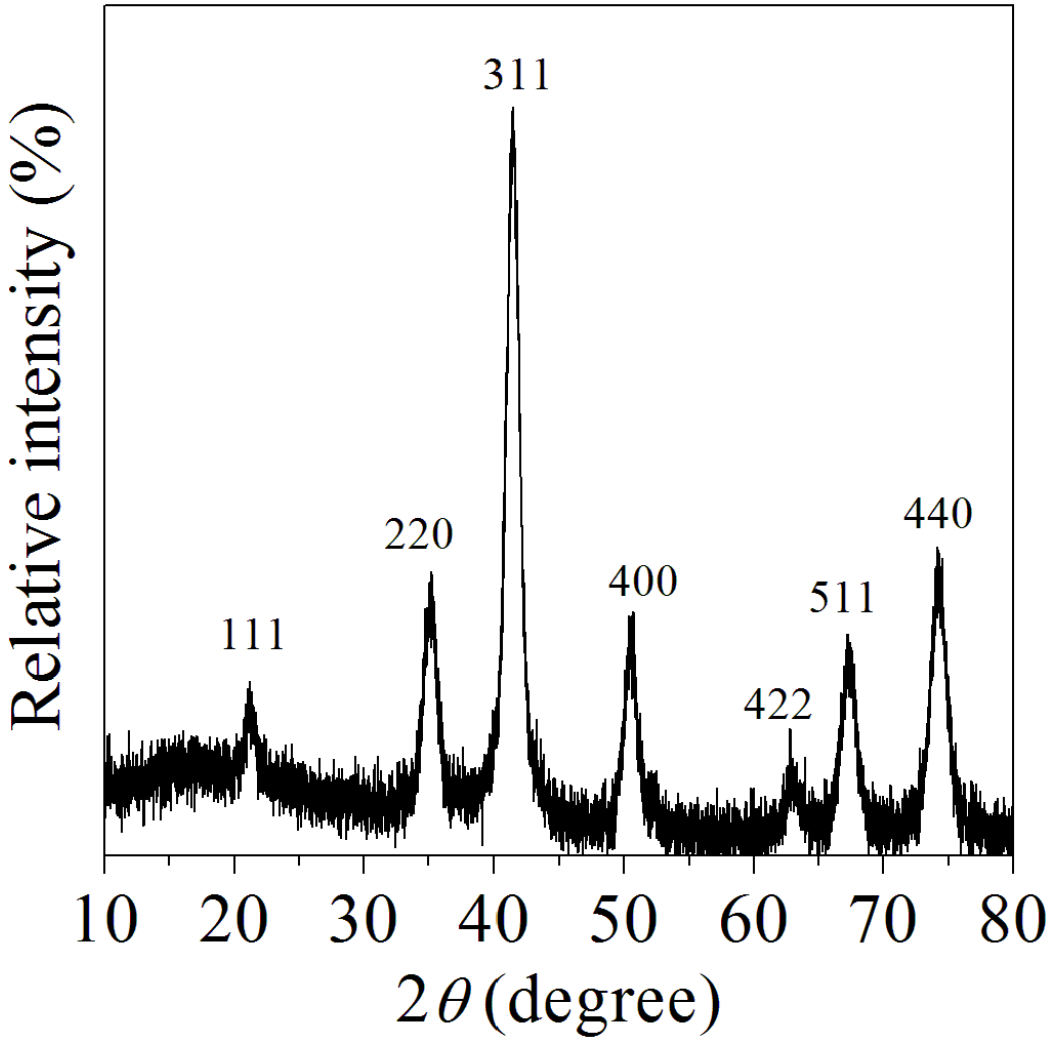

Figure 8.2: X-ray diffraction pattern for the synthesized $Ba_{1/3}Mn_{1/3}Co_{1/3}Fe_2O_4$ nanoparticles.

Figure 8.4 support the XRD result in terms of crystallinity and size of the synthesized nanoparticles.

The sample revealed high surface area of 116 m^2/g, as deduced from Brunauer-Emmet-Teller (BET) surface area measurement. The texture and character of the pores were studied using isothermal N_2 adsorption-desorption measurement. Figure 8.5 shows N_2 gas adsorption isotherms for the as-prepared $Ba_{1/3}Mn_{1/3}Co_{1/3}Fe_2O_4$ nanoparticles. The adsorption of N_2 increased to a maximum value of 222 cm^3/g at a relative pressure (P/P_0) of 99%, whilst the desorption of the gas decreased to a lowest value of 19 cm^3/g, as the P/P_0 decrease to 0.01%. The adsorption and

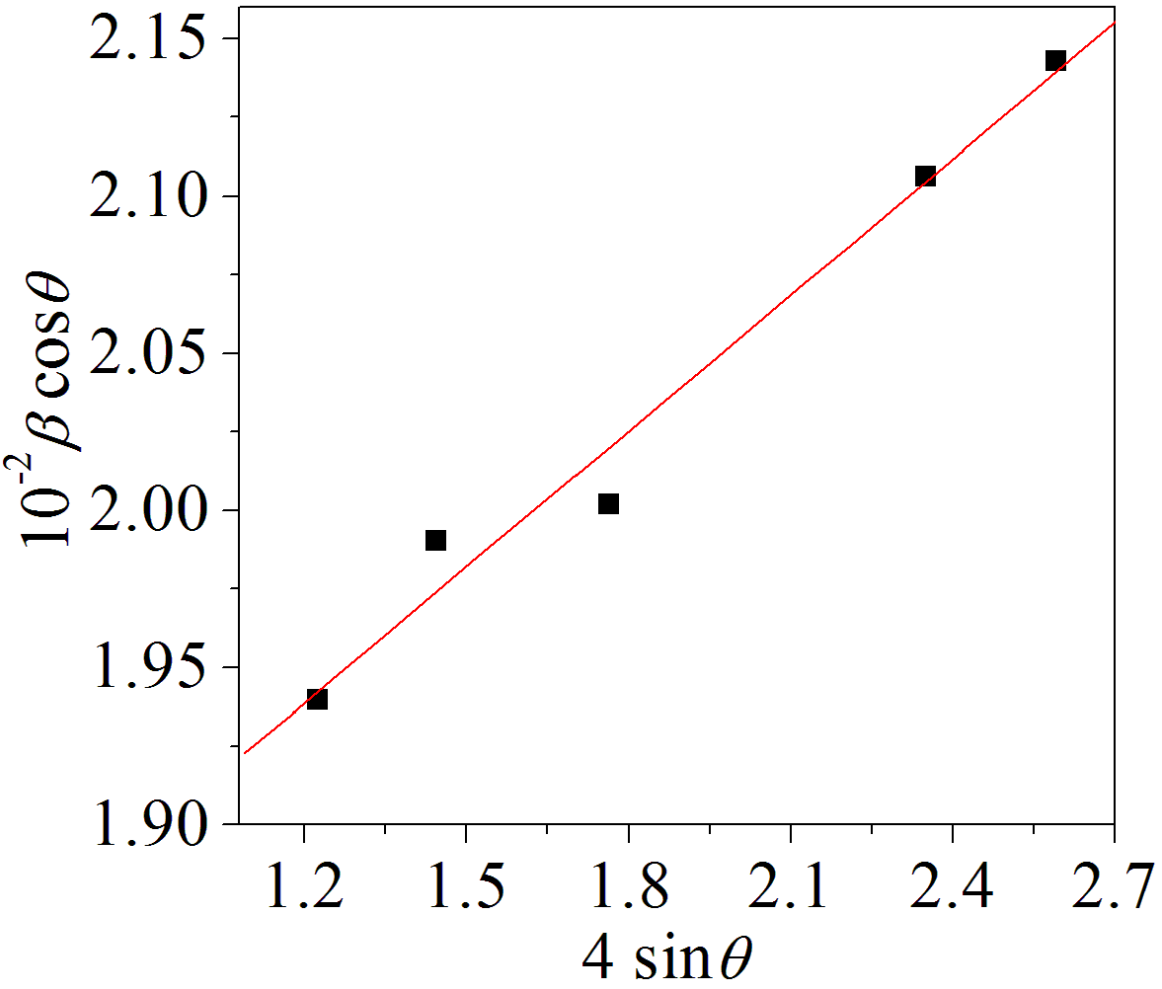

Figure 8.3: Plot of $\beta\cos\theta$ versus $4\sin\theta$ for the synthesized $Ba_{1/3}Mn_{1/3}Co_{1/3}Fe_2O_4$ nanoparticles.

desorption curves were found to merge, indicating that the hysteresis loop is associated with the N_2 condensation inside the sample pores [128]. The hysteresis loop can be classified into type IV isotherm, which suggests the mesoporous character of the sample [189]. A Barrett-Joyner-Halenda (BJH) measurement was carried out to explore the scattering of the pores. Most of the scatter points were placed in the range between 2-47 nm, further confirming the mesoporous nature of the nanoparticles [191]. Since the distribution peak of the pores is sharp (as demonstrated in the inset of Figure 8.5), it indicates homogeneous pore distribution.

Figure 8.6 depicts *M-H* loops at different measuring temperatures for the as-prepared $Ba_{1/3}Mn_{1/3}Co_{1/3}Fe_2O_4$ nanoparticles. The measurements were achieved

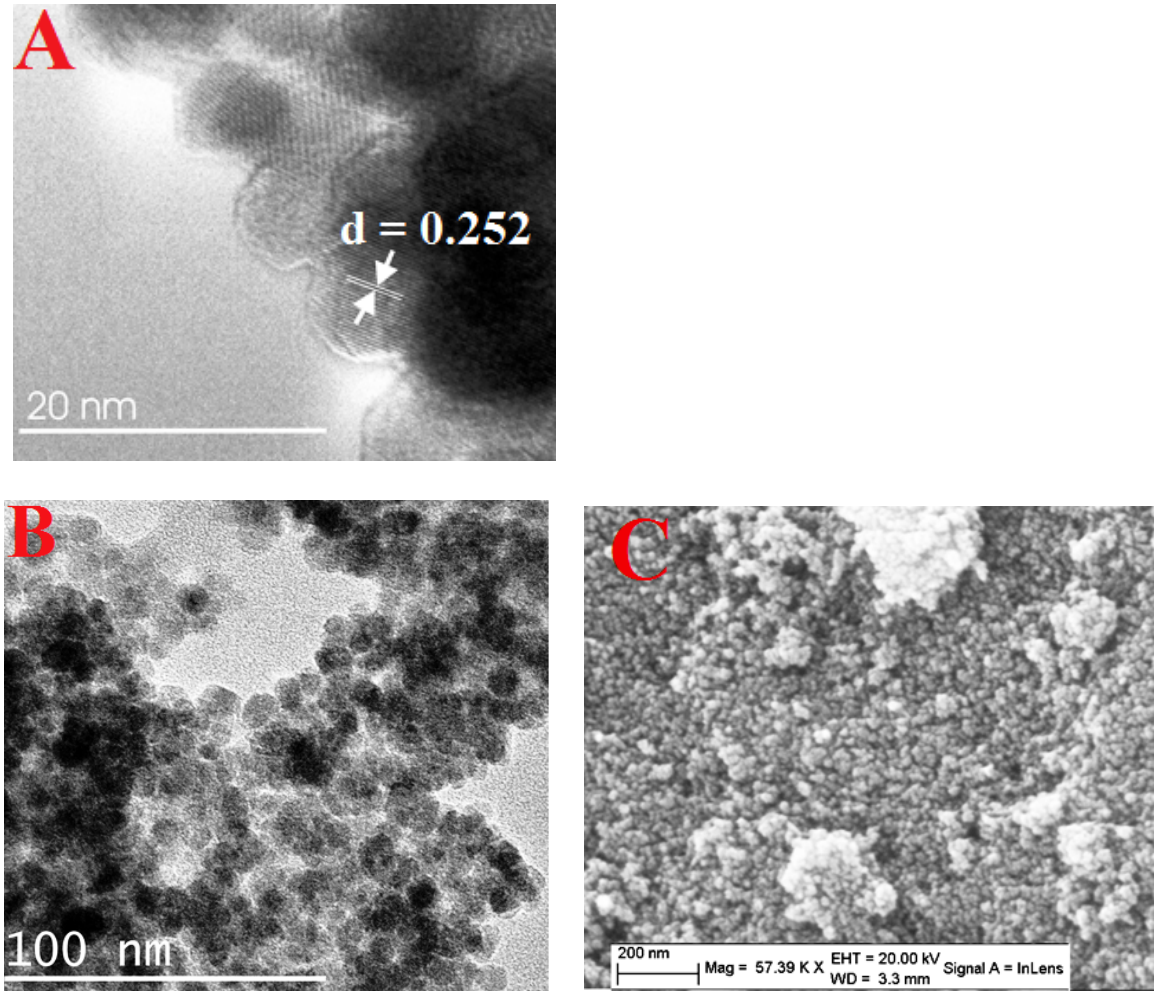

Figure 8.4: HRTEM with 20 nm magnification (A), HRTEM with 100 nm magnification (B), and HRSEM (C) images for $Ba_{1/3}Mn_{1/3}Co_{1/3}Fe_2O_4$ nanoparticles.

in external magnetic fields in the range from -50 kOe to +50 kOe. The results show an increase in the magnetization from 66.5±0.3 emu/g to 84.4±0.5 emu/g, as the measuring temperature decreased from 300 K to 4 K, respectively. The coercive field increased from 0.009±0.04 kOe to 10.10±0.04 kOe with decrease in temperature from 300 K to 4 K, respectively. The significant increase in the coercive field value with decrease in the measuring temperature indicates that the sample becomes magnetically harder at low temperature, which is related to the spin freezing effect. The sample also shows a distortion in the hysteresis loops at low temperature (as seen in Figure 8.6). This distortion is anticipated to be due to the combined effect of soft and hard magnetic phases. The spin disorder in the surface layer is

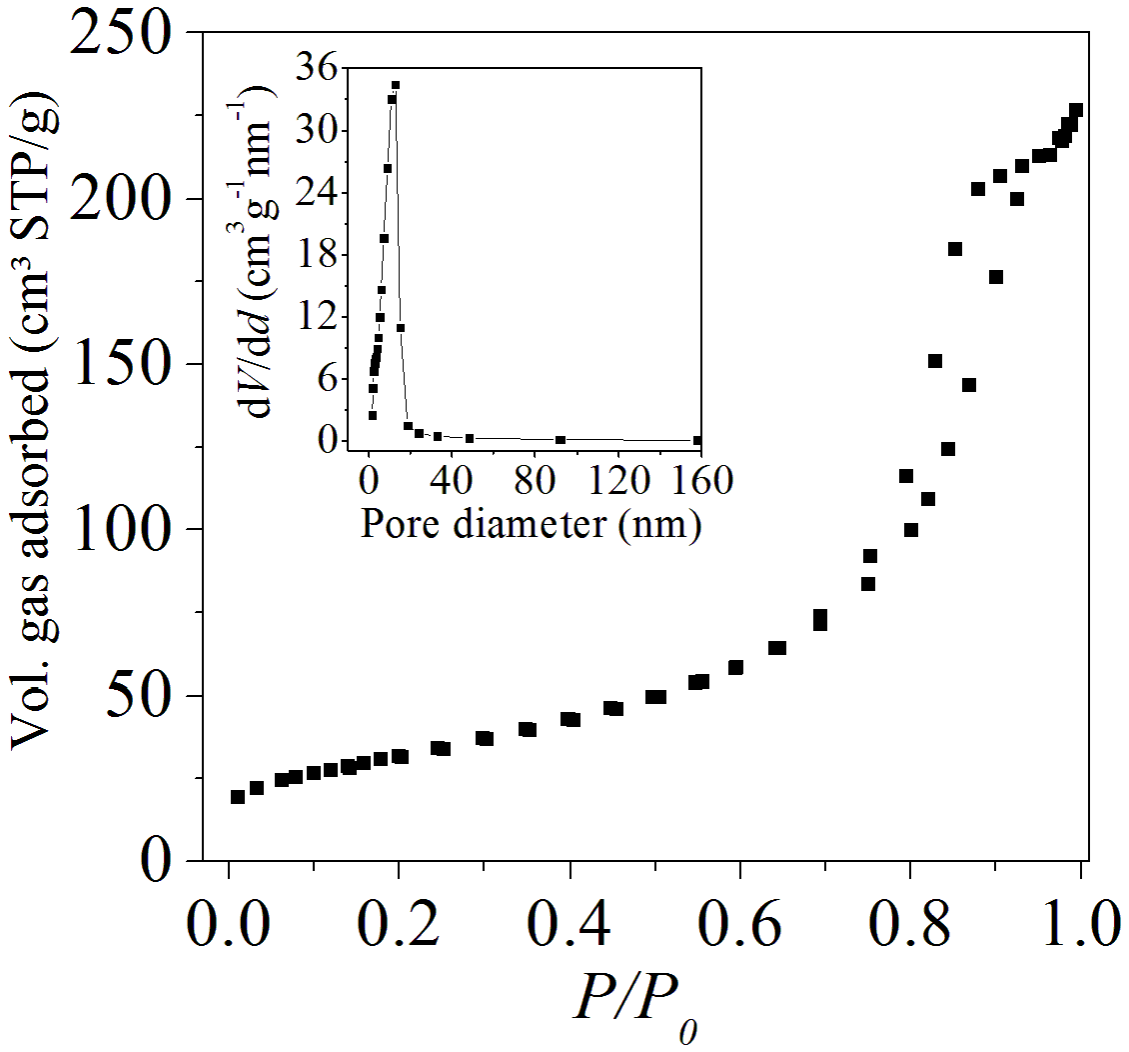

Figure 8.5: N_2 gas adsorption isotherms for the as-prepared $Ba_{1/3}Mn_{1/3}Co_{1/3}Fe_2O_4$ nanoparticles. The inset shows the pore size distribution.

also expected to lead to such behavior [282].

The approach to saturation of the magnetization M was used to obtain the values of M_S(T) as a function of the measuring temperature. Figure 8.7 exhibits the initial magnetization curves for the as-prepared $Ba_{1/3}Mn_{1/3}Co_{1/3}Fe_2O_4$ nanoparticles. The best fitting curves (in red), obtained for the initial magnetization curves of the sample, are based on the empirical law of approach to saturation magnetization given by equation 2.7.1. The magnetic parameters (maximum magnetization, saturation magnetization, coercive field, remanent magnetization and the squareness of the hysteresis loop) of the as-prepared $Ba_{1/3}Mn_{1/3}Co_{1/3}Fe_2O_4$ nanoparticles are

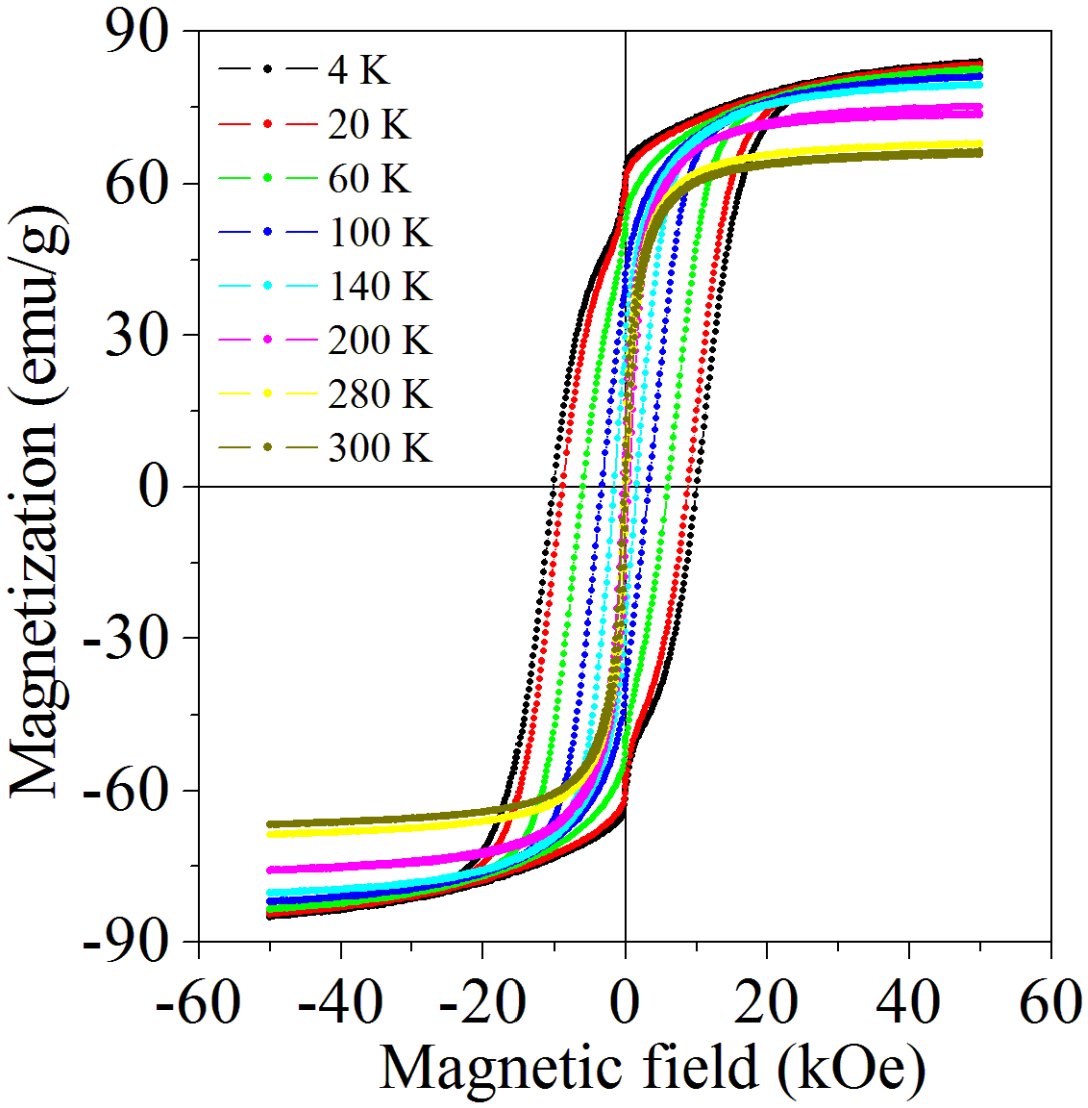

Figure 8.6: Hysteresis loops measurements at different temperature for as-prepared $Ba_{1/3}Mn_{1/3}Co_{1/3}Fe_2O_4$ ferrite nanoparticles.

summarized in Table 8.1.

The values of the remanent magnetization M_r and the squareness of the hysteresis loops M_r/Ms were found to increase dramatically with decrease in temperature. As reported in the literature [283], M_r values depend on the magnetic anisotropy, particle microstructure as well as stress sensitivity. Figure 8.8 shows that the decline in M_r is related to the reduction in the magnetic anisotropy strength. The inset in Figure 8.8 displays the variation of M_r/M_S with change in temperature. It is observed that as the temperature increases, M_r/M_S monotonically decreases. Based on

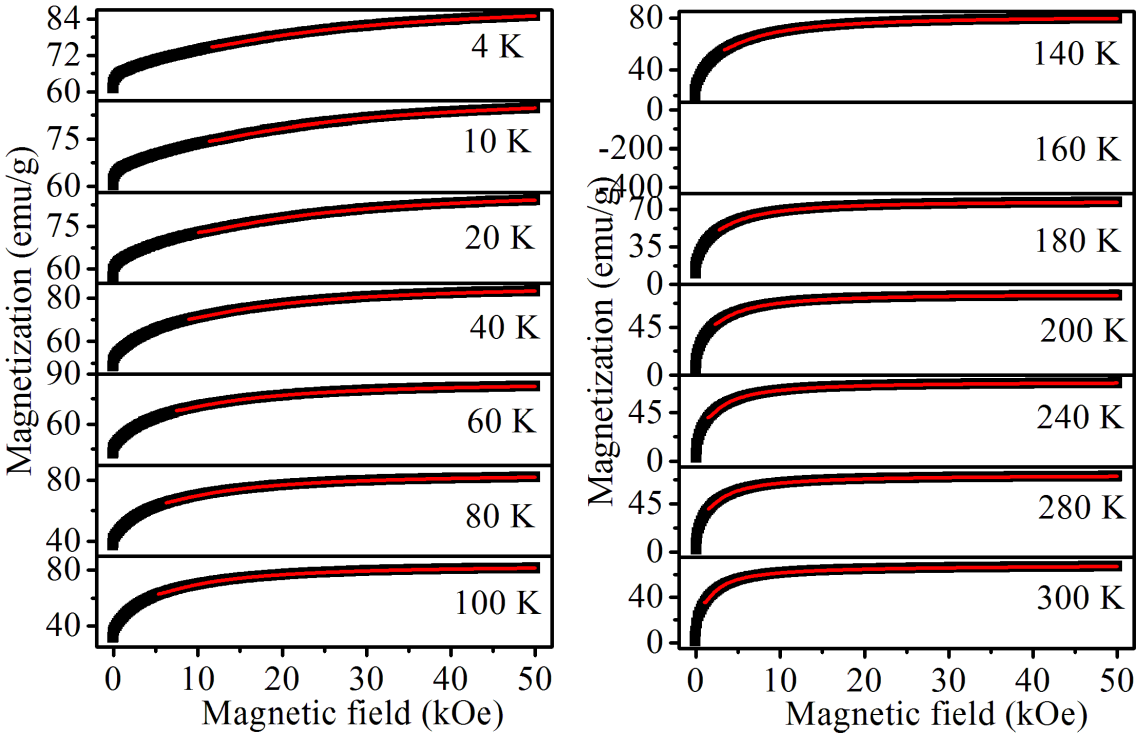

Figure 8.7: Initial magnetization curves at different temperature for as-prepared $Ba_{1/3}Mn_{1/3}Co_{1/3}Fe_2O_4$ nanoparticles.

the Stoner-Wohlfarth theory, the value of M_r/M_S for cubic and uniaxial anisotropy was found to be 0.832 and 0.5, respectively [195]. At low temperature ($T < 80$ K), the values of M_r/M_S were much higher than 0.5, as can be seen in the inset of Figure 8.8, suggesting that at low temperature the as-prepared $Ba_{1/3}Mn_{1/3}Co_{1/3}Fe_2O_4$ nanoparticles tend to have cubic magnetocrystalline anisotropy.

Figure 8.9 depicts the variation of the coercive field H_C as a function of the measuring temperature. Significant increase in H_C was observed at temperatures lower than 200 K. This was associated with the thermal oscillation of blocked moments through the anisotropy barrier [193]. The temperature dependence of H_C for non-interacting mono-domain particles in the temperature range below the blocking temperature T_B, is described by Kneller's law as in equation 2.7.2 [284]. For the modified Kneller's law, the value of α is 0.5. The H_C was found to follow T^{α} law with $\alpha = 0.77$, as reported by Pfeiffer *et al.* [129]. The Kneller's law is fitted to the data with a correlation coefficient of 0.9955. The value of $H_C(0)$, T_B and α

Table 8.1: Maximum magnetizations at 50 kOe M_m, saturation magnetizations obtained from empirical law of approach to saturation M_S, coercive fields H_C, remanent magnetizations M_r and squareness of the hysteresis loops M_r/M_S for the $Ba_{1/3}Mn_{1/3}Co_{1/3}Fe_2O_4$ nanoparticles.

T (K)	M_m (emu/g) ±0.5	M_S (emu/g) ±0.1	H_C (kOe) ±0.04	M_r (emu/g) ±1	M_R/M_S
4	84.4	90.5	10.10	60	0.716
10	84.1	90.4	9.48	60	0.659
20	83.8	90.2	8.86	59	0.650
40	83.5	89.6	7.42	55	0.614
60	82.5	88.7	5.99	51	0.573
80	82.3	87.7	4.61	46	0.522
100	81.6	86.7	3.25	39	0.483
120	80.5	85.1	2.11	32	0.372
140	79.8	84.0	1.53	26	0.309
180	77.0	80.4	0.66	14	0.169
200	75.1	78.5	0.42	8	0.100
240	71.8	74.9	0.42	5	0.069
280	68.3	72.9	0.10	4	0.075
300	66.5	67.6	0.09	4	0.0717

were found to be 10.8±0.3 kOe, 166±5 K and 0.77±0.07, respectively. The inset in Figure 8.9 demonstrates the linear variation of H_C with $T^{0.77}$ for the as-prepared $Ba_{1/3}Mn_{1/3}Co_{1/3}Fe_2O_4$ nanoparticles.

For ferromagnetic and ferrimagnetic systems, the temperature dependence of magnetization is associated with spin waves (magnons) with increase in the measuring temperature. The thermal behavior of the magnetization is usually described by Bloch's law based on equation 2.5.2. This model is effective for bulk systems with $\beta = 3/2$. For nano-scale materials, magnons with wavelength larger than the particle size (due of finite size effect) are excited. Thus, the modified Bloch's law with a β value greater than 3/2 is expected to be an appropriate model to describe such

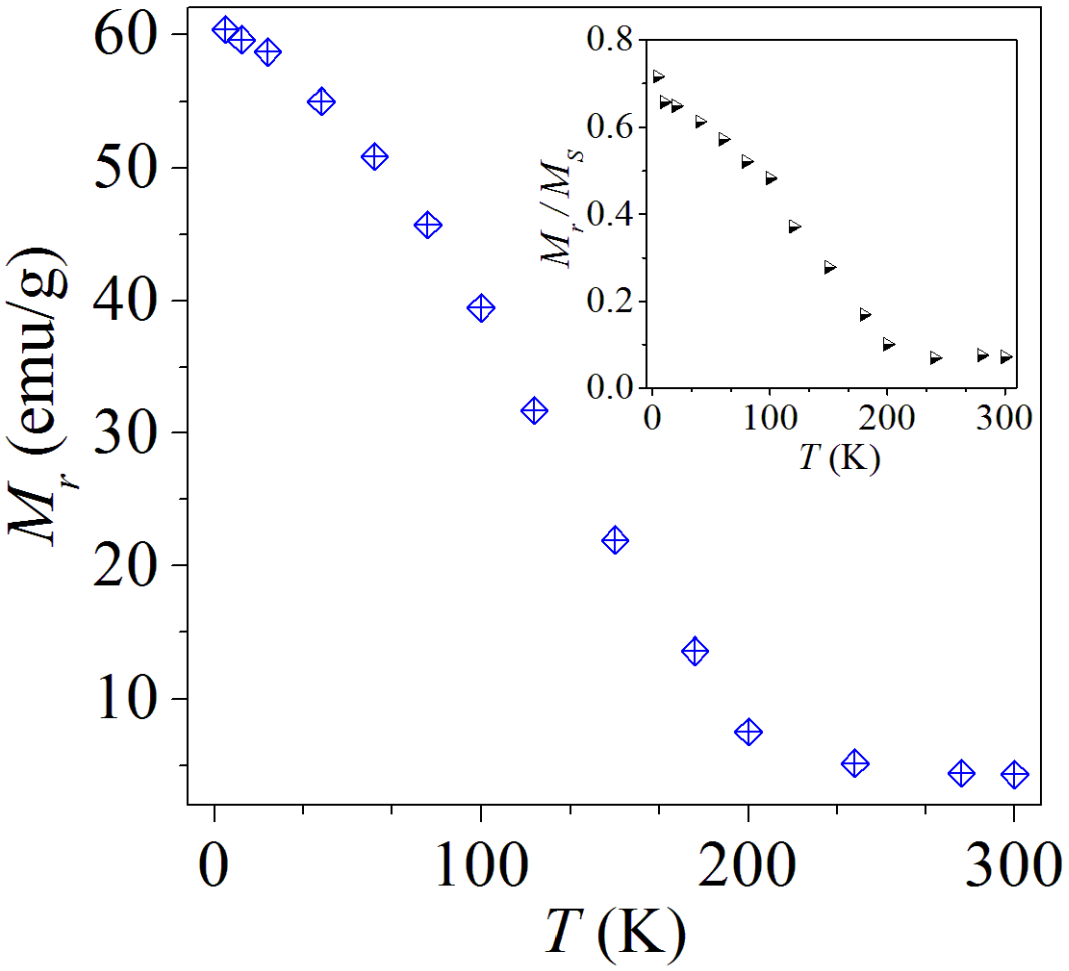

Figure 8.8: Variation of the remanent magnetization (M_r) plotted as a function of the measuring temperature. The inset shows the variation of the reduced remanent magnetization (M_r/M_S) with measuring temperature of $Ba_{1/3}Mn_{1/3}Co_{1/3}Fe_2O_4$ nanoparticles.

a system. In Figure 8.10, the temperature dependence of saturation magnetization is fitted in accordance with the modified Bloch's law with a correlation coefficient of 0.9995. The values of $M_S(0)$, T_0 and β, determined from the fitting curves, are 90.5±0.1 emu/g, 704±10 K and 1.62±0.02, respectively.

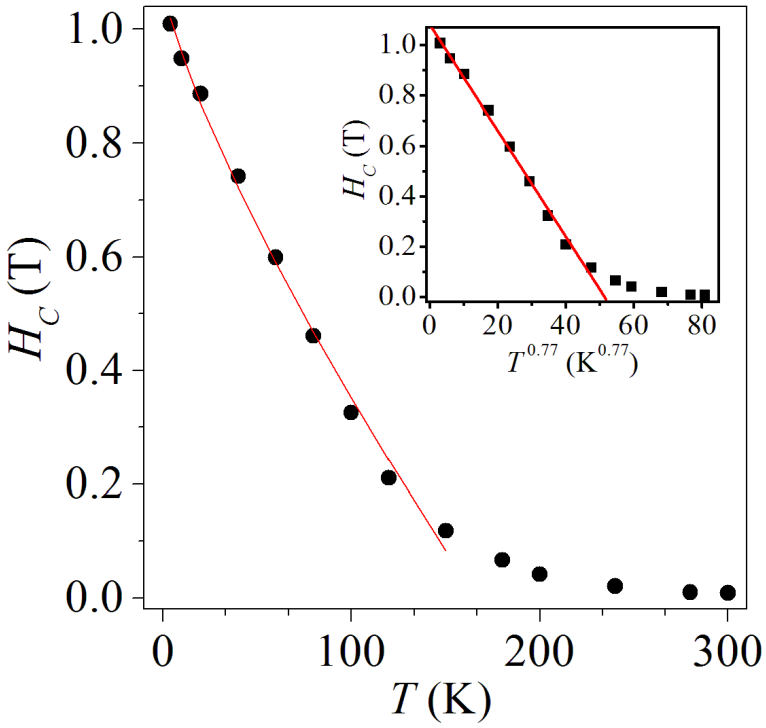

Figure 8.9: The temperature dependence for $Ba_{1/3}Mn_{1/3}Co_{1/3}Fe_2O_4$ nanoparticles. The red lines are the fits to the data.

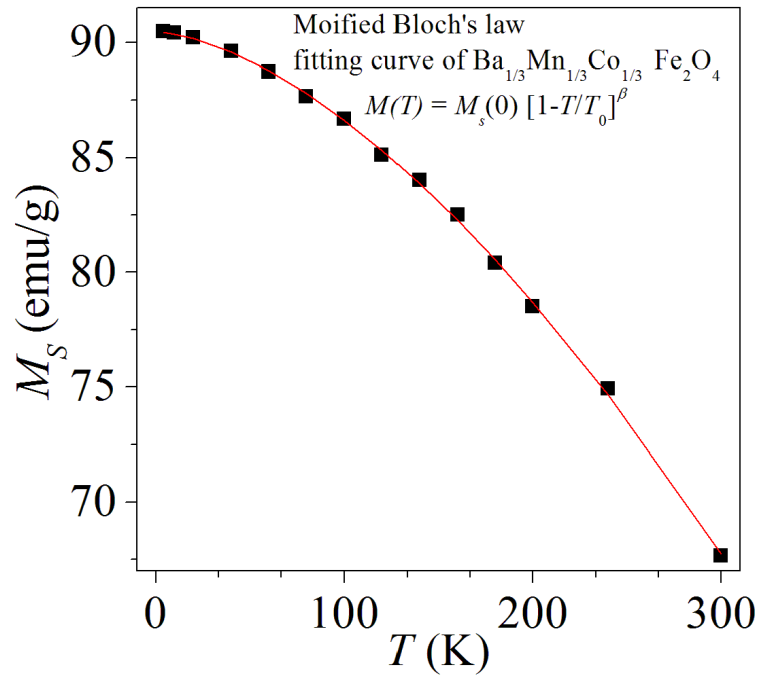

Figure 8.10: Thermal dependency of saturation magnetization for the as-prepared $Ba_{1/3}Mn_{1/3}Co_{1/3}Fe_2O_4$ nanoparticles. (The red line shows the fit curve according to the modified Bloch's law).

8.3.2 Electrochemical behavior of $Ba_{1/3}Mn_{1/3}Co_{1/3}Fe_2O_4$ nanoparticles

The electrochemical activity of the synthesized $Ba_{1/3}Mn_{1/3}Co_{1/3}Fe_2O_4$ nanoparticles nanoparticles was investigated using potassium ferricyanide $K_3[Fe(CN)_6]$ as the redox probe. Figure 8.11 shows the cyclic voltammetric response observed at bare glassy carbon electrode (GCE) and $Ba_{1/3}Mn_{1/3}Co_{1/3}Fe_2O_4$ nanoparticles/GCE in the presence of 1 mM $K_3[Fe(CN)_6]$ in 0.1 M KCl solution. Well-defined redox peaks are observed at both electrodes. However, the $Ba_{1/3}Mn_{1/3}Co_{1/3}Fe_2O_4$ nanoparticles/GCE was found to exhibit improved electrochemical behavior, exhibiting an increased peak current response and a negative shift in peak potential compared to the bare electrode. This suggests that the $Ba_{1/3}Mn_{1/3}Co_{1/3}Fe_2O_4$ nanoparticles effectively electrocatalyze the redox process of $K_3[Fe(CN)_6]$. This is attributed to an enhanced rate of electron transfer owing to the excellent electrical conductivity and high surface area of the synthesized $Ba_{1/3}Mn_{1/3}Co_{1/3}Fe_2O_4$ nanoparticles.

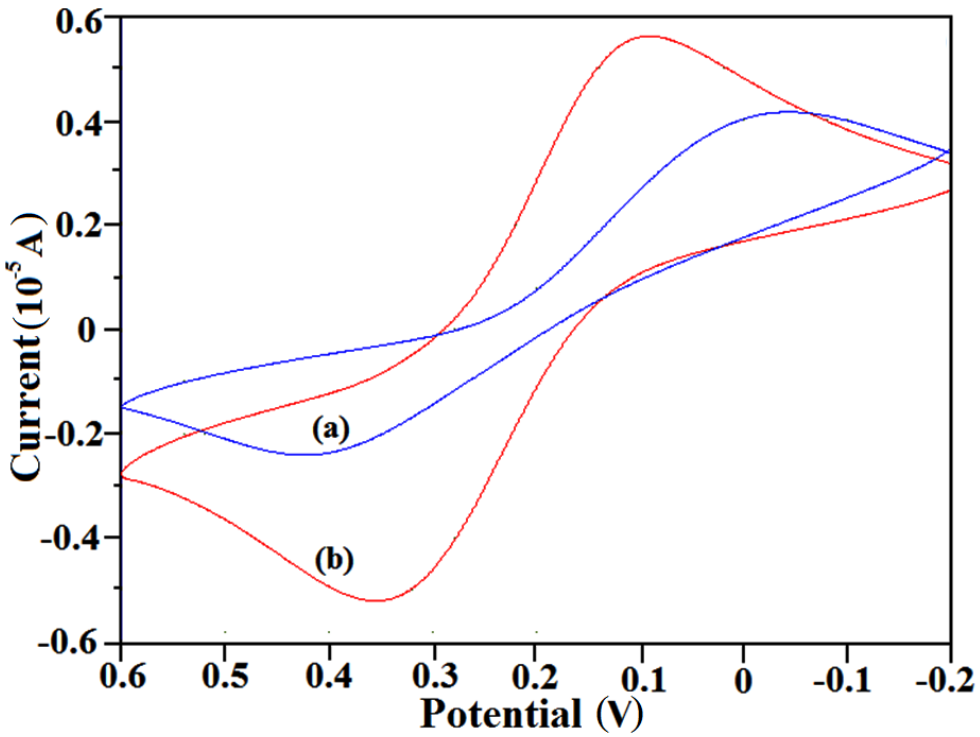

Figure 8.11: Cyclic voltammograms of 1.0 mM $K_3[Fe(CN)_6]$ in 0.1 M KCl solution at (a) bare GCE and (b) $Ba_{1/3}Mn_{1/3}Co_{1/3}Fe_2O_4$/GCE at 100 mV/s.

To establish that $Ba_{1/3}Mn_{1/3}Co_{1/3}Fe_2O_4$ nanoparticles improve the surface area of the electrode, the effective surface areas of the bare GCE and $Ba_{1/3}Mn_{1/3}Co_{1/3}Fe_2O_4$/GCE were determined by recording cyclic voltammograms in 1.0 mM $K_3[Fe(CN)_6]$ solution at different sweep rates (Figure 8.12). Using the equation 4.4.2, the diffusion coefficient D = 7.6×10^{-6} cm^2/s for $[Fe(CN)_6]^{3-}$, by employing the slope of i_{pa} versus v1/2 plot (inset of Figure 8.12), A was found to be 0.070 cm^2 and 0.218 cm^2 for bare GCE and $Ba_{1/3}Mn_{1/3}Co_{1/3}Fe_2O_4$/GCE, respectively. The surface area of the modified electrode was at least 3 times larger than that of the bare GCE electrode, indicating superior conductivity of the $Ba_{1/3}Mn_{1/3}Co_{1/3}Fe_2O_4$ nanoparticles. Thus, it is expected that the novel nanoferrites can lead to the development of a new group of electrochemical sensors.

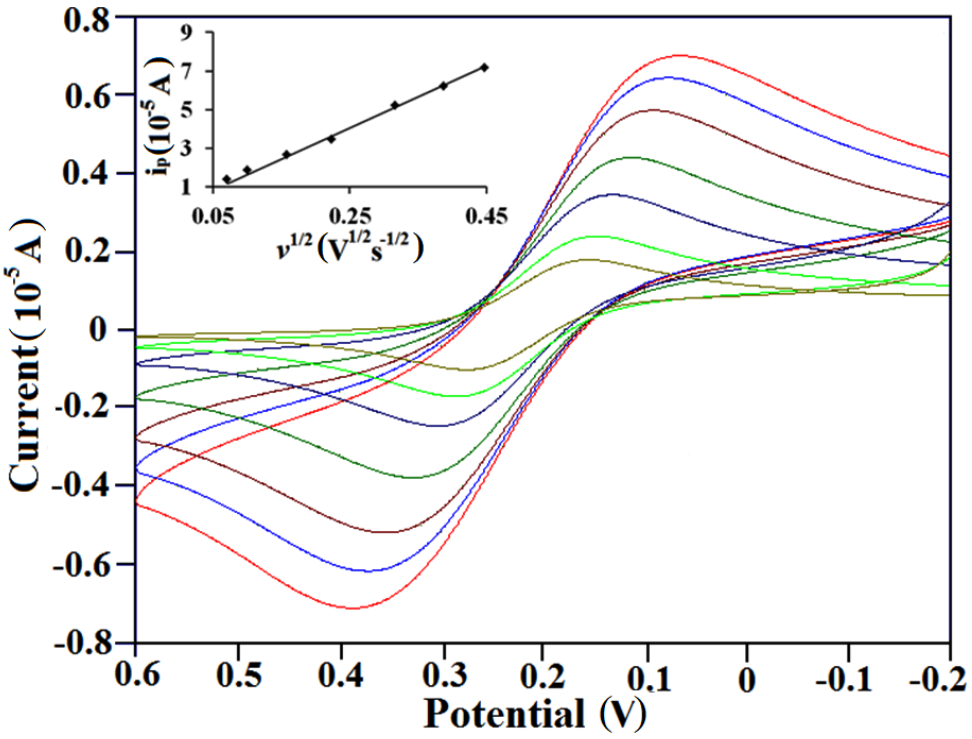

Figure 8.12: Cyclic voltammograms of 1.0 mM $K_3[Fe(CN)_6]$ in 0.1 M KCl solution at $Ba_{1/3}Mn_{1/3}Co_{1/3}Fe_2O_4$/GCE at sweep rates 5-200 mV/s. The inset displays plot of peak current versus square root of sweep rate.

8.3.3 The electrochemical behavior towards didanosine

Since the synthesized $Ba_{1/3}Mn_{1/3}Co_{1/3}Fe_2O_4$ nanoparticles shows significant electrochemical response with $K_3[Fe(CN)_6]$ we have therefore extended the study further by using didanosine (DDI) an HIV drug. Figure 8.13 depicts cyclic voltammograms recorded for 0.5 μM DDI in 0.1 M PBS (pH 7.2) at bare GCE and $Ba_{1/3}Mn_{1/3}Co_{1/3}Fe_2O_4$/GCE. No voltammetric peak was observed at the bare electrode. However, the voltammetric response improved significantly at the modified electrode, exhibiting a distinct peak at 0.75 V. This electrocatalytic activity of the $Ba_{1/3}Mn_{1/3}Co_{1/3}Fe_2O_4$/GCE is attributed to the unique properties of the synthesized nanoparticles and the large surface area of the electrode. Since the electrode is modified with transition metal nanoparticles, it is anticipated that when an electrochemical reaction takes place, these transition metal ions function as active sites [72], acting as catalysts for the oxidation of DDI. Hence, $Ba_{1/3}Mn_{1/3}Co_{1/3}Fe_2O_4$/GCE is demonstrated to enhance the electrochemical sensing property compared to the bare GCE.

8.3.3.1 Effect of scan rate and pH

The effect of scan rate v on the electrochemical behavior of DDI at $Ba_{1/3}Mn_{1/3}Co_{1/3}Fe_2O_4$/GCE was investigated in the range from 10-200 mV/s. The peak current i_p was found to increase linearly with an increase in v (as seen in Figure 8.14 (a)), indicating that the electrooxidation of DDI on the modified electrode is a typical adsorption-controlled process [163]. The relationship between i_p and v is expressed by the equation $i_p(\mu A) = 0.0087v + 0.1239$, with a correlation coefficient of 0.9967. Furthermore, $\log i_p$ is plotted against $\log v$ (Figure 8.14 (b)) and a linear relationship, expressed by the equation $\log i_p = 0.8089 \log v - 1.6004$ having a correlation coefficient of 0.9937, is obtained. A slope of 0.8 was observed, which is close to the theoretical value of 1.0 expected for an ideal adsorption-controlled electrode process [164]. This confirms that the electrooxidation of DDI is adsorption-controlled. The peak potential E_p is also observed to shift towards more positive values with an increase in v, suggesting the irreversible nature of the electrochemical process [285]. On plotting E_p versus $\log v$ (Figure 8.14 (c)), a straight line is observed that follows

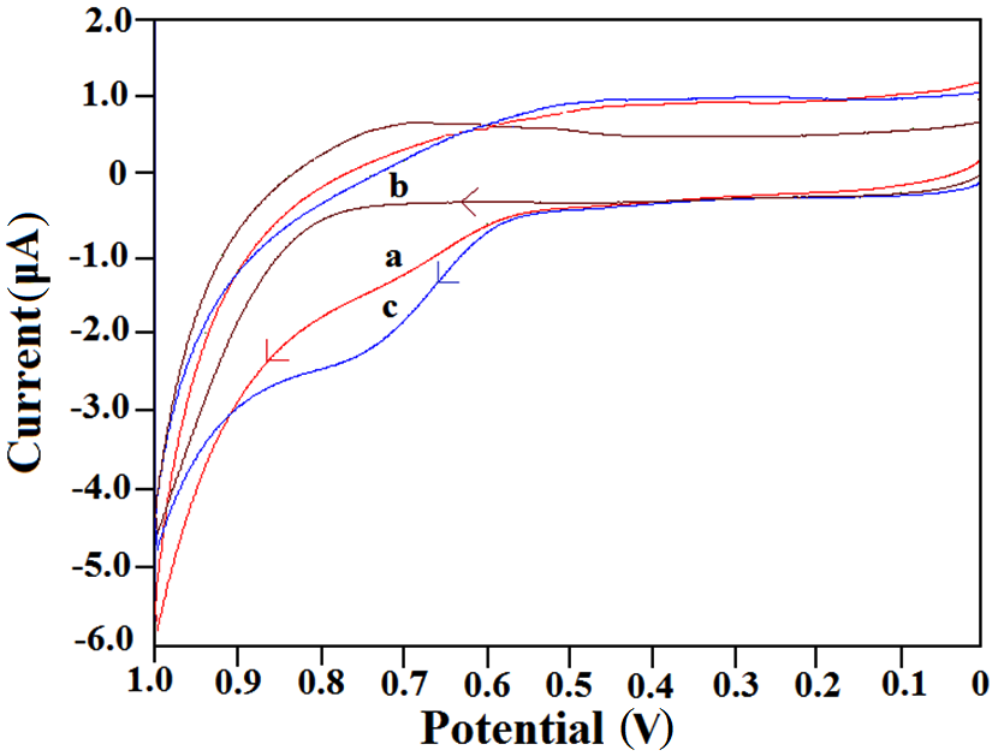

Figure 8.13: Typical cyclic voltammograms observed (a) in absence of DDI at $Ba_{1/3}Mn_{1/3}Co_{1/3}Fe_2O_4$/GCE and in presence of 0.5 μM DDI at (b) bare GCE and (c) $Ba_{1/3}Mn_{1/3}Co_{1/3}Fe_2O_4$/GCE in 0.1 M PBS (pH 7.2) at a scan rate of 100 mV/s.

the equation $E_p = 0.0681 \log v + 0.6134$, with a correlation coefficient of 0.9995. For an irreversible electron transfer, the E_p is expressed by the Laviron's equation (equation 4.4.4). The value of αn is calculated from the slope of E_p versus $\log v$ plot. With a slope of 0.0681 V. Considering $R = 8.314$ J/K mol, $F = 96480$ C/mol and $T = 298$ K, αn is calculated to be 0.87. The value of n is then calculated using equation 4.4.5 to give a value of $n = 1.64$ (~ 2). This indicates the involvement of two electrons in the oxidation of DDI at $Ba_{1/3}Mn_{1/3}Co_{1/3}Fe_2O_4$/GCE.

The pH of the supporting electrolyte exhibits significant influence on the electrooxidation of DDI at the modified electrode. Figure 8.14 (d) depicts the effect of pH on Ep of 0.5 μM DDI using $Ba_{1/3}Mn_{1/3}Co_{1/3}Fe_2O_4$/GCE in 0.1 M PBS in the pH range 3.1-9.0. It was observed that as the pH value of the solution increased, the E_p shifted linearly towards less positive potentials, with a slope of 54.2 mV/pH. This value is close to the theoretical value of 59 mV/pH, indicated for electrochemical processes involving same number of electrons and protons [165]. Hence, it is

suggested that two electrons and two protons participate in the electrooxidation of DDI, and the anticipated reaction mechanism is depicted in Figure 8.15.

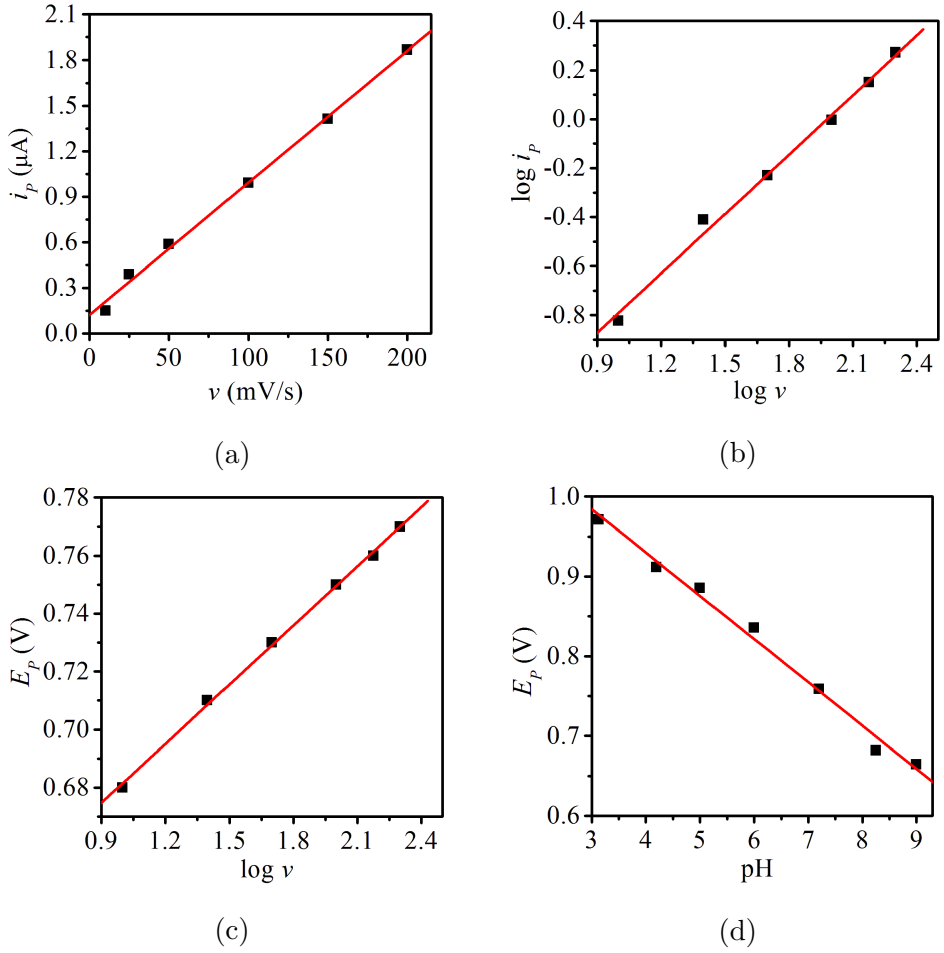

Figure 8.14: (a) Observed dependence of peak current on scan rate; (b) Variation of the logarithm of peak current with the logarithm of scan rate; (c) Plot of E_p versus logarithm of scan rate; and (d) Dependence of E_p on pH for 0.5 μM DDI in 0.1 M PBS.

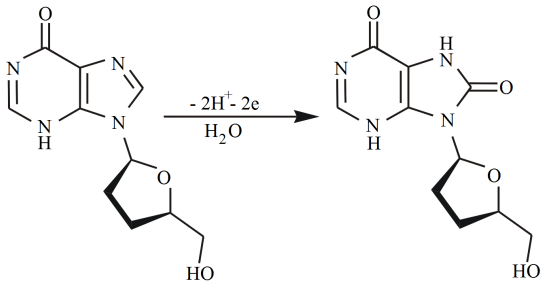

Figure 8.15: Proposed electro-oxidation mechanism of DDI.

8.3.3.2 Analytical performance

Cyclic voltammograms of DDI with varied concentrations were recorded at $Ba_{1/3}Mn_{1/3}Co_{1/3}Fe_2O_4$/GCE under optimum experimental conditions. The oxidation peak current (peak height) was found to increase linearly with DDI concentration in the range 1.0×10^{-9} M to 5.0×10^{-6} M (as depicted in Figure 8.16). The observed linear equation was $i_p(10^{-6}\text{ A}) = 2178.6C$ ($R^2 = 0.9989$), where C is the concentration of DDI (in mM). The detection limit (LOD) was found to be 1.0 nM.

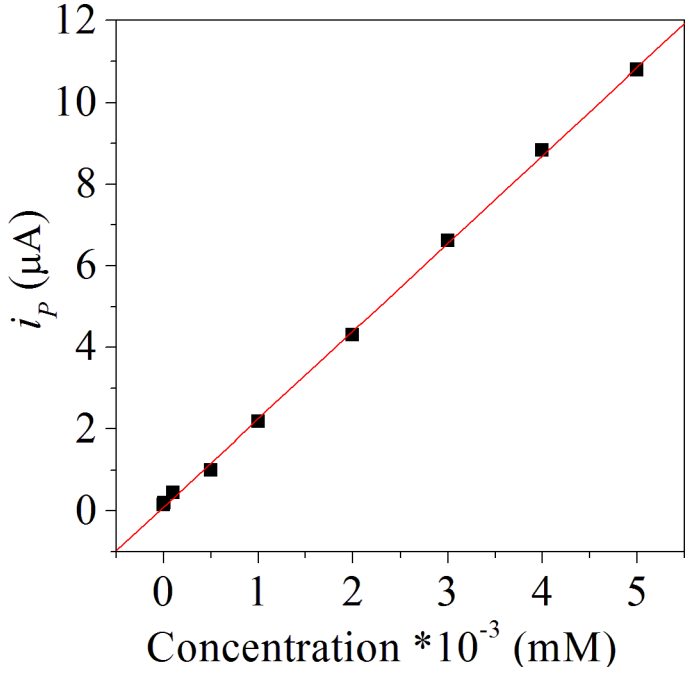

Figure 8.16: Calibration plot observed for DDI at $Ba_{1/3}Mn_{1/3}Co_{1/3}Fe_2O_4$/GCE at pH=7.2.

The reproducibility and stability of $Ba_{1/3}Mn_{1/3}Co_{1/3}Fe_2O_4$/GCE was also investigated. A series of five modified electrodes were fabricated using the same procedure and then used for the determination of 0.5 μM DDI in 0.1 M PBS. A relative standard deviation (RSD) of i_p values recorded at the five electrodes was found to be 4.2%, suggesting good fabrication reproducibility of the proposed electrode. For six successive determinations of 0.5 μM DDI solution at the same modified electrode, the calculated RSD was 3.6%. The CV response of $Ba_{1/3}Mn_{1/3}Co_{1/3}Fe_2O_4$/GCE was investigated for the same DDI concentration, after leaving the electrode un-

used for seven days. The peak potential did not exhibit any change and the peak current response also showed insignificant variation, suggesting good stability of the modified electrode. The selectivity of $Ba_{1/3}Mn_{1/3}Co_{1/3}Fe_2O_4$/GCE towards the determination of 0.5 μM DDI was examined in the presence of organic species commonly present in real samples. The tolerance limit was fixed at the concentration of interfering species exhibiting a signal change of 5% or more. It was found that over 10-fold excess concentration of ascorbic acid, dopamine and uric acid did not interfere with the voltammetric response of DDI, suggesting good selectivity of the method.

In order to evaluate the analytical applicability of the proposed method, assays were performed on two human urine samples. The samples were spiked with varying quantities of DDI and the recovery study of the drug was conducted. The observed results (summarized in Table 8.2) show satisfactory recoveries, thus validating that the proposed method has good accuracy. Figure 8.17 displays the cyclic voltammogram obtained for DDI spiked human urine sample (sample 1), where a peak is observed at 0.75 V that refers to the presence of DDI. An additional peak is observed at $\sim$ 0.4 V, which is attributed to the existence of uric acid in the urine sample, suggesting that the biological substances present in urine did not show any interference in the determination of the drug. Hence, the method can be used efficiently for quantification of DDI in real matrices.

Table 8.2: Recovery results obtained for DDI in human urine sample at modified $Ba_{1/3}Mn_{1/3}Co_{1/3}Fe_2O_4$/GCE.

Sr. No	Added (M)		Found (M)		Recoveries (%)	
	Sample 1	Sample 2	Sample 1	Sample 2	Sample 1	Sample 2
1	1.00×10^{-9}	1.00×10^{-9}	9.91×10^{-10}	1.01×10^{-9}	99.1	101.0
2	1.00×10^{-8}	1.00×10^{-8}	9.84×10^{-9}	9.92×10^{-9}	98.4	99.2
3	1.00×10^{-7}	1.00×10^{-7}	9.87×10^{-8}	1.01×10^{-7}	98.7	101.0
4	5.00×10^{-7}	5.00×10^{-7}	4.96×10^{-7}	5.04×10^{-7}	99.2	100.8
5	1.00×10^{-7}	1.00×10^{-7}	1.01×10^{-7}	1.02×10^{-7}	101.4	102.3

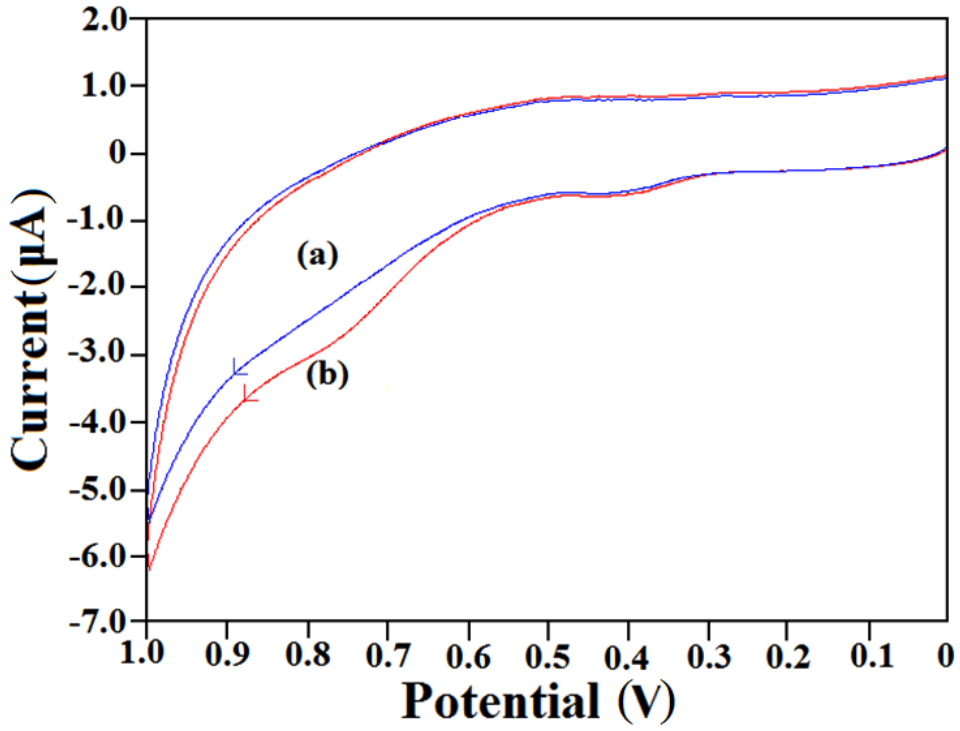

Figure 8.17: Cyclic voltammograms of (a) blank urine sample 1 and (b) urine sample 1 spiked with 0.5 μM standard solution of DDI, under optimum experimental conditions.

8.4 Conclusion

The present chapter reports simultaneous substitution of Ba, Mn and Co into ferrite spinel structure using glycol thermal method. The spinel phase of the sample was identified using X-ray powder diffraction technique. The microstrain was estimated from Williamson-Hall plot with the scattered data showing homogeneity in the sample microstrain. High-resolution transmission electron microscopy and high-resolution scanning electron microscopy were used to monitor the morphology of the as-prepared $Ba_{1/3}Mn_{1/3}Co_{1/3}Fe_2O_4$ nanoparticles. The results show mono-dispersive crystallite particles having high value surface area as deduced from Brunauer-Emmet-Teller testing. The sample was found to possess mesoporous character as observed from Barrett-Joyner-Halenda measurement. The magnetization investigation reveals that the sample tends to become magnetically harder at lower

temperature. The spontaneous magnetization increased with decrease in temperature. The remanent magnetization and reduced remanent magnetization values were also found to increase with decrease in the measuring temperature. The temperature dependence of the coercive field and magnetization are observed to follow Kneller's and modified Bloch's law, respectively. The electrocatalytic activity of the synthesized nanoparticles was also investigated by fabricating a $Ba_{1/3}Mn_{1/3}Co_{1/3}Fe_2O_4$ nanoparticle modified glassy carbon electrode as a voltammetric sensor towards didanosine. The modified electrode, with advantages such as simple fabrication procedure, excellent reproducibility, wide linear concentration range and significantly low detection limit, was successfully applied for the quantification of the drug in human urine samples, thus offering a promising substitute to the commonly reported chromatographic and spectrophotometric methods for quantification of didanosine.

Chapter 9

$Ti_{0.5}Ni_{0.5}Fe_2O_4$ nanoparticles and NiO-ZrO_2 nanocomposite synthesized by high energy ball milling

9.0.1 Introduction

Nano-crystalline materials can be produce by wet chemistry (such as hydrothermal, sol-gel, co-precipitation and combustion) or by solid state reaction methods [286]. Wet chemistry methods have an advantage of relatively low synthesis temperature which helps in providing nanoparticles with small sizes. However, some of wet chemistry techniques have tedious procedures and many steps to follow in order to obtain the final product. High energy ball milling is known as a simple and efficient synthesis technique to produce nanoparticles [287]. It belongs to solid state reaction category. In this technique the final product can be obtained directly by grinding stoichiometric amount of metal oxides of a desired compound by stainless steel balls in milling jars. The particle sizes are therefore expected to be slightly bigger compared to wet chemistry methods. However, increasing the milling time can lead to reduced

particle sizes. However, in some cases milling for a long time can destroy the phase that may initially form. In this chapter we present $Ti_{0.5}Ni_{0.5}Fe_2O_4$ nanoparticles and NiO-ZrO_2 nanocomposite both synthesized by high energy ball milling under similar synthesis conditions. To our surprise the spinel phase of $Ti_{0.5}Ni_{0.5}Fe_2O_4$ appears to form relatively easily after about 1.5 hours of milling. The structure, magnetic and electrochemical activity of $Ti_{0.5}Ni_{0.5}Fe_2O_4$ nanoparticles produced after 1.5 hours of milling are reported in this chapter. The structure and electrochemical behavior of ball milled NiO-ZrO_2 nanocomposite is also discussed. In this case the NiO-ZrO_2 nanocomposite is used to modify the glassy carbon electrode GCE for sensitivity and selectivity determination of Efavirenz, an Anti-HIV Drug [288].

9.1 Structural, magnetic and electrochemical activity of $Ti_{0.5}Ni_{0.5}Fe_2O_4$ nanoparticles

Nanomaterials tend to reveal unusual physical and chemical behavior compared to their corresponding bulk materials [45]. Nano materials are associated with quantum size effects and large surface areas [289, 290]. Magnetic nanoparticles have important uses in several applications such as high density magnetic recording, magnetic fluids, data storage, spintronics, solar cells, sensors, and in catalysis [291]. Nickel ferrite with spinel structure has attracted attention due to its interesting properties such as low coercivity, high saturation magnetization low eddy current loss, chemical and thermal stability [292, 293]. These qualities allow $NiFe_2O_4$ to be used in several applications such as gas-sensors, magnetic fluids, catalysts, magnetic storage systems, magnetic resonance imaging, drug delivery and microwave devices [294, 295, 296]. The properties of $NiFe_2O_4$ nanoparticles can also be tuned by doping with different cations in its tetrahedral (A) or octahedral sites (B). Furthermore, synthesis methods can also play a significant role in establishing nanoparticle sizes. In this section we discuss the synthesis and properties of $Ti_{0.5}Ni_{0.5}Fe_2O_4$ nanoparticle ferrites. The study involves structure, magnetic properties and electrochemical activity of the synthesized compound towards potassium ferricyanide $K_3[Fe(CN)_6]$.

9.1.1 Experimental details

$Ti_{0.5}Ni_{0.5}Fe_2O_4$ nanoparticle ferrite was produced from high purity metal oxides (TiO_2: 99%, NiO: 99% and F_3O_4: 95%) by high energy mechanical milling in air atmosphere at different milling times using a Retch planetary ball mill (type: PM 400) operated at 300 rev/min. The ball to mass ratio was 10:1. The phase formation was characterized by a Phillips X-ray diffractometer (type: PANalytical, EMPYREAN) using CoKα radiation. The morphology and micro-structure of the nanoparticles were investigated on a high-resolution transmission electron microscope (HRTEM) (type: Jeol_JEM-1010) and high-resolution scanning electron microscope (HRSEM) (Ultra Plus ZEISS-FEG HRSEM instrument). The elemental compositions was investigated by energy dispersive X-ray (EDX) spectroscopy and by inductively coupled plasma optical emission spectrometry (ICP-OES) (Optima 2100). ^{57}Fe Mössbauer spectra were obtained by a conventional spectrometer using a ^{57}Co source sealed in Rh matrix and vibrated at constant acceleration. The magnetic properties were investigated by using a LakeShore vibrating sample magnetometer (VSM). Potassium ferricyanide ($K_3[Fe(CN)_6]$) and potassium chloride (KCl) were purchased from Merck (Pty) Ltd South Africa and used as received without further purification. Cyclic voltammetry (CV) was performed on electrochemical analyzer (CHI660E, CH Instruments, Inc.). The three-electrode system consisted of a bare/modified glassy carbon working electrode, an Ag/AgCl reference electrode and a platinum counter electrode. Prior to the modification of the bare electrode, its surface was polished with 0.05 mm alumina slurry on a polishing cloth and then rinsed carefully with double distilled water to produce a clean shiny surface. The modified electrode was finally fabricated by drop-casting a 0.5 mg mL^{-1} aqueous solution of $Ti_{0.5}Ni_{0.5}Fe_2O_4$ nanoparticles onto the cleaned and dried electrode surface.

9.1.2 Results and discussion

The phase structure of $Ti_{0.5}Ni_{0.5}Fe_2O_4$ nanoparticles was confirmed by X-ray powder diffraction (XRD) as shown in Figure 9.1. A small additional peak at $\theta \approx 29^\circ$ is noticed for samples milled for 0.5, 1, 2 and 40 hours. However no impurity

peaks is observed for the sample milled for 1.5 hours. This appears to be a unique sample to study and a strong motivation to investigate the structural, magnetic properties and electrochemical properties for $Ti_{0.5}Ni_{0.5}Fe_2O_4$ milled for 1.5 hours. The lattice parameter a was calculated using Bragg's law (equations 4.1.1) and equation 4.1.2. The average particle sizes were calculated using Scherrer formula (equation 4.1.3). The obtained values of lattice parameter and crystallite sizes for the as-prepared $Ti_{0.5}Ni_{0.5}Fe_2O_4$ nanoparticles are found to be 0.840±0.003 nm and 29.01±0.2 nm. The XRD densities ρ_{XRD} were calculated using equation 4.1.4. The percentage porosity $P(\%)$ of the sample was obtained by using the equation 4.1.6. The calculated value of ρ_{XRD} and $P(\%)$ are found to be 3.46±0.04 g/cm^{-3} and 40% respectively. The microstrain ε was studied based in the Williamson plot as shown in Figure 9.2. The distribution of the data points shows homogeneous microstrain in the synthesized $Ti_{0.5}Ni_{0.5}Fe_2O_4$ nanoparticles that is based on the synthesis method. The value of microstrain ε from Figure 9.2 was found to be 0.0035±0.0007.

The elemental composition was identified by energy dispersive X-ray (EDX) as shown in Figure 9.3 (a). The results show only the expected elements of Ti, Ni, Fe and O in the synthesized $Ti_{0.5}Ni_{0.5}Fe_2O_4$ nanoparticles. The inset in Figure 9.3 shows weight percentages of the detected elements. The elemental composition was studied further by inductively coupled plasma optical emission spectrometry (ICP-OES) technique. The measurements show that the elemental mass percentages in the $Ti_{0.5}Ni_{0.5}Fe_2O_4$ nanoparticles are Ti: 16.33%, Ni: 21.43% and Fe: 62.24%. The expected values for Ti, Ni and Fe are 14.50 %, 17.85% and 67.65 % respectively. Figure 9.3 (b) shows the elemental distribution on the surface of the synthesized $Ti_{0.5}Ni_{0.5}Fe_2O_4$ nanoparticles. It is clear that the Ti and Ni are well distributed on the surfaces of the nanoparticles.

The morphology of the synthesized $Ti_{0.5}Ni_{0.5}Fe_2O_4$ nanoparticles was studied by high-resolution transmission electron microscopy (HRTEM) and high- resolution scanning electron microscopy (HRSEM). The images in Figure 9.4 show that the nanoparticles have regular shape and monodispersed with a small degree of agglomeration. The diffraction was also achieved by HRTEM measurements. The reflection from planes (111), (311) and (511) are shown in Figure 9.4 (b). The corre-

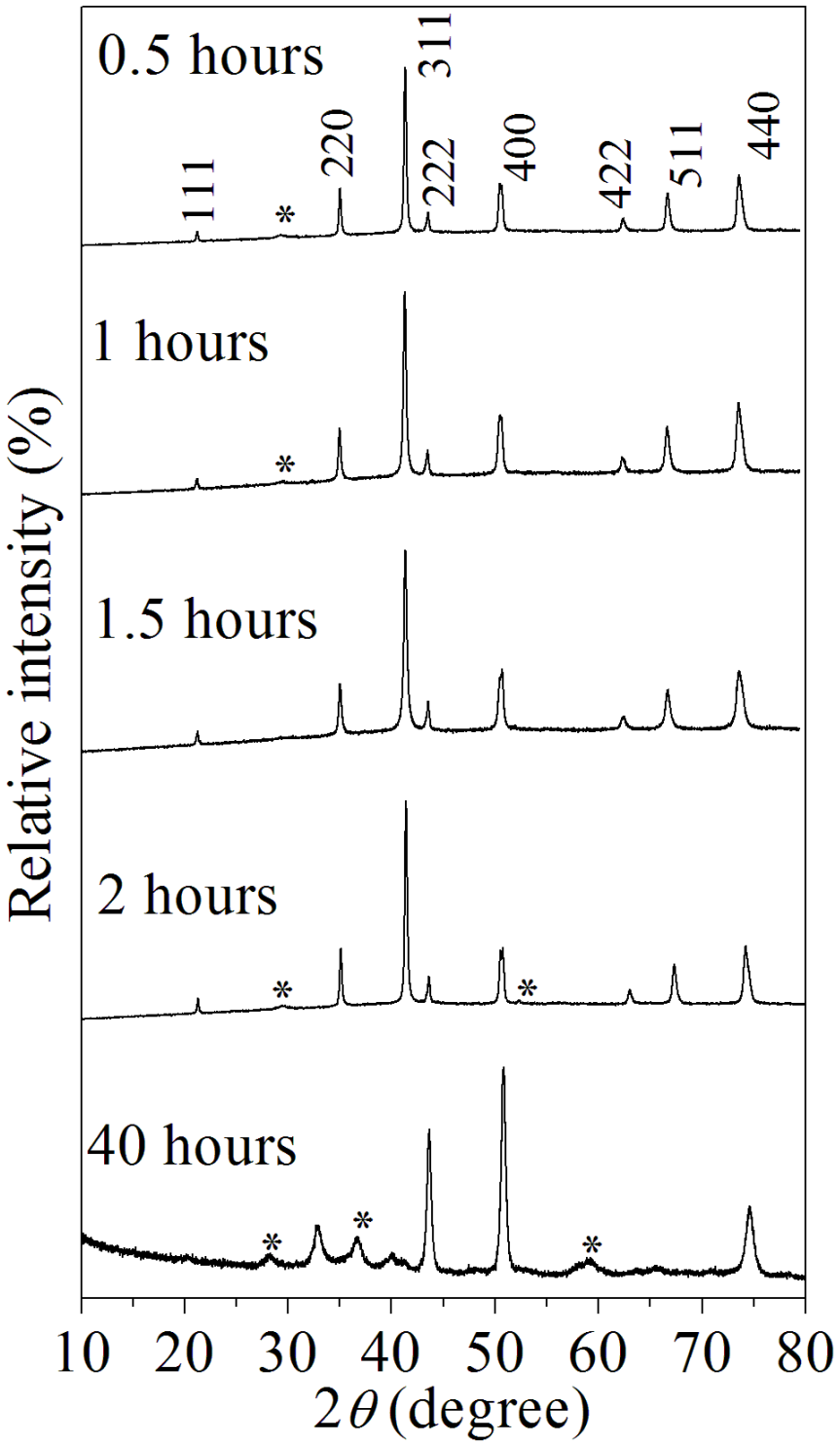

Figure 9.1: XRD patterns of $Ti_{0.5}Ni_{0.5}Fe_2O_4$ ferrite nanoparticles milled for different time.

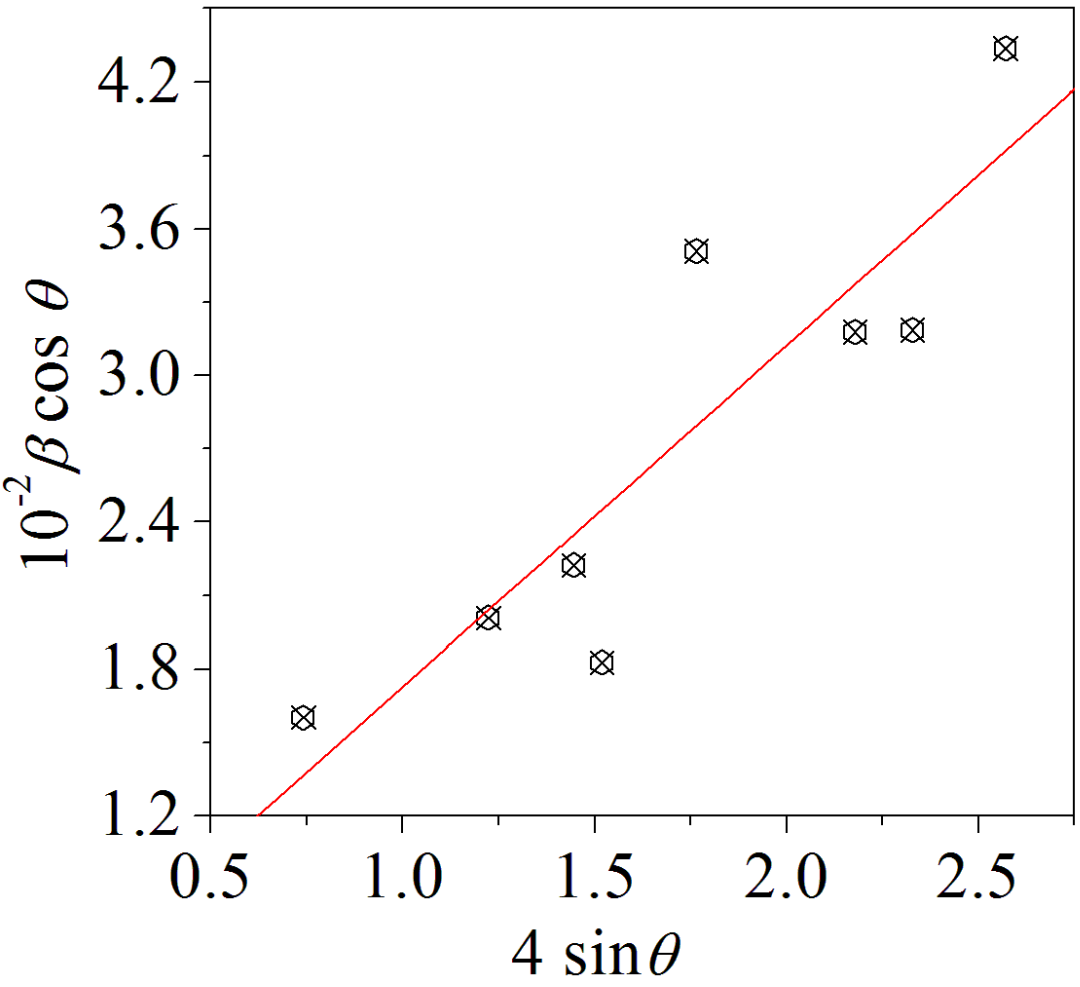

Figure 9.2: Williamson-Hall plot of $\beta\cos\theta$ Vs $4\sin\theta$ of $Ti_{0.5}Ni_{0.5}Fe_2O_4$ ferrite nanoparticles milled for 1.5 hours.

sponding diffraction planes confirm the crystalline spinel structure of the synthesized $Ti_{0.5}Ni_{0.5}Fe_2O_4$ nanoparticles. The HRTEM and XRD results are consistent with each other.

Figure 9.5 (a) shows room temperature ^{57}Fe Mössbauer spectrum of the synthesized $Ti_{0.5}Ni_{0.5}Fe_2O_4$ nanoparticles. The data were fitted using two Zeeman sextets. This is associated with the presence of Fe ions in tetrahedral (A) and octahedral (B) sub-lattices. The values of isomer shift δ were found to be 0.64±0.02 and 0.30±0.01 mm/s for A and B sites respectively. The values of δ in the range 0.6-1.7 mm/s are for Fe^{2+}, and 0.1-0.5 mm/s are for Fe^{3+} [227]. Therefore, the values of δ for the synthesized $Ti_{0.5}Ni_{0.5}Fe_2O_4$ nanoparticles reveal that both Fe^{3+} and Fe^{2+} ions

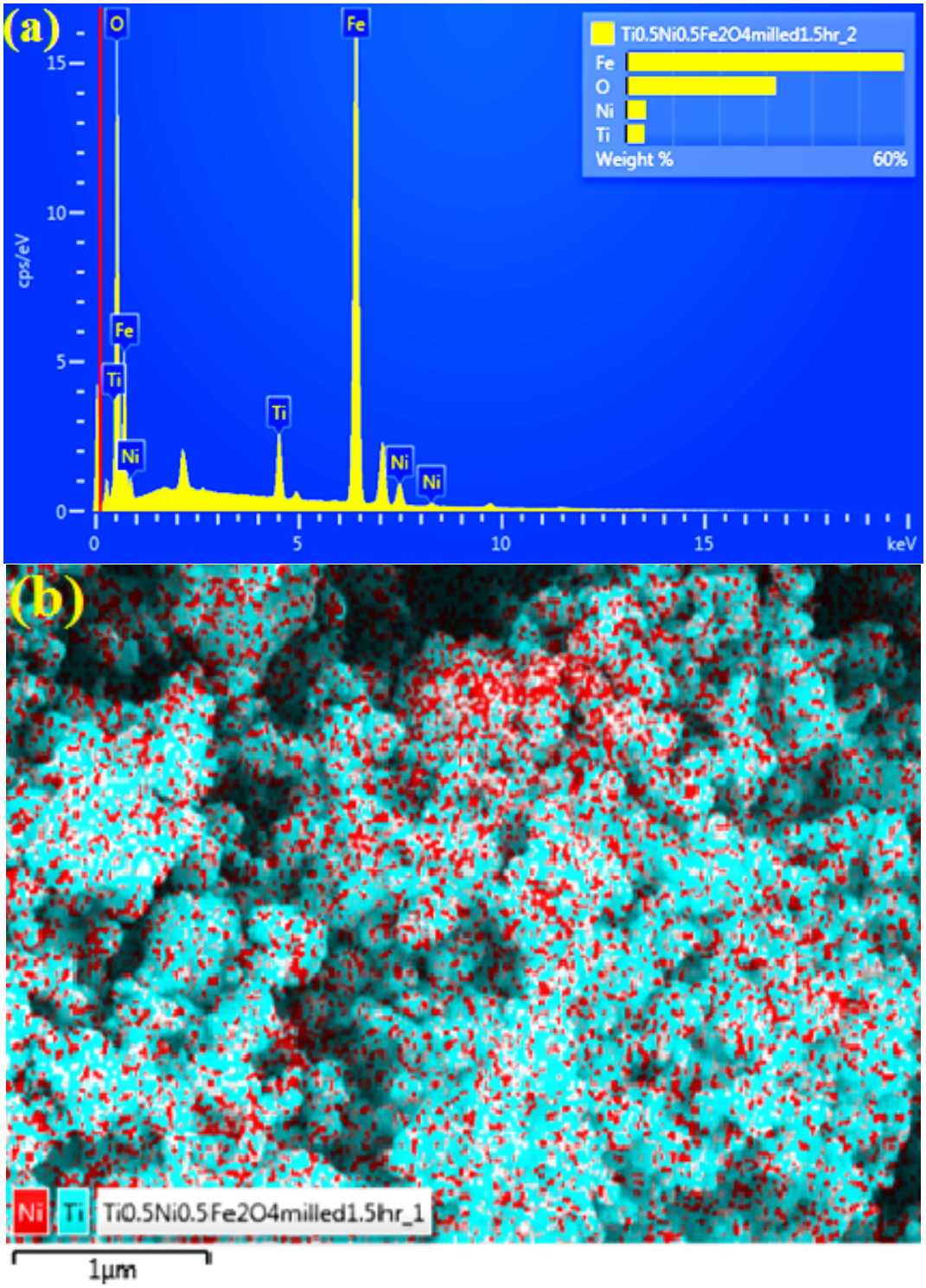

Figure 9.3: EDX results (a) and elemental mapping (b) of $Ti_{0.5}Ni_{0.5}Fe_2O_4$ milled for 1.5 hours.

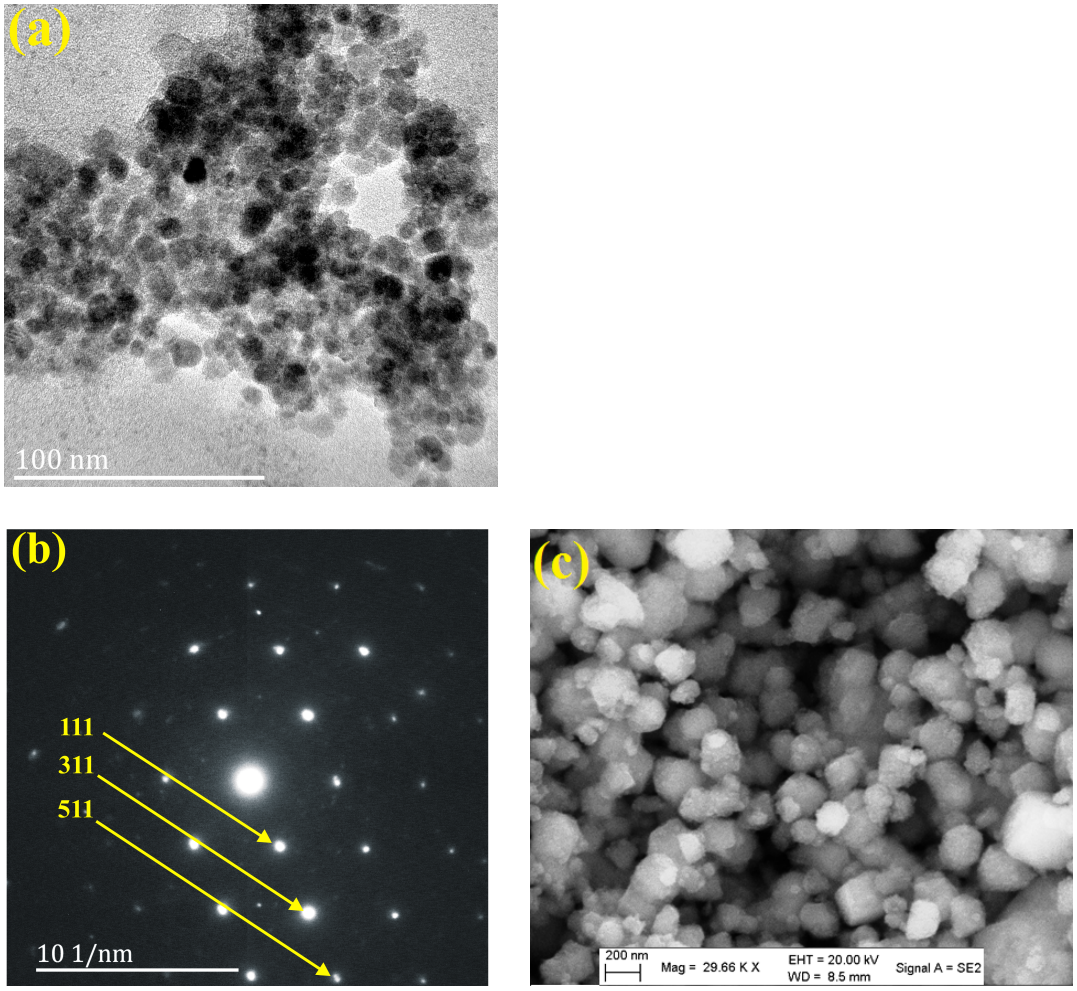

Figure 9.4: HRTEM (a), HRTEM diffraction (b) and ERSEM (c) images for $Ti_{0.5}Ni_{0.5}Fe_2O_4$ nanoparticles milled for 1.5 hours.

co-exist in the sample. The hyperfine field H values were found to be 453±2 kOe at tetrahedral (A) site and 491±1 kOe at octahedral (B) site. These fields are associated with super-exchange interactions between magnetic moments in A and B sub-lattices. The value of line width Γ at A site of 0.43±0.07 mm/s is greater than of 0.21±0.08 mm/s on B site. The larger broadening at A site is suspected to be due to the presence of Fe^{2+}. The values of the iron ions fraction population f were found to be 55% and 45% for A and B sites respectively.

The magnetization measurements were performed on a vibrating sample magnetometer (VSM) in external magnetic fields of ±14 kOe. Figure 9.5 (b) shows the room temperature M-H loop of the synthesized $Ti_{0.5}Ni_{0.5}Fe_2O_4$ nanoparticles.

The saturation magnetization M_S of 71.5±0.1 emu/g was obtained from fitting the initial magnetization curve as shown in the inset of Figure 9.5 (b). The initial magnetization curve is fitted according to the approach to saturation magnetization by equation 2.7.1. Room temperature magnetic properties are associated with strong super-exchange interactions between A and B sublattices as described by Néel's model [22]. The obtained values of coercive field H_C, remenance M_r and squareness M_r/M_S are found to be 216±16 Oe, 16±1 emu/g and 0.225, respectively.

The electrochemical behavior of the synthesized $Ti_{0.5}Ni_{0.5}Fe_2O_4$ nanoparticles modified electrode was explored using the redox species, $K_3[Fe(CN)_6]$. Figure 9.6 (A) shows the cyclic voltammograms (CVs) observed for 2.0 mM $K_3[Fe(CN)_6]$ in 0.1 M KCl solution at bare GCE and $Ti_{0.5}Ni_{0.5}Fe_2O_4$/GCE in the potential range from -0.2 to 0.6 V at a scan rate of 100 mV/s. Both electrodes exhibited distinct redox peaks. However, an improvement in the CV response was noted at the modified electrode. The peak potential was found to shift towards less positive values with a significant increase in the peak current compared to the bare electrode. This indicates that the $Ti_{0.5}Ni_{0.5}Fe_2O_4$ nanoparticles enhance the electron transfer rate thus electrocatalyzing the redox process of $K_3[Fe(CN)^6]$. The electrocatalytic activity is anticipated to be due to the high surface area and remarkable electrical conductivity of the synthesized $Ti_{0.5}Ni_{0.5}Fe_2O_4$ nanoparticles. In order to confirm that the $Ti_{0.5}Ni_{0.5}Fe_2O_4$ nanoparticles enhance the active surface area of the modified electrode, CVs of 2.0 mM potassium ferricyanide in 0.1 M KCl at varying scan rates were recorded at bare GCE and $Ti_{0.5}Ni_{0.5}Fe_2O_4$/GCE (as depicted in Figure 9.6 (B)). According to the Randles-Sevcik equation, for a reversible reaction at 25 °C the peak current i_P is given by $i_p = 2.99 \times 10^5 n(\alpha n_a)^{1/2} ACD^{1/2} Cv^{1/2}$ (see equation 4.4.3). The active surface area A was calculated from the slope of the oxidation peak current versus the square root of the scan rate (inset of Figure 9.6 (B)) and was found to be 0.069 cm^2 and 0.154 cm^2 for bare GCE and $Ti_{0.5}Ni_{0.5}Fe_2O_4$/GCE, respectively. The surface area of the modified electrode is approximately 2 times higher than that of the bare electrode, suggesting significant electrocatalytic activity of the $Ti_{0.5}Ni_{0.5}Fe_2O_4$ nanoparticles.

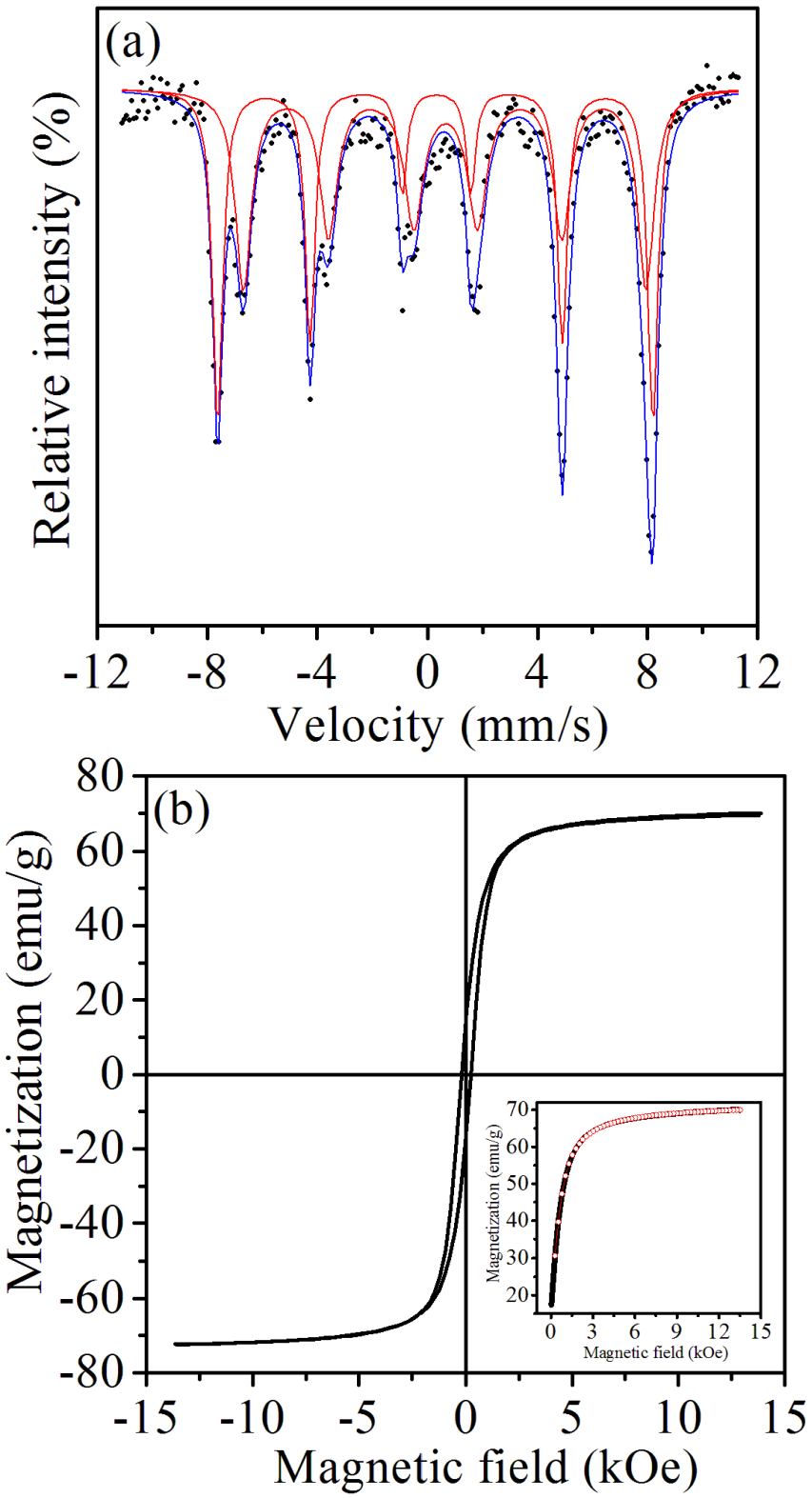

Figure 9.5: Room temperature (a) Mössbauer (b) $M - H$ curve of $Ti_{0.5}Ni_{0.5}Fe_2O_4$ milled for 90 minutes. The inset in (b) is the initial magnetization curve fitted according to the empirical approach law to saturation magnetization.

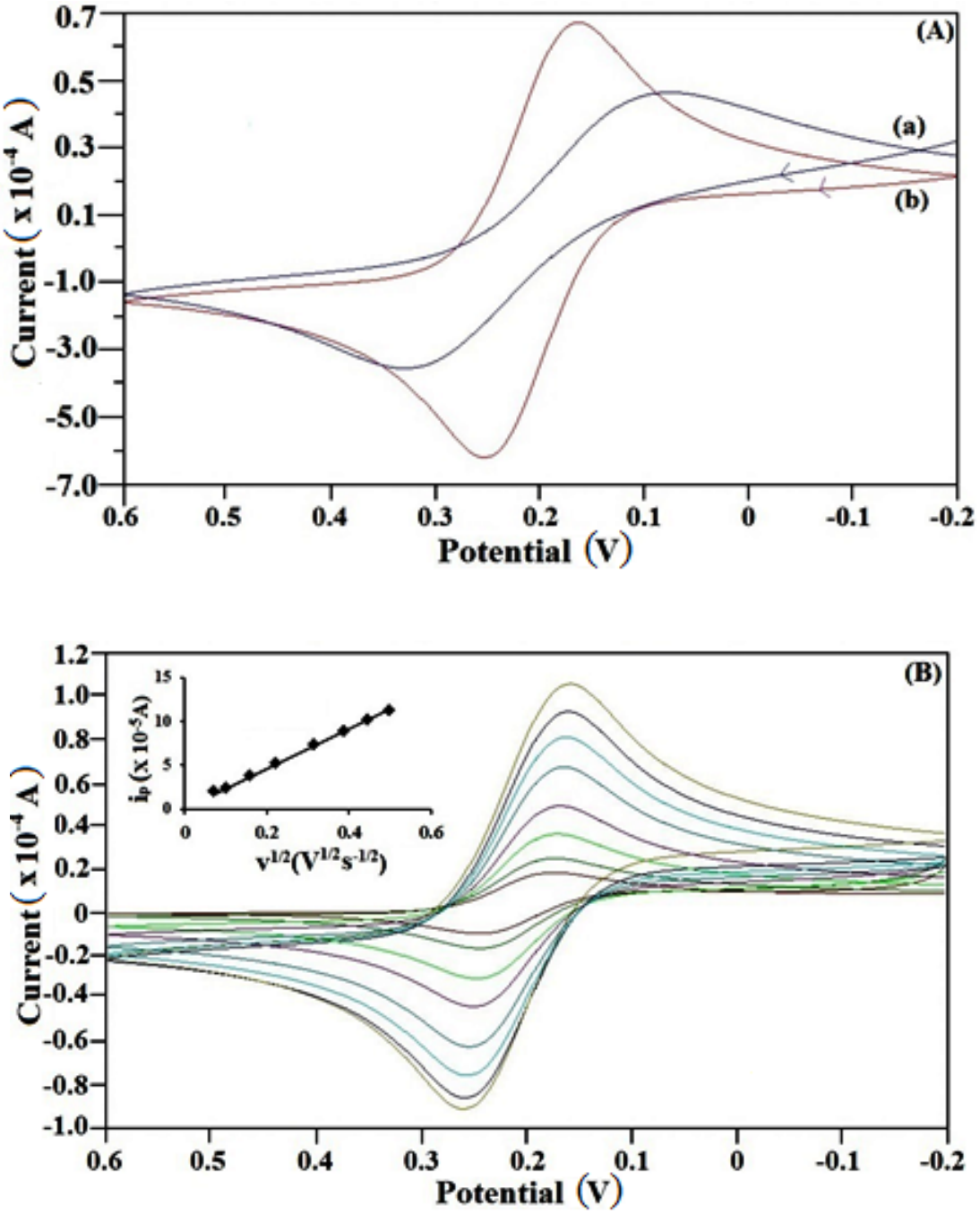

Figure 9.6: (A) Cyclic voltammograms of 2.0 mM $K_3[Fe(CN)^6]$ in 0.1 M KCl solution at (a) bare GCE and (b) $Ti_{0.5}Ni_{0.5}Fe_2O_4$/GCE at a scan rate of 100 mV/s. (B) Cyclic voltammograms of 2.0 mM $K_3[Fe(CN)^6]$ in 0.1 M KCl solution at $Ti_{0.5}Ni_{0.5}Fe_2O_4$/GCE at different scan rates ranging from 5 mV/s to 250 mV/s. (Inset displays plot of peak current versus square root of scan rate).

9.2 Structural and electrochemical activity of NiO-ZrO_2 nanocomposite

Efavirenz (EFV, Scheme 9.7) is a well-known human immunodeficiency virus (HIV) type 1 specific non-nucleoside reverse transcriptase inhibitor [297]. Chemically, EFV (marketed as Sustiva) is known as 6-chloro-4-(2-cyclopropylethynyl)-4-(trifluoromethyl)-2,4-dihydro-1H- 3,1-benzoxazin-2-one. The drug is a vital part of highly active antiretroviral therapy (HAART) and is usually prescribed in combination with other anti-HIV drugs for the management of the disease as a first line of treatment in HIV-infected patients [298]. Approved by the FDA in 1998, EFV functions via suppressing reverse transcriptase activity by binding to the catalytic site of the enzyme, thus prohibiting it from transcribing viral RNA into DNA and infecting more cells [299].

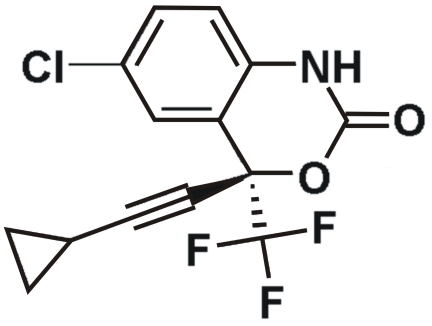

Figure 9.7: Scheme shows the chemical structure of Efavirenz.

It is a poorly water soluble BCS (Biopharmaceutics Classification System) class-II drug which metabolizes in the liver, and may interact with other livermetabolized drugs necessitating change in the administered dose [300]. Though well tolerated, EFV is associated with a range of mild to moderate adverse effects, which include skin rash, dizziness, headache, insomnia, light-headedness, impaired concentration, subclinical hearing loss, aggression, anxiety, hallucinations and depression [301, 302, 303, 304]. High level of drug overdose may induce toxicity with more pronounced side effects. Recently, reports on misuse of EFV for recreational purpose have surfaced due to its psychedelic effects allegedly similar to LSD [304]. EFV

analysis is thus considered essential for quality control, drug screening and to attain optimum therapeutic concentration, while minimizing the risk of overdosage. Hence, the development of a simple and sensitive method for the determination of EFV is of high importance and interest. Various chromatographic, spectrophotometric and spectrometric methods have been developed for the quantification of EFV [305, 306, 307, 308, 309, 310, 311, 312]. These methods are expensive and involve time consuming derivatization steps. Electrochemical methods have therefore attracted considerable interest in the field of drug analysis because of their simplicity, low cost, fast response and high sensitivity in detecting drugs without requiring tedious extraction or pretreatment processes. However, to date only two electroanalytical methods have been reported for the analysis of the drug. Dogan-Topal *et al.* [313] investigated the differential pulse voltammetric behavior of EFV at a dsDNA modified disposable pencil graphite electrode and quantified the drug in commercial tablets. Later, Castro *et al.* [314] developed a differential pulse adsorptive stripping voltammetric method at the mercury film electrode to measure EFV concentration.

The modification of conventional electrodes with nanoparticles has been the focus of attention in recent decades since it conveys unique physical and chemical properties of the nanoparticles to the electrode surface, exhibiting obvious advantages in the field of electroanalysis and electrocatalysis [315]. In recent years, various transition metal oxide nanoparticles, such as zinc oxide, copper (II) oxide, nickel oxide and cobalt oxide, have been used for electrode fabrication in order to improve the selectivity and sensitivity of the electrochemical sensor. Among these, nickel oxide (NiO) is one of the most promising metal oxide nanoparticle having diverse applications in electrochemical supercapacitors, magnetic materials, electrocatalysis and biosensors due to its abundance, low cost, high electrical conductivity and exceptional catalytic activities [316, 317]. Zirconia (ZrO_2) nanoparticles are also of great interest due to their appreciable chemical inertness, thermal stability, adaptable structure, high electrical conductivity along with the property to enhance strength and toughness leading to applications in optics, catalysis, adsorption, catalytic support, sensors, electrical, thermal and magnetic fields of interest [318, 319]. It is well-known that the properties of nanoparticles could be effectively tuned by mixing two or more

elements/oxides together. NiO and ZrO_2 nanoparticles offer various functions for electroanalysis, with these nanoparticles being reported for their enhanced catalytic and conductivity properties owing to the nano dimensions that facilitate the electrical contact of redox-sites in the analyte with the electrode surface. High probability of amplification of the electrochemical response in the presence of both of these nanoparticles motivated us to combine NiO and ZrO_2 nanoparticles and use the nanocomposite to modify the electrode for detection of the analyte. Thus, the combination of NiO and ZrO_2 nanoparticles provides an attractive approach to fabricate the electrode surface with an aim to achieve enhanced sensitivity and selectivity. The present work reports the synthesis and characterization of NiO-ZrO_2 nanocomposite followed by its immobilization on the surface of a glassy carbon electrode (GCE) to develop a voltammetric sensor to determine the anti-HIV drug, EFV. The method displays a novel efficient protocol for the sensitive and selective quantification of the drug in real samples [288].

9.3 Experimental details

9.3.1 Materials and reagents

Pure powdered EFV, NiO and ZrO_2 was purchased from Sigma-Aldrich. Other chemicals used were of analytical grade and obtained from Merck. 0.1 M phosphate buffer solutions (PBS), used as a supporting electrolyte, were prepared by mixing solutions of Na_2HPO_4 and NaH_2PO_4 according to the method given by Christian and Purdy [320]. Standard stock solution of EFV (1 mM) was prepared by dissolving it in pure methanol and stored in the dark when not in use. Double distilled water was used throughout the experiments. Prior to each measurement, pure nitrogen gas was purged into the EFV containing solution for 5 minutes in order to remove dissolved oxygen from the solution.

9.3.2 Apparatus

The electrochemical experiments were performed using electrochemical analyzer (Model 800B Series, CH Instruments, Inc.) arranged in conjunction with a computer for data storage and processing along with a conventional three-electrode system. The three-electrode system comprised of an Ag/AgCl reference electrode, a platinum counter electrode and a bare/modified glassy carbon working electrode (3 mm diameter). All the three electrodes (working, reference and counter) were provided by CH Instruments, Inc. (USA). The pH of the buffer solutions was checked using CyberScan pH 510 bench pH meter (Eutech Instruments). The applicability of the proposed method for analysis of the drug in commercial pharmaceutical preparations was verified using a Shimadzu UV spectrophotometer (Model UV-1800, Shimadzu Corporation, Japan) with a quartz cell (optical path of 1 cm). Bruker D8 advance X-ray powder diffractometer (XRD) using CuKα radiation was used for X-ray diffraction measurement of the sample. High-resolution scanning electron microscopy (HRSEM) and high-resolution transmission electron microscopy (HRTEM) measurements were performed on a Carl Zeiss Ultra Plus ZEISS-FEG and Jeol_JEM-1010 instruments, respectively.

9.3.3 Synthesis of nanoparticles

The NiO-ZrO_2 nanoparticles mixture was in mole proportion of 2:1 and was produced from high purity metal oxides (NiO: 99% and ZrO_2: 99%) by high energy mechanical milling in an atmosphere of air for 10 hours using a Retch planetary ball mill (type: PM 400) operated at 300 rev/min. The ball to mass ratio in milling the sample was 10:1.

9.3.4 Preparation of modified electrode

Prior to the electrode modification, the GCE surface was cleaned by polishing with 0.05 mm alumina slurry on a polishing cloth until the surface had a shiny appearance. The polished electrode was then rinsed thoroughly with double-distilled water and then dried in air at room temperature. 5.0 μL of an aqueous suspension of the NiO-

ZrO_2 nanoparticles (0.02 mg mL^{-1}) was drop coated onto the cleaned GCE surface and dried. A uniform adherent dark red coating of the synthesized nanoparticles was formed on the GCE surface and the resultant electrode was denoted as NiO-ZrO_2/GCE.

9.3.5 Sample preparation

The commercially available EFV tablet was grounded to a homogeneous fine powder and then each of the pharmaceutical formulations (tablet and capsule powder) was diluted with methanol. Appropriate solutions were prepared by taking suitable diluted aliquots and the proposed procedure was applied for analysis of the drug in the respective pharmaceutical samples under similar conditions as used to attain the calibration plot. The urine samples were obtained from laboratory personnel and diluted 100 times by phosphate buffer of pH 7.2, with the dilution process greatly reducing the matrix effect. The cyclic voltammetric method was then applied to quantify the drug in spiked human urine samples.

9.4 Results and discussion

9.4.1 Characterization of synthesized NiO-ZrO_2 nanocomposite

Figure 9.8 shows the XRD patterns for NiO-ZrO_2 nanocomposite. The average crystallite size D was calculated from the highest peaks using the Scherrer formula as shown in equation 4.1.3. The average crystallite sizes are displayed in Figure 9.8. There is contrast in the crystallite sizes among the NiO and ZrO_2 nanocomposite particles. The average crystallite sizes of NiO of 14.$\pm$1 nm is greater than 11$\pm$0.4 nm for ZrO_2.

The morphology of the NiO nanoparticles, ZrO_2 nanoparticles and the synthesized nanocomposite was studied using HRSEM and HRTEM, as depicted in Figure 9.9 and Figure 9.10, respectively. The NiO-ZrO_2 nanocomposite shows a low degree of agglomeration since the boundaries between the particles are well-defined (Figure

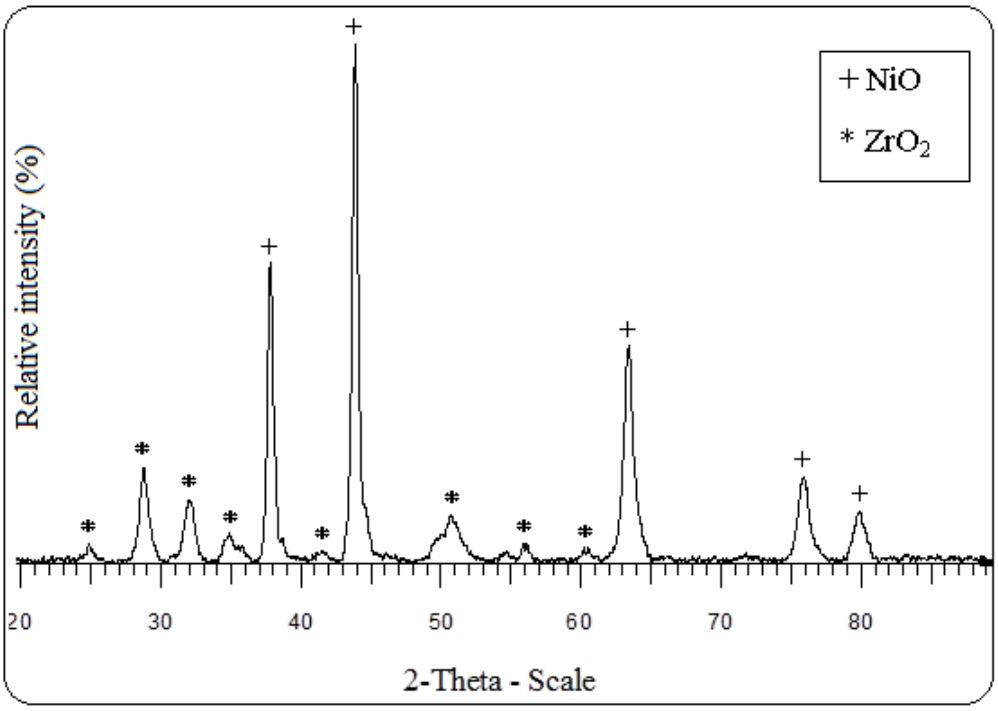

Figure 9.8: XRD patterns of NiO-ZrO_2 nanocomposite.

9.9 (C)). Furthermore, it is anticipated that smaller particles represent ZrO_2 particles whilst the larger ones show the average particle size of NiO. Figure 9.10 (D) displays the HRTEM images of NiO-ZrO_2 nanocomposite in the magnification on a 10 nm scale. The image displays lattice fringes, which indicate that the particles are crystalline. Qualitatively, the elemental composition of the nanoparticle composite was determined by EDX, revealing the presence of only Ni, Zr and O_2 in the sample, which is consistent with the composition of the starting materials. The EDX measurement for NiO-ZrO_2 nanocomposite is depicted in Figure 9.11. The nanoparticles do not interact chemically since no secondary phase was detected between NiO and ZrO_2 nanoparticles. However, there are attractive forces such as van der Waals and electrostatic forces present between the particles that lead to their agglomeration.

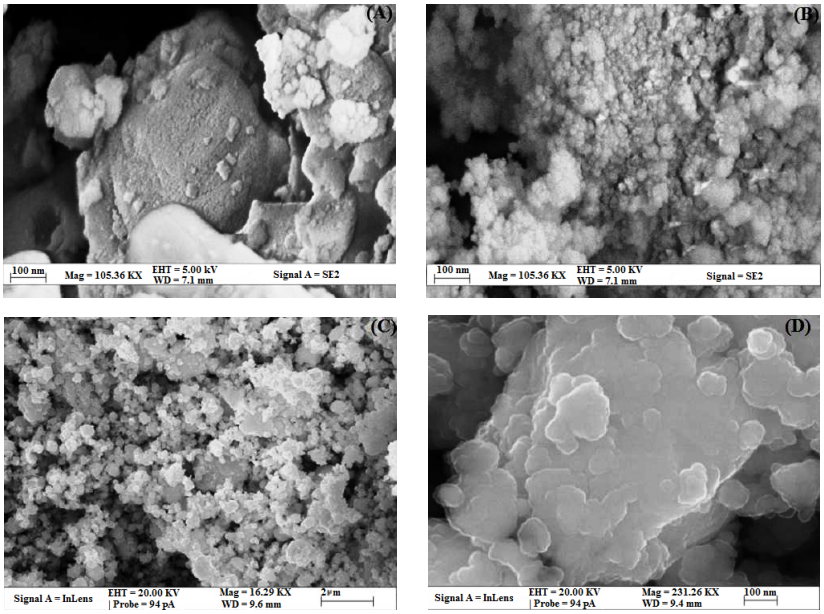

Figure 9.9: HRSEM images of (A) NiO, (B) ZrO_2 and (C) NiO-ZrO_2 nanocomposite (low magnification) and (D) NiO-ZrO_2 nanocomposite (high magnification).

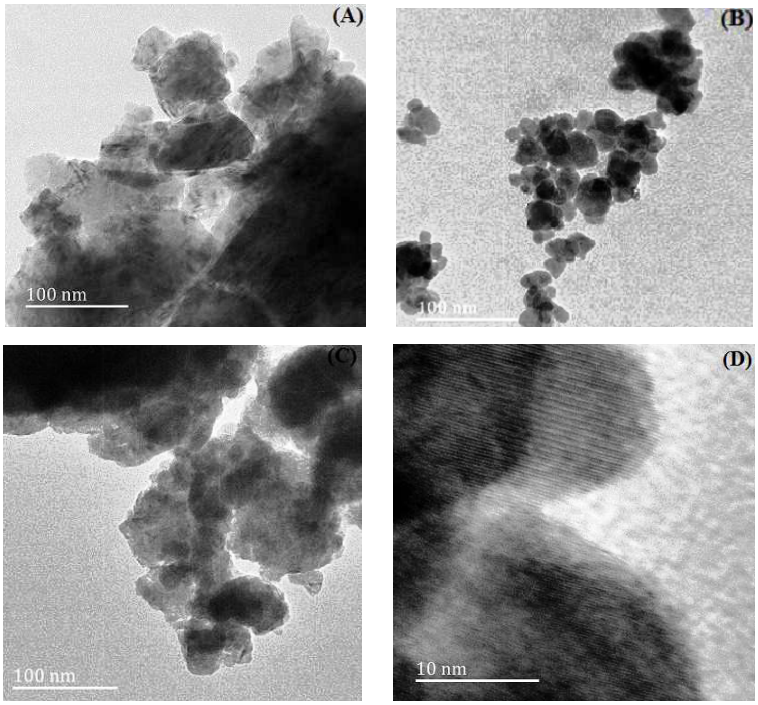

Figure 9.10: HRTEM images of (A) NiO, (B) ZrO_2 and (C) NiO-ZrO_2 nanocomposite (low magnification) and (D) NiO-ZrO_2 nanocomposite (high magnification).

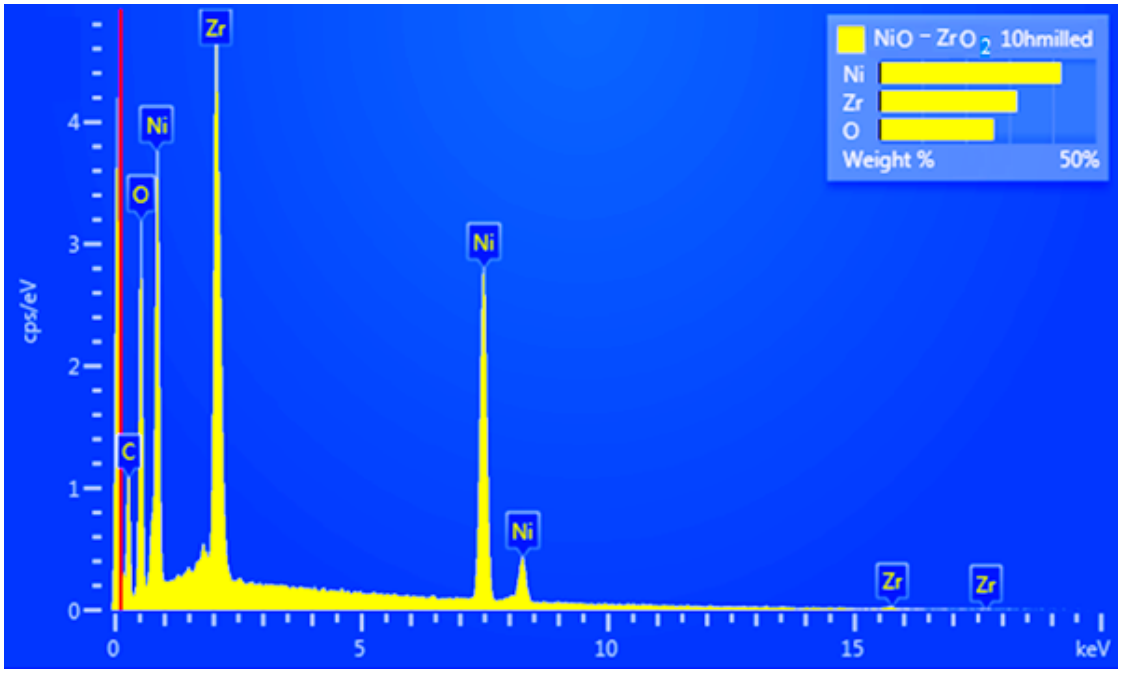

Figure 9.11: EDX image for NiO-ZrO_2 nanocomposite.

9.4.2 Electrochemical behavior of NiO-ZrO_2/GCE

The electrochemical behavior of NiO-ZrO_2/GCE was investigated using potassium ferricyanide, $K_3[Fe(CN)_6]$, as the redox probe. The cyclic voltammograms for the bare, ZrO_2 nanoparticle modified GCE (ZrO_2/GCE), NiO nanoparticle modified GCE (NiO/GCE) and NiO-ZrO_2/GCE were observed in the presence of 1 mM $K_3[Fe(CN)_6]$ in 0.1 M KCl solution, exhibiting well-defined redox peaks, as depicted in Figure 9.12. Both the ZrO_2/GCE and NiO/GCE displayed an improved peak current response as compared to the bare electrode, with the latter also showing a slight reduction in peak potential E_p. However, a significant increase in peak current accompanied with a noticeable shift in E_p was observed at the NiO-ZrO_2/ GCE, which suggests that the presence of the nanoparticle composite accelerates the rate of electron transfer at the electrode/electrolyte interface. This is attributed to the synergistic influence of NiO and ZrO_2 nanoparticles leading to good stability, strong adherence, high surface area and superior electrical conductivity of the synthesized

nanoparticles.

To determine the electroactive surface area A of NiO-ZrO_2/GCE, cyclic voltammograms of 1 mM $K_3[Fe(CN)_6]$ in 0.1 M KCl solution were recorded at varying scan rates (Figure 9.13). The area A was determined using the Randles-Sevcik equation as shown in equation 4.4.2. The diffusion coefficient D for $[Fe(CN)_6]^{3-}$ is 7.6×10^{-6} cm^2/s. Based on the slope of the i_{pa} versus $v^{1/2}$ plot (inset of Figure 9.13), the effective surface area of the modified electrode was calculated to be 0.651 cm^2, which is almost ten times more than that at bare GCE.

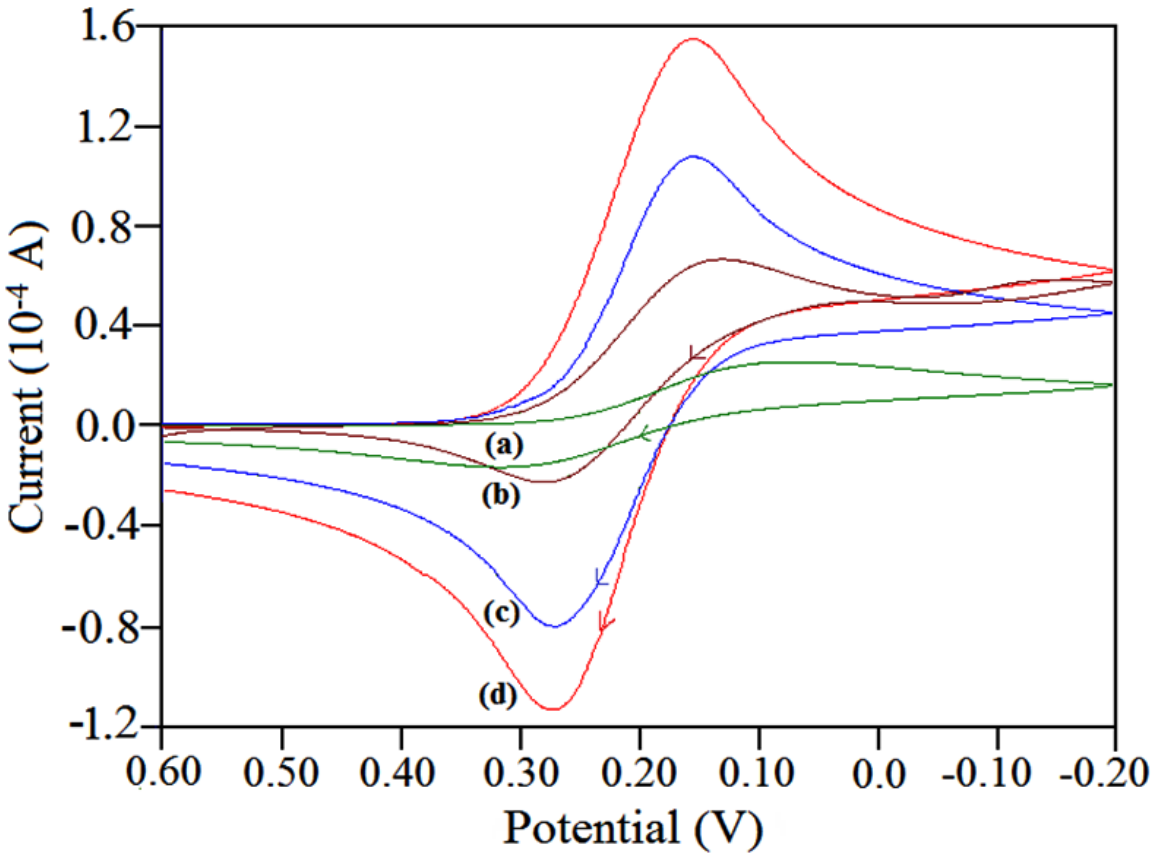

Figure 9.12: Typical cyclic voltammograms of 1 mM $K_3[Fe(CN)_6]$ in 0.1 M KCl solution at (a) bare GCE, (b) ZrO_2/GCE, (c) NiO/GCE and (d) NiO-ZrO_2/GCE at a scan rate of 50 mV/s

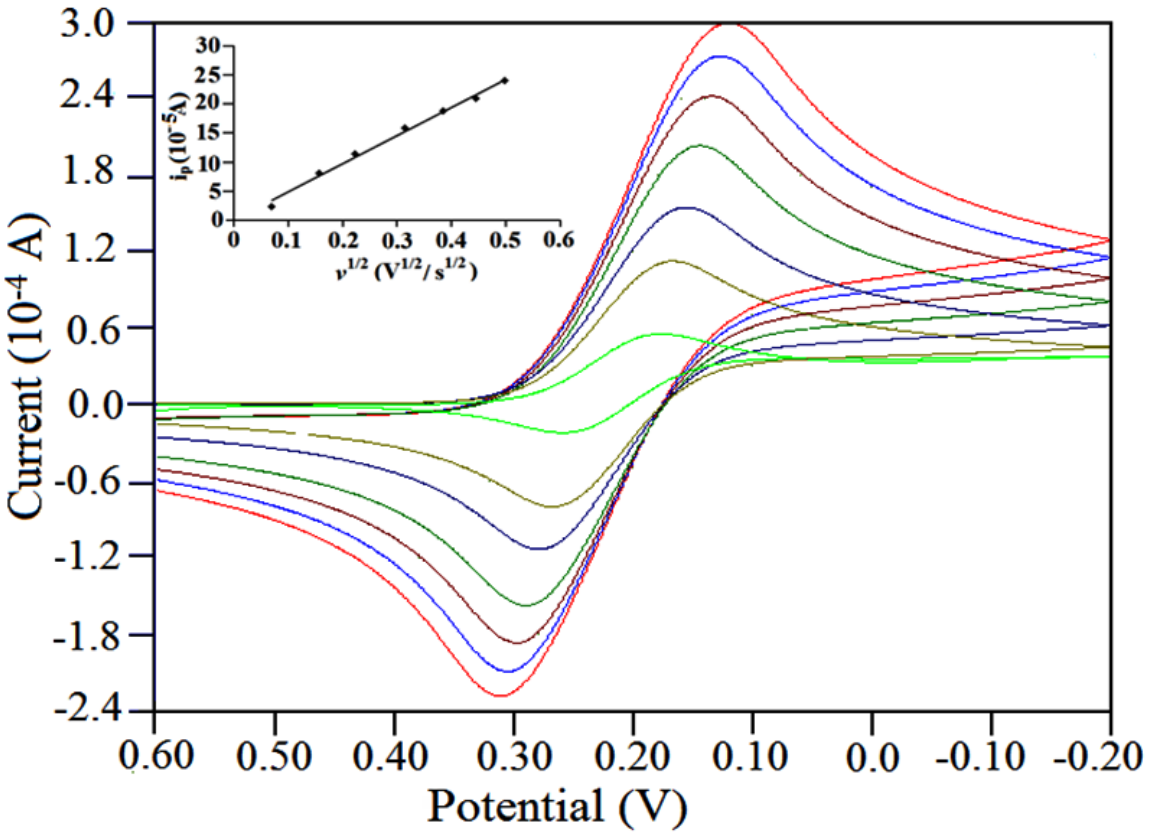

Figure 9.13: Cyclic voltammograms of 1 mM $K_3[Fe(CN)_6]$ in 0.1 M KCl solution at various scan rates (5 mV/s to 250 mV/s) using NiO-ZrO2/GCE. The inset shows the plot of dependence of i_{pa} on $v^{1/2}$ at NiO-ZrO_2/GCE.

9.4.3 Electrochemical behavior of EFV at NiO-ZrO_2/GCE

The electrochemical behavior of 10 μM EFV at bare electrode and NiO-ZrO_2/GCE was investigated at physiological pH of 7.2 using cyclic voltammetry (CV), with a weak irreversible oxidation peak being observed at 1.2 V at bare GCE. However, under similar conditions and using the modified electrode in the same solution, a well-defined oxidation peak was noticed at 1.1 V. The enhanced peak current response along with a simultaneous negative shift in peak potential clearly indicate that the NiO-ZrO_2 nanoparticle composite expresses strong electrocatalytic activity towards EFV oxidation. This is attributed to the increased surface area and improved conductivity provided by the nanocomposite leading to a significant increase in the electron transfer. Cyclic voltammograms obtained for electrochemical oxida-

tion of 10 μM EFV are illustrated in Figure 9.14. Since no peak was noticed in the reverse scan, it suggests that the electrode process is irreversible in nature.

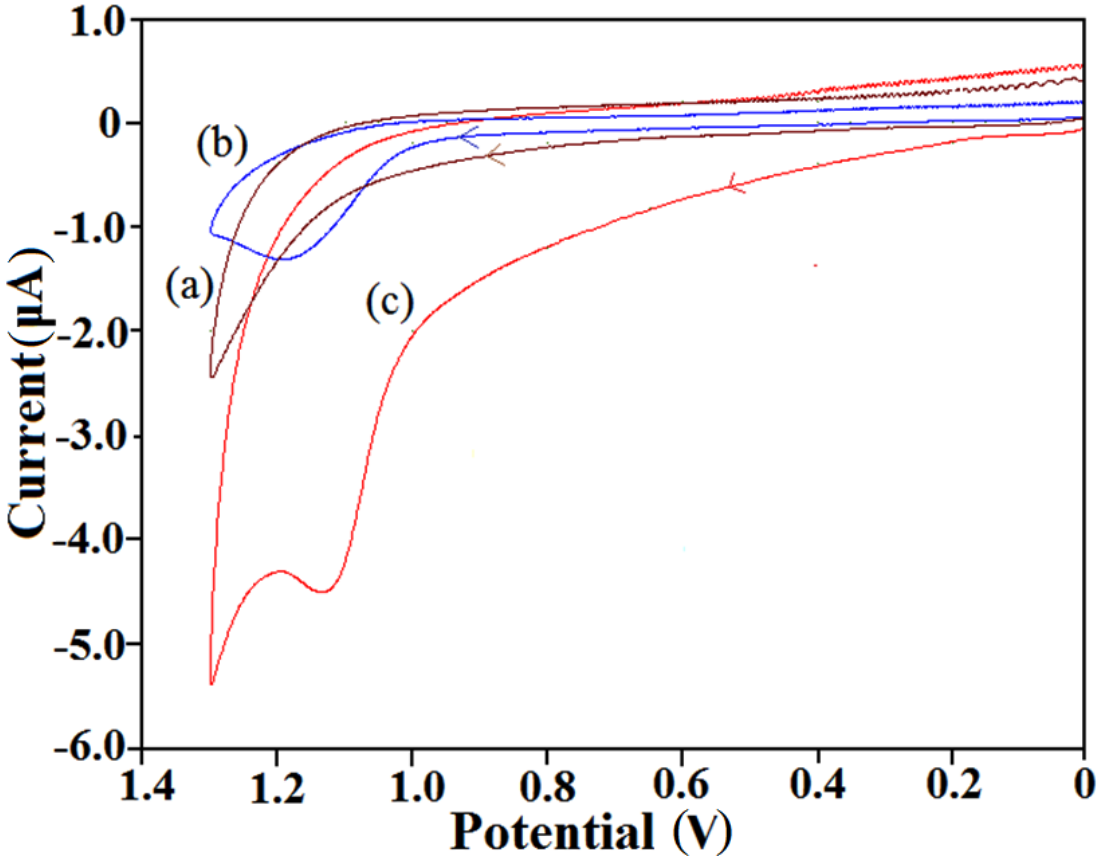

Figure 9.14: Cyclic voltammograms observed (a) in absence of EFV at NiO-ZrO_2/GCE and in presence of 10 μM EFV at (b) bare GCE and (c) NiO-ZrO_2/GCE in 0.1 M PBS (pH 7.2) at a scan rate of 100 mV/s.

The influence of scan rate on the voltammetric response of EFV was investigated at the modified electrode under similar experimental conditions. The i_p was found to be proportional to v in the range of 5 mV/s to 250 mV/s (Figure 9.15 (A)), with the linear equation being $i_p = 0.019v + 0.1274$ (R^2=0.9969), indicating an adsorption-controlled electrochemical process [163]. This is further confirmed by plotting log i_p verses log v (Figure 9.15 (B)) that exhibits a straight line with a slope of 0.9, which is close to the theoretical value of 1.0 for an ideal adsorption-controlled process [164]. It was also observed that the E_p shifted towards more positive values with an increase in scan rate (Figure 9.15 (C)), confirming the irreversibility of the

oxidation process [285]. The linear relationship between E_p and $\log v$ is represented by the equation: $E_p = 0.0485 \log v + 1.0334$, with a correlation coefficient of 0.9957. According to Laviron [161], for an irreversible electrode process, E_p can be expressed by equation $E_p = E^0 + \left[\frac{2.303RT}{\alpha nF}\right] \log \left[\frac{RTk^0}{\alpha nF}\right] + \left[\frac{2.303RT}{\alpha nF}\right] \log v$. Thus, the value of αn can be calculated from the slope of E_p versus $\log v$ by considering $T = 298$ K, $R = 8.314$ J/K mol, and $F = 96480$ C/mol. The αn value was then employed to calculate n using the equation 4.4.5 [162]. The number of electrons exchanged n was found to be one suggesting that one electron is involved in the oxidation of EFV at NiO-ZrO_2/GCE.

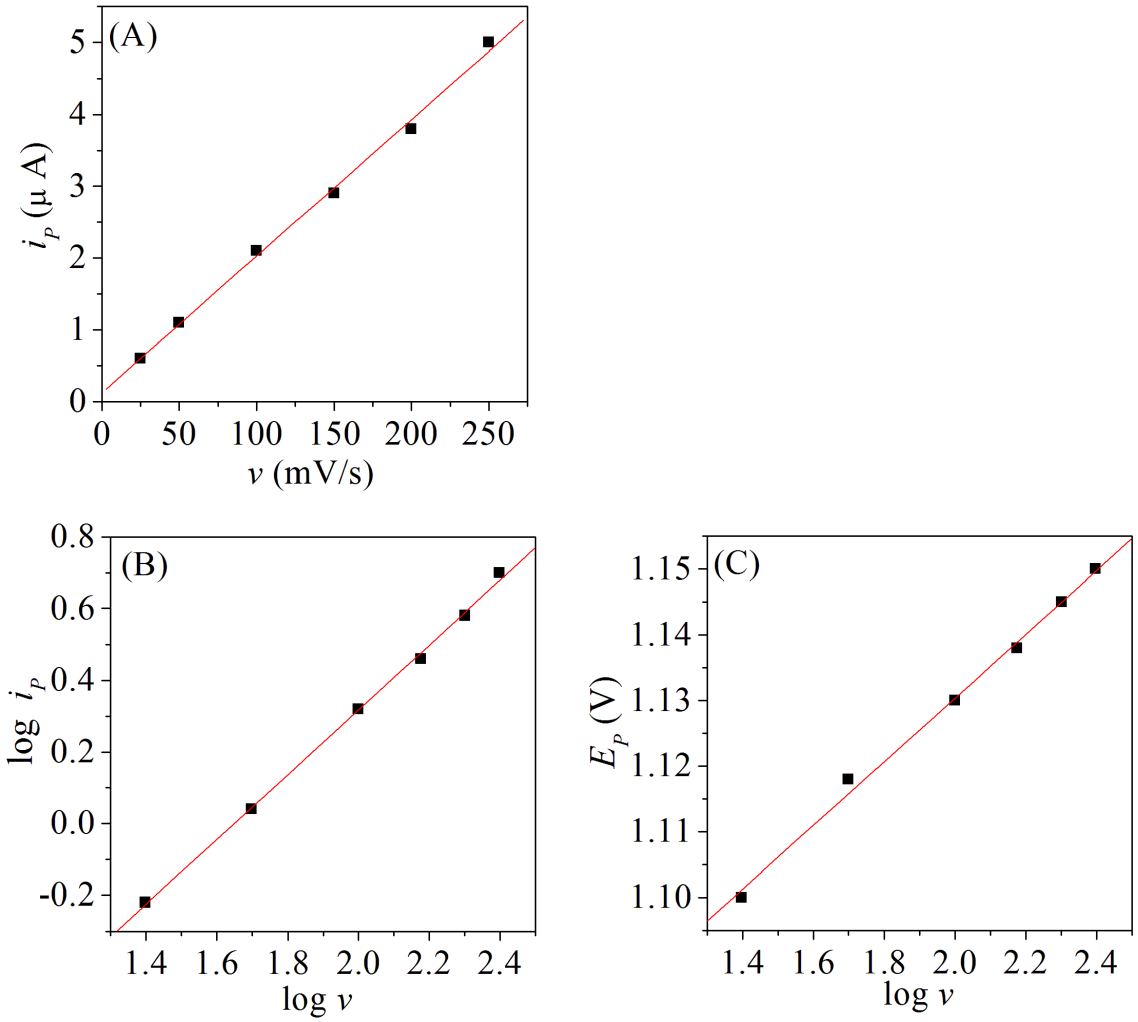

Figure 9.15: (A) Observed dependence of peak current on scan rate for 10 μM EFV at pH 7.2; (B) Variation of the logarithm of peak current with the logarithm of scan rate; (C) Plot of E_p verses logarithm of scan rate for 10 μM EFV at pH 7.2.

The effect of pH on electro-oxidation of 5 μM EFV at NiO-ZrO_2/GCE in 0.1 M PBS was investigated with pH values ranging from 4.0 to 11.0. It was observed that the E_p shifted negatively with increase in the pH value. A linear relationship was observed between E_p and pH, which is expressed by the equation: E_p (mV) = 1.549 - 0.0597 pH, with a correlation coefficient of 0.9911. A slope value of 0.0597 V/pH was obtained, which is almost equal to the theoretical Nernstian value characteristic for an electrode reaction involving same numbers of electrons and protons [165]. This suggests that equal number of protons and electrons participate in the electro-oxidation of the drug. It is anticipated that the oxidation of the nitrogen atoms occur, involving one electron and one proton and producing free radical species, as depicted in Figure 9.16.

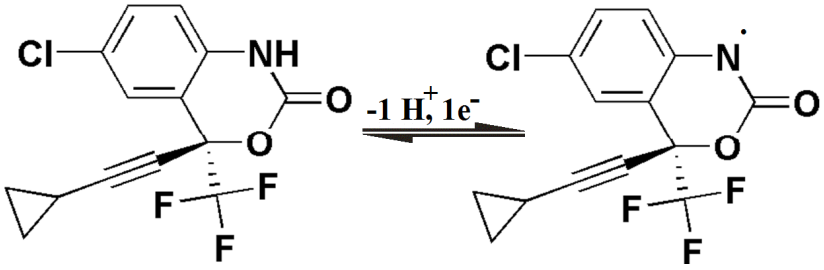

Figure 9.16: Proposed electro-oxidation mechanism of EFV.

Under optimum experimental conditions, the anodic peak current (peak height) was found to have a linear relationship with EFV concentration in the range 1.0×10^{-8} to 1.0×10^{-5} mol L^{-1} (Figure 9.17) and the linear regression equation is expressed as: i_p (μA) = $220.49C$, with a correlation coefficient of 0.9989, and where C is the concentration of EFV in mM. The detection limit for the determination of EFV was calculated to be 1.36 nM (based on three times signal-to-noise ratio). The proposed method exhibits wide linear range, high sensitivity and low detection limit.

The stability of NiO-ZrO_2/GCE was investigated by storing the electrode for 15 days and later using it to determine 10 μM EFV. A slight decrease in the peak current was observed with a relative standard deviation (RSD) of 3.6% suggesting that the modified electrode has good stability. The reproducibility of NiO-ZrO_2/GCE was checked by analysing the voltammetric response of 10 μM EFV using six electrodes

prepared independently and the RSD was found to be 2.7%. Minute variation in i_p was observed when six replicate measurements were recorded for 10 μM EFV using the same electrode (RSD = 2.11%). These results indicate that the modified electrode possesses significant stability, reproducibility and repeatability.

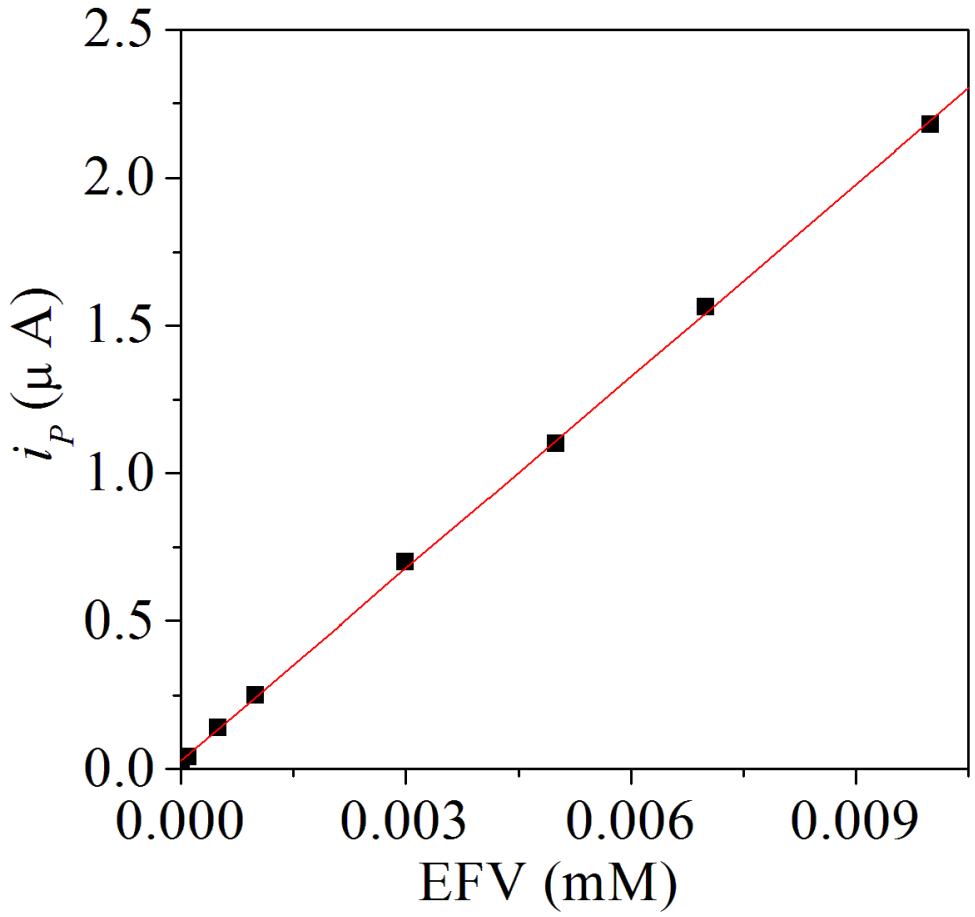

Figure 9.17: Calibration plot observed for EFV at NiO-ZrO_2/GCE at pH 7.2.

In order to evaluate the practical utility of the proposed method, the amount of EFV was quantified in three commercial pharmaceutical samples, one 600 mg tablet and two (50 mg and 200 mg) capsules. UV spectrophotometry was employed as the reference technique. Prior to the determination of EFV, the samples were dissolved in methanol and then diluted by water, so that the concentration of the drug was in the working concentration range. Cyclic voltammograms were then recorded using NiO-ZrO2/GCE. The results were found to be accurate and in good agreement with the claimed amount stated by the manufacturer (as demonstrated in Table 9.1). It

was also observed that presence of excipients in the tablet did not interfere in the quantification of the drug. Thus, the proposed method presented good accuracy and precision for determination of EFV in pharmaceutical preparations.

Table 9.1: Determination of EFV in pharmaceutical preparations at NiO-ZrO_2/GCE [a] and using UV-visible spectrophotometer[b].

Sample	Stated content (g/tablet)	Detected content (g/tablet)		R.S.D. (%) (n=3)	
		Proposed Method[a]	Reference Method[b]	Proposed Method[a]	Reference Method[b]
Tablet	0.050	0.049	0.048	1.22	0.88
Capsule-1	0.200	0.197	0.204	1.47	1.70
Capsule-2	0.600	0.602	0.602	1.03	0.75

The analytical utility of NiO-ZrO_2/GCE was also examined for drug analysis in two human urine samples. Urine samples were spiked with different quantities of EFV and the recovery study of the drug was then performed using the standard addition method. The observed results of the recovery studies are summarized in Table 9.2. The recovery rates of the spiked samples were found to be between 97.6 and 102.8%, indicating that the accuracy of the proposed method is excellent. Figure 9.18 depicts the cyclic voltammograms of the blank and EFV spiked human urine (sample 1), where the peak at 1.1 V is due to the presence of EFV, while the peak at $\sim$ 0.4 V suggests the existence of uric acid in the sample, eventually establishing that the presence of biological substances in urine did not interfere in the determination of the drug. Hence, it is clear that NiO-ZrO_2/GCE has great potential for the determination of EFV in human body fluids. A comparison of the electrochemical methods reported to determine EFV (depicted in Table 9.3) indicates that the proposed method is superior to other methods, particularly in terms of detection limit and practical analytical applicability.

Table 9.2: Recovery results obtained for EFV in human urine sample at NiO-ZrO2/GCE.

Sr. No	Added (M)		Found (M)		Recoveries (%)	
	Sample 1	Sample 2	Sample 1	Sample 2	Sample 1	Sample 2
1	1.00×10^{-6}	1.00×10^{-6}	9.84×10^{-7}	9.76×10^{-7}	98.4	97.6
2	3.00×10^{-6}	3.00×10^{-6}	2.98×10^{-6}	3.03×10^{-6}	99.3	100.4
3	5.00×10^{-6}	5.00×10^{-6}	4.99×10^{-6}	5.02×10^{-6}	99.8	100.4
4	7.00×10^{-6}	7.00×10^{-6}	7.08×10^{-6}	7.20×10^{-6}	101.1	102.8
5	1.00×10^{-5}	1.00×10^{-5}	9.89×10^{-6}	1.01×10^{-5}	98.9	101.0

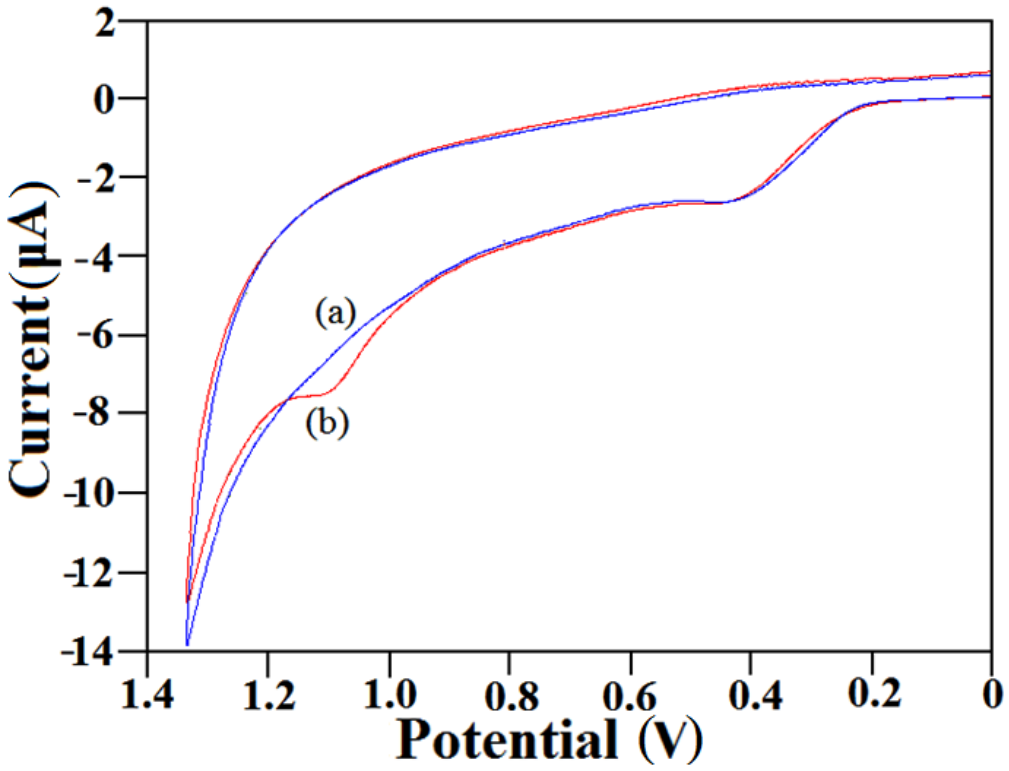

Figure 9.18: Cyclic voltammograms of (a) blank urine sample 1 and (b) urine sample 1 spiked with 10 μM standard solution of EFV, other conditions being same as in Figure 9.14.

Table 9.3: A comparison of electrochemical methods reported for determination of EFV.

Electrode	Concentration range (in M)	LOD (in M)	Applicability	Ref. No
PGE	5.70×10^{-8} to 8.11×10^{-6}	1.33×10^{-8}	In pharmaceutical	17
dsDNA/PGE	6.33×10^{-6} to 7.60×10^{-5}	1.90×10^{-6}	preparations	
TFME	3.17×10-8 to 7.92×10-7	3.00×10^{-9}	N/R	18
NiO-ZrO_2/GCE	1.00×10^{-8} to 1.00×10^{-5}	1.36×10^{-9}	In pharmaceutical preparations and human urine	Present work

LOD: Limit of detection; PGE: Pencil graphite electrode; dsDNA/ PGE: dsDNA modified PGE; TFME: Thin film mercury electrode; NiO-ZrO_2/GCE: NiO-ZrO_2 mixed nanoparticles modified glassy carbon electrode; N/R: Not Reported.

9.5 Conclusion

$Ti_{0.5}Ni_{0.5}Fe_2O_4$ nanoparticle ferrite was successfully produced by high energy ball milling. The phase structure was confirmed by XRD measurements. The spinel phase structure was formed within milling time of about 1.5 hours. Continued milling seems to be destroy the phase as shown by XRD results. The energy dispersive X-ray (EDX) results show that the elemental distribution is well spread in the sample surface. The results also confirm the presence of only Ti, Ni, Fe and O in the sample. The elemental analysis was further studied by inductively coupled plasma optical emission spectrometry (ICP-OES) measurements which provide more quantitative measurement of the elements in the sample. Room temperature ^{57}Fe Mössbauer measurements show evidence of Fe^{2+} and Fe^{3+} in the sample. We suspect that Fe^{2+} causes broadening in the line width at tetrahedral (A) site. The electrochemical measurements show enhancement in cyclic voltammetery response in the presence of potassium ferricyanide $K_3[Fe(CN)_6]$. The surface area of the modified electrode was enhanced by abut double that compared of the bare electrode.

A simple and sensitive voltammetric sensor for determination of EFV using NiO-ZrO_2/GCE was developed. The increase in the peak current at the modified sensor

is assigned to higher electrocatalytic activity and can be attributed to the combined effects of the high surface area and conductivity of NiO and ZrO_2 nanoparticles in the nanocomposite. The modified electrode has been successfully applied in the determination of EFV in pharmaceutical preparations and human urine samples. The NiO-ZrO_2/GCE can therefore be considered as a novel and promising tool for the electrochemical analysis of a range of analytes, including EFV.

Chapter 10

General conclusions

The glycol-thermal method was used to synthesize $Mg_xSr_xMn_xCo_{1-3x}Fe_2O_4$ (x = 0, 0.1, 0.2, 0.3, 1/3), $Ba_{0.5}Co_{0.5}Fe_2O_4$, $Sr_{1/3}Mn_{1/3}Co_{1/3}Fe_2O_4$ and $Ba_{1/3}Mn_{1/3}Co_{1/3}Fe_2O_4$ nanoparticles. Single phase spinel structure of the synthesized compounds was confirmed by X-ray powder diffraction (XRD). The average particle sizes of the synthesized nanoparticles were found to be in the range between 7 to 9 nm. This is associated with the low synthesis temperature of glycol-thermal technique at 200 °C. The Williamson plots show that the synthesized nanoparticles have homogeneous strain. The morphology of the samples were investigated by high resolution transmission electron microscopy (HRTEM) and high resolution scanning electron microscopy (HRSEM). The images obtained from HRTEM show that the synthesized nanoparticles have well defined crystalline structures and lattice fringes. The HRTEM measurements support the XRD results in term of crystallinity and particle sizes. The HRSEM images show regular shapes and some degree of agglomeration.

The magnetic properties were investigated by magnetization and Mössbauer measurements. Room temperature measurements for the series $Mg_xSr_xMn_xCo_{1-3x}Fe_2O_4$ (x = 0, 0.1, 0.2, 0.3, 1/3) show that substitution of Co by Mg, Sr, and Mn collapse the sextets of Mössbauer spectra gradually from x = 0 up to 1/3 by showing decreasing magnetic hyperfine fields at room temperature. The magnetizations were investigated first by a vibrating sample magnetometer (VSM) in external magnetic

fields of 14 kOe and on cryogen free measurement system CFMS in external magnetic fields of up to 50 kOe. The magnetization did not saturate even at 50 kOe indicating significant spin canting. However, the approach to saturation was deduced by fitting an empirical formula to the initial magnetization curves in order to obtain the saturation magnetization M_S. We have found significant correlation between M_S and particle sizes. The magnetization measurements were also performed in the temperature range of 2 K to 300 K, which show samples that are magnetically harder at low temperature. The results also reveal distortion in the M-H loops. The temperature dependence of the magnetization was fitted using modified Bloch's law whilst the coercive field followed Kneller's law. The sample $Mg_{0.2}Sr_{0.2}Mn_{0.2}Co_{0.4}Fe_2O_4$ shows that the substitution in the present work significantly enhances the M_S and H_C compared to the work reported in reference [170].

Triple substitution to produce (Sr, Ba)$_{1/3}$Mn$_{1/3}$Co$_{1/3}$Fe$_2$O$_4$ were achieved successfully. The Brunauer-Emmett-Teller (BET) surface area measurements and Barrett-Joyner-Halenda (BJH) measurements show high surface areas of 109.3 m^2/g and 116 m^2/g for Sr- and Ba- based samples respectively with associated mesoporous characteristic of the synthesized samples. The saturation magnetization M_S follows modified Bloch's law. The fitting of M_S values were needed an extra term to represent frozen spins at low temperature for the sample $Sr_{1/3}Mn_{1/3}Co_{1/3}Fe_2O_4$ nanoparticles. The magnetization M_S increased from 67.5 emu/g and 66.5 emu/g at 300 K to 83.5 emu/g and 84.4 emu/g at 300 K for Sr- and Ba based samples respectively. The increase of the coercive field from 0.20 kOe and 0.09 kOe at 300 K to 11.2 kOe and 10.1 kOe at 4 K for Sr- and Ba based samples respectively indicates that the samples become magnetically harder at lower temperature. The coercive field was fitted by Kneller's law in the temperature range $T < T_B$. This synthesized $Sr_{1/3}Mn_{1/3}Co_{1/3}Fe_2O_4$ nanoparticles show a significantly higher value of coercive field at room temperature compared to the work reported in reference [169]. Thermal annealing affects the structure and magnetic properties of the $Sr_{1/3}Mn_{1/3}Co_{1/3}Fe_2O_4$ nanoparticles. The sample annealed at T_A = 500 °C and measured at 4 K shows higher value of coercive field of 9.2±0.03 kOe compared to 0.24±0.03 kOe for the as-prepared sample. We associate this with the increase in crystallite sizes.

The compound $Ba_{0.5}Co_{0.5}Fe_2O_4$ was found to have a high surface area of 137 m^2/g as deduced from BET surface area measurements. The temperature dependence of its magnetization shows evidence of spin freezing at low temperature and was investigated by performing zero field cooling (ZFC) and field cooling (FC) measurements. The influence of annealing temperature T_A on the structural and magnetic properties was also investigated. As expected, the particle sizes increased as T_A increased from 200 °C to 500 °C. The saturation magnetization decreased as the T_A increased whilst the coercive field increased. The onset of an impurity phase appeared in the XRD pattern for $T_A = 600$ °C.

$Ba_{0.5}Co_{0.5}Fe_2O_4$ was used to develop highly sensitive sensor for voltammetric determination of ciprofloxacin (CFX). The results show that the $Ba_{0.5}Co_{0.5}Fe_2O_4$/GCE has excellent electrocatalytic activity towards the oxidation of CFX in a linear concentration range from 1.0×10^{-8} M to 0.5×10^{-3} M and a detection limit of 5.8 nM. The suggested method of using modified $Ba_{0.5}Co_{0.5}Fe_2O_4$/GCE was found to be simple, accurate, precise, specific and inexpensive for the determination of CFX in bulk as well as in tablet dosage forms [40].

The electrochemical activity of the synthesized $Ba_{1/3}Mn_{1/3}Co_{1/3}Fe_2O_4$ nanoparticles show high-performance of the modified GCE. Hence the electrocatalytic activity of the modified electrode further extended towards detection of didanosine, an anti-HIV drug. The modified GCE appears to have excellent electrocatalytic activity. The new electrode was highly stable, gave reproducible results and was successful in determining trace amounts of didanosine in human urine samples [321].

We have also undertaken preliminary studies of $Ti_{0.5}Ni_{0.5}Fe_2O_4$ nanoparticles and NiO-ZrO_2 nanocomposites produced by high energy ball milling techniques. The synthesis of spinel ferrites by mechanical milling usually tend to take many hours of milling and maybe followed by a long sintering process. However, the spinel structure of $Ti_{0.5}Ni_{0.5}Fe_2O_4$ was formed by milling the starting oxides for about 1.5 hours. This is a relatively short time for single phase to form in spinels. Milling for at least 2 hours appears to destroy the spinel phase. The $Ti_{0.5}Ni_{0.5}Fe_2O_4$ nanoparticles show easy single phase formation and good electrochemical activity. These are interesting results that we want to pursue in a future study. The electrocatalytic activity of

modified NiO-ZrO_2/GCE towards Efavirenz was also studied which were found to show strong electrocatalytic response. The modified electrode shows simplicity in preparation, appreciable stability, reproducibility and high sensitivity [288]. The modified electrodes discussed in this thesis are expected to lead to the development of a new class of electrochemical sensors.

The technological needs for different applications and theoretical interests have encouraged researchers to devote their efforts to the synthesis, characterization and optimization of properties of nanoparticle materials. This thesis has shown that the spinel structure can accommodate a considerable number of different cations which can lead to a large number of diverse compounds. We have undertaken structural, magnetic and electrochemical studies of $Ba_{0.5}Co_{0.5}Fe_2O_4$ nanoparticles. This work was expanded to include the study of $Ba_xCo_{1-x}Fe_2O_4$ nanoparticles (for $0 < x \leq 1$). The effect of annealing temperature on the structure and magnetic properties were investigated for the samples of $Mg_xSr_xMn_xCo_{1-3x}Fe_2O_4$ (where $0 < x \leq 1/3$) and $Ba_{1/3}Mn_{1/3}Co_{1/3}Fe_2O_4$.

The electrochemical study has provided the opportunity to synthesize nanoparticles that can lead to low detection limits in wider concentration ranges for cyclic voltammetry (CV). We now plan to produce nanomaterials with other metal substitutions that can optimize the sensitivity of CV detection with possible applications for malaria drugs in human hosts. The sample of $Ti_{0.5}Ni_{0.5}Fe_2O_4$ nanoparticles shows interesting results. Further investigations of the structure, magnetic and electrochemical behaviour will be required. Ti and Ni substituted perovskites will also be interesting to study because of possible Ni-Ti interactions that are known to be associated with memory effects in alloys.

Future work can also involve the study of electrical properties of the compounds studied here.

Bibliography

[1] C. Carter, M. Norton, *Ceramic Materials Science and Engineering*, Springer, New York (2007) 212–15.

[2] M. Sugimoto, The Past, Present and Future of Ferrites, J. Am. Ceram. **82** (1999) 269–280.

[3] P. Lorrain, F. Lorrain, S. Houle, *Magneto-Fluid Dynamics*, Springer Science + Business Media, 1st Ed, New York (2006) 4–13.

[4] S. Algude, S. Patange, S. E. Shirsath, D. Mane, K. Jadhav, Elastic Behaviour of Cr^{3+} Substituted Co-Zn Ferrites, J. Magn. Magn. Mater. **350** (2014) 39–41.

[5] A. Goldman, *Modern Ferrite Technology*, Van Nostrand Reinhold, New York **350** (1990) 64–65.

[6] E. Roess, Soft Magnetic Ferrites and Applications in Telecommunication and Power Converters, IEEE Trans. Magn. Magn. **18** (1982) 1529.

[7] S. Rybchenko, Y. Fujishiro, H. Takagi, M. Awano, Effect of Grain Boundaries on the Magnetoresistance of Magnetite, Phys. Rev. B. **72** (2005) 054424.

[8] J. García, G. Subias, The Verwey Transition-a New Perspective, J. Phys: Condens. Matter. **16** (2004) R145.

[9] M. Bibes, A. Barthelemy, Oxide Spintronics, IEEE Trans. Elec Dev. **54** (2007) 1003.

[10] D. Mathew, R. Juang, An Overview of the Structure and Magnetism of Spinel Ferrite Nanoparticles and Their Synthesis in Microemulsions, J. Chem. Eng. **129** (2007) 51–65.

[11] P. Tailhades, C. Bonningue, A. Rousset, L. Bouet, I. Pasquet, S. Lebrun, About the Interesting Properties of Mixed-Valence Defect Spinel Ferrites for Mass Storage Media, J. Magn. Magn. Mater. **193** (1999) 148–151.

[12] K. Standley, *Oxide Magnetic Materials*, Oxford University Press, 2nd Ed. (1972) 291.

[13] T. Shanmugavel, S. Raj, G. K. G. Rajarajan, Tailoring the Structural and Magnetic Properties and of Nickel Ferrite by Auto Combustion Method, Proc. Mater. Sci. **6** (2014) 1725–1730.

[14] M. Kooti, M. Afshari, Magnetic Cobalt Ferrite Nanoparticles as an Efficient Catalyst for Oxidation of Alkenes, Sci. Iranica. **19** (2012) 1991–1995.

[15] G. White, C. Patton, Magnetic Properties of Lithium Ferrite Microwave Materials, J. Magn. Magn. Mater. **9** (1978) 299–317.

[16] A. Vassiliev, A. Lagrange, Propriétés des Ferrites de Lithium Partiellement Substitués par l' Aluminum Destines aux Dispositifs Micro-Ondes, IEEE Trans. Magn. Magn. **2** (1966) 707.

[17] M. Pena, J. Fierro, Chemical Structure and Performance of Perovskite Oxides, Chem. Rev. **101** (2001) 1981.

[18] J. Sloczynski, J. Janas, T. Machej, J. Rynkowski, J. Stoch, Catalytic Activity of Chromium Spinels in SCR of NO with NH_3, J. Appl. Catal B. **25** (2000) 45–60.

[19] Y. Kim, D. Kim, C. Lee, Synthesis and Characterization of $CoFe_2O_4$ Magnetic Nanoparticles Prepared by Temperature-Controlled Coprecipitation Method, Physica B. **337** (2003) 42–51.

[20] H. He, Magnetic Properties of $Co_{0.5}Zn_{0.5}Fe_2O_4$ Nanoparticles Synthesized by a Template-Assisted Hydrothermal Method, J. Nanotech. **2011** (2011) 182543.

[21] L. Bracke, High-Frequency Ferrite Power Transformer and Choke Design-Part 2: Switched-Mode Power Supply Magnetic Considerations and Core Selection, Eletr. Comp. Appl. **5** (1983) 171.

[22] X. Zuo, B. Barbiellini, C. Vittoria, Calculation of Exchange Constants in Manganese Ferrite ($MnFe_2O_4$), J. Magn. Magn. Mater. **272** (2004) 306–311.

[23] J. Smit, H. Wijn, *Ferrites*, Holand, 2nd Ed, 1959.

[24] T. Ahmed, I. Rahman, M. Rahman, Study on the Properties of the Copper Substituted NiZn Ferrites, J. Mater. Proces. Technol. **153-154** (2004) 797–803.

[25] X. Meng, H. Li, J. Chen, L. Mei, K. Wang, X. Li, Mössbauer Study of Cobalt Ferrite Nanocrystals Substituted with Rare-Earth Y^{3+} ions, J. Magn. Magn. Mater. **321** (2009) 1155–1158.

[26] D. McClure, The Distribution of Transition Metal Cations in Spinels, J. Phys. Chem. Solids. **3** (1957) 311–317.

[27] J. Dunitz, L. Orgel, Electronic Properties of Transition-metal Oxides-—: Distortions from Cubic Symmetry, J. Phys. Chem. Solids. **3** (1957) 20–29.

[28] M. Isfahani, M. Myndyk, V. Šepelák, J. Amighian, A Mössbauer Effect Investigation of the Formation of MnZn Nanoferrite Phase, J. Alloys. Comps. **470** (2009) 434–437.

[29] T. Verdier, V. Nachbour, M. Jean, Mechanosynthesis of Zinc Ferrite in Hardened Steel Vials: Influence of ZnO on the Appearance of Fe(II), J. Solid State Chem. **178** (2005) 3243–3250.

[30] D. Varshney, K. Verma, A. Kumar, Substitutional Effect on Structural and Magnetic Properties of $A_xCo_{1-x}Fe_2O_4$ (A = Zn, Mg and x = 0.0, 0.5) Ferrites, J. Mol. Struct. **1006** (2011) 447–452.

[31] V. Harris, N. Koon, C. Williams, M. A. Q. Zhang, J. Kirkland, Cation Distribution in NiZn-Ferrite Films via Extended X-ray Absorption Fine Structure, Appl. Phys. Lett. **68** (1996) 2082.

[32] A. Goldman, *Modern Ferrite Technology*, 2nd Ed. Springer (2010) 9–14,17–21, 52, 55.

[33] S. Yu, T. Fujino, M. Yoshimura, Hydrothermal Synthesis of $ZnFe_2O_4$ Ultrafine Particles with High Magnetization, J. Magn. Magn. Mater. **256** (2003) 420–424.

[34] A. Lakshman, K. Rao, R. Mendiratta, Magnetic Properties of In^{3+} and Cr^{3+} Substituted Mg-Mn Ferrites, J. Magn. Magn. Mater. **250** (2002) 92–97.

[35] L. Kong, W. Zhu, O. Tan, $PbTiO_3$ Ceramics Derived from High-Energy Ball Milled Nano-sized Powders, J. Mater. Sci. Lett. **19** (2000) 1963–1966.

[36] A. Lakshman, P. Rao, K. Rao, Mössbauer Spectroscopic Analyses of $Mg_{0.9}Mn_{0.1}In_xFe_{2-x}O_4$ Spinel Ferrites, J. Magn. Magn. Mater. **284** (2004) 352–357.

[37] C. Torres, L. Schaeffer, Effect of High Energy Milling on the Microstructure and Properties of WC-Ni Composite, Mater Res. **13** (2010) 293–298.

[38] V. Chakka, B. Altuncevahir, Z. Jin, Y. Li, J. Liu, Magnetic Nanoparticles Produced by Surfactant-Assisted Ball Milling, J. App. Phys. **99** (2006) 08E912.

[39] R. Rameshbabu, R. Ramesh, S. Kanagesan, A. Karthigeyan, S. Ponnusamy, Synthesis of Superparamagnetic $ZnFe_2O_4$ Nanoparticle by Surfactant Assisted Hydrothermal Method, J Mater Sci: Mater Electron. **24** (2013) 4279–4283.

[40] N. Osman, N. Thapliyal, W. Alwan, R. Karpoormath, T. Moyo, Synthesis and Characterization of $Ba_{0.5}Co_{0.5}Fe_2O_4$ Nanoparticle Ferrites: Application as Electrochemical Sensor for Ciprofloxacin, J Mater Sci: Mater Electron. **24** (2015) 1–9.

[41] C. Yan, Z. Xu, F. Cheng, C. L. Z.M. Wang, L.D. Sun, J. Jia, Nanophased $CoFe_2O_4$ Prepared by Combustion Method, Solid State Commun. **111** (1999) 287–291.

[42] M. Atif, S. Hasanain, M. Nadeem, Magnetization of Sol-Gel Prepared Zinc Ferrite Nanoparticles: Effects of Inversion and Particle Size, Solid State Commun. **138** (2006) 416–421.

[43] J. Livage, M. Henry, C. Sanchez, Sol-Gel Chemistry of Transition Metal Oxides, Solid State Chem. **18** (1988) 259–341.

[44] A. Chatterjee, D. Das, S. Pradhan, D. Chakravorty, Synthesis of Nanocrystalline Nickel-zinc Ferrite by the Sol-Gel Method, J. Magn. Magn. Mater. **127** (1993) 214–218.

[45] D.-H. Chen, X. He, Synthesis of Nickel Ferrite Nanoparticles by Sol-Gel Method, Mater. Res. Bull. **36** (2001) 1369–1377.

[46] J. Kingsley, K. Patil, A Novel Combustion Process for the Synthesis of Fine Particle α-Alumina and Related Oxide MaterialsOriginal, Mater. Lett. **6** (1998) 427–432.

[47] L. Néel, Magnetic Properties of Femtes: Ferrimagnetism and Antiferromagnetism, Annu. Phs. **3** (1948) 137–98.

[48] A. Gadkari, T. Shinde, P. Vasambekar, Synthesis, Characterization and Magnetic Properties of La^{3+} Added Mg-Cd Ferrites Prepared by Oxalate Co-Precipitation Method, J. Alloys Comp. **509** (2011) 966–972.

[49] Q. Zhang, D. Li, W. Cui, J. Li, Z. Zhang, Magnetic Properties and Spin-Glass-Like Behavior in Stoichiometric Mn_3In Compound, J. App. Phys. **106** (2009) 113915.

[50] C. Alves, R. Aquino1, J. Depeyrot, T. A. Cotta, M. Sousa, F. Tourinho, H. Rechenberg, G. Goya, Surface Spin Freezing of Ferrite Nanoparticles Evidenced by Magnetization Measurements, Appl. Phys. **99** (2006) 08M905.

[51] K. Nadeem, H. Krenn, Exchange Bias, Memory and Freezing Effects in $NiFe_2O_4$ Nanoparticles, J Supercond Nov Magn. **24** (2011) 717–720.

[52] Q. Chen, Z. Zhang, Size-dependent Superparamagnetic Properties of $MgFe_2O_4$ spinel Ferrite Nanocrystallites, Appl Phys Lett. **73(21)** (1998) 3156.

[53] T. Sugimoto, Fine Particles: Synthesis, Characterization, and Mechanisms of Growth, Marcel Dekker, Inc. New York. **92** (2000) 663.

[54] S. Shannigrahi, K. Pramoda, F. Nugroho, Synthesis and Characterizations of Microwave Sintered Ferrite Powders and their Composite Films for Practical Applications, J. Magn. Magn. Mater. **324** (2012) 140–145.

[55] P. Sivakumar, R. Ramesh, A. Ramanand, S. Ponnusamy, C. Muthamizhchelvan, Synthesis and Characterization of $NiFe_2O_4$ Nanoparticles and Nanorods, J. Alloys Comp. **563** (2013) 6–11.

[56] B. Viswanathan, V. Murthy, *Indian Institute of Technology Madras*, Vol. **3**, 1990.

[57] P. Thang, G. Rijnders, D. Blank, Spinel Cobalt Ferrite by Complexometric Synthesis, J. Magn. Magn. Mater. **295** (2005) 251–256.

[58] Q. Dai, D. Berman, K. Virwani, J. Frommer, P.-O. Jubert, M. Lam, T. Topuria, W. Imaino, Self-Assembled Ferrimagnet-Polymer Composites for Magnetic Recording Media, A. Nelson, Nano. Lett. **10** (2010) 3216–3221.

[59] L. Boutiuc, I. Dumitru, O. Caltun, M. Feder, V. Vilceanu, Coprecipitated Cobalt Ferrite for Sensors, Sens. Lett. **7** (2009) 244–246.

[60] K. Stojak, S. Pal, H. Srikanth, C. Morales, J. Dewdney, T. Weller, J. Wang, Polymer Nanocomposites Exhibiting Magnetically Tunable Microwave Properties, Nanotech. **22** (2011) 135602.

[61] N. Mostafaa, M. Hessiena, A. Shaltouta, Hydrothermal Synthesis and Characterizations of Ti Substituted Mn-Ferrites, J. Alloy. Comp. **529** (2012) 29–33.

[62] S. Maensiri, M. Sangmanee, A. Wiengmoon, Magnesium Ferrite ($MgFe_2O_4$) Nanostructures Fabricated by Electrospinning, Nanoscale Res Lett. **4(3)** (2009) 221–228.

[63] A. Pradeep, P. Priyadharsini, G. Chandrasekaran, Sol-Gel Route of Synthesis of Nanoparticles of $MgFe_2O_4$ and XRD, FTIR and VSM study, J. Magn. Magn. Mater. **320** (2008) 2774–2779.

[64] D. Bahadur, Current Trends in Applications of Magnetic Ceramic Materials, Bull. Mater. Sci. **15** (1992) 431–439.

[65] I. Sharifi, H. Shokrollahi, S. Amiri, Ferrite-Based Magnetic Nanofluids Used in Hyperthermia Applications, J. Magn. Magn. Mater. **324** (2012) 903–915.

[66] J. Lee, Y. Huh, Y. Jun, J. Seo, J. Jang, H. Song, S. Kim, E. Cho, H. Yoon, J. S. uh, J. Cheon, Artificially Engineered Magnetic Nanoparticles for Ultra-Sensitive Molecular Imaging, Nat. Med. **13** (2007) 95–99.

[67] A. Gupt, M. Gupta, Synthesis and Surface Engineering of Iron Oxide Nanoparticles for Biomedical Applications, Biomate. **26(18)** (2005) 3995–4021.

[68] M. Latorre-Esteves, A. Cortés, M. Torres-Lugo, C. Rinaldi, Synthesis and Characterization of a Novel Carboxymethyl Dextran-Coated Mn/Zn Ferrite for Biomedical Applications, J. Magn. Magn. Mater. **321** (2009) 3061–3066.

[69] Y. Ahn, E. Choi, S. Kim, H. Ok, Magnetization and Mössbauer Study of Cobalt Ferrite Particles from Nanophase Cobalt Iron Carbonate, Mater. Lett. **50** (2001) 47.

[70] S. Gangopadhyay, G. Hadjipanayis, B. Dale, C. Sorenson, K. Klabunde, V. Papaefthymiou, A. Kostikas, Magnetic Properties of Ultrafine Iron Particles, Phys. Rev. B. **45** (1992) 9778.

[71] M. Pumera, M. Castaneda, M. Pividori, R. Eritja, A. Merkoçi, S. Alegre, Magnetically Trigged Direct Electrochemical Detection of DNA Hybridization Using Au67 Quantum Dot as Electrical Tracer, Langmuir. **21** (2005) 9625–9629.

[72] D. Ye, Y. Xu, L. Luo, Y. Ding, Y. Wang, X. Liu, $LaNi_{0.5}Ti_{0.5}O_3/CoFe_2O_4$-Based Sensor for Sensitive Determination of Paracetamol, J. Solid State Electrochem. **16** (2012) 1635–1642.

[73] J. Wang, A. Kawde, Magnetic-Field Stimulated DNA Oxidation, Electrochem. Commun. **4** (2002) 349–352.

[74] J. Wang, D. Xu, R. Polsky, Magnetically-Induced Solid-state Electrochemical Detection of DNA Hybridization, J. Am. Chem. Soc. **124** (2002) 4208–4209.

[75] G. Zhao, J. Feng, Q. Zhang, S. Li, H. Chen, Synthesis and Characterization of Prussian Blue Modified Magnetite Nanoparticles and Its Application to the Electrocatalytic Reduction of H_2O_2, Chem. Mater. **17** (2005) 3154–3159.

[76] R. Goyal, A. Tyagi, N. Bachheti, S. Bishnoi, Voltammetric Determination of Bisoprolol Fumarate in Pharmaceutical Formulations and Urine Using Single-Wall Carbon Nanotubes Modified Glassy Carbon Electrode, Electrochim. Acta. **53** (2008) 2802–2808.

[77] R. Goyal, N. Bachheti, A. Tyagi, A. Pandey, Differential Pulse Voltammetric Determination of Methylprednisolone in Pharmaceuticals and Human Biological Fluids, Anal. Chim. Acta. **605** (2007) 34–40.

[78] J. Bockris, B. Conway, R. White, *Modern aspects of electrochemistry*, Vol. vol. 34, New York, 2001.

[79] C. Brett, A. Brett, *Electroanalysis*, Vol. , Oxford University Press, Oxford, 1998.

[80] A. Andrew, Focus on Electrochemistry: Bringing Electrochemistry to Life, Chem. Soc. Rev. **26** (1997) iiib–iv.

[81] S. Setford, S. White, J. Bolbot, Measurement of Protein Using an Electrochemical Bi-Enzyme Sensor, Biosens. Bioelectron. **17** (2002) 79–86.

[82] T. Hong, J. Kyong, H. Lee, M. Czae, Determination of Estrone by Adsorptive Stripping Voltammetry, Anal. Sci. Technol. **12** (1999) 34–39.

[83] K. Shiu, K. Shi, Selective Determination of Vitamin B-2 at Electrochemically Activated Glassy Carbon Electrode, Electroanal. **12** (2000) 134–139.

[84] M. Goulart, A. Sant́Ana, E. Rocha, G. Fontes, *in Electroanalytical Aspects of Biological Significant Compounds*, Transworld Research Network, (2006) pp. 1.

[85] D. Li, Y. Chen, *Computer and Computing Technologies in Agriculture VII*, Springer Heidelberg New York Dordrecht London, (2014) pp. 454.

[86] S. Aravamudhan, *Development of Micro/Nanosensors Elements and Packaging Techniques for Oceanography*, University of South Florida, (2007) pp. 112.

[87] M. Couper, D. Pletcher, F. Walsh, Electrode Material for Electrosynthesis, Chem. Rev. **90** (1990) 837–860.

[88] A. Kaplin, N. Pikula, E. Neiman, Electrodes in Voltammetry, Zhurn. Analyt. Khim. **45** (1990) 2086–120.

[89] W. Heineman, H. Wieck, A. Yacynych, Polymer Film Chemically Modified Electrode as a Potentiometric Sensor, Anal. Chem. **52** (1980) 345–346.

[90] A. Merkoci, Electrochemical Biosensing with Nanoparticles, FEBS J. **274** (2007) 310–316.

[91] X. Luo, A. Morrin, A. Killard, M. Smyth, Application of Nanoparticles in Electrochemical Sensors and Biosensors, Electroanal. **18** (2006) 319–326.

[92] S. Higson, *Biosensors for Medical Applications*, Woodhead Publishing Limited, Sawston, Cambridge. (2012) pp. 67.

[93] L. Zhang, X. Jiang, E. Wang, S. Dong, Attachment of Gold Nanoparticles to Glassy Carbon Electrode and its Application for the Direct Electrochemistry and Electrocatalytic Behavior of Hemoglobin, Biosens. Bioelectron. **21** (2005) 337–45.

[94] J. Tashkhourian, S. Nami-Ana, A Sensitive Electrochemical Sensor for Determination of Gallic Acid Based on SiO_2 Nanoparticle Modified Carbon Paste Electrode, Mater. Sci. Eng. C: Mater. Biol. Appl. **52** (2015) 103–110.

[95] M. Fouladgar, H. Maleh, V. Gupta, Highly Sensitive Voltammetric Sensor Based on NiO Nanoparticle Room Temperature Ionic Liquid Modified Carbon Paste Electrode for Levodopa Analysis, J. Mol. Liq. **208** (2015) 78–83.

[96] I. Gul, E. Pervaiz, Comparative Study of $NiFe_{2-x}Al_xO_4$ Ferrite Nanoparticles Synthesized by Chemical Co-Precipitation and Sol-Gel Combustion Techniques, Mater. Res. Bull. **47** (2012) 1353–1361.

[97] L. Jaswal, B. Singh, Ferrite Materials: A Chronological Review, J Integr Sci Technol. **2** (2014) 69–71.

[98] K. Zaharieva, Z. Cherkezova-Zheleva, B. Kunev, I. Mitov, S. Dimova, Impact of Chemical Composition on Preparation of Nanodimensional Spinel Ferrites, BULG CHEM COMMUN. **47** (2015) 261–267.

[99] S. Disch, *The Spin Structure of Magnetic Nanoparticles and in Magnetic Nanostructures*, Forschungszentrum Jülich GmbH, Aachen University, (2011) p. 2.

[100] J. Keithley, *The Story of Electrical and Magnetic Measurements*, Institute of Electrical and Electronice Engineers. Inc, New York, (2011) p. 2.

[101] D. Lovejoy, *Magnetism and magnetic properties of materials*, Springer (1993) pp. 321–343.

[102] F. Shellock, *Magnetic Resonance Procedures: Health Effects and Safety*, Printed in United State of America, Florida (2001) pp. 3.

[103] W. Lowrie, *Fundamentals of Geophysics*, United State of America, Cambridge Press, New York, (2007) pp. 281.

[104] J. Coey, *Magnetism and Magnetic Materials*, Cambridge University (2010) 2, 24–25, 110–111, 218–244.

[105] A. Guimaräes, *Magnetism and Magnetic Resonance in Solids*, John Wiley & Sons, Inc. (1988) 47–49.

[106] M. Getzlaff, *Fundamentals of Magnetism*, Springer-Verlag Berlin Heidelberg, (2008) P. 1–4, 96–133.

[107] A. P. Guimaräes, *Magnetism and Magnetic Resonance in Solids*, John Wiley and Sons, Inc (1998) 12–18.

[108] N. Spaldin, *Magnetic Materials Fundamentals and Applications*, 2^{nd}edition Cambridge, New York, (2011) pp. 42.

[109] M. Simon, A. Geim, Diamagnetic levitation: Flying frogs and floating magnets (invited), J. Appl. Phys. **87** (2000) 9.

[110] M. Bruce, *Hitchhiker's Guide to Magnetism*, Environmental Magnetism Workshop held at the Institute for Rock Magnetism, University of Minnesota USA, 5-8 June 1991 .

[111] S. Blundell, *Magnetism in Condensed Matter*, University of Oxford (2001) p.23, 141, 197.

[112] C. Hurd, *Varieties of Magnetic Order in Solids*, Contemporary Phys. **23(5)** (1982) 469.

[113] G. Dionne, *Magnetism and Magnetic Materials*, Springer, London, UK, p. 400-410, 2009.

[114] H. Abdallah, *Synthesis, Magnetic and Electrical Characterizations of Nanoparticle Ferrites*, University of KwaZulu-Natal (2012) PhD thesis,.

[115] J. Solyom, *Fundamentals of the Physics of Solids*, Springer-Verlag Berlin, (2007) p. 450–496.

[116] M. Fujimoto, *Physics of Classical Electromagnetism*, Springer Science & Business Media, LLC, New York, USA, (2007) p. 85.

[117] T. Moyo, *Lectures notes in Magnetism,*, University of KwaZulu-Natal.

[118] H. Ibach, H. Lüth, *Solid State Physics: An Introduction ti Theory and Experiment,*, third edition, Springer-Verlage, Berlin Heidleberg, (1190) p. 127–158.

[119] J. Wang, H. Duan, X. Lin, V. Aguilar, A. Mosqued, G. Zhao, Temperature Dependence of Magnetic Anisotropy Constant in Iron Chalcogenide Fe_3Se_4: Excellent Agreement with Theories, J. Appl. Phys. **112** (2012) 103905.

[120] A. Goldman, *Modern Ferrite Technology*, Springer Science + Business Media, New York, (2006) P.24, 52–53.

[121] K. Buschow, F. Boer, *Physics of Magnetism and Magnetic Materials*, Universiteit van Amsterdam, (2004) P. 10.

[122] S. BLUNDELL, *Magnetism in Condensed Matter*, Oxford University, (2001) P. 141.

[123] C. Liu, B. Zou, A. Rondinone, Z. Zhang, Chemical Control of Superparamagnetic Properties of Magnesium and Cobalt Spinel Ferrite Nanoparticles Through Atomic Level Magnetic Couplings, J. Am. Chem. **122** (2000) 6263.

[124] A. Putnis, *Introduction to mineral Sciences*, Cambridge University Press, UK, (1992) p. 440.

[125] J. Stöhr, H. Siegmann, *Magnetism from Fundamentals to Nanoscale Dynamics*, Springer-Verlag Berlin Heidelberg, (2006) p. 511–521.

[126] D. Pelecky, Magnetic Properties of Nanostructured Materials, Chem. Mater. **8** (1996) 1770–1783.

[127] J. Liu, W. Ren, D. Li, N. Sun, X. Zhao, J. Li, Z. Zhang, Magnetic Transitions and Magnetostrictive Properties of Tb_x Dy_{1-x} $(Fe_{0.8}$ $Co_{0.2})2$ $(0.20 \leq x \leq 0.40)$, Phys. Rev. B. **75** (2007) 064429.

[128] C. Bean, J. Livingston, Superparamagnetism, J. Appl. Phys. **30** (1959) S120.

[129] H. Pfeiffer, W. Schüppel, Investigation of Magnetic Properties of Barium Ferrite Powders by Remanence Curves, Phys. Status Solidi A. **119** (1990) 259–269.

[130] L. Vlack, *Elements of Material Science and Engineering*, Addison-Wesley Co. Publishers Ltd, 6^{th} Ed New York, (1989) P. 450–459.

[131] E. Gordon, Fish, Soft Magnetic Materials, Proc. IEEE. **6** (1990) 78.

[132] A. Gadkari, T. Shinde, P. Vasambekar, Structural Analysis of Y^{3+}-Doped Mg-Cd Ferrites Prepared by Oxalate Co-Precipitation MethodReview, Mater. Chem. Phys. **144** (2009) 505–510.

[133] D. William, J. Callister, *Materials Science and Engineering An Introduction*, John Wiley and Sons, Inc, (2007) 784–786, 787.

[134] D. Dickson, F. Berry, *Mössbauer Specrtoscopy*, Cambridge University Press, Cambridge, UK (2005) P. 1–16.

[135] G. Wertheim, *Mössbauer effect: Principles and Applications*, Academic Press INC., New York, USA, (1964) p. 1–35, 4748.

[136] N. Greenwood, T. Gibb, *Mössbauer Spectroscopy*, Chapman and Hall, UK, London, (1971) p. 46–122.

[137] U. Gonser, *Mössbauer Spectroscopy*, Springer-Verlage Heidelberg, Germany, (1975) p. 1–48, 98–122.

[138] P. Gütlich, E. Bill, A. Trautwein, *Mössbauer Spectroscopy and Transition Metal Chemistry*, Springer Heidelberg Dordrecht London New York, (2011) p. 11–15, 80.

[139] Y. Chen, D. Yang, *Mössbauer Effect in Lattice Dynamics*, Wiley-VCH Verlage GmbH & Co. Weinheim, Germany, (2007) p. 1–26, 29–78.

[140] H. Verma, *and Nuclear Analytical Methods*, Springer-Verlag Berlin Heidelberg, (2007) p. 198, 382.

[141] P. Dominic, E. Dickson, F. Berry, *Mössbauer Spectroscopy*, Cambridge University Press, London, (1986) p. 22.

[142] H. Jakubke, H. Jeschkeit, *Concise Encyclopedia Chemistry*, Treanslated to English and revised by: M. Eagleson. Walter de Gruyter Berlin. New York, (1994) p. 670.

[143] J. Msomi, Synthesis, Structural and Magnetic Properties of Bulk and Nano-sized (Zn, Cd, Cu)$_{0.5}$Ni$_{0.5}$ Fe_2O_4 and $NiFe_2O_4$ Ferrites, University of KwaZulu-Nztal (2007) PhD thesis. .

[144] P. Narayanan, *Essentials of Biophysics*, New Age International (P) Ltd., New Delhi, (2000) p. 243.

[145] D. Dickson, F. Berry, *Mössbauer Spectroscopy*, Cambridge University Press, New York, (1986) p. 10.

[146] C. Kittel, *Introduction to Solid State Physics*, John Wiley & Sons. 5th edition, (2005) p. 302–304.

[147] H. Chung, D. Smith, *Industrial applications of X-ray diffraction*, Marcel DekkerNew, York (1999) p. 798.

[148] A. Salunkhe, V. Khot, M. Phadatare, N. Thorat, R. Joshi, H. Yadav, S. Pawar, Low Temperature Combustion Synthesis and Magnetostructural Properties of Co-Mn Nanoferrites, J. Magn. Magn. Mater **352** (2014) 91–98.

[149] K. Sing, D. Everett, R. Haul, L. Moscou, R. Pierotti, J. Rouquerol, T. Siemieniewska, Pure Appl. Chem **57** (1985) 603–619.

[150] G. Li, P. Miao, *Electrochemical Analysis of Proteins and Cells*, Springer Briefs in Molecular Science. DOI: 10.1007/978-3-642-34252-3, (2013) p. 7.

[151] O. Farghaly, R. A. Hameed, A. Abu-Nawwas, Analytical Application Using Modern Electrochemical Techniques, Int J Electrochem Sci. **9** (2014) 3287–3318.

[152] A. Shrivastava, J. Sharma, V. Soni, Various Electroanalytical Methods for the Determination of Uranium in Different Matrices, Bull Fac Pharm Cairo Univ. **51** (2013) 113–129.

[153] M. Ghoneim, M. Abdel-Azzem, H. El-Desoky, A. M. Ghoneim, A. Khattab, Electrochemical Reduction and Stripping Voltammetric Determination of the Anti-Glaucoma Drug Levobunolol HCl in Formulation and Human Serum at the Mercury Electrode, J Braz Chem Soc. **25** (2014) 1407–1418.

[154] A. Wieckowski, K. Itaya, *Electrode Processes VI*, The electrochemichal society, Inc. United State of America-New Jersey (1996) p. 29.

[155] C. Brett, A. Brett, *Electrochemistry: Principles Methods and Applications*, Oxford University Press (1993) p. 45–50.

[156] G. Mabbott, An Introduction to Cyclic Voltammetry, J. Chem. Educ. **60** (1983) 697–712.

[157] R. Vyas, B. Wang, Electrochemical Analysis of Conducting Polymer Thin Films, Int. J. Mol. Sci. **11** (2010) 1956–1972.

[158] B. Rezaei, S. Damiri, Voltammetric Behavior of Multi-Walled Carbon Nanotubes Modified Electrode-Hexacyanoferrate(II) Electrocatalyst System as a Sensor for Determination of Captopril, Sens. Actuators B. **134** (2008) 324–331.

[159] A. Bard, L. Faulkner, *Electrochemical Methods-Fundamentals and Applications, Wiley* (2001) p45–65.

[160] J. Gonzalez-Rodriguez, J. Sevilla, T. Pineda, M. Blazquez, Electrochemical Analysis on Compounds of the Vitamin B_6 Family Using Glassy Carbon Electrodes, Int. J. Electrochem. Sci. **7** (2012) 2221–2229.

[161] E. Laviron, General Expression of the Linear Potential Sweep Voltammogram in the Case of Diffusionless Electrochemical Systems, J. Electroanal. Chem. **101** (1979) 19–28.

[162] A. Bard, L. Faulkner, *in Electrochemical methods: Fundamentals and applications*, 2nd ed, Wiley, New York, (2004) pp. 236.

[163] E. Laviron, A. Vallat, R. Maunier-Prest, The Reduction Mechanism of Aromatic Nitro Compounds in Aqueous Medium: Part V. The Reduction of Nitrosobenzene Between pH 0.4 and 13, J. Electroanal. Chem. **379** (1994) 427–435.

[164] D. Gosser, *in Cyclic Voltammetry: Simulation and Analysis of Reaction Mechanisms*, VCH, New York, (1993) p. 43.

[165] L. Fotouhi, M. Fatollahzadeh, M. Heravi, Electrochemical Behavior and Voltammetric Determination of Sulfaguanidine at a Glassy Carbon Electrode Modified With aMulti-Walled Carbon Nanotube, Int. J. Electrochem. Sci. **7** (2012) 3919–3928.

[166] M. Ashiq, S. Saleem, M. Malana, A. Ur-Rehman, Physical, Electrical and Magnetic Properties of Nanocrystalline Zr-Ni Doped Mn-Ferrite Synthesized by the Co-Precipitation Method, J. Alloys Comp. **486** (2009) 640–644.

[167] S. Jigajeni, S. Kulkarni, Y. Kolekar, P. J. S.B. Kulkarni, $Co_{0.7}Mg_{0.3}Fe_{2-x}Mn_xO_4$ – $Sr_{0.5}Ba_{0.5}Nb_2O_6$ Magnetoelectric Composites, J. Alloys Comp. **492** (2010) 402–405.

[168] H. Abdallah, T. Moyo, J. Msomi, A. Lancók, Mössbauer and Magnetic Studies of $Co_{0.5}Mn_{0.5}Fe_2O_4$ and $Mn_{0.1}Mg_{0.2}Co_{0.7}Fe_2O_4$ Nanoferrites, J. Supercond. Nov. Magn. **25** (2012) 2619–2623.

[169] H. Abdallah, J. Msomi, T. Moyo, J. Dolo, A. Lancók, Mössbauer and Magnetic Studies of $Mn_{0.1}Sr_{0.2}Co_{0.7}Fe_2O_4$ Nanoferrite, Hyperfne Interact. **203** (2011) 99–104.

[170] H. Abdallah, T. Moyo, Structural and Magnetic Studies of $(Mg, Sr)_{0.2}Mn_{0.1}Co_{0.7}Fe_2O_4$ Nanoferrites, J. Alloys Comp. **562** (2013) 156–163.

[171] G. Williamson, W. Hall, X-ray Line Broadening from Filed Aluminium and Wolfram, Acta. Metall. **1** (1953) 22–31.

[172] D. Nikam, S. Jadhav, V. Khot, R. Bohara, C. Hong, S. Malib, S. Pawar, Cation Distribution, Structural, Morphological and Magnetic Properties of $Co_{1-x}Zn_xFe_2O_4$ (x = 0-1) Nanoparticles, Roy. Soc. Chem. **5** (2015) 2338–2345.

[173] B. Aslibeiki, P. Kameli, H. Salamati, M. Eshraghi, T. Tahmasebi, Superspin Glass State in $MnFe_2O_4$ Nanoparticles, Magn. Magn. Mater. **322** (2010) 2929–2934.

[174] E. Manova, B. Kunev, D. Paneva, I. Mitov, L. Petrov, C. Estournes, C. DÓrleans, J. Rehspringer, M. Kurmoo, Mechano-Synthesis, Characterization, and Magnetic Properties of Nanoparticles of Cobalt Ferrite, $CoFe_2O_4$, Chem. Mater. **16** (2004) 5689–5696.

[175] J. Jing, F. Zhao, X. Yang, U. Gonser, Magnetic Relaxation in Nanocrystalline Iron-Oxides, Hyperfine Interact. **54** (1990) 571–575.

[176] S. Chakrabarti, S. Mandal, S. Chaudhuri, Cobalt doped γ-Fe_2O_3 Nanoparticles: Synthesis and Magnetic Properties, Nanotechnology. **16** (2005) 506–511.

[177] R. Kambale, P. Shaikh, S. Kamble, Y. Kolekar, Effect of Cobalt Substitution on Structural, Magnetic and Electric Properties of Nickel Ferrite, J. Alloys Comp. **478** (2009) 599–603.

[178] C. Upadhyay, H. Verma, V. Sathe, A. Pimpale, Effect of size and synthesis route on the magnetic properties of chemically prepared nanosize $ZnFe_2O_4$, J. Magn. Magn. Mater. **312** (2007) 271.

[179] C. Alves, A. Auino, M. Sousa, H. Rechenbrg, G. Goya, F. Tourinho, J. Depeyrot, Low Temperature Experimental Investigation of Finite-Size and Surface Effects in $CuFe_2O_4$ Nanoparticles of Ferrofluids, J. Metastable Nanocryst. Mater. **20** (2004) 694–699.

[180] L. Tung, V. Kolesnichenko, D. Caruntu, N. Chou, C. Connor, L. Spinu, Magnetic Properties of Ultrafine Cobalt Ferrite Particles, J. Appl. Phys. **93** (2003) 7486.

[181] G. Papaefthymiou, S. Ahmed, S. Kofinas, Magnetic and Structural Charachterization of $CoFe_2O_4$ Nanoparticles Encapsulated Within Block Copolymer Films, Rev. Adv. Mater. Sci. **10** (2005) 306–313.

[182] S. Pardeshi, R. Pawar, $SrFe_2O_4$ Complex Oxide an Effective and Environmentally Benign Catalyst for Selective Oxidation of Styrene, J. Mol. Catal. A. Chem. **334** (2011) 35–43.

[183] V. Kumar, A. Rana, M. Yadav, R. Pant, Size-Induced Effect on Nano-Crystalline $CoFe_2O_4$, J. Magn. Magn. Mater. **320** (2008) 1729–1734.

[184] S. Kumar, V. Singh, S. Aggarwal, U. Mandal, R. Kotnala, Synthesis of Nanocrystalline $Ni_{0.5}Zn_{0.5}Fe_2O_4$ Ferrite and Study of its Magnetic Behavior at Different Temperatures, Mat. Sci. Eng: B. **166** (2010) 76–28.

[185] R. Arulmurugan, G. Vaidyanathan, S. Sendhilnathan, B. Jeyadevan, Co-Zn Ferrite Nanoparticles for Ferrofluid Preparation: Study on Magnetic Properties, Physica B. **368** (2005) 225–231.

[186] Y. Muraoka, H. Tabata, T. Kawai, Effects of Light-Irradiation on Spin-Glass State and Magnetoresistive Properties of $Zn_{0.5}Co_{0.5}Fe_2O_4$ Spinel Ferrite Films, Sol. State Commun. **120** (2001) 255–258.

[187] A. Junior, E. Lima, M. Novak, Synthesis of Nanoparticles of $Co_xFe_{(3-x)}O_4$ by Combustion Reaction Method, J. Magn. Magn. Mater. **308** (2007) 198–202.

[188] R. Kambale, P. Shaikh, N. Harare, V. Bilur, Y. Kolekar, C. Bhosale, K. Rajpure, Structural and Magnetic Properties of $Co_{1-x}Mn_xFe_2O_4$ ($0 \leq x \leq 0.4$) spinel ferrites synthesized by combustion route, J. Alloys Compd. **490** (2010) 568–571.

[189] M. Kruk, M. Jaroniec, Gas Adsorption Characterization of Ordered Organic-Inorganic Nanocomposite Materials, J. Chem. Mater. **10** (2001) 3169–3183.

[190] M. Rajendran, R. Pullar, A. Bhattachary, D. Das, S. Chintalapudi, C. Majumdar, Magnetic Properties of Nanocrystalline $CoFe_2O_4$ Powders Prepared

at Room Temperature: Variation with Crystallite Size, J. Magn. Magn. Mater. **232** (2001) 71–83.

[191] P. Lihitkar, S. Violet, M. Shirolkar, J. Singhc, O. Srivastava, R. Naik, S. Kulkarni, Confinement of Zinc Oxide Nanoparticles in Ordered Mesoporous Silica MCM-41, Mater. Chem. Phys. **133** (2012) 850–856.

[192] Y. Köseoğlu, F. Alan, M. Tan, R. Yilgin, M. Öztürk, Low Temperature Hydrothermal Synthesis and Characterization of Mn Doped Cobalt Ferrite Nanoparticles, Ceramic Intern. **38** (2012) 3625–3634.

[193] K. Maaz, A. Mumtaz, S. Hasanain, M. Bertino, Temperature Dependent Coercivity and Magnetization of Nickel Ferrite Nanoparticles, J. Magn. Magn. Mater. **322** (2010) 2199–2202.

[194] F. Bloch, Zur Theorie des Ferromagnetismus, Z. Phys. **61** (1931) 206.

[195] E. Stoner, Wohlfarth, E. Philos, A Mechanism of Magnetic Hysteresis in Heterogeneous Alloys, J. Trans. R. Soc. Lond. A Math. Phys. Eng. Sci. **240** (1948) 642.

[196] N. Chaudhari, R. Kambale, D. Bhosale, S. Suryavanshi, S. Sawant, Thermal Hysteresis and Domain States in Ni-Zn Ferrites Synthesized by Oxalate Precursor Method, J. Magn and Magn Mater. **322** (2010) 1999–2005.

[197] P. Hendriksen, S. Linderoth, P. Lindgard, Finite-Size Modifications of the Magnetic Properties of Clusters, Phys. Rev B. **48** (1993) 7259.

[198] R. Aquino, J. Depeyrot, M. Sousa, F. A. Tourinho, E. Dubois, R. Perzynski, Magnetization Temperature Dependence and Freezing of Surface Spins in Magnetic Fluids Based on Ferrite Nanoparticles, Phys. Rev B. **B 72** (2005) 184435.

[199] J. Rupp, A. Infortuna, L. Gauckler, Microstrain and Self-Limited Grain Growth in Nanocrystalline Ceria Ceramics, Acta Mater. **54** (2006) 1721–1730.

[200] G. El-Shobaky, A. Turky, N. Mostafa, S. Mohamed, Effect of Preparation Conditions on Physicochemical, Surface and Catalytic Properties of Cobalt Ferrite Prepared by Coprecipitation, J. Alloy Compd. **493** (2010) 415–422.

[201] X. Li, C. Xu, X. Han, L. Qiao, T. Wang, F. Li, Synthesis and Magnetic Properties of Nearly Monodisperse $CoFe_2O_4$ Nanoparticles Through a Simple Hydrothermal Condition, Nanoscale Res Lett. **5** (2010) 1039–1044.

[202] T. Han, K. J. Huang, J. Li, Y. M. Liu, M. Yu, β-Cyclodextrin-Cobalt Ferrite Nanocomposite as Enhanced Sensing Platform for Catechol Determination, Colloids Surface B. **98** (2012) 58–62.

[203] L. Cui, P. Guo, Peizhi, G. Zhang, Q. Li, R. Wang, M. Zhou, L. Ran, X. Zhao, Facile Synthesis of Cobalt Ferrite Submicrospheres with Tunable Magnetic and Electrocatalytic Properties, Colloids Surface A. **423** (2013) 170–177.

[204] M. Shizuya, M. Isobe, E. Takayama-Muromachi, Structure and Properties of the $CaFe_2O_4$–Type Cobalt Oxide $CaCo_2O_4$, J. Solid State Chem. **180** (2007) 2550–2557.

[205] J. Qiu, L. Le, M. Gu, Nanocrystalline Structure and Magnetic Properties of Barium Ferrite Particles Prepared via Glycine as a Fuel, Mat. Sci. Eng. A-Struct. **393** (2005) 361–365.

[206] O. Palchik, J. Zhua, A. Gedanken, Microwave Assisted Preparation of Binary Oxide Nanoparticles, J. Mater. Chem. **10** (2000) 1251–1254.

[207] J. Nelson, T. Chiller, J. Powers, F. Angulo, Fluoroquinolone-Resistant Campylobacter Species and the Withdrawal of Fluoroquinolones from Use in Poultry: A Public Health Success Story, Clin. Infec. Dis. **44** (2007) 977–980.

[208] M. Adorka, M. Lubbe, J. Serfontein, H. K. K. Allen, Making Antibiotic Choices: Formula Derivation and Usage in the Rational Selection of Antibiotics in the Empirical Treatment of Infections, Trop. J. Pharm. Res. **12** (2013) 1029–1034.

[209] V. Saraswathi, J. Padmavathy, B. Mamatha, N. Bindu, S. Vijayalakshmi, A Sin of Biotechnology, Bioterrorism - Anthrax, Int. J. Pharm.Tech. Res. **2** (2010) 2044–2047.

[210] G. Kim, J. D. Rosso, The Risk of Fluoroquinolone-induced Tendinopathy and Tendon Rupture, J. Clin. Aesthet. Dermatol. **3** (2010) 49–54.

[211] M. Upadya, K. Ruxana, Toxic Epidermal Necrolysis and Agranulocytosis: Rare Adverse Effects of Ciprofloxacin, Indian J. Med. Sci. **63** (2009) 461–463.

[212] J. Hällgren, M. Tengvall-Linder, M. Persson, C. Wahlgren, Stevens-Johnson Syndrome Associated with Ciprofloxacin: a Review of Adverse Cutaneous Events Reported in Sweden as Associated with this Drug, J. Am. Acad. Dermatol. **49** (2003) S267–9.

[213] M. Chaudhry, N. Tarneja, A. Gundale, D. Roa, R. Levey, Bone Marrow Suppression: a Side Effect of Ciprofloxacin Therapy., Am. J. Ther. **17** (2010) 167–8.

[214] C. Alan, H. Koçoğlu, A. Ersay, Y. Ertung, H. Kurt, Unexpected Severe Hepatotoxicity of Ciprofloxacine: Two Case Reports. Drug Chem Toxicol, Drug Chem. Toxicol. **34** (2011) 189–91.

[215] M. Amorim, K. L. Marques, J. Santos, J. Lima, Ciprofloxacin and Norfloxacin Spectrophotometric Determination in a Fully Automated Multi-Pumping Flow System, Anal. Lett. **44** (2011) 2074–2084.

[216] K. Basavaiah, P. Nagegowda, Titrimetric and Spectrophotometric Assay Methods for Ciprofloxacin in Pharmaceuticals Based on Neutralization Reaction, Nat. Acad. Sci. Lett. **29** (2006) 189–94.

[217] S. Shtykov, T. Smirnova, Y. Bylinkin, N. Kalashnikova, D. Zhemerichkin, Determination of Ciprofloxacin and Enrofloxacin by the Sensitized Fluorescence of Europium in the Presence of the Second Ligand and Micelles of Anionic Surfactants, J. Anal. Chem. **62** (2007) 136.

[218] B. Aksoy, I. Kucukguzel, S. Rollas, Development and Validation of a Stability-Indicating HPLC Method for Determination of Ciprofloxacin Hydrochloride and its Related Compounds in Film-Coated Tablets, Chromatographia. **66** (2007) S57.

[219] B. Shrestha, H. Basnett, S. Patel, R. Karki, S. Agarwal, R. Mazumder, B. Stephenrathinaraj, Stability Indicating RP-HPLC Method for Analysis of Ciprofloxacin in Tablet Dosage Form, Res. J. Pharm. Tech. **3** (2010) 221–23.

[220] A. Ensafi, A. Allafchian, R. Mohammadzadeh, Characterization of $MgFe_2O_4$ Nanoparticles as a Novel Electrochemical Sensor: Application for the Voltammetric Determination of Ciprofloxacin, Anal. Sci. **28** (2012) 705–10.

[221] M. Malviya, J. Singh, R. Singh, Electrochemical Characterization of Polypyrrole/Cobalt Ferrite Composite Films for Oxygen Reduction, Indian J. Chem. A. **44A** (2005) 2233.

[222] V. Simonsen, D. Find, M. Lilliedal, R. P. abd K. Kammer, Spinels as Cathodes for the Electrochemical Reduction of O_2 and NO, Top. Catal. **45** (2007) 143–148.

[223] V. Kumary, J. Divya, T. Nancy, K. Sreevalsan, Voltammetric Detection of Paracetamol at Cobalt Ferrite Nanoparticles Modified Glassy Carbon Electrode, Int. J. Electrochem. Sci. **8** (2013) 6610–6619.

[224] A. Vidyadharan, D. Jayan, T. Nancy, $Ni_{0.1}Co_{0.9}Fe_2O_4$–Based Electrochemical Sensor for the Detection of Paracetamol, J. Solid State Electrochem. **18** (2014) 2513–2519.

[225] A. Rumplecker, F. Kleitz, E. Salabas, F. Schuth, Hard Templating Pathways for the Synthesis of Nanostructured Porous Co_3O_4, J. Chem. Mater. **19** (2007) 485–496.

[226] A. Lakshman, P. S. Rao, K. Rao, Mössbauer Spectroscopic Analyses of $Mg_{0.9}Cu_{0.1}Mn_{0.05}Cr_xFe_{1.95-x}O_4$ Spinel Ferrites, Mater. Lett. **60** (2006) 7–10.

[227] B. Rao, P. S. Rao, G. Murthy, K. Rao, Mössbauer Study of the System $Ni_{0.65}Zn_{0.35}Fe_{2-x}Sc_xO_4$, J. Magn. Magn. Mater. **268** (2004) 315–320.

[228] A. Ghasemi, A. P. Jr, C. F. C. Machado, Structural and Magnetic Characteristics of $Co_{1-x}Ni_{x/2}Sr_{x/2}Fe_2O_4$, J. Magn. Magn. Mater. **324** (2012) 2193–2198.

[229] C. Vázquez-Vázquez, M. López-Quintela, M. B.-N. nez, Finite Size and Surface Effects on the Magnetic Properties of Cobalt Ferrite nanoparticles , J. Rivas, J Nanopart Res. **13** (2011) 1663–1676.

[230] H. Nathani, R. Misra, Surface Effects on the Magnetic Behavior of Nanocrystalline Nickel Ferrites and Nickel Ferrite-Polymer Nanocomposites, Mater.Sci.Eng: B. **113** (2004) 228–235.

[231] C. Lin, H. Chen, A. Nakaruk, P. Koshy, C. Sorrell, Effect of Annealing Temperature on the Photocatalytic Activity of TiO_2 Thin Films, Energ. Procedia. **34** (2013) 627–636.

[232] A. Sudha, S. Sharma, T. Maity, Effects of Annealing Temperature on Structural and Electrical Properties of Indium Oxide Thin Films Prepared by Thermal Evaporation, Mater. Lett. **157** (2015) 19–22.

[233] A. Birgani, M. Niyaifar, A. Hasanpour, Study of Cation Distribution of Spinel Zinc Nano-Ferrite by X-ray, J. Magn. Magn. Mater. **374** (2015) 179–181.

[234] A. Bhattacharjee, D. Bhakat, Molecular Material–N(n-$C_4H_9)_4[Ni(II)_{0.5}Fe(II)_{0.5}FE(III)(C_2O_4)_3]_\infty$: Magnetic, Mössbauer and Electrical Conductivity Studies, Physica B: Condens. Matter. **404** (2009) 3448–3451.

[235] O. Lemine, M. Sajieddine, M. Bououdina, S. M. R. Msalam, A. Alyamani, Rietveld Analysis and Mössbauer Spectroscopy Studies of Nanocrystalline Hematite α-Fe_2O_3, J. Alloys Compd. **502** (2010) 279–282.

[236] A. Albuquerque, J. Ardisson, W. Macedo, A Study of Nanocrystalline NiZn-Ferrite-SiO_2 Synthesized by Sol-Gel, J. Magn. Magn. Mater. **192** (1999) 277–280.

[237] S. Singh, N. Kumar, A. Jha, M. Sahni, R. Bhargava, A. Chawla, R. Chandra, S. Kumar, S. Chaubey, Effect of Annealing Temperature on the Physical Properties of Zn-Ferrite Nanoparticles, J Supercond Nov Magn. **27** (2014) 821–826.

[238] G. Zhang, M. Liu, Effect of Particle Size and Dopant on Properties of SnO_2-Based Gas Sensors, Sens. Actuators, B: Chem. **69** (2000) 144–152.

[239] B. Martínez, X. Obradors, L. Balcells, A. Rouanet, , C. Monty, Low Temperature Surface Spin-Glass Transition in γ-Fe_2O_3 Nanoparticles, Phys. Rev. Lett. **80** (1998) 181–184.

[240] J. Hochepied, M. Pileni, Ferromagnetic Resonance of Nonstoichiometric Zinc Ferrite and Cobalt-Doped Zinc Ferrite Nanoparticles, J. Magn. Magn. Mater. **231** (2001) 45–52.

[241] V. Moncada, A. Álvarez Lueje, Development of A Modified Carbon Electrode with Ionic Liquid and its Application for Electrocatalytic Oxidation and Voltammetric Determination of Levodopa, J. Chil. Chem. Soc. **59** (2014) N^0 2.

[242] M. Wu, C. Chung, Z. Ceng, Cyclic Voltammetric Deposition of Discrete Nickel Phosphide Clusters with Mesoporous Nanoparticles on Fluorine-Doped Tin Oxide Glass as a Counter Electrode for Dye-Sensitized Solar Cells, RSC Adv. **5** (2015) 4561.

[243] K. Anuar, W. Tan, M. Atan, K. Dzulkefly, S. Ho, H. M. Jelas, N. Saravanan, Cyclic Voltammetry Study of Copper Tin Sulfide Compounds, Pacific J. Sci. Technol. **8** (2007) 252–260.

[244] E. Laviron, A Multilayer Model for the Study of Space Distributed Redox Modified Electrodes: Part II. Theory and Application of Linear Potential Sweep Voltammetry for a Simple Reaction, J. Electroanal. Chem. **112** (1980) 11–32.

[245] E. Brown, R. large, *Physical Methods of Chemistry*, Wiley Interscience, New York .

[246] S. Zhang, S. Wei, Electrochemical Determination of Ciprofloxacin Based on the Enhancement Effect of Sodium Dodecyl Benzene Sulfonate, Bull. Korean Chem. Soc. **28** (2007) 543–546.

[247] H. Yi, C. Li, Voltammetric Determination of Ciprofloxacin Based on the Enhancement Effect of Cetyltrimethylammonium Bromide (CTAB) at Carbon Paste Electrode, Russ. J. Electrochem. **43** (2007) 1377–1381.

[248] L. Ming, X. Xi, Y. Sun, J. Liu, Voltammetric Determination of Ciprofloxacin Hydrochloride on Multi-Wall Carbon Nanotube Modified Electrode, Chin. J. Antibiot. **34** (2009) 767–768.

[249] B. Uslu, B. Bozal, M. Kuscu, Anodic Voltammetry of Ciprofloxacin and its Analytical Applications, Open Chem. Biomed. Met. J. **3** (2010) 108–114.

[250] A. Ensafi, M. T. M, T. Khayamian, F. Hasanpour, Simultaneous Voltammetric Determination of Enrofloxacin and Ciprofloxacin in Urine and Plasma Using Multiwall Carbon Nanotubes Modified Glassy Carbon Electrode by Least-Squares Support Vector Machines, Anal. Sci. **26** (2010) 803–8.

[251] B. Chethana, Y. Naik, Electrochemical Studies of Antibiotic Drug Ciprofloxacin Using Tyrosine Modified Carbon Paste Electrode, Inventi Impact Med. Chem. **3** (2012) 138.

[252] V. Hoang, T. Nguyen, Adsorptive Cathodic Stripping Voltammetric Determination of Ciprofloxacin in Bulk Powder, Pharmaceutical Dosage Forms and Urine, Trop. J. Pharm. Res. **12** (2013) 783.

[253] F. Zhang, S. Gu, Y. Ding, Z. Zhang, L. Li, A Novel Sensor Based on Electropolymerization of β-Cyclodextrin and L-Arginine on Carbon Paste Electrode for Determination of Fluoroquinolones, Anal. Chim. Acta. **770** (2013) 53–61.

[254] M. Shamsipur, M. Gholivand, S. Dehdashtian, M. Feyzi, F. Jafari, Synthesis of Co/TiO_2 Nanocomposite and its Use in Construction of a Sensitive and Selective Sensor for Determination of Ciprofloxacin, Adv. Mater. Res. **829** (2014) 563–567.

[255] A. Kawde, M. A. Aziz, N. Odewunmi, N. Hassan, A. A. Sharaa, Electroanalytical Determination of Antibacterial Ciprofloxacin in Pure Form and in Drug Formulations, Arab. J. Sci. Eng. **39** (2014) 131–138.

[256] R. Montes, M. Marra, M. Rodrigues, R. M. E.M. Richter, Fast Determination of Ciprofloxacin by Batch Injection Analysis with Amperometric Detection and Capillary Electrophoresis with Capacitively Coupled Contactless Conductivity Detection, Electroanalysis. **26** (2014) 432–438.

[257] N. Diab, I. Abu-Shqair, R. Salim, M. Al-Subu, The Behavior of Ciprofloxacin at a DNA Modified Glassy Carbon Electrodes, Int. J. Electrochem. Sci. **9** (2014) 1771.

[258] A. Al-Ghamdi, A. Bani-Yaseen, Electrochemical Reduction of Ciprofloxacin at the Mercury Electrode and its Voltammetric Determination in Tablet and Urine, Russ. J. Electrochem. **50** (2014) 355–362.

[259] X. Zhang, Y. Wei, Y. Ding, Electrocatalytic Oxidation and Voltammetric Determination of Ciprofloxacin Employing Poly(Alizarin Red)/Graphene Composite Film in the Presence of Ascorbic Acid, Uric Acid and Dopamine, Anal. Chim. Acta. **835** (2014) 29–36.

[260] G. Sohn, R. Cohen, Processible Optically Transparent Block Copolymer Films Containing Superparamagnetic Iron Oxide Nanoclusters, Chem. Mater. **9** (1997) 264–269.

[261] R. Gopathi, V. Katrapally, V. Chetty, Synthesis, Structural and Magnetic Properties of Copper Substituted Nickel Ferrites by Sol-Gel Method, Mat. Sc. Appl. **3** (2012) 87–91.

[262] Y. Purushotham, M. Singh, S. Sud, P. Reddy, Electrical and Elastic Behavior of In and Al Substituted Mg-Mn Ferrites, Int. J. Mod. Phys. B. **12** (1998) 2247–2262.

[263] M. Reddy, X. Zhou, A. Yann, S. Du, Q. Huang, A. Mohamed, Low Temperature Hydrothermal Synthesis, Structural Investigation and Functional Properties of $Co_xMn_{1-x}Fe_2O_4$ ($0 \leq x \leq 1.0$) nanoferrites, Superlatt. Microstr. **81** (2015) 233–242.

[264] S. Diodati, L. Nodari, M. Natile, U. Russo, E. Tondello, L. Lutterotti, S. Gross, Highly Crystalline Strontium Ferrites $SrFeO_{3-\delta}$: an Easy and Effective Wet-Chemistry Synthesis, Dalton Trans. **41** (2012) 5517–5525.

[265] A. Ensafi, F. Saeid, B. Rezaei, A. Allafchian, $NiFe_2O_4$ Nanoparticles Decorated with MWCNTs as a Selective and Sensitive Electrochemical Sensor for the Determination of Epinephrine Using Differential Pulse Voltammetry, Anal. Methods. **6** (2014) 6885–6892.

[266] B. Ul-ain, S. Ahmed, M. ur Rehman, Y. Huang, C. Randall, Electrical and Thermoelectric Attributes of $Ba_2Co_2Fe_{12-2x}(Ti\text{-}Mn)_xO_{22}$ and their Catalytic Activity for Complete N_2O Decomposition, New J. Chem. **37** (2013) 2768–2777.

[267] M. Hasanzadeh, N. Shadjou, M. de la Guardia, Iron and Iron-oxide Magnetic Nanoparticles as Signal-Amplification Elements in Electrochemical Biosensing, Tr. Anal. Chem. **72** (2015) 1–9.

[268] G. Absalan, M. Akhond, A. Bananejad, H. Ershadifar, Highly Sensitive Determination of Nitrite Using a Carbon Ionic Liquid Electrode Modified with Fe_3O_4 Magnetic Nanoparticle, J. Iran. Chem. Soc. **12** (2015) 1293–1301.

[269] D. Grieshaber, R. MacKenzie, J. Vörös, Electrochemical Biosensors - Sensor Principles and Architectures, Sensors. **8** (2008) 1400–1458.

[270] H. Wei, E. Wang, Electrochemiluminescence of Tris(2,2'-Bipyridyl) Ruthenium and its Applications in Bioanalysis: A Review, Luminescence. **26** (2011) 77–85.

[271] B. Roca, C. Lapuebla, B. Vidal-Tegedor, HAART with Didanosine Once Versus Twice Daily: Adherence and Efficacy, Int. J. Infect. Dis. **9** (2005) 195–200.

[272] B. Ahidjo, R. Veale, A. Duse, P. Becker, E. Marais, The Nucleoside Reverse Transcriptase Inhibitors Didanosine, Lamivudine, Stavudine and Zidovudine Show Little Effect on the Virulence of Candida Albicans in Vitro, Int. J. Antimicrob. Agents. **32** (2008) 186–191.

[273] C. Reust, Common Adverse Effects of Antiretroviral Therapy for HIV Disease, Am. Fam. Physician. **83** (2011) 1443–1451.

[274] A. de Oliveira, T. Loewen, L. Cabral, E. dos Santos, C. Rodrigues, H. Castro, T. dos Santos, Development and Validation of a HPLC-UV Method for the Determination in Didanosine Tablets, J. Pharm. Biomed. Anal. **38** (2005) 751–756.

[275] S. B. H. Sura, T. Murthy, Quantization of Didanosine in Human Plasma using High-Performance Liquid Chromatography-Tandem Mass Spectrometry, J. Adv. Pharm. Edu. Res. **3** (2013) 187–195.

[276] R. Kane, P. Bhokare, C. Nalawade, M. Sayyed, R. Paliwal, Spectrophotometric Estimation of Didanosine in Bulk Drug and its Formulation, Int. J. Pharm. Chem. Sc. **1** (2012) 2277–5005.

[277] J. Sangshetti, P. Kulkarni, D. Shinde, Spectrophotometric Determination of Didanosine in Bulk and Tablet Formulation, Tr. App. Sc. Res. **2** (2007) 71–75.

[278] K. Ozoemena, R. S. van Staden, T. Nyokong, Metallophthalocyanine Based Carbon Paste Electrodes for the Determination of 2',3'-Dideoxyinosine, Electroanal. **21** (2009) 1651–1654.

[279] P. Farias, A. Castro, A. Cordoves, Didanosine Determination in Diluted Alkaline Electrolyte by Adsorptive Stripping Voltammetry at the Mercury Film Electrode, J. Electrochem. Sci. Eng. **2** (2012) 133–142.

[280] M. Khan, A. Haque, K. Kim, Electrochemical Determination of Uric Acid in the Presence Ascorbicacid on Electrochemically Reduced Graphene Oxide Modified Electrode, J. Electroanal. Chem. **700** (2013) 54–59.

[281] R. Kadara, N. Jenkinson, C. Banks, Characterisation of Commercially Available Electrochemical Sensing Platforms, Sens. Act. B: Chem. **138** (2009) 556–562.

[282] R. Kodama, C. Seaman, A. Berkowitz, M. Maple, Low-Temperature Magnetic Relaxation of Organic Coated $NiFe_2O_4$ Particles, J. Appl. Phys. **75** (1994) 5639–5641.

[283] G. Dionne, A Review Of Ferrites For Microwave Applications , Proc. IEEE. **63** (1975) 777–789.

[284] K. Maaz, S. Karim, K. Lee, M. Jung, G. Kim, Effect of Tmperature on the Magnetic Characteristics of $Ni_{0.5}Co_{0.5}Fe_2O_4$ Nanoparticles, Mater. Chem. Phys. **133** (2012) 1006–1010.

[285] J. Gowda, S. Nandibewoor, Electrochemical Behavior of Paclitaxel and its Determination at Glassy Carbon Electrode, Asian J. Pharm. Sc. **9** (2014) 42–49.

[286] H. Nalwa, *Handbook of Nanostructured Materials and Nanotechnology*, Academic Press, A Harcourt Science and Technology Company USA. (2000) p. 535.

[287] S. Bid, S. Pradhan, Preparation of Zinc Ferrite by High-Energy Ball-Milling and Microstructure Characterization by Rietveld's Analysis, Mater. Chem. Phys. **82** (2003) 27–37.

[288] N. Thapliyal, N. Osman, H. Patel, R. Karpoormath, R. Goyal, T. Moyo, R. Patel, NiO-ZrO_2 Nanocomposite Modified Electrode for the Sensitive and Selective Determination of Efavirenz, an Anti-HIV Drug, RSC advance **5** (2015) 40057–40064.

[289] F. Heiligtag, M. Niederberger, The Fascinating World of Nanoparticle Research, Mater. Today. **16** (2013) 262–271.

[290] S. Chaturvedi, P. Dave, N. Shah, Applications of Nano-Catalyst in New Era, J SAUDI CHEM SOC. **16** (2012) 307–325.

[291] Z. Zi, Y. Sun, X. Zhu, Z. Yang, J. Dai, W. Song, Synthesis and Magnetic Properties of $CoFe_2O_4$ Ferrite Nanoparticles, J. Magn. Magn. Mater. **321** (2009) 1251–1255.

[292] Z. Zhang, L. Wang, X. Xu, Y. Dong, L. Zhang, Development of a Validated HPLC Method for the Determination of Tenofovir Disoproxil Fumarate Using a Green Enrichment Process, J Anal Methods. **7** (2015) 6290–6298.

[293] X. Li, G. Tan, W. Chen, B. Zhou, D. Xue, Y. Peng, F. Li, N. Mellors, Nanostructural and Magnetic Studies of Virtually Monodispersed $NiFe_2O_4$ Nanocrystals Synthesized by a Liquid-Solid-Solution Assisted Hydrothermal Route, J Nanopart Res. **14** (2012) 1–9.

[294] P. Sivakumar, R. Ramesh, A. Ramanand, S. Ponnusamy, C. Muthamizhchelvan, Preparation and Properties of Nickel Ferrite ($NiFe_2O_4$) Nanoparticles Via Sol-Gel Auto-Combustion Method, Mater. Res. Bull. **46** (2011) 2208–2211.

[295] C. Xiangfeng, J. Dongli, Z. Chenmou, The Preparation and Gas-Sensing Properties of $NiFe_2O_4$ Nanocubes and Nanorods, Sens. Actuators, B. **123** (2007) 793–797.

[296] D. Zhang, X. Zhang, X. Ni, H. Zheng, D. Yang, Synthesis and Characterization of $NiFe_2O_4$ Magnetic Nanorods Via a PEG-Assisted Route, J. Magn. Magn. Mater. **292** (2005) 79–82.

[297] S. Young, S. Britcher, L. Tran, L. Payne, W. Lumma, T. Lyle, J. Huff, P. Anderson, D. Olsen, S. Carroll, A novel, Highly Potent Nonnucleoside Inhibitor of the Human Immunodeficiency Virus Type 1 Reverse Transcriptase, Antimicrob. Agents Chemother. **39** (1995) 2602–2605.

[298] S. Sungkanuparph, A. Vibhagool, P. Mootsikapun, P. Chetchotisakd, S. Tansuphaswaswadikul, C. Bowonwatanuwong, W. Chantratita, Efavirenz-Based Regimen as Treatment of Advanced AIDS with Cryptococcal Meningitis, J. Acquir. Immune Defic. Syndr. **33** (2003) 118–119.

[299] E. Arts, D. Hazuda, HIV-1 Antiretroviral Drug Therapy, Cold Spring Harb. Perspect. Med. **2** (2012) 1–23.

[300] I. Metzger, T. Quigg, N. Epstein, A. Aregbe, N. Thong, J. Callaghan, D. Flockhart, A. Nguyen, C. Stevens, S. Gupta, Z. Desta, Substantial Effect of Efavirenz Monotherapy on Bilirubin Levels in Healthy Volunteers, Curr. Ther. Res. **76** (2014) 64–69.

[301] P. Leutscher, C. Stecher, M. Storgaard, C. Larsen, Discontinuation of Efavirenz Therapy in HIV Patients Due to Neuropsychiatric Adverse Effects, Scand. J. Infect. Dis. **45** (2013) 645–651.

[302] K. Khoza-Shangase, Highly Active Antiretroviral Therapy: Does it Sound Toxic?, J. Pharm. Bioallied Sci. **3** (2011) 142–153.

[303] D. Cooper, J. Heera, P. Ive, M. Botes, E. Dejesus, R. Burnside, N. Clumeck, S. Walmsley, A. Lazzarin, G. Mukwaya, M. Saag, E. van Der Ryst, Efficacy and Safety of Maraviroc VS. Efavirenz in Treatment-Naive Patients with HIV-1: 5-Year Findings, AIDS. **28** (2014) 717–725.

[304] M. Gatch, A. Kozlenkov, R. Huang, W. Yang, J. Nguyen, J. Gonzalez-Maeso, K. Rice, C. France, G. Dillon, M. Forster, J. Schetz, The HIV Antiretroviral Drug Efavirenz has LSD-Like Properties, Neuropsychopharmacol. **38** (2013) 2373–2384.

[305] S. Ramesh, S. Alexandar, S. Muniyappan, A Validated RP-HPLC Method for Estimation of Efavirenz in Pharmaceutical Forulation, World J. Pharm. Pharmaceut. Sc. **2** (2013) 2003–2010.

[306] B. Prathap, A. Dey, G. Rao, Analytical Method Development and Validation of Invitro Dissolution Studies of Efavirenz, Lamivudine and Tenofovir Disoproxil Fumarate in Pharmaceutical Dosage form by RP-HPLC, J. Global Trends Pharmcol. Sc. **5** (2014) 1634–1640.

[307] R. Heydari, M. Rashidipour, N. Naleini, Determination of Efavirenz in Plasma by Dispersive Liquid-Liquid Microextraction Coupled to High-Performance Liquid Chromatography Rouhollah Heydari, Marzieh Rashidipour, Nasim Naleini, Current Analytical Chemistry, Curr. Anal. Chem. **10** (2014) 280–287.

[308] Y. Kumar, N. Rao, Development of Rapid UV Spectrophotometric Method for the Estimation of Efavirenz in Formulations, J. Chem. **7** (2010) 856–860.

[309] S. Gurav, D. Prakash, A. Deshpande, S. Walsangikar, Spectrophotometric Method for Estimation of Efavirenz from Tablet Formulation, Asian J. Res. Chem. **4** (2011) 754–756.

[310] A. Smith, G. Maruthi, A. Velmurugan, S. Parimalakrishnan, Development of Analytical Method for Efavirenz by UV Spectrophotometry Using Sodium Hydroxide as Solvent, Chem. Sin. **4** (2013) 144–149.

[311] A. Theron, D. Cromarty, M. Rheeders, M. Viljoen, Determination of Salivary Efavirenz by Liquid Chromatography Coupled with Tandem Mass Spectrometry, J. Chromatogr. B. **878** (2010) 2886–2890.

[312] P. Srivastava, G. Moorthy, R. Gross, J. Barrett, A Sensitive and Selective Liquid Chromatography/Tandem Mass Spectrometry Method for Quantitative Analysis of Efavirenz in Human Plasma, PLoS One. **8** (2013) 1–9.

[313] B. Dogan-Topal, B. Uslu, S. Ozkan, Voltammetric Studies on the HIV-1 Inhibitory Drug Efavirenz: The Interaction Between dsDNA and Drug Using

Electrochemical DNA Biosensor and Adsorptive Stripping Voltammetric Determination on Disposable Pencil Graphite Electrode, Biosens. Bioelectron. **24** (2009) 2358–2364.

[314] A. Castro, M. de Souza, N. Rey, P. Farias, Determination of Efavirenz in Diluted Alkaline Electrolyte by Cathodic Adsorptive Stripping Voltammetry at the Mercury Film Electrode, J. Braz. Chem. Soc. **22** (2011) 1662–1668.

[315] C. Sánchez-Sánchez, J. Solla-Gullón, V. Montiel, Electrocatalysis at Nanoparticles, Electrochem. **11** (2013) 34–70.

[316] A. Maringa, T. Mugadza, E. Antunes, T. Nyokong, Characterization and Electrocatalytic Behaviour of Glassy Carbon Electrode Modified with Nickel Nanoparticles Towards Amitrole Detection, J. Electroanal. Chem. **700** (2013) 86–92.

[317] R. Babu, P. Prabhu, S. Narayanan, Green Synthesized Nickel Nanoparticles Modified Electrode in Ionic Liquid Medium and its Application Towards Determination of Diomolecules, Talanta. **110** (2013) 135–143.

[318] X. Huang, R. Yuan, Y. Chai, J. Wang, Study on Hydrogen Peroxide Biosensor Based on Zirconium Dioxide and Carbon Nanotubes Modified Glass Carbon Electrode, Chem. Res. Appl. **21** (2009) 1687–1692.

[319] J. Qu, Y. Wang, J. Guo, T. Lou, Y. Dong, Determination of Catechol by a Laccase Biosensor Based on Silica-Modified Zirconia Nanoparticles, Anal. Lett. **47** (2014) 2537–2547.

[320] G. Christian, W. Purdy, The Residual Current in Orthophosphate Medium, J. Electroanal. Chem. **3** (1962) 363–367.

[321] N. Osman, N. Thapliyal, T. Moyo, R. Karpoormath, Investigation of magnetic and electrochemical sensing properties of novel $Ba_{1/3}Mn_{1/3}Co_{1/3}Fe_2O_4$ nanoparticles, New J. Chem. **39** (2015) 9596–9604.